

Concrete Beams Subjected to Repeated Drop-Weight Impact and Static Load

Assessment of structural response in experimental testing and predicted response with numerical analyses

Master's Thesis in the Master's Programme Structural Engineering and Building Technology

JACK JÖNSSON
ANTON STENSEKE

MASTER'S THESIS ACEX30-18-34

Concrete Beams Subjected to Repeated Drop-Weight Impact and Static Load

Assessment of structural response in experimental testing and predicted response with numerical analyses

Master's Thesis in the Master's Programme Structural Engineering and Building Technology

JACK JÖNSSON
ANTON STENSEKE

Architecture and Civil Engineering

Division of Structural Engineering

Concrete Structures

CHALMERS UNIVERSITY OF TECHNOLOGY

Gothenburg, Sweden 2018

Concrete Beams Subjected to Repeated Drop-Weight Impact and Static Load
Assessment of structural response in experimental testing and predicted response with numerical analyses
JACK JÖNSSON
ANTON STENSEKE

© JACK JÖNSSON , ANTON STENSEKE, 2018

Master's Thesis ACEX30-18-34
ISSN 1652-8557
Architecture and Civil Engineering
Division of Structural Engineering
Concrete Structures
Chalmers University of Technology
SE-412 96 Gothenburg
Sweden
Telephone: +46 (0)31-772 1000

Cover:
Strain fields in a reinforced concrete beam subjected to impact load at different time steps, from both experimental results and numerical modelling.

Chalmers Reproservice
Gothenburg, Sweden 2018

Concrete Beams Subjected to Repeated Drop-Weight Impact and Static Load

Assessment of structural response in experimental testing and predicted response with numerical analyses

Master's Thesis in the Master's Programme Structural Engineering and Building Technology

JACK JÖNSSON

ANTON STENSEKE

Architecture and Civil Engineering

Division of Structural Engineering

Concrete Structures

Chalmers University of Technology

ABSTRACT

The behaviour of a reinforced concrete structure subjected to dynamic loading differ compared to static loading. Examples of dynamic loads can be high wind loads, explosions or an impact. The purpose of this thesis was to increase the knowledge about dynamic loaded structures by conducting experiments on simply supported beams and evaluate their behaviour. The beams were subjected to an impact from a drop-weight, both repeatedly and once, and thereafter statically tested until failure. Undamaged beams were also tested statically to be able to form a basis of comparison.

The behaviour of the beams during the experiments were captured with a high speed camera and thereafter processed through digital image correlation (DIC). One of the main objectives with this thesis was to try to predict the response of the beams with different numerical methods such as a two-degree of freedom (2DOF) system and a non-linear finite element analysis in LS-DYNA. Deflection, plastic rotation capacity, internal work, impact force and impulse load are some of the parameters that were evaluated using the numerical methods with support by hand calculations.

When subjected to repeated impacts the beams experienced extensive local damage, resulting in a large reduction in load capacity. The extent of the local damages was unexpected and something that is difficult to predict with the numerical methods used. The local damages gave rise to spalling of the concrete which made the postprocessing in DIC difficult as well. Both the 2DOF model and LS-DYNA tended to overestimate the deflection of the beam, but still within reasonable limits. The crack pattern from the experiments had a good resemblance with the crack pattern obtained from LS-DYNA, where only the first drops was modelled.

The experimental results had a good overall resemblance with the results from the numerical methods for one drop. Regarding numerous drops, the local damage needs to be taken into account if the response is to be described in a more accurate way using such numerical methods.

Keywords: Reinforced concrete, impact loading, repeated impact loading, static loading, Digital image correlation, DIC, two-degree-of-freedom, 2DOF, LS-DYNA, non-linear finite element analysis, impact force, internal work, impulse load, plastic rotation capacity

Betongbalkar Utsatta för Upprepade Fallviktsförsök och Påföljande Statisk Belastning
Utvärdering av Strukturrespons från Experiment och Förutsedd Respons med Numeriska Analyser
Examensarbete i Structural Engineering and Building Technology

JACK JÖNSSON

ANTON STENSEKE

Arkitektur och samhällsbyggnadsteknik

Avdelningen för Konstruktionsteknik

Betongbyggnad

Chalmers Tekniska Högskola

SAMMANFATTNING

Beteendet hos en armerad betongkonstruktion som utsätts för dynamisk belastning skiljer sig från statisk belastning. Exempel på dynamiska laster kan vara höga vindlaster, explosioner eller en stöt. Syftet med avhandlingen var att öka kunskapen om dynamiskt belastade konstruktioner genom att utföra experiment på fritt upplagda balkar och sedan utvärdera deras beteende. Balkarna utsattes för olika antal stötar från en fallvikt och testades därefter statiskt till brott. Oskadade balkar testades också statiskt för att skapa en jämförelsebasis.

Balkarnas beteende under experimenten fångades med en höghastighetskamera och behandlades sedan med hjälp av digital bildkorrelation (DIC). Ett av målen med avhandlingen var att försöka förutsäga beteendet hos balkarna med hjälp av olika numeriska metoder såsom ett tvåfrihetsgradssystem (2DOF) och icke linjära finita elementmetodanalyser i LS-DYNA. Nedböjning, plastisk rotationskapacitet, inre arbete, stötlast och impuls är några av parametrarna som utvärderades med de olika numeriska metoderna, med stöd av handberäkningar.

När balkarna utsattes för upprepad stötbelastning uppstod stora lokala skador vilket ledde till en stor minskning i lastkapacitet. Storleken av de lokala skadorna var oväntad och någonting som är svårt att förutsäga med de numeriska metoderna som användes. Dom lokala skadorna gav upphov till splittring av betongen vilket gjorde efterbehandlingen i DIC svår. Både 2DOF modellen och LS-DYNA tenderade att överskatta nedböjningen av balken, men inom rimliga gränser. Sprickbildningen från experimenten hade en god överensstämmelse med sprickbildningen från LS-DYNA, där endast den första stöten modellerades.

Resultaten från experimenten stämde överlag bra med resultaten från de numeriska metoderna för det första släppet. Om man ska modellera upprepad stötar på ett mer korrekt sätt behöver de lokala skadorna tas i beaktning när man använder sådana numeriska metoder.

Nyckelord: Armerad betong, stötbelastning, upprepad stötbelastning, statisk belastning, Digital Image Correlation, DIC, tvåfrihetsgradssystem, 2DOF, LS-DYNA, olinjär finita elementmetodanalys, stötlast, inre arbete, impuls, plastisk rotationskapacitet

Contents

Abstract	i
Sammanfattning	ii
Preface	ix
Nomenclature	xi
1 Introduction	1
1.1 Background	1
1.2 Aim	1
1.3 Method	1
1.4 Limitations	2
1.5 Thesis Outline	3
2 Materials and Structural Behaviour	4
2.1 Introduction	4
2.2 Structural Response	4
2.2.1 Introduction	4
2.2.2 Linear Elastic Response	4
2.2.3 Plastic Response	5
2.2.4 Elasto-Plastic Response	5
2.2.5 Tri-Linear Response	6
2.3 Materials	7
2.3.1 Introduction	7
2.3.2 Concrete	7
2.3.2.1 Mechanical Properties	7
2.3.2.2 Compressive Strength	9
2.3.2.3 Tensile Strength	10
2.3.2.4 Modulus of Elasticity	11
2.3.3 Reinforcing Steel	12
2.3.4 Reinforced Concrete	13
2.4 Strain Rate Effects	15
2.4.1 Introduction	15
2.4.2 Influence on Concrete Strength	15

2.4.3	Influence on Reinforcement	17
2.4.4	Other Interesting Previous Studies	18
3	Plastic Rotation Capacity	19
3.1	Introduction	19
3.2	Curvature	19
3.3	Plastic Rotation	21
3.4	Different Methods to Determine Plastic Rotation	25
3.4.1	Introduction	25
3.4.2	From Test Results	25
3.4.3	Eurocode 2	26
3.4.4	Betonghandboken (ABC-Method)	28
3.4.5	Tamminens D-factor	30
3.4.6	Bk25	31
3.4.7	Methods Based on Equivalent Plastic Hinge Length	34
3.4.7.1	Introduction	34
3.4.7.2	Baker and Amarkone	34
3.4.7.3	ACI-ASCE Comittee 428	35
3.4.7.4	Paulay and Priestley	35
3.4.7.5	Panagiotakos and Fardis	36
4	Fundamentals of Dynamics	37
4.1	Introduction	37
4.2	Impulse	37
4.3	Work, Kinetic Energy and External Work	38
4.4	Internal Work	38
4.4.1	Introduction	38
4.4.2	Linear Elastic Response	39
4.4.3	Plastic Response	39
4.4.4	Elasto-Plastic Response	40
4.5	Equation of Motion	41
4.6	Impact and the Influence of Mass	42
4.6.1	Introduction	42
4.6.2	Elastic Impact	43
4.6.3	Plastic Impact	43
4.7	Response during Repeated Impacts	43
4.7.1	Introduction	43
4.7.2	Plastic and Elasto-Plastic Response	44
4.7.3	Equivalent Impulse Load for Elasto-Plastic Response	45
4.7.4	Residual Strength	47
5	Discrete Model for Dynamic Analysis	48
5.1	Introduction	48
5.2	Definition of SDOF and Impulse Loading	48

5.3	Transforming the Beam to SDOF	49
5.4	Transforming the Drop-weight to SDOF	51
5.5	2DOF Systems	52
5.5.1	General Description	52
5.5.2	2DOF for a Drop-weight and RC Beam System	54
5.6	Central Difference Method	55
6	Experimental Procedure	58
6.1	General Description	58
6.2	Manufacturing of Concrete Beams	58
6.2.1	Introduction	58
6.2.2	Geometry of the Specimens	59
6.2.3	Manufacturing of Moulds	59
6.2.4	Casting	60
6.2.5	Tests Made on Fresh Concrete	62
6.3	Experimental Setup for Dynamic Testing	64
6.4	Experimental Setup for Static Testing	66
6.4.1	Introduction	66
6.4.2	Static Testing of Damaged Beams	67
6.4.3	Static Testing of Undamaged Beams	67
7	Predictions	69
7.1	Introduction	69
7.2	Load Capacity	70
7.2.1	Ultimate Limit State	70
7.2.2	Cracking and Yielding	71
7.2.3	Theoretical Load-deflection Curve	72
7.3	Rotational Capacity	73
7.3.1	Introduction	73
7.3.2	Eurocode 2	74
7.3.3	Betonghandboken (ABC-Method)	74
7.3.4	Tamminens D-factor	75
7.3.5	Bk25	75
7.3.6	Methods based on Equivalent Plastic Hinge Length	76
7.4	Predictions with 2DOF	76
7.4.1	Overview	76
7.4.2	Internal Resistance	77
7.4.3	Stiffness	77
7.4.4	Transformation Factors	77
7.4.5	Results from 2DOF Predictions	78
7.4.5.1	Deflections	78
7.4.5.2	Impulse	79

8	Experimental Results	81
8.1	Introduction	81
8.2	Material Properties	81
8.2.1	Introduction	81
8.2.2	Concrete Properties	81
8.2.3	Steel Properties.	82
8.2.4	Location of Reinforcement	82
8.3	Dynamic Testing	83
8.3.1	Introduction	83
8.3.2	Methodology	83
8.3.3	Midpoint Deflection over Time during First Impact	84
8.3.3.1	Introduction	84
8.3.3.2	Series-1	84
8.3.3.3	Series-2	85
8.3.3.4	Series-3	85
8.3.3.5	Series-4	86
8.3.3.6	Comparison of Deflection over Time	87
8.3.4	Midpoint Deflection over Time during Repeated Impacts	88
8.3.4.1	Introduction	88
8.3.4.2	Series-1	88
8.3.4.3	Series-2	91
8.3.4.4	Series-3	93
8.3.5	Strain Fields from DIC during First Impact	95
8.3.6	Strain Fields from DIC during Repeated Impacts	99
8.3.7	Deformed Shape	100
8.3.8	Velocities of Initial Deflection	103
8.3.9	Impact Force and Impulse Load	104
8.3.9.1	Introduction	104
8.3.9.2	Series-1	105
8.3.9.3	Series-2	106
8.3.9.4	Series-3	107
8.3.9.5	Series-4	107
8.3.9.6	Comparison of Impact Force	108
8.3.9.7	Comparison of Impulse Load	109
8.4	Static Testing	109
8.4.1	Introduction	109
8.4.2	Undamaged Beams	109
8.4.3	Strain Fields of Undamaged Beams	113
8.4.4	Series-1	114
8.4.5	Series-2	117
8.4.6	Series-3	119
8.4.7	Series-4	121
8.4.8	Comparison of Series-1-4	123

9	Finite Element Modelling in LS-DYNA	127
9.1	LS-DYNA Theory	127
9.1.1	Introduction	127
9.1.2	Model and Elements	127
9.1.3	Material Model	127
9.1.3.1	Concrete	127
9.1.3.2	Reinforcement	129
9.1.3.3	Supports and Drop-weight	129
9.1.4	Interaction between Reinforcement and Concrete	129
9.2	LS-DYNA Predictions	130
9.2.1	Introduction	130
9.2.2	Midpoint Deflection over Time	130
9.2.3	Deflection-length Relationship	131
9.2.4	Strain Fields	134
10	Comparison with Experiments	138
10.1	Introduction	138
10.2	Verification of Load Capacity Predictions	138
10.2.1	General	138
10.2.2	Verification using Internal Work	139
10.3	Verification of Rotational Capacity Predictions	140
10.4	Verification of Stiffness Predictions	141
10.5	Verification of 2DOF Predictions	141
10.5.1	Deflections	141
10.5.2	Impulse	144
10.6	LS-DYNA	144
10.6.1	Midpoint Deflection over Time	144
10.6.2	Deflection-length Relationship	145
10.6.3	Strain Fields	148
11	Discussion	151
12	Final Remarks	153
12.1	General Description	153
12.2	Conclusions	153
12.3	Further Studies	154
	References	155
	Appendix A Material Properties Testing of Concrete	A-1
A.1	Introduction	A-1
A.2	Density	A-2
A.3	Compressive Strength	A-3
A.4	Tensile Strength	A-4

A.5 Fracture Energy	A-5
Appendix B Material Properties Testing of Steel	B-1
Appendix C Damaged Beams After Testing	C-1
Appendix D DIC Facet Analysis	D-1
Appendix E Beams Subjected to Static Loading only	E-1
Appendix F Determination of Plastic Deformation at Midpoint	F-1
F.1 Method 1 - Image Sequence from actual Impact	F-1
F.2 Method 2 - From next Image Sequence	F-2
F.3 Comparison of the Two Methods	F-3
Appendix G Determination of Plastic Deformation in Static Tests	G-1
Appendix H Calculation of Impulse Load	H-1
Appendix I Calculation of Stiffness	I-1
Appendix J Calculation of Internal Work	J-1
Appendix K Mathcad Calculations	K-1
Appendix L MATLAB Script for 2DOF Model	L-1
Appendix M LS-DYNA Input File	M-1

PREFACE

In this master's thesis, the response of simply supported concrete beams subjected to a single or repeated impact loading has been investigated, as well as the response under static loading. Experiments were carried out and the response were compared to the results obtained from different numerical methods.

The work has been carried out between January and June 2018 at Chalmers and Norconsult's office in Gothenburg. The project is a part of an ongoing research project which is a collaboration between the Structural Engineering Division at Chalmers University of Technology, Norconsult and RISE (The Swedish Research Institute) and is financed by the Swedish Civil Contingencies Agency (MSB), Fortifikationskårens forskningsfond and Brosamverkan. The project was supervised by Ph.D. Morgan Johansson and examined by Ph.D Joosef Leppänen.

First of all, we would like to express our deepest gratitude to Morgan Johansson who has guided us through the project with his infinite knowledge and encouraging spirit. We would also like to thank Joosef Leppänen who has provided us with very helpful feedback and guidance during the project. Research Engineer Sebastian Almfeldts help before, during and after the experiments is also very appreciated. M.Sc Fabio Lozano Mendoza is also appreciated for his help regarding LS-DYNA and other helpful tips during the project. We would like to thank Ph.D Mathias Flansbjerg for his help with the DIC software and Ph.D Ingemar Löfgren who provided us with the recipe for the concrete. Lastly, we would like to thank M.Sc Gonzalo Sanz-Díez for his tips regarding the DIC software and Michaela Munther and Josefine Runebrant for their help with the LS-DYNA model.

NOMENCLATURE

Abbreviations

2DOF	Two-degree of freedom
SDOF	Single-degree of freedom
BC	Boundary conditions
DIC	Digital image correlation
DIF	Dynamic increase factor
EC	Eurocode
FE	Finite element
FEA	Finite element analysis
RC	Reinforced concrete
WST	Wedge splitting test

Roman upper case letters

A	Area
E	Modulus of elasticity
E_c	Modulus of elasticity of concrete
E_k	Kinetic energy
F	Force, load
F_{dyn}	Dynamic load
F_{sta}	Static load
G_F	Fracture energy
I	Impulse, moment of inertia
L	Total length of beam member
M	Bending moment
R	Internal resistance
R_m	Maximum internal resisting force
V	Shear force
W	Work
W_e	External work
W_i	Internal work

Roman lower case letters

a	Acceleration
b	Width of beam cross-section
c	Damping coefficient, concrete cover thickness
d	Effective height
$f_{0.2}$	0.2% proof stress of reinforcing steel
f_c	Compressive cylinder strength of concrete
$f_{cm,cube}$	Compressive cube strength of concrete

f_{ct}	Tensile strength of concrete
$f_{ctk0,05}$	Tensile strength; lower characteristic value
$f_{ctk0,95}$	Tensile strength; upper characteristic value
$f_{ct,fl}$	Flexural tensile strength of concrete
$f_{ct,sp}$	Splitting tensile strength of concrete
f_t	Tensile strength of reinforcing steel
g	Gravitational constant
h	Height of beam cross section, drop-height
k	Linear elastic stiffness, constant used in Tamminens method, constant for flexural tensile strength
k_λ	Factor for plastic rotation according to Eurocode
k'	Stiffness after cracking
l	Distance along beam
l_0	Distance from zero moment section to point of maximum moment
l_{pl}	Equivalent plastic hinge length
l_y	Length of yielding region
m	Mass
n	Number
p	Momentum of a particle
r	Radius of curvature
t	Time
u	Deflection or deformation
u_{cr}	Deflection or deformation when cracking occurs
u_s	Deflection in system point
\dot{u}	First time derivative of displacement (velocity)
\ddot{u}	Second time derivative of displacement (acceleration)
v	Velocity
x	Distance to neutral axis from top edge
x_0	Distance from zero moment section to point of maximum moment after plastic redistribution

Greek letters

α_R	Stress block factor for average stress
β_R	Stress block factor for resultant location
Δt	Time increment
δ	Displacement
$\dot{\epsilon}$	Rate of strain
ϵ	Strain
ϵ_{cc}	Concrete strain; compression
ϵ_{ct}	Concrete strain; tension
ϵ_{cs}	Concrete strain at reinforcement level
φ	Curvature
κ	Transformation factor
λ	Slenderness
ω	Angular eigenfrequency

ω_{bal}	Balanced mechanical reinforcement ratio
ω_s	Mechanical ratio of tensile reinforcement
$\omega_{s,crit}$	Critical mechanical ratio
ω'_s	Mechanical ratio of compression reinforcement
ω_v	Mechanical ratio of shear reinforcement
ϕ	Angle
ρ	Reinforcement ratio parameter, density
σ	Stress
θ	Rotation
$\theta_{pl,x\%}$	Plastic rotation at a given load level

Index

0	Initial
<i>b</i>	Beam
<i>d</i>	Design value
<i>f</i>	Field
<i>imp</i>	Impact
<i>k</i>	Characteristic value
<i>m</i>	Mean value
<i>s</i>	Reinforcing steel
<i>sup</i>	Support
<i>u</i>	Ultimate value
<i>y</i>	Yield value
<i>el</i>	Elastic
<i>pl</i>	Plastic
<i>tot</i>	Total
'	Compressive zone
<i>I</i>	State I
<i>II</i>	State II
<i>cr</i>	Cracking
<i>max</i>	Maximum value

1 Introduction

1.1 Background

Impulse loading, such as explosions or collisions, are important issues to take care of when determining the structural response of protective structures. Since these events can be critical for the capacity of a structure it is important to have a good understanding of how impulse loading affect the structure. The structural response of an impulse loaded beam can be very different compared to a statically loaded beam. Concrete are commonly used for these kind of protective structures and this master's thesis will focus on how a reinforced concrete beam (RC beam) behaves when subjected to an impact load, followed by a static load. A large plastic deformation capacity results in a large energy absorption and this is essential for an impact loaded structure.

This master's thesis project is a part of an ongoing research project by the Structural Engineering Division at Chalmers University of Technology, Norconsult and RISE. It is also a part of a series of master's thesis projects supported by Norconsult in this specific field and will build upon the knowledge, conclusions and suggestions made in those projects.

1.2 Aim

One aim of the thesis is to increase the understanding of the structural response of RC beams subjected to repeated impact loading and evaluate methods to predict this response. Further, another aim is to study the plastic rotation capacity of undamaged and damaged RC beams. To achieve these aims, the following objectives need to be fulfilled:

- Evaluate theories about dynamic loading and how concrete and steel as a material behaves in such cases.
- Predict the structural response of a statically loaded structure with hand calculations.
- Predict the dynamic response using a simplified two-degree of freedom (2DOF) model and a non-linear finite element model in LS-DYNA.
- Evaluate the response of an impact loaded simply supported beam by performing experiments and process the information with digital image correlation (DIC).
- Evaluate the response of statically loaded beams and compare with suggestions in the literature.
- Study the residual capacity after impact by static loading of the damaged beam until failure.
- Compare predictions with the results from experiments to evaluate the numerical methods used.

1.3 Method

Firstly, to deepen the knowledge concerning structural dynamics and the response of impact loaded structures, a literature survey was done. The centre parts of the survey were the understanding of plastic rotation capacity and the dynamic response of structures.

Secondly, by the use of simplified hand calculations and a 2DOF-system, a prediction of the behaviour of RC beams subjected to impact loads was performed. Parameters such as load capacity, deflections, rotation capacity, internal work and impulse were predicted. The calculations were based on different theoretical models which is supported by the findings in the literature survey.

Thirdly, experiments with a combination of drop-weight impact and static loading of RC beams were performed. The experimental beams were casted within the project and the concrete properties of both fresh and hardened concrete were evaluated according to relevant standards and recommendations. The material properties were then used as input data for the calculations performed. During the testing the beams were simply supported with a free span of 1.0 m. Different combinations of drop height, mass of drop-weight and number of drops were used to form a basis of comparison between different impact loading cases. When the beams were subjected to drop-weight impacts, it resulted in an initial deformation and afterwards the residual deformation capacity was tested under four-point deformation-controlled static loading. Static loading on undamaged beams were also carried out and the difference in capacity between damaged and undamaged beams were evaluated. Cameras were used during the experiments to capture the response of the beam. Afterwards, the frames from the experiments were processed by using DIC in the software GOM Correlate 2017. Information such as propagation of cracks and deformations of the beam were extracted and presented. In GOM Correlate, the strain fields were shown in a similar way to that in a FEA which simplified the comparisons between the experiments and the FE-modelling.

Lastly, the software LS-DYNA was used to perform dynamic FEA. These results were compared with the results from the experiments and the 2DOF calculations. In the analysis 3D solid elements and the material model CDPM2 was used.

1.4 Limitations

This study of the response of impact loaded structures was limited to the study of three-point-loaded simply supported RC beams only. However, statically loaded beams were subjected to four-point-loading. The number of beams tested were limited to 18 beams and the configuration was the same for all beams. The high-speed camera used for capturing response during the dynamic tests featured a frame-rate of 5 000 fps.

The beams were manufactured in two different batches, using normal strength concrete and four longitudinal reinforcement bars, giving a double symmetrical concrete section. The expected failure was bending failure and therefore the beams were not provided with transversal reinforcement.

The FEA were limited to the software LS-DYNA with the use of 3D continuum solid elements and material model CDPM2. Only the first impact was modelled in LS-DYNA due to the complexity of modelling of repeated impacts.

1.5 Thesis Outline

The thesis consists of four parts which can be connected to each other. Firstly, Chapters 2-5 is focused the theory which is important to understand to be able to understand the rest of the thesis. Chapter 6-8 cover the experimental setup and results as well as the predicted response. Chapter 9-10 is focused on the theory behind the FE model and the results obtained from it. Lastly, Chapter 11-13 presents how well the response was predicted as well as some general conclusions and discussion.

Chapter 2: General concepts about the structural behaviour of materials is presented together with some basic theory about steel and concrete as a material. Furthermore, the phenomena of strain rate effects are presented.

Chapter 3: The theory behind rotation capacity is described followed by an investigation on different methods to calculate plastic rotation capacity.

Chapter 4: The basic theory of dynamics is presented here, which is essential to comprehend before creating the numerical models to predict the structural response of the impact loaded beams.

Chapter 5: Introduces the way of thinking when creating both SDOF and 2DOF models, especially how to transform the beam and drop-weight into such systems.

Chapter 6: Covers the procedure during the experiments. The casting of the beams is described with some material tests performed on the fresh concrete followed by the experimental setup for both dynamic and static testing.

Chapter 7: The predicted load capacity and load-deflection curve is calculated according to conventional static methods. The different methods presented in Chapter 3 are thereafter used to calculate the plastic rotation capacity and lastly the 2DOF model is used to predict a number of parameters.

Chapter 8: Covers all the experimental results. Firstly, the material properties and location of reinforcement are presented. Secondly, the results from the dynamic testing are presented where the midpoint deflection during different timesteps, strain fields, impact force and impulse load are of special interest. Lastly, the results from the static testing are presented and the load-deflection relationship, plastic rotation capacity, stiffness and internal work are of special interest. Some comparisons and conclusions are made between the results from the different series.

Chapter 9: Theory behind the model used in LS-DYNA is presented and especially the material model CDPM2 is described.

Chapter 10: Results from the analyses in LS-DYNA are presented where the midpoint deflection during different timesteps, displacement-length relationship and strain fields are of special interest.

Chapter 11: Some general discussion on the results and findings within the thesis is presented.

Chapter 12: Conclusions based on the results are made and possibilities for future studies are discussed.

2 Materials and Structural Behaviour

2.1 Introduction

The purpose of this chapter is to give a brief introduction of how the materials that is of interest in this project behaves under loading. Since all of the tests was performed on RC beams, concrete and steel reinforcement is treated within this chapter. The chapter treats how the materials response is idealized to be able to perform calculations in a simplified manner. Even though this is a basic introduction, it will introduce some important expressions and material parameters that is considered fundamental to be able to comprehend the subsequent chapters.

2.2 Structural Response

2.2.1 Introduction

Four different types of behaviour can be used to describe the response of a structure; elastic, plastic, elasto-plastic and tri-linear. These are simplified models but works well as approximations for calculations. Basic equations and expressions are given based on (Lozano and Makdesi, 2017), (Lovén and Svavarsdóttir, 2016), (Nyström, 2006) and (Johansson and Laine, 2012).

2.2.2 Linear Elastic Response

In a linear elastic response, the structure is assumed to have a constant linear relationship between the internal resisting force R and the displacement u_{el} .

$$R(u) = k \cdot u_{el} \quad (2.1)$$

where k corresponds to the stiffness of the structure. The relation between the internal resisting force and the displacement can be seen in Figure 2.1. The deformation u_{el} is considered to be fully elastic and will return to zero when the structure is unloaded.

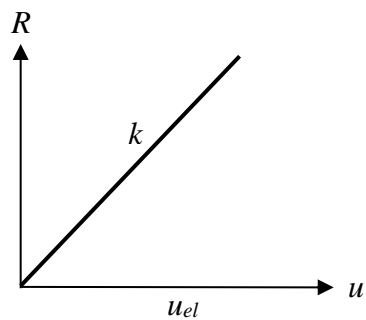


Figure 2.1 Relationship between internal resistance and displacement.

2.2.3 Plastic Response

In an ideal plastic response, deformations will not occur until the capacity of the structure is reached. If the maximum internal resistance R_m is reached, the material will show an unlimited deformation until the load is removed. The relation between R and u can now be expressed as

$$R(u) = \begin{cases} F & \text{if } u = 0 \\ R_m & \text{if } u > 0 \end{cases} \quad (2.2)$$

where R_m is the maximum value of the internal force F .

The deformation u_{pl} is considered to be fully plastic and is not reversible when the structure is unloaded. The relation between the internal resisting force and then displacement can be seen in Figure 2.2.

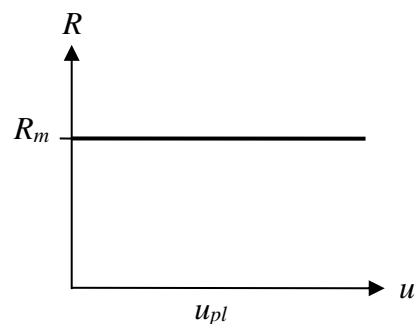


Figure 2.2 Relationship between internal resistance and displacement.

2.2.4 Elasto-Plastic Response

A combination of elastic and plastic response can be used to predict the response of a structure in a more accurate way. This is called elasto-plastic response and exhibits an elastic response until the maximum internal resistance is reached and from that point it behaves in a plastic way. The relation between R and u can now be expressed as

$$R(u) = \begin{cases} k \cdot u & \text{if } u \leq u_{el} \\ R_m & \text{if } u > u_{el} \end{cases} \quad (2.3)$$

The deformation will now consist of one elastic part and one plastic part and the relation between these and the internal resisting force can be seen in Figure 2.3. The elastic part of the deformation returns to zero when the structure is unloaded while the plastic part will remain. If the structure is loaded again, the same stiffness is assumed.

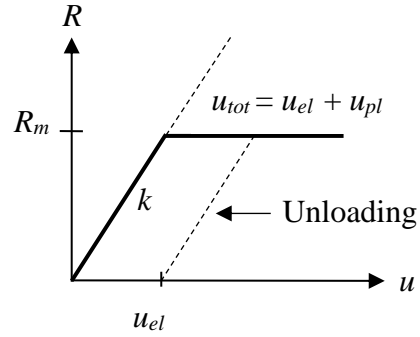


Figure 2.3 Relationship between internal resistance and displacement.

The total deformation u_{tot} can be expressed as

$$u_{tot} = u_{el} + u_{pl} \quad (2.4)$$

where

$$u_{el} = \frac{R_m}{k} \quad (2.5)$$

2.2.5 Tri-Linear Response

The response can be even more refined by assuming a tri-linear material response. The part which are exposed to an internal resisting force lower than R_m will now be divided in two parts with two different stiffnesses. This response corresponds very well with RC since a change of stiffness will occur when the first cracks appear. In this case u_{cr} represents the displacement when cracking occurs, R_{cr} is the internal resisting force when cracking occurs, k is the stiffness before cracking and k' is the stiffness after cracking has occurred. The relationship can now be expressed as

$$R(u) = \begin{cases} k \cdot u & \text{if } u \leq u_{cr} \\ R_{cr} + k'(u - u_{cr}) & \text{if } u_{cr} \leq u \leq u_{pl} \\ R_m & \text{if } u > u_{pl} \end{cases} \quad (2.6)$$

The relation between the internal resisting force and displacement is also shown in Figure 2.4.

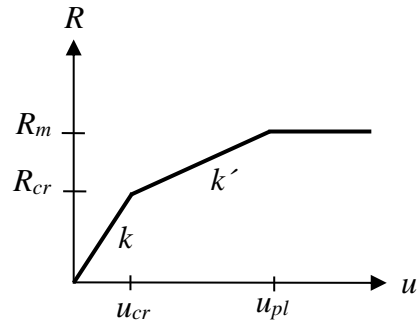


Figure 2.4 Relationship between internal resistance and displacement.

A tri-linear material can be divided in three different types of deformation ranges which can be seen in Figure 2.5. Even though this is the most accurate way to describe the response of RC, a bi-linear elasto-plastic response will be used in this report. This will be further explained in Section 2.3.4.

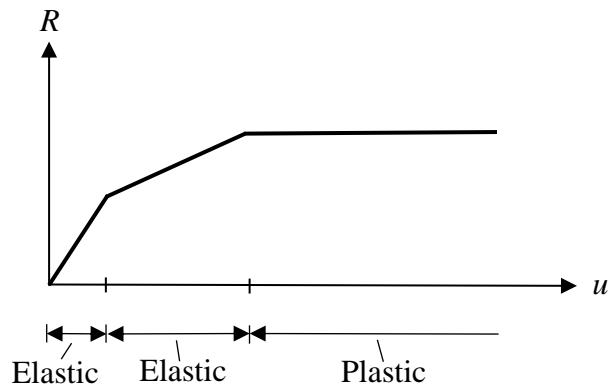


Figure 2.5 Illustration of the three types of deformation ranges.

2.3 Materials

2.3.1 Introduction

This subchapter covers basic knowledge about concrete, reinforcing steel and RC as well as how the properties of these materials is evaluated. This chapter is based on knowledge obtained in (Engström, 2013) and (CEN, 2004).

2.3.2 Concrete

2.3.2.1 Mechanical Properties

Concrete is a composite material made out of aggregates, cement and water. Its strength in compression exceeds its strength in tension and this is why reinforcement, that is strong in tension, is needed in concrete elements subjected to tension. The stress-strain (σ - ϵ) relation of plain concrete under uniaxial loading can be seen in Figure 2.6, which clearly illustrates the big difference between the capacity in compression and tension.

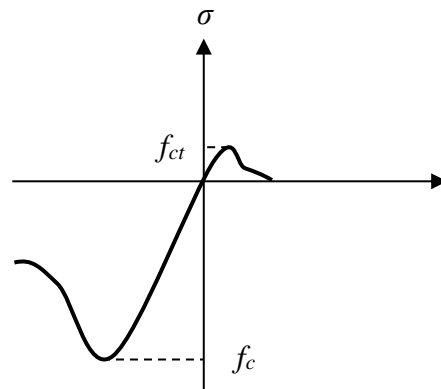


Figure 2.6 Stress-strain relation for concrete under uniaxial loading. f_c and f_{ct} corresponds to compression strength and tension strength of concrete.

The steep slope that can be observed in Figure 2.6 after it has reached its maximum tensile capacity shows that concrete is a brittle material in tension. This is true for compression as well but in this case the strength of the concrete has an influence on how brittle, or ductile, the material behaves. This is illustrated in Figure 2.7 where it can be seen that concrete with low strength allows for larger deformations after the maximum stress has been reached. This means that high strength concrete is more brittle while low strength concrete is more ductile.

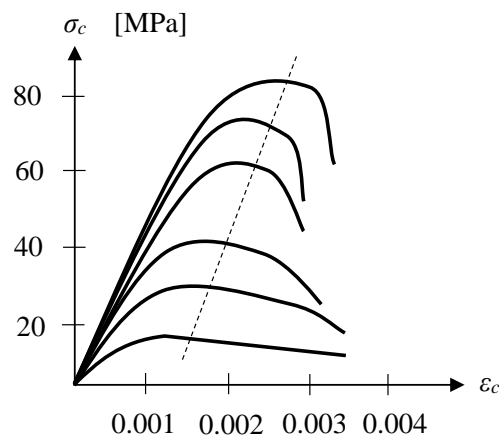


Figure 2.7 Compressive stress-strain relation for different concrete strengths. Inspired by (Engström, 2013).

The compressive strength of concrete also depends on the loading rate, which is illustrated in Figure 2.8. Compared to a normal compressive test, that takes a few minutes to perform, the compressive strength will be higher during fast loading processes. The ultimate compressive strain will simultaneously be lower, i.e. the stiffness increase with increasing load rate, this is further treated in Section 2.4. During rapid loading the compressive strength can increase up to 20 % (Engström, 2013). According to Boverket (2004) it is possible to increase the compressive strength by a factor 1.1 if a fast loading process is a part of a load combination containing accident loads or a progressive collapse. However, this is not considered in CEN (2004).

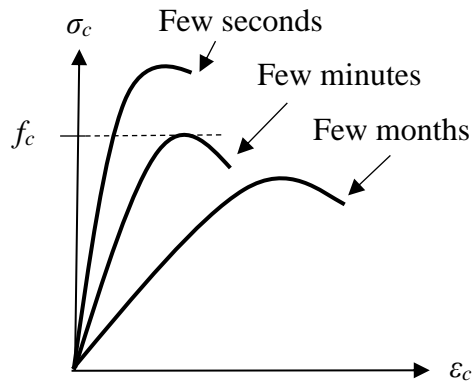


Figure 2.8 Compressive strengths dependency of loading rate. Inspired by (Engström, 2013).

The results from a series of tests made on the same type of concrete will naturally have some dispersion in the results. This can be presented as a frequency distribution where it is possible to determine mean value, standard deviation or variation coefficient and fractile values. A principal frequency distribution of the concretes tensile strength can be seen in Figure 2.9. The lower characteristic value $f_{ctk0,05}$ is defined as the 5 %-fractile, that is the value that 5 % of the samples is lower than. The upper characteristic value, $f_{ctk0,95}$ is the value that 95 % of the samples is lower than. The mean tensile strength f_{ctm} is the mean value of the curve. Similar, when determining the compressive strength of concrete, the 5 %-fractile strength is used and is referred to as the characteristic value f_{ck} .

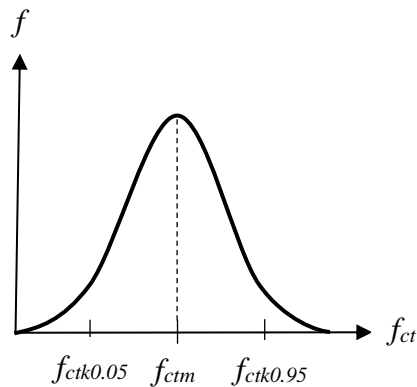


Figure 2.9 Principal frequency distribution for the tensile strength of concrete.

2.3.2.2 Compressive Strength

The compressive strength of concrete is measured in a test and the result depends on the method used. Uniaxial compressive strength is therefore determined according to CEN (2009e). All factors that may influence the results are controlled, such as temperature, loading rate and age of concrete. The testing of concrete according to this standard is further treated in Section A.3. A principle sketch of how the compressive strength is determined by uniaxial loading is shown in Figure 2.10, which is normally done on cylinders.

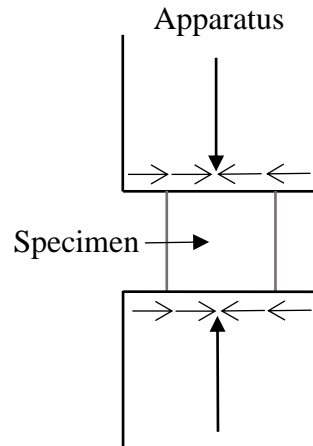


Figure 2.10 Principle sketch of uniaxial loading test. Inspired by (Engström, 2013).

Internationally, it is common to determine the compressive strength using cylinders. In Sweden though, cubes are normally used instead of cylinders, which results in a higher strength. This is considered by using

$$f_{cm} = \frac{f_{cm,cube}}{1.20} \quad (2.7)$$

where f_{cm} is the mean value of the compressive strength of a cylinder and $f_{cm,cube}$ is the mean value of the compressive strength of a cube.

2.3.2.3 Tensile Strength

The tensile strength of concrete can be tested by pure tensioning, flexure or by a splitting test. The results from the different methods may differ and it is difficult to accurately predict the tensile strength. According to CEN (2004), the mean tensile strength at 28 days can be determined from the characteristic compressive strength.

$$f_{ctm} = 0.30 f_{ck}^{2/3} \quad \text{for concrete class } \leq C50/60 \quad (2.8)$$

$$f_{ctm} = 2.12 \ln \left(1 + \frac{f_{ck} + 8}{10} \right) \quad \text{for concrete class } > C50/60 \quad (2.9)$$

$$f_{ctk0,05} = 0.7 f_{ctm} \quad (2.10)$$

$$f_{ctk0,95} = 1.3 f_{ctm} \quad (2.11)$$

where f_{ck} is the characteristic value of the compressive strength and f_{ctm} is the mean concrete tensile strength. From a splitting test, the splitting tensile strength $f_{ct,sp}$, can according to CEN (2004) be used to calculate the mean tensile strength as

$$f_{ctm} = 0.9 f_{ct,sp} \quad (2.12)$$

In a flexural test, the flexural tensile strength $f_{ctm,fl}$, can according to CEN (2004) be used to express f_{ctm} as

$$f_{ctm} = \frac{f_{ct,fl}}{k} \quad (2.13)$$

where

$$k = 1.6 - \frac{h}{1000} \geq 1.0 \quad \text{with } h \text{ in [mm]} \quad (2.14)$$

2.3.2.4 Modulus of Elasticity

There are both simplified and idealized stress-strain relations in EC 2 and Figure 2.11 shows an ideal model that represents the response under uniaxial compression. The stress-strain relation is almost linear and the mean value of the modulus of elasticity, E_{cm} , is determined as a secant modulus between the origin and $\sigma_c = 0.4f_{cm}$.

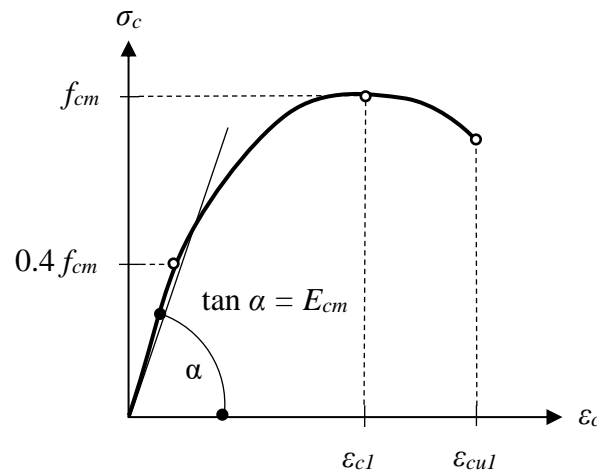


Figure 2.11 Ideal stress-strain relation for concrete under compression. ϵ_{c1} is the strain at peak stress and ϵ_{cul} corresponds to the ultimate compressive strain (CEN, 2004).

The modulus of elasticity can also be approximated as

$$E_{cm} = 22 \left(\frac{f_{cm}}{10} \right)^{0.3} \quad [\text{GPa}] \quad (2.15)$$

where f_{cm} is the compressive mean strength in [MPa].

More simplified compressive stress-strain relations can also be used in design. Figure 2.12a shows a parabolic relation and an even more simplified bi-linear relation can be seen in Figure 2.12b, the latter can be related to the elasto-plastic behaviour described in Section 2.2.4. The relationships described in these two figures are used when calculating structures subjected to bending. The values of the strains $\epsilon_{c(2-3)}$ and $\epsilon_{cu(2-3)}$ are given in (CEN, 2004) depending on the concrete class and analytical relation.

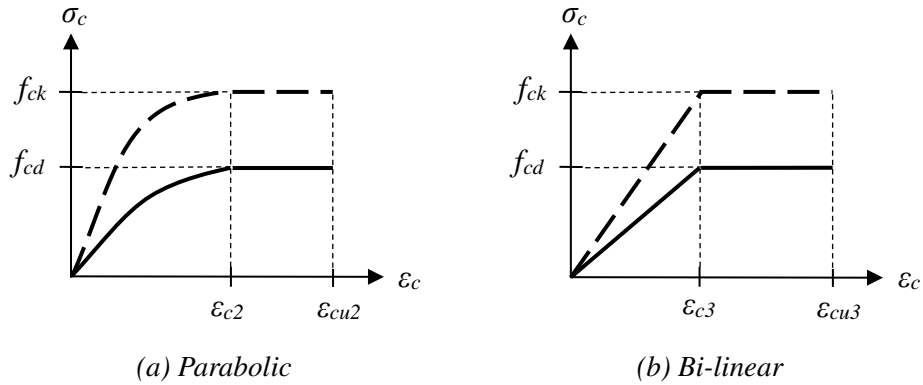


Figure 2.12 Simplified stress-strain relation for concrete under compression (Engström, 2013).

2.3.3 Reinforcing Steel

As mentioned in Section 2.3.2, reinforcement are used to compensate for the unsatisfactory tensile strength of concrete. Therefore it is mainly the strength and behaviour under tension that is of interest when analysing the reinforcement. Depending on the production method, the reinforcement is distinguished in two categories: heat treated and cold worked. This is since they show a significantly different stress-strain relation, see Figure 2.13 where f_u corresponds to maximum tensile strength, f_y to yield strength and ϵ_{su} to the ultimate strain at maximum force.

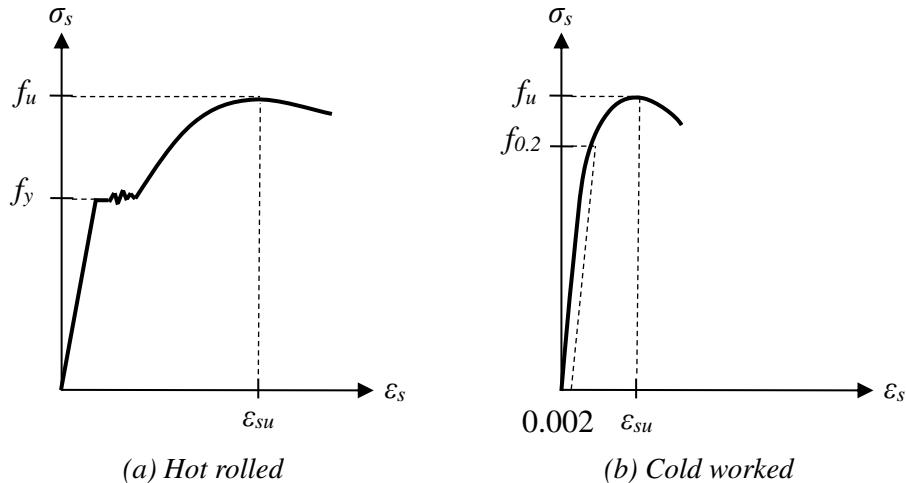


Figure 2.13 Principal stress-strain relations.

Hot-rolled steel has four clear stages: Elastic stage, plastic stage (yield plateau), strain hardening up to maximum tensile stress and a fracture stage until failure. Cold-worked steel has three different stages: Elastic, strain hardening and a fracture stage. Cold-worked steel lack a clear transition between the elastic stage and the strain hardening and is therefore lacking a clear yield plateau. According to CEN (2004), a yield strength can be defined as the stress for which the remaining strain after unloading is 0.2 %. This stress is named proof stress, $f_{0.2}$. It can be observed from Figure 2.13 that cold-worked steel in general has a lower ultimate strain and strain hardening, which results in a more brittle behaviour.

Reinforcement are classified based on a large number of properties such as: strength, fatigue strength, ductility class, size, weldability etc. The ductility class is of special interest in this project since it represents the steel’s ability to deform under large tensile forces. A ductile response is preferred when considering the uptake of impulse loads (Johansson and Laine, 2012). In CEN (2004) three different ductility classes are used and they are summarized in Table 2.1. The ductility classes are defined with regard to both the ultimate strain and the relation between the maximum strength and yield strength.

Table 2.1 Classification of steel regarding ductility properties according to EC 2 (Lozano and Makdesi, 2017).

Property	Class		
	A	B	C
Characteristic yield strength, f_{yk} or $f_{0.2k}$ [MPa]	400 to 600		
Minimum value of $(f_u/f_y)_k$	≥ 1.05	≥ 1.08	≥ 1.15 & < 1.35
Characteristic strain at maximum force, ϵ_{su} [%]	≥ 2.5	≥ 5.0	≥ 7.5

2.3.4 Reinforced Concrete

When combining steel and concrete, a composite material is formed which utilizes the high compressive strength of concrete together with the tensile strength and ductility of steel. A beam is a good example of a structure where the concrete and reinforcement has to act together to ensure sufficient load bearing capacity in the structure. This is also the type of structure that will be used during the tests further on in this thesis. The response of a RC structure can be divided in three different states. This is illustrated in Figure 2.14 where the response is expressed as tri-linear.

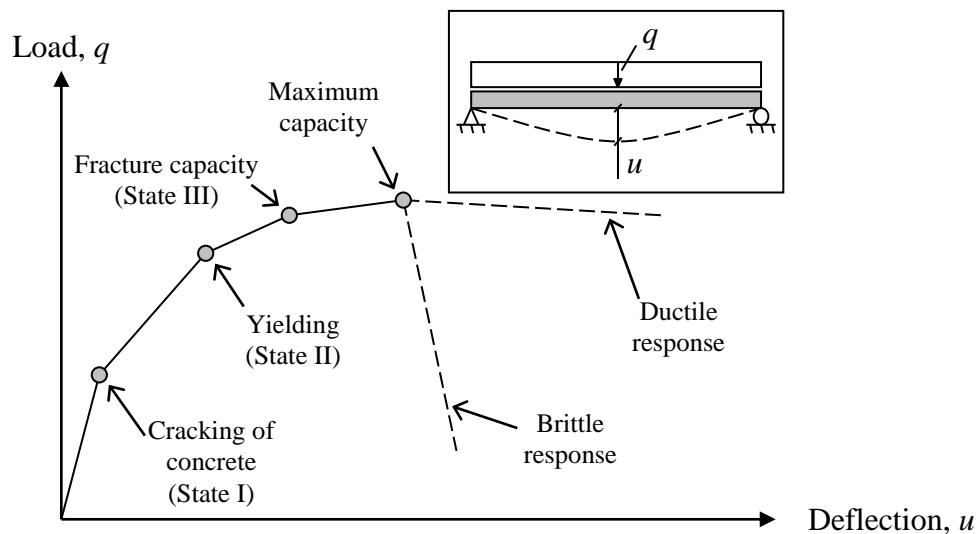


Figure 2.14 Schematic tri-linear response of the structural response of a RC beam, showing both brittle and ductile behaviour. Inspired by (Johansson and Laine, 2012).

In state I, the concrete is assumed to be uncracked and the response is assumed to be linear elastic and the stiffness is determined by the properties of the concrete. This is not entirely true since the properties of the reinforcement will affect the response and may increase the stiffness up to 20 % (Engström, 2015). It is however common to ignore this contribution.

In state II, the concrete is fully cracked and the contribution from the concrete in the tensile zone is neglected. The stiffness will now also depend on the reinforcement. The response is considered to be linear elastic once again but this time it will have a much lower stiffness.

In state III, the reinforcement has reached its yield limit and the cross-section will have a rapid loss of stiffness. The material response is no longer considered to be linear.

Even though the reinforcement has reached yielding, the structure may still not collapse. Plastic redistribution of the stresses will occur and the structure will not fail until either the reinforcement or the concrete reaches its ultimate strain. From this stage the load will increase slightly while the deformation may increase a lot. This will be further treated in Chapter 3.

According to Johansson and Laine (2012) a simplification of the response can be done where the response is considered to be bi-linear elasto-plastic, as shown in Figure 2.15. The structure is here assumed to be fully cracked from the beginning and state II stiffness is used to describe the elastic response. When the structure reaches its fracture capacity, state III, it will change to a plastic response.

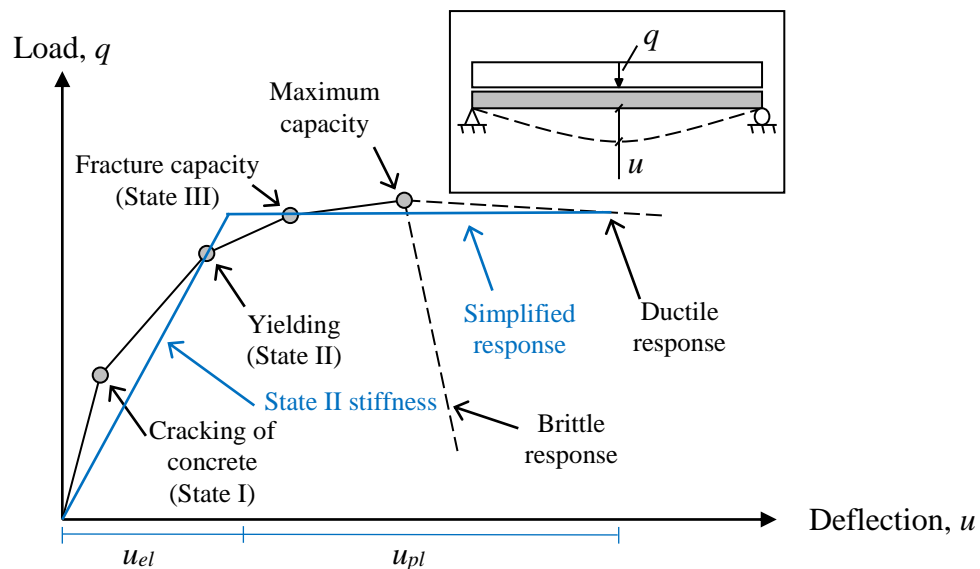


Figure 2.15 Schematic bi-linear response of the structural response of a RC beam, showing both brittle and ductile behaviour. Inspired by (Johansson and Laine, 2012).

2.4 Strain Rate Effects

2.4.1 Introduction

When loads are applied fast there is also an influence on the mechanical properties of the materials involved, in this case concrete and reinforcement. This is called strain rate effects and is the change of strain over time, denoted $\dot{\epsilon}$ and with the unit 1/s. The effect varies with the rate of the loading, where studies show that there is an increase of the strength at higher load rates. The phenomenon is well treated in Johansson (2000) and the information in this section is mainly based on the knowledge gained from there. The magnitude of strain rates for different loading conditions can be seen in Figure 2.16. The common way to account for the strain rates is to use the dynamic increase factor (DIF) which is defined as

$$DIF = \frac{F_{dyn}}{F_{sta}} \quad (2.16)$$

where F_{dyn} and F_{sta} is the dynamic and static load respectively. Due to the complexity of dynamic testing compared to static testing, the range of the DIF from different tests is very broad but all of them show an increased strength to some extent with higher strain rates.

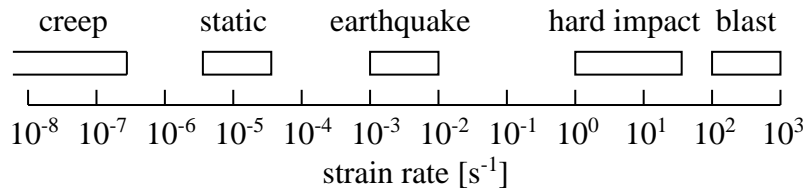


Figure 2.16 Strain rates for different loading conditions (Johansson, 2000).

2.4.2 Influence on Concrete Strength

For the two materials involved in RC-structures concrete has the largest effect of strain rates. The DIF for different strain rates can be seen in Figure 2.17 for concrete in compression and 2.18 for concrete in tension.

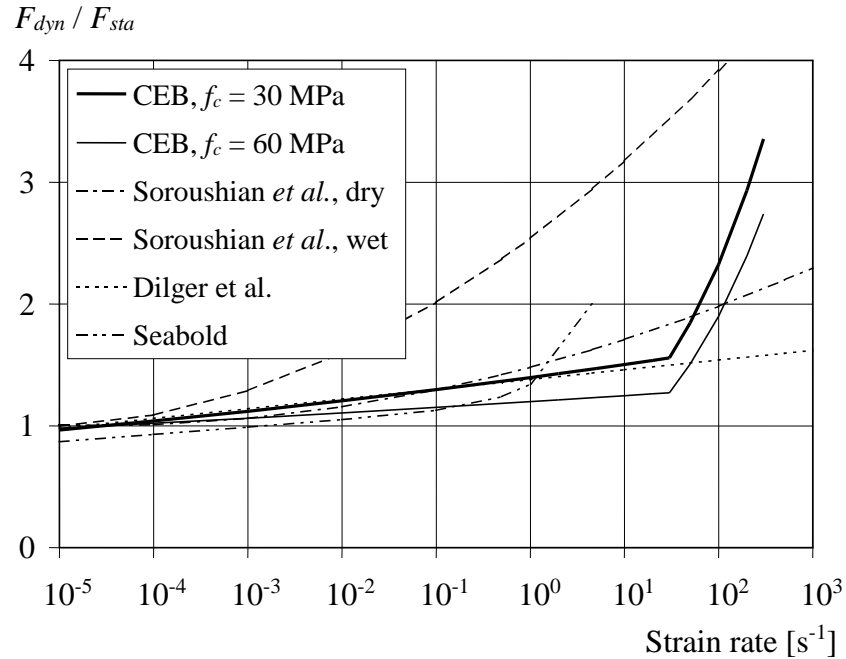


Figure 2.17 Studies of DIF and strain rate relation for concrete in compression (Johansson, 2000).

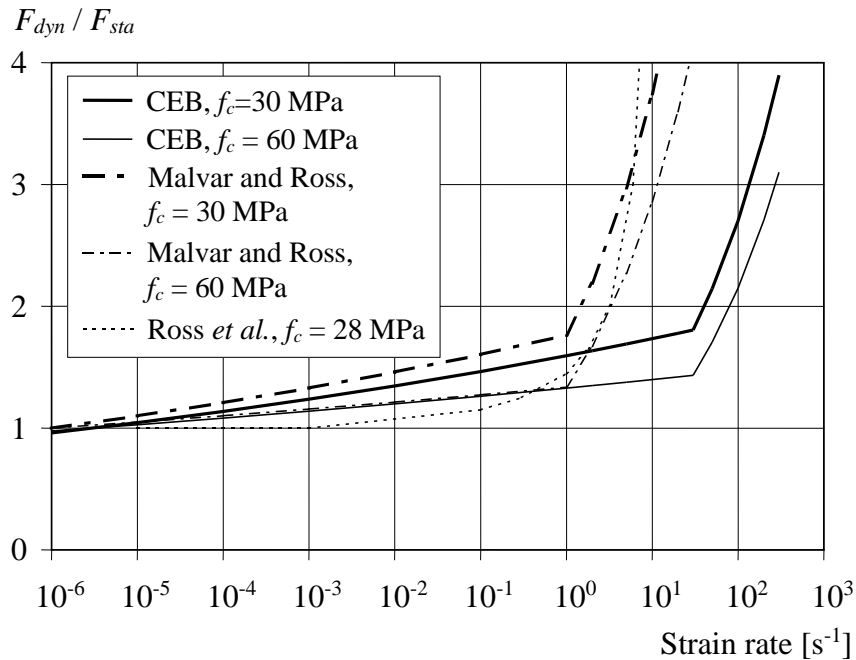


Figure 2.18 Studies of DIF and strain rate relation for concrete in tension (Johansson, 2000).

At strain rates around $10^0 - 10^2$ $1/s$ there is a so called transition zone at which there is a drastic increase in DIF at increased strain rate. This can, a bit simplified, be explained by two types of strain rate effects of concrete, viscous and structural, and can be seen in Figure 2.19. The change increase of the DIF in the viscous zone depends mainly on the difference of crack propagation for dynamic loads compared to

static loads. For a static load there is enough time for the cracks to be formed in the weaker parts of the concrete, i.e in the cement paste. In this way the cracks demands lower energy consumption. When the load is applied at a higher rate there is no such time for the cracks to propagate in the weaker parts. This means that the cracks takes shorter routes at a high strain rate and is therefore formed in stronger parts, sometimes through the strong aggregates. Since the cracks propagates both through the weaker and stronger parts the homogeneity of the concrete increases with increased strain rate in the viscous zone. One theory that is commonly accepted is that the increase of DIF at high strain rates in the viscous zone is mainly due to the presence of free water in the pores. Johansson (2000) presents numerous studies where the effects of free water in the pores is studied for concrete in both compression and tension.

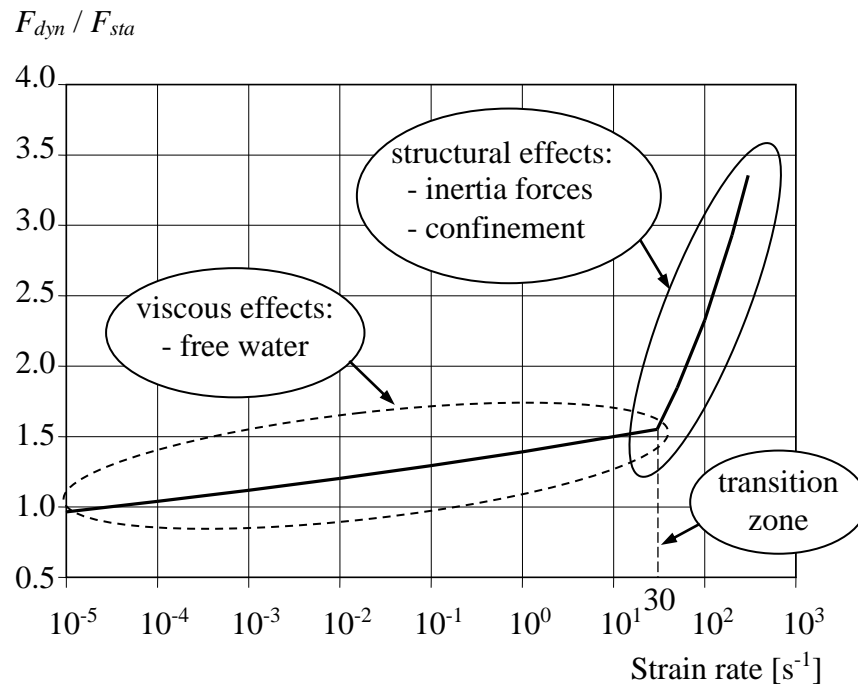


Figure 2.19 Different stages of strain rate effects of concrete (Johansson, 2000).

In the transition zone the structural behaviour becomes important for the DIF. The explanation for this increase is not that well studied but for the tensile strength an explanation given is that the increase is due to the change in stress and energy distribution due to inertia effects at the concrete crack tips. It is not entirely clear if the increase at the transition zone for compression could be explained in the same manner, but it is reasonable. Another possibility for compression is that there is inertia confinement effects. This means that, when the load is applied fast, there is no time for the concrete to react and a plain strain state is obtained, which entails a drastic increase of the compression strength due to the multiaxial stress state.

2.4.3 Influence on Reinforcement

The strain rate also has an influence of the strength of the reinforcement steel, although it is not as eminent as for concrete. Figure 2.20 shows a comparison of the DIF and strain rate relation of two studies. The reinforcement bar in the comparison is hot-rolled with the yield strength of 500 MPa and an

ultimate strength of 550 MPa.

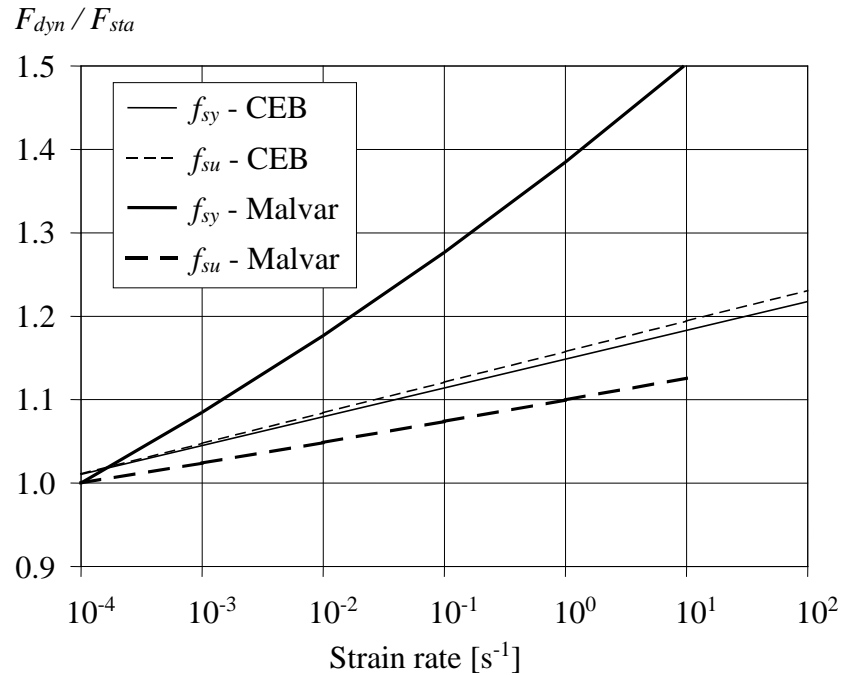


Figure 2.20 Studies of DIF and strain rate relation for yield and ultimate strength of reinforcement steel (Johansson, 2000).

2.4.4 Other Interesting Previous Studies

In Adhikary *et al.* (2012) the influence of the longitudinal reinforcement ratio of RC beams is treated. By a parametric study in a numerical simulation it was found out that the DIF increased with a decreased reinforcement ratio. This result seem a bit contradictory since the ultimate load carrying capacity increased with the increased reinforcement ratio. It was concluded that with a low reinforcement ratio in the beam there is an increase in the strain rate sensitivity, causing a higher DIF.

Cotsovos and Pavlovic (2008) investigates the correlation between experimental results and results obtained from FE analyses with regard to strain rate effects. The possibility to describe the behaviour of concrete as a material from the behaviour of a specimen is discussed. It is concluded that concrete specimens under dynamic loading cannot be used to describe the behaviour of concrete as a material, which is usually assumed. This is since concrete specimens under dynamic loading should be seen as a structure since their response is linked to the inertia effect of their mass and the active boundary conditions.

3 Plastic Rotation Capacity

3.1 Introduction

The ductility of RC is mainly dependent on the reinforcement properties since concrete is a brittle material compared to steel. Depending on the amount of reinforcement and its properties, a ductile or brittle response can therefore be obtained. A ductile response enables the formation of plastic hinges, which is regions where the reinforcement yields. These regions will now have a lower stiffness than the rest of the beam. Due to the nonlinear behaviour of the beam when the stiffness decreases, there will be a redistribution of the forces and the beam can still keep its capacity with an increasing deformation (Johansson and Laine, 2012). Johansson and Laine (2012) further states that the plastic hinges enables plastic redistribution of the stresses in the structure which leads to a larger energy absorption, which is preferred during impact loading. The difference in deformation capacity between a brittle and a ductile response is schematically illustrated in Figure 2.14. A large plastic rotation capacity can also be coupled to a high energy absorption since it is dependent of ductility. The plastic hinges are often assumed to be concentrated to a single section while the real distribution of a plastic hinge is spread over a plastic region, see Figure 3.1.

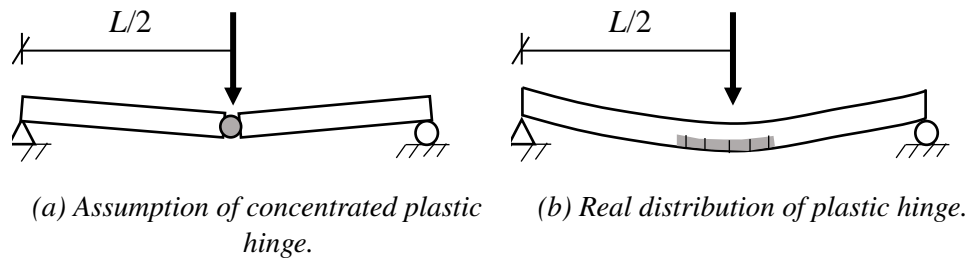


Figure 3.1 Concentrated and distributed plastic hinge. Inspired by (Lozano and Makdesi, 2017).

Plastic rotation is a complex phenomena and it depends on many parameters such as definition of yielding curvature, ultimate curvature, geometry, material properties, tension stiffening and bond slip, among others (Kheyroddin and Naderpour, 2007). Many researchers have investigated the possibility to determine plastic rotation capacity. Kheyroddin and Naderpour (2007) point out that there is a difference between different researcher's methods to predict the rotation capacity. It is therefore of interest to compare some different methods when determining the rotation capacity.

To be able to understand plastic rotation it is important to comprehend the concept of curvature, therefore this will be treated initially in this chapter. Secondly, the definition of plastic rotation and various methods used to calculate it will be presented.

3.2 Curvature

The deformation of a cross-section can be described by its strain distribution. The strain distribution can then be characterized by a mean strain ϵ_{cm} and a curvature $1/r$. The mean strain corresponds to the strain in the centre of gravity in the equivalent cross-section, see Figure 3.2. The curvature represents the

strain gradient and can, according to Engström (2011), be used to describe the strain in any section

$$\epsilon_c(z) = \epsilon_{cm} + \frac{1}{r}z \quad (3.1)$$

where z is the distance from the centre of gravity and r is the radius of curvature.

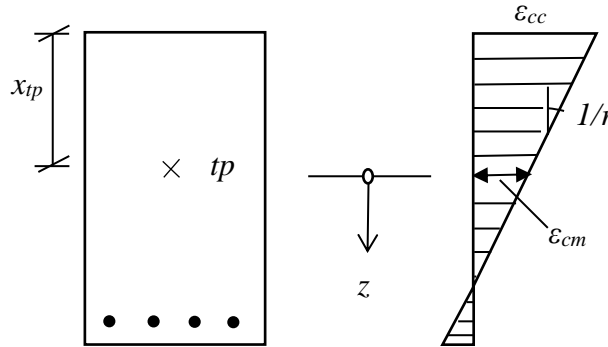


Figure 3.2 Cross-section deformation characterized by mean strain and curvature. Inspired by (Engström, 2011).

The curvature can also be denoted φ and can be further expressed from the radius of curvature. When considering a beam with constant curvature, see Figure 3.3, the element length dx along the gravity axis can be expressed as

$$dx = r \cdot d\varphi \Rightarrow \frac{1}{r} = \frac{d\varphi}{dx} \quad (3.2)$$

where $d\varphi$ is the change of angle over the element length.

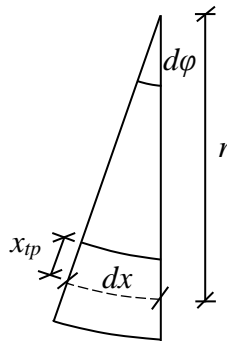


Figure 3.3 Relationship between curvature radius and deformation in a beam with constant curvature (Engström, 2011).

The curvature can thus be described as the change of angle per unit length. Considering an infinitesimal element, the curvature can be expressed from known values of strains and the geometry of the cross-section, see Figure 3.4.

$$\varphi = \frac{1}{r} = \frac{\epsilon_{cc}}{x} = \frac{\epsilon_{cc} + \epsilon_{ct}}{h} \quad (3.3)$$

$$\varphi = \frac{1}{r} = \frac{\varepsilon_s}{d - x} = \frac{\varepsilon_{cc} + \varepsilon_s}{d} \quad (3.4)$$

where ε_{cc} and ε_{ct} is the concrete strain in compression and tension, respectively, and ε_s represents the reinforcement strain.

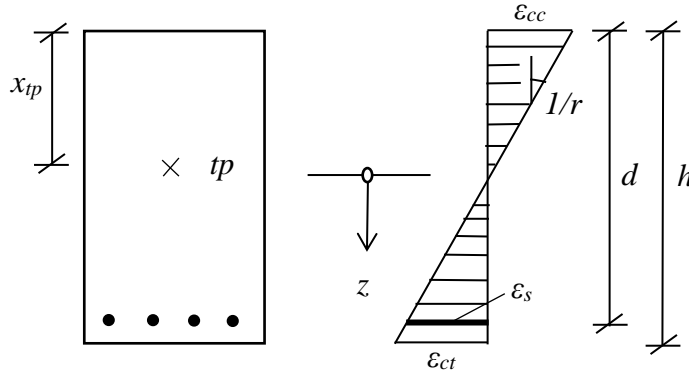


Figure 3.4 Geometry for calculation of curvature from known strains. Inspired by (Engström, 2011).

The relationships in Equations (3.3) and (3.4) is always true, regardless of whether the material is in state I, II or III. However, the position of the neutral axis will change due to cracking which in turn also leads to a change in curvature.

3.3 Plastic Rotation

The rotation of the plastic hinge when the load increases from yielding to collapse is denoted as plastic rotation capacity, θ_{pl} (Engström, 2015). Engström (2015) further states that the general expression for calculating the plastic rotation is done by integrating the plastic curvature over the length, l_y , which is the length of which the steel strain exceeds the yield strain

$$\theta_{pl} = \int_{l_y} (\varphi(x) - \varphi_y) dx \quad (3.5)$$

This can be expressed with the strain distribution in the same manner as in Section 3.2. Figure 3.5 shows a typical moment-curvature diagram with the corresponding strains in the cross-section.

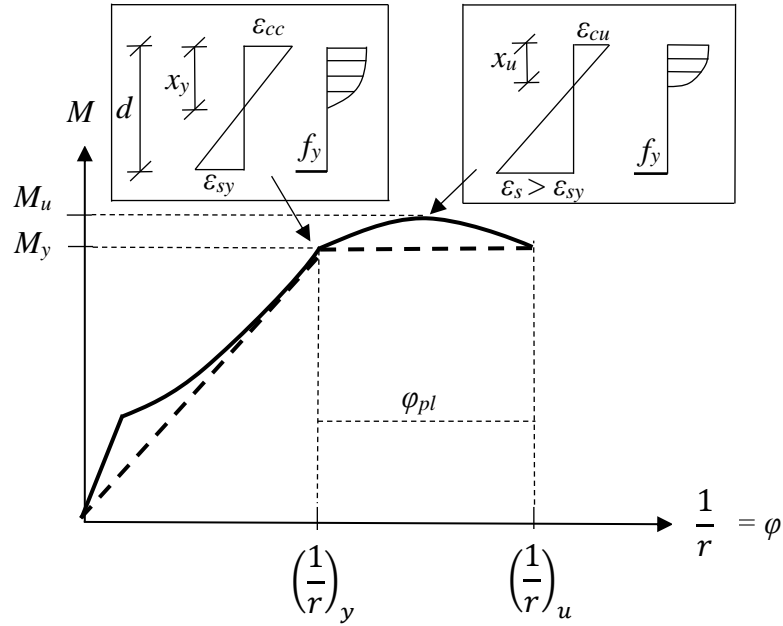


Figure 3.5 Typical moment-curvature diagram for an under-reinforced concrete cross-section together with a simplified bi-linear response. Inspired by (Engström, 2015).

The response is simplified by assuming a bi-linear elasto-plastic response and the curvature when the plastic deformations start can be expressed as

$$\varphi_y = \left(\frac{1}{r}\right)_y = \frac{\varepsilon_{cy}}{x_y} = \frac{\varepsilon_{sy}}{d - x_y} \quad (3.6)$$

where ε_{cy} and ε_{sy} is the strain of the concrete and steel, respectively, when the tensile reinforcement starts to yield, and x_y is the depth of the compressive zone when the steel starts to yield and can be determined by a sectional analysis in state II or III. The curvature obtained when the structure collapses can be expressed in two different ways, depending on which type of failure that will take place. When the concrete's strain ε_{cu} is critical it can be expressed as

$$\varphi_u = \left(\frac{1}{r}\right)_u = \frac{\varepsilon_{cu}}{x_u} = \frac{\varepsilon_s}{d - x_u} \quad (3.7)$$

where ε_{cu} is the ultimate concrete strain at the compressive edge, ε_s is the steel strain in the ultimate state and x_u is the depth of the compressive zone in the ultimate limit state. When the steels strain capacity is decisive it can be expressed as

$$\varphi_u = \left(\frac{1}{r}\right)_u = \frac{\varepsilon_{cc}}{x_u} = \frac{\varepsilon_{su}}{d - x_u} \quad (3.8)$$

where ε_{cc} is the concrete strain at the compressive edge when the ultimate steel strain is reached and ε_{su} is the ultimate steel strain. The plastic curvature can now be found by subtracting the curvature at yielding from the ultimate curvature

$$\varphi_{pl} = \left(\frac{1}{r}\right)_{pl} = \left(\frac{1}{r}\right)_u - \left(\frac{1}{r}\right)_y \quad (3.9)$$

which can be expressed by the steel strains as

$$\varphi_{pl} = \left(\frac{1}{r} \right)_{pl} = \frac{\varepsilon_s}{d - x_u} - \frac{\varepsilon_{sy}}{d - x_y} \approx \frac{\varepsilon_s - \varepsilon_{sy}}{d - x_u} \quad (3.10)$$

The steel strain will vary between the yield strain and the maximum strain in the plastic region, which means that the plastic curvature will also vary within this section. The plastic rotation can be calculated by integrating the plastic curvature from all sections along the length l_y as

$$\theta_{pl} = \int_0^{l_y} \left(\frac{\varepsilon_s(x) - \varepsilon_{sy}}{d - x_u} \right) dx \quad (3.11)$$

This expression is theoretically correct but Engström (2015) states that it is difficult to estimate the plastic rotation from it since several factors influence the parameters, as mentioned in Section 3.1. It should also be noted that it is important to understand which angle the calculations refers to. The calculation procedure presented here refers to the rotation illustrated in Figure 3.6.

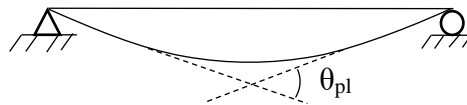


Figure 3.6 Relation between plastic hinge rotation and support rotation. Inspired by (Engström, 2015).

When determining the plastic rotation of a structure it is important to clearly define how the point of yielding and ultimate value is defined. When comparing research results it is also important to be aware of which method that is used since the measured rotations might vary significantly (Latte, 1999).

Latte (1999) states further that the point of yielding most often is clearly visible in a load-deformation relation, and that the main difficulty lies in the definition of the ultimate rotation capacity. This is since the moment diagram often can be horizontal at maximum load and that considerable deformations can be achieved after the maximum value has been reached. Two definitions is commonly used when determining the ultimate rotation capacity. The first one is based on the assumption that failure takes place when the maximum moment has been reached in the critical section. This point can easily be defined in theory but might be difficult to compare with tests since the moment-rotation diagram can be almost horizontal at the peak value and allow for additional deformations after the ultimate value has been reached, see Figure 3.7. These deformations can be utilized by defining the plastic rotation at 95 % of the maximum moment on the descending branch of the moment-rotation diagram.

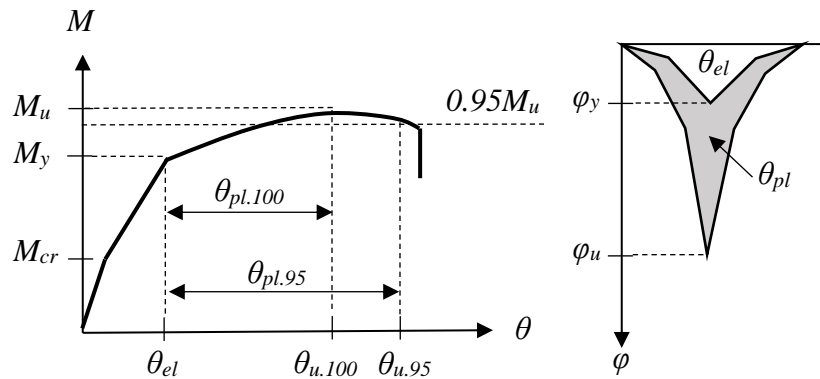


Figure 3.7 Definitions of plastic rotation capacity. Inspired by (Latte, 1999).

The two different values of the plastic rotation can be calculated from Figure 3.7 as

$$\theta_{pl,100} = \theta_{u,100} - \theta_{el} \quad (3.12)$$

$$\theta_{pl,95} = \theta_{u,95} - \theta_{el} \quad (3.13)$$

where θ_{el} is the integration of all curvatures along the beam under the load which causes the first yielding of reinforcement. $\theta_{u,100}$ and $\theta_{u,95}$ is the integration of all curvatures along the beam when the maximum moment and when 95 % of the moment has been reached, respectively, on the descending branch. Unless stated otherwise θ_{pl} refers to the value of $\theta_{pl,100}$. It can be seen from Figure 3.7 that the approach when considering the peak value of the ultimate moment is more conservative than the other one. Latte (1999) states further that $\theta_{u,95}$ should be used with care, when considering statically loaded structures, since the descending branch of the diagram is dependent on the post peak behaviour of the steel. If there is a low reinforcement ratio the steel might rupture at the ultimate load, leading to $\theta_{u,100} \simeq \theta_{u,95}$.

Some factors that affect the curvature and the plastic length, and therefore the plastic rotation, has been raised in the previous sections and a more detailed description of these can be found in (Latte, 1999) and (Lozano and Makdesi, 2017), a summary of these effects can be seen in Table 3.1.

Table 3.1 Factors that influence the curvature or plastic length. Modified from (Latte, 1999).

Influence on:	Curvature	Plastic length
Factors:	Reinforcement ratio Concrete strength and confinement Member size Compressive reinforcement Steel type - ultimate strain	Bond and tension stiffening Crack pattern -Shear cracks and crack spacing Type of load application Slenderness Steel type - hardening ratio

3.4 Different Methods to Determine Plastic Rotation

3.4.1 Introduction

The following sections will cover numerous methods to determine the plastic rotation capacity of beams. It is important to keep in mind what factors the different methods take into account when determining the rotation capacity, one method might include the influence of stirrups while another may not. This will of course affect the result if stirrups are present. Another thing that needs to be kept in mind is that the different methods does not state clearly which loading conditions the method was derived from, for example if a point load or a distributed load were used. This further emphasizes the perception that the results might not be entirely accurate for the specific conditions present.

3.4.2 From Test Results

When considering deformation-controlled tests, the deformations will still increase after the ultimate load has been reached since the applied load is reduced according to the remaining capacity of the beam. This means that it is possible to also describe the descending branch of a load-deflection relation from a test. Figure 3.8 shows an example for the response during a deformation-controlled test. Based on the same way of thinking as in Section 3.3, the plastic rotation capacity can be determined from the load-displacement relation as well as for the moment-curvature relation. Based on the deformations, the plastic rotation can be determined at a certain percentage of the ultimate load on the descending branch of the load-displacement curve, which is also illustrated in Figure 3.8.

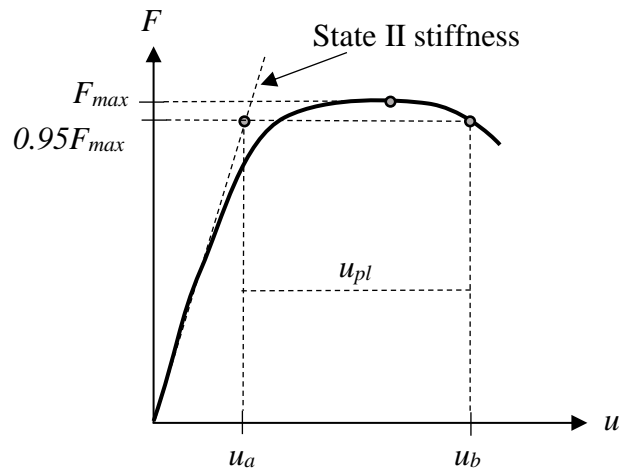


Figure 3.8 Response of deformation-controlled test with rotation capacity at 95 % of the ultimate load.

The plastic rotation $\theta_{pl,x\%}$ can be determined for a certain load $(x\%/100) \cdot F_{max}$ on the descending branch of the load-displacement curve where u_a and u_b corresponds to the elastic and plastic deformation at a certain load. Figure 3.9 illustrates the case presented in this report where the plastic hinge will be located at a distance $0.35L$ from the edge of the beam.

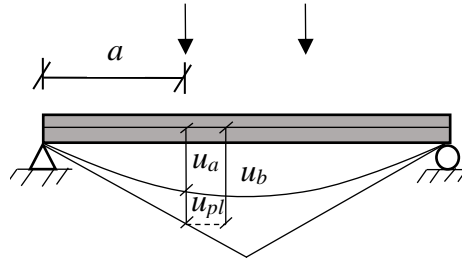


Figure 3.9 Illustration of the plastic and elastic deformations measured in experiments.

By assuming that the angle is very small, trigonometry can be used and the expression for the plastic rotation capacity can be expressed as

$$\theta_{pl,x\%} = \frac{(u_{b,x\%} - u_{a,x\%})}{a} = \frac{u_{pl,x\%}}{a} \quad (3.14)$$

If the beam has been subjected to an impact load before the static test. The rotational capacity may be determined according to the alternative method described in Lozano and Makdesi (2017), where the load at the different levels on the descending branch will be coupled to the undamaged beams, which is illustrated in Figure 3.10.

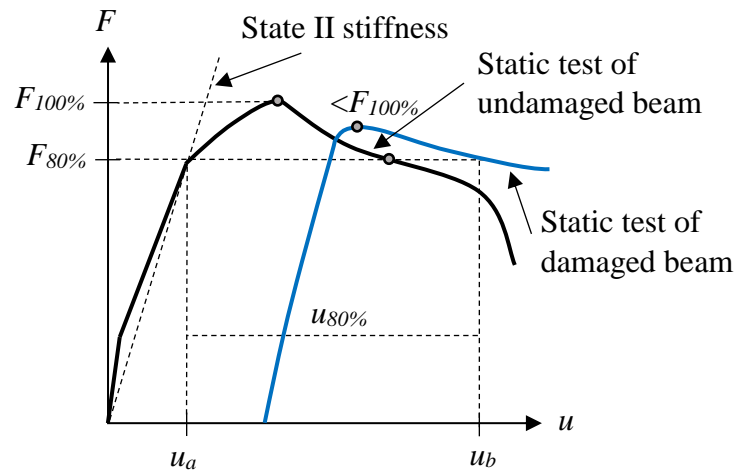


Figure 3.10 Illustration of method used to determine $u_{80\%}$ for a damaged beam.

3.4.3 Eurocode 2

The model presented in EC 2 is designed to be used under static loading (Johansson and Laine, 2012). The following section is based on the information given in (CEN, 2004) and (Johansson and Laine, 2012). The procedure is based on the rotation around a plastic hinge, and the rotation obtained can be coupled to the rotation θ_{pl} in Figure 3.6, while all of the other methods can be coupled to half that angle. The rotation capacity is based on a zone with the length of approximately 1.2 times the effective depth of the element. It is assumed that this zone will undergo plastic deformations, i.e plastic hinges is

formed, under the applied load. The plastic rotation obtained here represents the maximum value in the moment-rotation diagram in Figure 3.5.

The method presented can be used if the following conditions are fulfilled:

- In regions of yield hinges, $x_u/d \leq 0.45$ for concrete classes $\leq C50/60$ and $x_u/d \leq 0.35$ for concrete classes $\geq C55/67$.
- Reinforcement should be of class B or C.

The design value for the plastic rotation capacity can be obtained from Figure 3.11 where the ratio between the height of the compressive zone in the ultimate state x_u and the effective height of the cross-section d is the governing parameters. The position on the curve in Figure 3.11 also indicates which failure mode that will be expected between rupture of reinforcement and crushing of concrete.

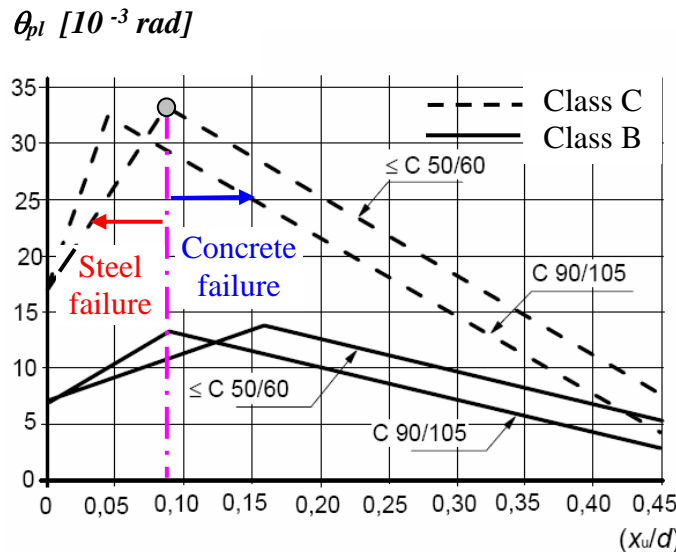


Figure 3.11 This figure is only valid for a slenderness $\lambda = 3.0$ and if this is not the case, the plastic rotation capacity should be multiplied by a factor k_λ . Inspired by (CEN, 2004).

$$\theta_{pl,d} = k_\lambda \theta_{pl} \quad (3.15)$$

where k_λ is defined as

$$k_\lambda = \sqrt{\frac{\lambda}{3}} \quad (3.16)$$

and λ is defined as

$$\lambda = \frac{x_0}{d} \quad (3.17)$$

where x_0 is the distance between the considered maximum moment section and the adjacent zero moment section after plastic redistribution and d is the effective depth of the cross-section.

3.4.4 Betonghandboken (ABC-Method)

This is an empirical method designed to be used under static loading and the following section is based on information given in (Fransson, 1997) and (Cederwall *et al.*, 1990).

The method is based on three factors: A , B and C which takes different influences on the rotation capacity into account. The factor A considers the influence of stirrups and reinforcement in both compression and tension, B considers mechanical properties of the reinforcement and C considers the location of the plastic hinges, in relation to the moment distribution. When combining these three factors, the plastic rotation can be calculated as

$$\theta_{pl,95} = A \cdot B \cdot C \cdot 10^{-3} \quad (3.18)$$

It should be noted that the plastic rotation obtained from this method is based on the value obtained when 95 % of the ultimate value is reached on the descending branch, Latte (1999) and Fransson (1997). Further, it refers to the rotation around a support, i.e. the angle θ_{pl} in Figure 3.6, or one side of the rotation around a plastic hinge. When considering partial safety factors and characteristic values of material strength, the factor A in the design can be calculated as

$$A = 1 + 0.6\omega_v + 1.7\omega'_s - 1.4\frac{\omega_s}{\omega_{bal}} \geq 0.05 \quad (3.19)$$

but when measured values of the material strength is used, the following equation can be used

$$A = 1 + 1.3\omega_v + 3\omega'_s - 5\omega_s \quad 0.05 \leq A \leq 2.30 \quad (3.20)$$

where ω_v , ω'_s and ω_s represents the mechanical ratio of the shear, compression and tension reinforcement, respectively, and can be calculated as

$$\omega_v = \frac{A_v}{b \cdot s} \frac{f_{sv}}{f_{ct}} \quad (3.21)$$

$$\omega'_s = \frac{A'_s}{b \cdot d} \frac{f_{sc}}{f_{cc}} \quad (3.22)$$

$$\omega_s = \frac{A_s}{b \cdot d} \frac{f_{st}}{f_{cc}} \quad (3.23)$$

where A_v , A'_s and A_s is the area of the shear, compression and tension reinforcement respectively. Further, f_{sv} , f_{sc} and f_{st} is the strength of the shear, compression and tension reinforcement, respectively, while f_{ct} and f_{cc} is the concretes tension and compression strength. The parameter s is the distance between the shear reinforcement, b is the width of the compressive zone and d is the effective height of the cross-section. Lastly, ω_{bal} is called mechanic reinforcement ratio and is calculated via the strains as

$$\omega_{bal} = \frac{0.8\epsilon_{cu}}{\epsilon_{cu} + \epsilon_{sy}} \quad (3.24)$$

where $\varepsilon_{cu} = 3.5 \text{ ‰}$ represents the ultimate strain of the concrete and ε_{sy} represents the reinforcements yield strain which can be calculated as

$$\varepsilon_{sy} = \frac{f_{st}}{E_s} \quad (3.25)$$

where E_s is the modulus of elasticity of the reinforcement. There are a number of limitations of the values for the different mechanical ratios

- ω_v is limited to 2.0 in Equation (3.19) and to 1.35 in Equation (3.20)
- The spacing of the stirrups must be $< 0.8d$, otherwise $\omega_v = 0$
- ω'_s is limited to ω_s if the spacing of the stirrups $< 15\phi_{sc}$ where ϕ_{sc} is the smallest diameter of the compression reinforcement, otherwise $\omega'_s = 0$
- ω_s must not exceed ω_{bal}

The factor B can be found in Table 3.2 and depending on the type of reinforcement, it is further restricted by the product of factor A and B . Note that the classification of the reinforcement is from the old Swedish regulations used until 1995.

Table 3.2 Values of factor B . Based on *Betonghandboken (1990) (Johansson and Laine, 2012)*. ε_p is the strain of the prestressing steel.

Type of reinforcement	B	Max A · B
Ks 60, Ks 40, Ss 26, Ss 26S	1.0	1.7
Ks 60S, Ks 40S	0.8	1.1
Cold-worked steel with $\varepsilon_{su} \geq 3 \text{ ‰}$ and $f_{su}/f_{sy0.2} \geq 1.1$	$0.6 \left(1 - 0.7 \frac{\varepsilon_p}{\varepsilon_{su}} \right)$	0.5

¹⁾ If $f_{su}/f_{sy0.2} \geq 1.4$ and $\varepsilon_{su} \geq 8 \text{ ‰}$, values for Ks60 and Ks40 is used.

The factor C can be calculated from two different equations, depending on whether the plastic hinge is located in the span or over the supports

$$C_{sup} = 10 \cdot l_{0,sup}/d \quad (3.26)$$

$$C_f = 7 \cdot l_{0,f}/d \quad (3.27)$$

where $l_{0,sup}$ and $l_{0,f}$ is the distance from the plastic hinge to the position where the moment is zero, according to Figure 3.12.

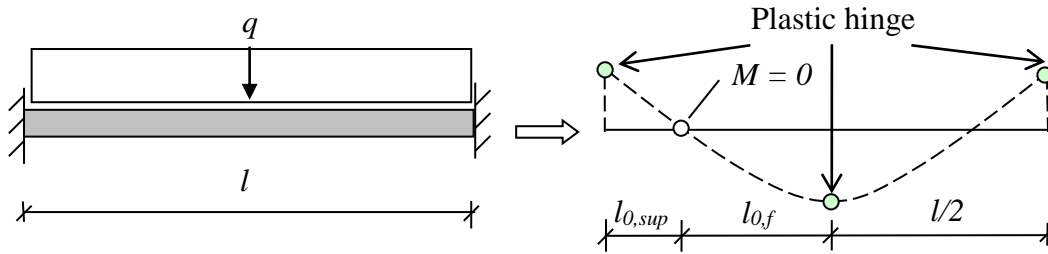


Figure 3.12 Definition of $l_{0,sup}$ and $l_{0,f}$ depending on the moment diagram. Inspired by (Johansson and Laine, 2012).

3.4.5 Tamminens D-factor

In a paper written by Tamminen (1993), a method to improve the method used in Betonghandboken is presented. This is done by introducing another variable D which takes the height of the member into account. Tamminen points out that the rotation capacity increases with increasing strength of the concrete but decreases with increasing size of the member. The formula in Betonghandboken provides an increase in rotation capacity when the concrete strength increases but the size of the member does not have any influence. Therefore he gives a suggestion for the factor D as

$$D = \frac{k}{d} \geq 1 \quad (3.28)$$

where d is the effective height of the member and k varies depending on the quality of the concrete, see Table 3.3. It should be noted that the tests made by Tamminen (1993) is done on beams made out of high strength concrete. It is however interesting to see how much extra capacity this method provides in relation to the ordinary method. It should be noted that the concrete classes in Table 3.3 corresponds to the old standards. If a comparison is made between the concrete classes in Cederwall *et al.* (1990) and in CEN (2004) it can be seen that K30 corresponds to C25/30 and that K100 corresponds to high performance concrete. It should be noted that the factor k is only given for two different concrete classes and that Tamminen gives no suggestion on how to choose the factor if the concrete class present does not correspond to one of these. One suggestion could be to interpolate but since he gives no suggestions regarding interpolation, it is not done in this project.

Table 3.3 Values of k depending on the concrete quality.

Concrete class	K30	K100
k	0.3	0.5

The equation for calculating the plastic rotation can therefore be expressed as

$$\theta_{pl,95} = A \cdot B \cdot C \cdot D \cdot 10^{-3} \quad (3.29)$$

3.4.6 Bk25

Johansson and Laine (2012) describes a method that is presented in Fortifikationsförvaltningen (1973) and this chapter is based on the knowledge obtained from those. This method is designed to be used under impulse loading and the type of load considered is an air blast. The plastic rotation obtained here represents the maximum value in the moment-rotation diagram presented in Figure 3.7.

The plastic hinge is assumed to be spread over a distance $2l_{pl}$, which has a constant radius of curvature, see Figure 3.13. From Figure 3.13 it is also clear which angle the method refers to.

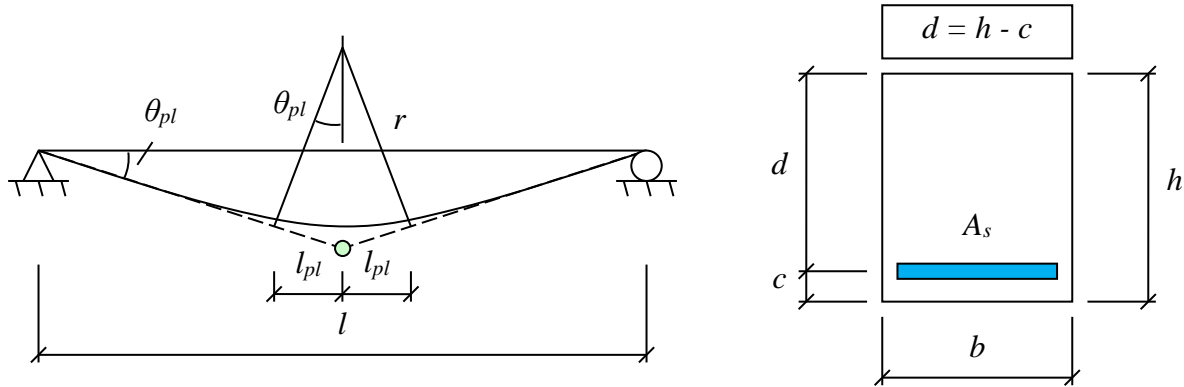


Figure 3.13 Model for rotation capacity. Inspired by (Johansson and Laine, 2012).

The equivalent plastic hinge length, l_{pl} , can be calculated as

$$l_{pl} = 0.5d + 0.15l \quad (3.30)$$

The rotation capacity is directly proportional to the length of the plastic hinge

$$\theta_{pl} = \frac{l_{pl}}{r} \quad (3.31)$$

The maximum radius of curvature can be obtained through the same way of thinking as in Section 3.2

$$\frac{1}{r} = \frac{\epsilon_{cu}}{x} = \frac{\epsilon_s}{d - x} \quad (3.32)$$

where ϵ_{cu} is the concrete's ultimate strain and ϵ_s is the mean strain of the reinforcement over the distance l_{pl} . The failure criterion will be reached either by crushing of concrete or rupture of reinforcement when they reach ϵ_{cu} or ϵ_s , respectively. Figure 3.14 shows a principal cross-section.

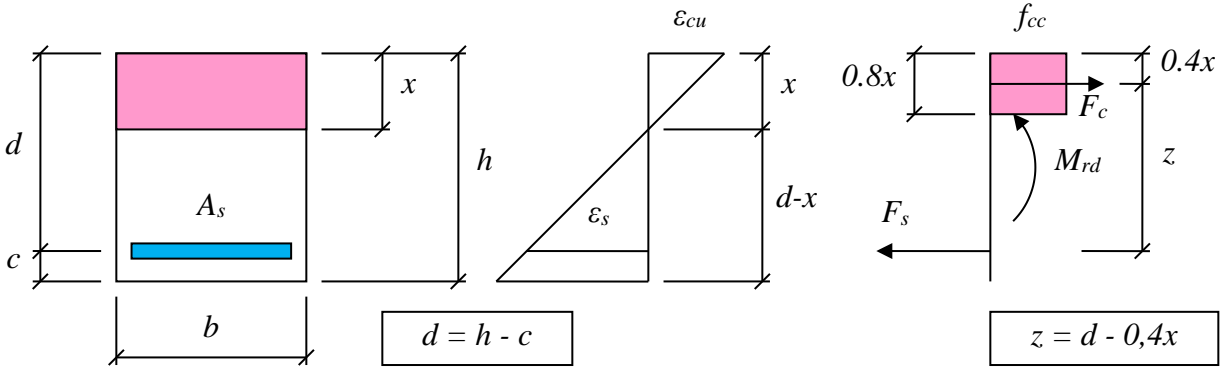


Figure 3.14 Cross-section subjected to a bending moment, from Johansson and Laine (2012).

From Figure 3.14, a horizontal equilibrium can be obtained as

$$f_{cc} b 0.8x = f_{st} A_s \quad (3.33)$$

With the definition of the reinforcement ratio parameter, ρ

$$\rho = \frac{A_s}{b \cdot d} \quad (3.34)$$

and the mechanical reinforcement ratio

$$\omega_s = \frac{A_s}{b \cdot d} \frac{f_{st}}{f_{cc}} \quad (3.35)$$

The height of the compressive zone can be expressed from Equation (3.33) as

$$x = \rho \cdot d \frac{1}{0.8} \frac{f_{st}}{f_{cc}} = \frac{\omega_s d}{0.8} \quad (3.36)$$

or

$$\frac{x}{d} = \frac{\omega_s}{0.8} \quad (3.37)$$

The limit for when different failure modes occur can be expressed from Equation (3.32) as

$$\omega_{s,crit} = \frac{0.8 \epsilon_{cu}}{\epsilon_{cu} + \epsilon_s} \quad (3.38)$$

This means that if $\omega_s > \omega_{s,crit}$, the beam is expected to fail due to crushing of concrete. Otherwise, it is expected to fail due to rupture of reinforcement. When crushing of concrete is critical, the plastic rotation capacity can be calculated by combining Equations (3.30), (3.31) and (3.33) as

$$\theta_{pl,f} = \frac{l_{pl}}{r} = \frac{0.8 \epsilon_{cu}}{\omega_s d} (0.5d + 0.15l) = \frac{0.4 \epsilon_{cu}}{\omega_s} \left(1 + 0.3 \frac{l}{d} \right) \quad (3.39)$$

and when rupture of reinforcement is critical as

$$\theta_{pl,f} = \frac{l_{pl}}{r} = \frac{0.8\varepsilon_s}{d(0.8 - \omega_s)} (0.5d + 0.15l) = \frac{0.4\varepsilon_s}{0.8 - \omega_s} \left(1 + 0.3\frac{l}{d}\right) \quad (3.40)$$

Equations (3.39) and (3.40) are true when the plastic hinge develops in the span. When a plastic hinge is formed at the support, though, the definition of the plastic hinge length is defined as

$$l_{pl} = 0.5d + 0.1l_0 \quad (3.41)$$

where l_0 is the shear span and can be calculated as

$$l_0 = \frac{M_{sup}}{V_{sup}} \quad (3.42)$$

where M_{sup} and V_{sup} is the moment and shear over the support. For a beam with the length l and a uniformly distributed load q , the moment and shear can be calculated by the well-known equations:

$$M_{sup} + M_f = \frac{ql^2}{2} \quad (3.43)$$

$$V_{sup} = \frac{ql}{2} \quad (3.44)$$

where

$$M_{sup} = \alpha M_f \quad (3.45)$$

where α is a parameter that depends on the reinforcement amount in the span ρ_f and over the support ρ_{sup} . It can be expressed approximately as

$$\alpha = \frac{\rho_{sup}}{\rho_f} \quad (3.46)$$

When combining Equations (3.42) to (3.46), the length l_0 can be rewritten as

$$l_0 = \frac{\rho_{sup}}{\rho_{sup} + \rho_f} \cdot \frac{l}{4} \quad (3.47)$$

By using the same analogy as before, the plastic rotation capacity over the support $\theta_{pl,sup}$, when crushing of concrete is critical, can be expressed as

$$\theta_{pl,sup} = \frac{0.4\varepsilon_{cu}}{\omega_s} \cdot \left(1 + \frac{1}{20} \cdot \frac{\rho_{sup}}{\rho_{sup} + \rho_f} \cdot \frac{l}{d}\right) \quad (3.48)$$

and when rupture of reinforcement is critical as

$$\theta_{pl,sup} = \frac{0.4\varepsilon_{cu}}{0.8 - \omega_s} \cdot \left(1 + \frac{1}{20} \cdot \frac{\rho_{sup}}{\rho_{sup} + \rho_f} \cdot \frac{l}{d}\right) \quad (3.49)$$

3.4.7 Methods Based on Equivalent Plastic Hinge Length

3.4.7.1 Introduction

Many researchers have presented a method to approximate the plastic rotation by assuming a constant plastic curvature over an equivalent plastic hinge length l_{pl} , see Figure 3.15.

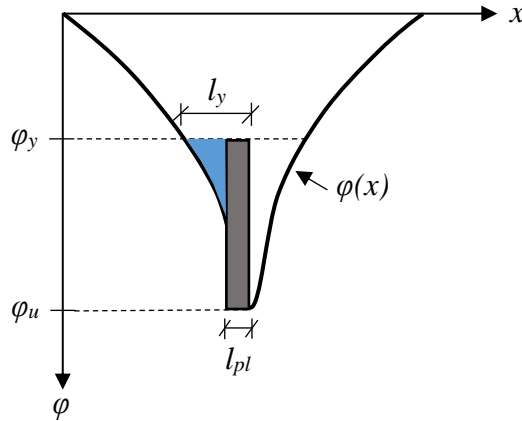


Figure 3.15 Concept of equivalent plastic hinge. Inspired by (Lozano and Makdesi, 2017).

In the method described in Section 3.3, the plastic rotation is calculated by integrating the curvatures over the length of the plastic hinge, which is represented by the grey area in Figure 3.15. This area can be approximated by a rectangle with the height $\varphi_u - \varphi_y$ and the width l_{pl} (Kheyroddin and Naderpour, 2007). The plastic rotation around the hinge can then be calculated as

$$\theta_{pl} = (\varphi_u - \varphi_y)l_{pl} = \varphi_{pl}l_{pl} \quad (3.50)$$

There are several methods to estimate the equivalent plastic hinge length and some of them is treated in Lozano and Makdesi (2017). However, Arbulu (2006) covers several other methods and the methods that are applicable on beams is presented in the following sections.

3.4.7.2 Baker and Amarkone

The method developed by Baker and Amarkone (1964) is valid for both beams and columns and they give one expression for confined concrete and one for unconfined concrete. Only the method for unconfined concrete is presented here and in that case the equivalent plastic hinge length can be calculated as

$$l_{pl} = k_1 k_2 k_3 \left(\frac{l_0}{d} \right)^{0.25} d \quad (3.51)$$

where k_1 is a factor that considers the influence of the tension reinforcement. It is equal to 0.7 for mild steel and 0.9 for cold-worked-steel. Further, k_2 is a factor that considers axial loading and can be calculated as

$$k_2 = 1 + 0.5 \frac{P}{P_u} \quad (3.52)$$

where P is the axial load and P_u is the axial compressive strength of the member without any bending moment. Finally, k_3 is a factor that considers the influence of the strength of the concrete and can be calculated as

$$k_3 = 0.9 - \frac{f_{cc} - 13.8}{92} \quad (3.53)$$

where f_{cc} is given in [MPa].

3.4.7.3 ACI-ASCE Committee 428

ACI-ASCE-Committee-428 (1968) presented a model that is valid for both beams and columns as well. It is presented as a lower and upper limit for the equivalent plastic hinge length as

$$\min \left[R_\epsilon \left(\frac{d}{4} + 0.03l_0 R_m \right), R_\epsilon d \right] < l_{pl} < R_\epsilon \left(\frac{d}{2} + 0.10l_0 R_m \right) \quad (3.54)$$

where R_ϵ is the strain ratio

$$R_\epsilon = \frac{0.004 - \epsilon_{ce}}{\epsilon_{cu} - \epsilon_{ce}} \quad (3.55)$$

and ϵ_{ce} is the concrete strain in the extreme compression fiber at yield curvature. This strain can be calculated or assumed a value between 0.001 and 0.002. ϵ_{cu} is the concrete strain in the extreme compression fiber at ultimate curvature. The effects of confinement, loading rate and strain gradients are neglected and ϵ_{cu} is assumed to be between 0.003 and 0.004. R_m is the moment ratio and can be calculated as

$$R_m = \frac{M_{max} - M_y}{M_u - M_y} \quad (3.56)$$

where M_{max} is the maximum moment in the length of the member. An expression for calculating the distance l_0 from the section of maximum moment to the section of zero moment was also presented as

$$l_0 = \frac{4M_{max}}{4V_z + \sqrt{w_z M_{max}} R_m} \quad (3.57)$$

where V_z is the shear force adjacent to a concentrated load or the reaction at the section of maximum moment and w_z is the uniformly distributed load at the section of maximum moment. This expression for l_0 is however only valid for members subjected to a uniformly distributed load.

3.4.7.4 Paulay and Priestley

Paulay and Priestley (1992) developed a method in 1992 that is valid for both beams and columns as well and it is expressed as

$$l_{pl} = 0.08l_0 + 0.022f_y d_b \geq 0.044f_y d_b \quad (3.58)$$

Where f_y is given in [MPa] and d_b is the diameter of the tensile reinforcement. It is also stated that for commonly used dimensions, Equation (3.58) will give plastic hinge lengths of approximately $0.5h$.

3.4.7.5 Panagiotakos and Fardis

Panagiotakos and Fardis (2001) developed a method in 2001 that is valid for beams, columns and walls. They made predictions and tested over 1 000 specimens to see how well they could predict the behaviour of them. 266 of the specimens were beams which had a rectangular cross-section, except two which had a T-section. The reinforcement was placed unsymmetrical and the beams were not subjected to any axial loads. Most of the specimens were tested as cantilevers, but some of them were tested as simply supported beams with a concentrated load at the midspan. The specimens were subjected to monotonic or cyclic loading and an expression for the equivalent plastic hinge length were derived for both cases as

$$l_{pl,cy} = 0.12l_0 + 0.014a_{sl}d_b f_y \quad (3.59)$$

for cyclic loading and

$$l_{pl,mon} = 1.5l_{p,cy} = 0.18l_0 + 0.021a_{sl}d_b f_y \quad (3.60)$$

for monotonic loading. a_{sl} is equal to one if slippage of the longitudinal reinforcement is possible and zero if it is not and f_y is given in [MPa].

4 Fundamentals of Dynamics

4.1 Introduction

The response of a dynamic loaded structure can be described using a single-degree of freedom (SDOF) system. Some basic fundamentals of dynamics is used to create the SDOF system that is used within this project. The main part of the theoretical background in this section is based on Johansson and Laine (2012).

4.2 Impulse

When a mass particle m has a certain velocity v the momentum p of the body is defined as

$$p = m \cdot v \quad (4.1)$$

If a body with an initial velocity v_0 is subjected to an applied force $F(t)$ where $t_0 \leq t \leq t_1$, the momentum will change to

$$m \cdot v_1 = m \cdot v_0 + \int_{t_0}^t F(t)dt \quad (4.2)$$

where the last part is the change in momentum and is defined as the impulse I acting on the body. The impulse can be represented as the area under the curve in a load-time graph, see Figure 4.1.

$$I = \Delta p = m \cdot \Delta v = \int_{t_0}^t F(t)dt \quad (4.3)$$

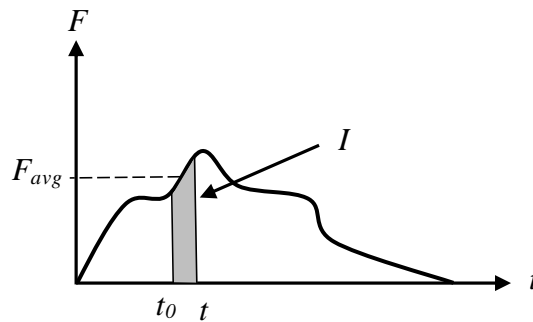


Figure 4.1 The impulse over a time interval. F_{avg} is the average force acting on the body.

4.3 Work, Kinetic Energy and External Work

If a force F is applied to a particle and it is displaced the distance δ the work W performed by the force is defined as

$$W = F\delta \cos \phi = F_x \delta \quad (4.4)$$

where ϕ is the angle between the force and the direction of the particle, see Figure 4.2. When a variable force is applied, the work from the force can be described as

$$W = \int_0^{\delta} F_x(x) dx \quad (4.5)$$

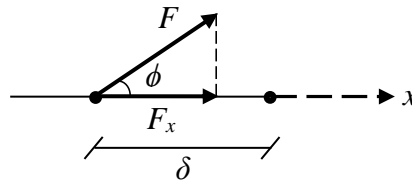


Figure 4.2 Work explained as the force projected to the direction of displacement.

Work W and energy E has the same quantity. The kinetic energy E_k of a particle of mass moving at a velocity v is defined as

$$E_k = \frac{m \cdot v^2}{2} \quad (4.6)$$

which gives the possibility to explain the external work W_e done by a force as the change in kinetic energy

$$W_e = \Delta E_k = \frac{m \cdot v_1^2}{2} - \frac{m \cdot v_0^2}{2} \quad (4.7)$$

By combining this expression with Equation (4.3) the external work can be described based on the characteristic impulse as

$$W_e = \frac{I_k^2}{2m} \quad (4.8)$$

4.4 Internal Work

4.4.1 Introduction

An impulse acting on a structure causes an external work and to maintain the energy equilibrium there must be an internal work W_i that equals the external work

$$W_i = W_e \quad (4.9)$$

This equilibrium constitutes the conceptual basis of a calculation model for an impulse-loaded constructions.

4.4.2 Linear Elastic Response

According to Equation (2.1) the relation between the internal force R and the elastic deformation u_{el} is

$$R = k \cdot u_{el} \quad (4.10)$$

The internal work performed by the system can then be defined as

$$W_i = \frac{R \cdot u_{el}}{2} = \frac{k \cdot u_{el}^2}{2} \quad (4.11)$$

The energy equilibrium for a linear elastic response is shown schematically in Figure 4.3.

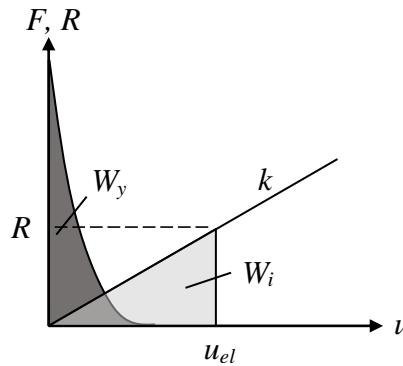


Figure 4.3 Energy equilibrium with linear elastic response.

By combining Equations (4.8), (4.9) and (4.11), the internal work can be expressed as

$$W_i = \frac{k \cdot u_{el}^2}{2} = \frac{I_k^2}{2m} = W_e \quad (4.12)$$

from which the elastic response can be expressed as

$$u_{el} = \frac{I_k}{m \cdot \omega} \quad (4.13)$$

where

$$\omega = \sqrt{\frac{k}{m}} \quad (4.14)$$

corresponds to the angular eigenfrequency of the system.

4.4.3 Plastic Response

As explained in Section 2.2.3, deformations do not occur until the capacity of the structure is reached. At the point where the maximum value of the internal resistance R_m is reached, the structure starts to deform. The internal work can then be expressed as

$$W_i = R \cdot u = R_m \cdot u \quad (4.15)$$

The relationship between internal and external energy can be seen in Figure 4.4.

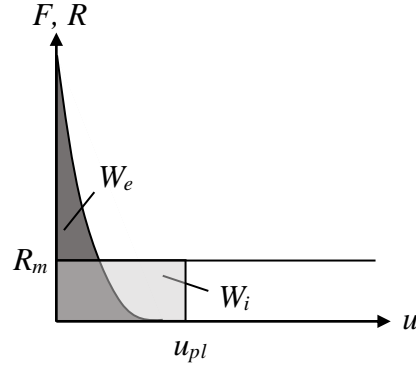


Figure 4.4 Energy equilibrium with plastic response.

The plastic deformation can, by combining Equations (4.8), (4.9) and (4.15), be expressed as

$$u_{pl} = \frac{I_k^2}{2m \cdot R_m} \quad (4.16)$$

4.4.4 Elasto-Plastic Response

The internal force R is in the elasto-plastic case expressed as Equation (2.3) and the internal work depends on both the elastic and plastic deformations and is calculated as

$$W_i = \frac{R_m}{2}(u_{el} + 2u_{pl}) \quad (4.17)$$

where

$$u_{el} = \frac{R_m}{k} \quad (4.18)$$

is the point from where the plastic deformation starts. By combining Equations (4.8), (4.9) and (4.17) it is also possible to express the plastic part as

$$u_{pl} = \frac{I_k^2}{2m \cdot R_m} - \frac{u_{el}}{2} \quad (4.19)$$

The relationship between internal and external energy can be seen in Figure 4.5.

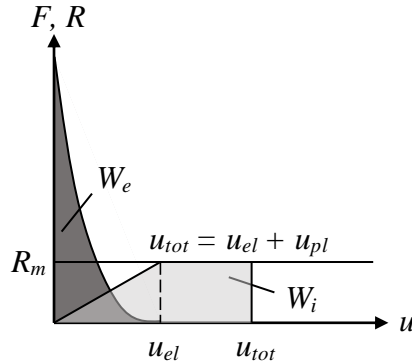


Figure 4.5 Energy equilibrium with elasto-plastic response.

4.5 Equation of Motion

In order to understand the SDOF system used in this project it is essential to understand the equation of motion. The derivation and description of the equation is based on the knowledge gained from (Craig and Kurdila, 2006) and (Johansson and Laine, 2012). Newton's second law

$$\sum F = m \cdot a \quad (4.20)$$

is applied where m is the mass and a the acceleration of the mass, which is given as the second time derivative of the displacement, $a = \ddot{u}$. In a similar way the velocity is given as the first time derivative of the displacement, $v = \dot{u}$. If the mass in a system with a spring and a damper is displaced the distance u , positive to the right, by an external force $F(t)$, the free body diagram can be described by Figure 4.6.

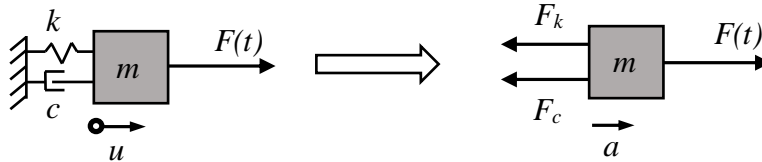


Figure 4.6 Free body diagram.

The relationships for the two resistance forces F_k and F_c are

$$F_k = k \cdot u \quad (4.21)$$

and

$$F_c = c \cdot \dot{u} \quad (4.22)$$

where k is the linear stiffness of the spring and c is the damping coefficient. The damping is usually defined as a linear function of the velocity but it is a complex phenomenon and there are several mathematical methods to describe it. By using Equation (4.20) the dynamic equilibrium of the free body diagram in Figure 4.6 gives

$$F(t) - F_k - F_c = m \cdot a \quad (4.23)$$

With some rearrangement and application of Equations (4.21) and (4.22) the equation of motion for a SDOF system is

$$m \cdot \ddot{u} + c \cdot \dot{u} + k \cdot u = F(t) \quad (4.24)$$

4.6 Impact and the Influence of Mass

4.6.1 Introduction

When a moving mass m_1 , with an initial velocity v_0 , impacts a non-moving mass m_2 , see Figure 4.7, there are two extreme cases to describe the collision: perfectly elastic or perfectly plastic impact, see Figure 4.8. In the elastic response the two bodies will have different velocities, v_1 and v_2 , after the impact whereas in the plastic case they will have the same velocity v_{12} . In the usual occasion, the collision are somewhere in between the elastic and the plastic case, but they are often treated separately for simplicity. The incoming mass m_1 represents as an example the impulse from a shock wave or a vehicle hitting a barrier. In this study of impulse loaded structures it represents the drop-weight that hits the RC beam.

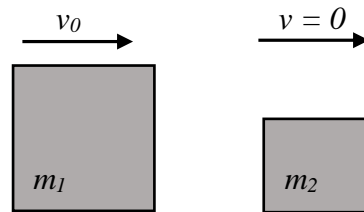


Figure 4.7 Before impact.

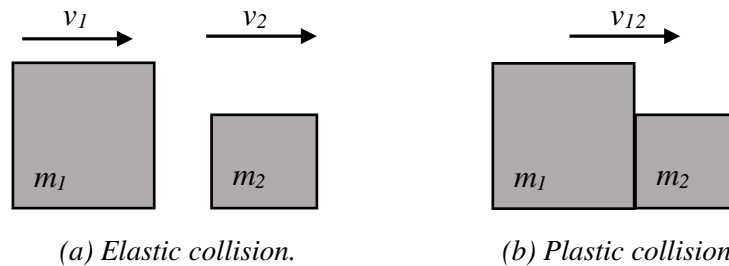


Figure 4.8 After impact.

The kinetic energy and momentum of the incoming mass m_1 is

$$E_{k,0} = \frac{m_1 v_0^2}{2} \quad (4.25)$$

$$p_0 = m_1 v_0 \quad (4.26)$$

4.6.2 Elastic Impact

In the perfectly elastic collision the two velocities after impact v_1 and v_2 can be calculated as

$$v_1 = \frac{m_1 - m_2}{m_1 + m_2} v_0 \quad (4.27)$$

and

$$v_2 = \frac{2m_1}{m_1 + m_2} v_0 \quad (4.28)$$

Both the kinetic energy and the momentum will be the same before and after impact. The kinetic energies for the two bodies then become

$$E_{k,1} = \frac{m_1 v_1^2}{2} = \frac{m_1}{2} \left(\frac{m_1 - m_2}{m_1 + m_2} \right)^2 v_0^2 = \left(\frac{m_1 - m_2}{m_1 + m_2} \right)^2 E_{k,0} \quad (4.29)$$

$$E_{k,2} = \frac{m_2 v_2^2}{2} = \frac{m_2}{2} \left(\frac{2m_1}{m_1 + m_2} \right)^2 v_0^2 = \frac{4m_1 m_2}{(m_1 + m_2)^2} E_{k,0} \quad (4.30)$$

4.6.3 Plastic Impact

If the collision is plastic, the kinetic energy is no longer the same before and after impact. However, the momentum remain the same before and after impact and the velocity v_3 of the system is

$$v_3 = \frac{m_1}{m_1 + m_2} v_0 \quad (4.31)$$

The kinetic energy of the system is

$$E_{k,3} = \frac{(m_1 + m_2) v_3^2}{2} = \frac{m_1 + m_2}{2} \left(\frac{m_1}{m_1 + m_2} \right)^2 v_0^2 = \frac{m_1}{m_1 + m_2} E_{k,0} \quad (4.32)$$

4.7 Response during Repeated Impacts

4.7.1 Introduction

In this project the RC beam will be subjected to both single and repeated impacts. The aim of this section is to explain the expected structural behaviour for the latter case. The methodology presented in this section is based on the information gained from Johansson and Laine (2012) where the structural behaviour is explained by an equivalent impulse load, determined from the effect of several impacts. From this, the residual strength can be estimated. It is based on the assumption that the time interval between the impacts is large enough to get a stagnant structure before the next impact occurs. The repeated impact theory is only explained from the plastic and elasto-plastic point of view. The ideally elastic response is not of interest since the structure, in such a case, will revert to the original position without any decrease in residual deformation capacity.

4.7.2 Plastic and Elasto-Plastic Response

The elasto-plastic response is explained in Section 2.2.4 and is once again illustrated in Figure 4.9, where the response of the mass m is showed in a force-displacement relation.

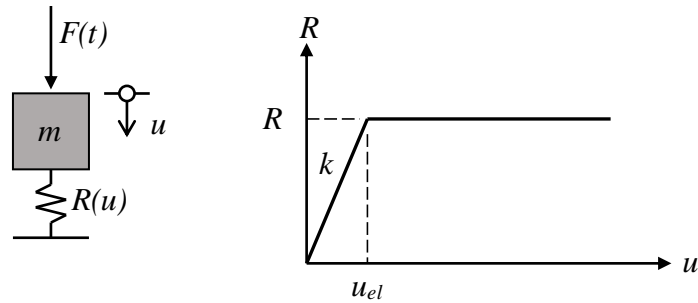


Figure 4.9 Force-displacement response of an elasto-plastic structure (Johansson and Laine, 2012).

If the system is loaded with a characteristic impulse I_1 , an external work $W_{e,1}$ is generated, which with the use of Equations (4.9) and (4.17), gives

$$W_{e,1} = W_{i,1} = W_{1,el} + W_{1,pl} = \frac{R_m}{2}(u_{1,el} + 2u_{1,pl}) \quad (4.33)$$

with the total deformation for the first impulse given as

$$u_1 = u_{1,el} + u_{1,pl} \quad (4.34)$$

The total response from the first impulse can be seen in Figure 4.10. When the impulse load disappears the only deformation that remains is the plastic deformation $u_{2,0}$ and it can be expressed as

$$u_{2,0} = u_{1,pl} \quad (4.35)$$

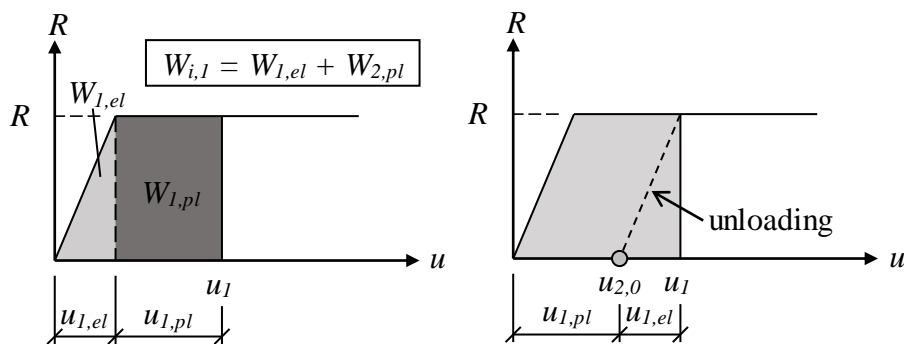


Figure 4.10 The response after the first impulse I_1 .

If the system is loaded with a subsequent impulse I_2 , see Figure 4.11, the deformation will start from the point for plastic deformation $u_{2,0}$ from the first impulse.

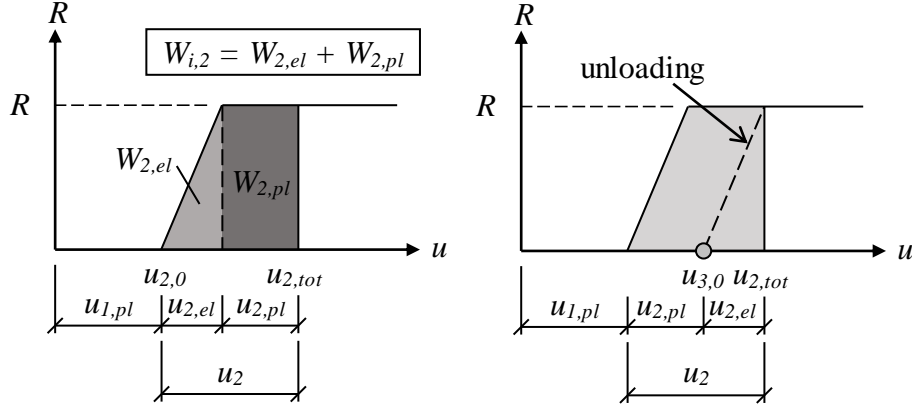


Figure 4.11 The response after the second impulse I_2 .

The work performed on the structure from the second impulse is determined in the same way as for the first impulse, i.e.

$$W_{e,2} = \frac{R_m}{2}(u_{2,el} + 2u_{2,pl}) \quad (4.36)$$

where the deformation from I_2 itself can be determined as

$$u_2 = u_{2,el} + u_{2,pl} \quad (4.37)$$

and this gives the total deformation as

$$u_{2,tot} = u_{2,0} + u_2 = u_{1,pl} + u_{2,el} + u_{2,pl} \quad (4.38)$$

When the impulse load I_2 disappears, this gives a total deformation of

$$u_{3,0} = u_{1,pl} + u_{2,pl} \quad (4.39)$$

which is the point of start if the impulse loading continues. It is worth mentioning that this methodology does not consider any potential decrease in stiffness due to local damages that might occur in the structure. For a case with local damaging it is likely that the elastic stiffness changes during the repeated impacts, which results in larger deformations.

4.7.3 Equivalent Impulse Load for Elasto-Plastic Response

Based on the concept presented in Section 4.7.2 the response from several impacts can be explained by a single impulse, the equivalent impulse I_{tot} . The equivalent impulse is only explained for the elasto-plastic case. Worth mentioning is that neglecting the elastic contribution to the internal work gives a result on the safe side but it is considered in this methodology. If the structural response after an impulse load does not reach the plastic region, the effect from that impulse will not contribute to the equivalent impulse. This means that the contribution from the impulse is only considered if the external work $W_{e,i}$ from the impulse is larger than the elastic part in the internal work $W_{i,el}$. With a combination of Equations (4.10) and (4.11) the internal elastic work can be expressed as

$$W_{i,el} = \frac{R^2}{2k} \quad (4.40)$$

and from this, by using Equations (4.8) and (4.9), the maximum allowed impulse I_{el} from which there is no damage of the structure is

$$I_{el} = \sqrt{R \cdot m \cdot u_{el}} = R \sqrt{\frac{m}{k}} = \frac{R}{\omega} \quad (4.41)$$

with ω from Equation (4.14). If the impulse is larger than I_{el} there will be a remaining damage in the structure, i.e. plastic deformation after the impulse. The total external work $W_{e,tot}$ on the structure is

$$W_{e,tot} = n \cdot W_{el} + \sum_{i=1}^n W_{i,pl} \quad (4.42)$$

which, with Equations (4.11), (4.15) and (4.12), can be rewritten as

$$\frac{1}{2m} \sum_{i=1}^n I_i^2 = R \left(n \cdot \frac{u_{el}}{2} + u_{tot,pl} \right) \quad (4.43)$$

From this the total plastic deformation $u_{tot,pl}$ can be expressed as

$$u_{tot,pl} = \frac{1}{2} \left(\frac{1}{R \cdot m} \sum_{i=1}^n I_i^2 - n \cdot u_{el} \right) \quad (4.44)$$

The plastic deformation can also be expressed with the equivalent impulse load as

$$u_{tot,pl} = \frac{1}{2} \left(\frac{1}{R \cdot m} I_{tot}^2 - u_{el} \right) \quad (4.45)$$

Combining Equations (4.44) and (4.45) gives

$$I_{tot} = \sqrt{\sum_{i=1}^n I_i^2 - (n-1) \cdot R \cdot m \cdot u_{el}} \quad (4.46)$$

and can, with Equation (4.41) be rewritten as

$$I_{tot} = \sqrt{\sum_{i=1}^n I_i^2 - (n-1) \cdot I_{el}^2} = \sqrt{\sum_{i=1}^n (I_i^2 - I_{el}^2) + I_{el}^2} \quad (4.47)$$

where $I_1 \geq I_{el}$ if the impulse load should be accounted for.

4.7.4 Residual Strength

From Equation (4.47) it is possible to determine the magnitude of the impulse load for collapse of an already damaged structure. If the structure has sustained $n - 1$ number of impulses, the maximum magnitude allowed of the next impulse becomes

$$I_n = \sqrt{I_{tot}^2 - \sum_{i=1}^{n-1} (I_i^2 - I_{el}^2)} \quad (4.48)$$

It can also be expressed as

$$I_n = \sqrt{2R \cdot m \cdot u_{n,pl}} \quad (4.49)$$

where

$$u_{n,pl} = u_{tot,pl} - u_{n,0} \quad (4.50)$$

and this means that the ultimate plastic deformation $u_{tot,pl}$ need to be known in advance. $u_{n,0}$ is the residual plastic deformation from previous impulse loads and can be calculated as

$$u_{n,0} = \sum_{i=1}^{n-1} u_{i,pl} \quad (4.51)$$

5 Discrete Model for Dynamic Analysis

5.1 Introduction

The response of a dynamic loaded RC beam can be described based on a SDOF-system. This chapter treats how a SDOF-system can be determined and how it can be transformed into a 2-DOF system. This chapter is based on the information gained from (Johansson and Laine, 2012).

5.2 Definition of SDOF and Impulse Loading

Figure 5.1 illustrates a dynamic SDOF where the mass m is exposed to an external time dependent load $F(t)$. The free movement of the mass is prevented by a static force $R_{sta}(u)$ and a viscous force $R_{dyn}(\dot{u})$. A simplification used by Johansson and Laine (2012) is that the viscous force is neglected and it is explained to be a fair and conservative assumption due to the the short duration of loading and that the maximum displacement is the only result of interest. With this assumption, the only counteracting force is the static one, giving $R(u) = R_{sta}(u)$.

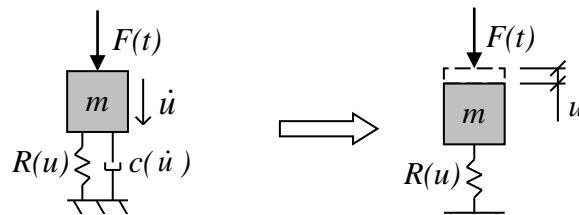


Figure 5.1 Definition of a SDOF system with the damping force neglected.

There are two extreme cases to explain the loading: ideal impulse load and pressure load. The characteristic impulse I_k , see Figure 5.2a, is generated when a time dependent load with an infinite high pressure acts for an infinitesimal time step. The characteristic pressure load F_k , see Figure 5.2b, is instead a load that is acting for an infinite long duration.

In an arbitrary case, $F(t)$ will be somewhere in between these two extreme cases. If the load is defined as long or short depends not only on the actual duration, but also on the properties of the loaded structure. The relatively short duration of the drop-weight impact used in the test of this report is deemed to be similar to that of a characteristic impulse load I_k and will therefore be treated as such further on.

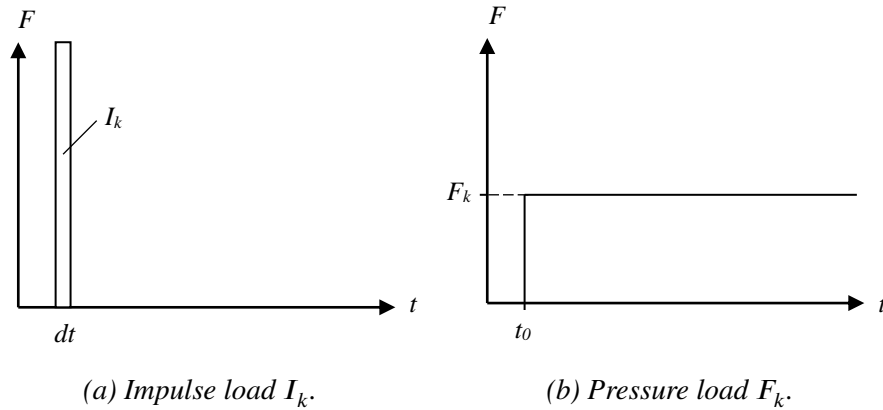


Figure 5.2 Illustration of dynamic extreme cases.

5.3 Transforming the Beam to SDOF

The SDOF system defined in Section 5.2 can be used to describe a structure in a simplified way. The deformation of a statically loaded beam with linear elastic response is a function of the load and the boundary conditions (BC). Since it is a linear elastic behaviour the shape of the deformation is independent of the magnitude of the load and this gives the opportunity to describe the displacement along the beam by using one point only, the system point, see Figure 5.3. The system point can be any point along the beam but is usually determined as the mid-point of the beam, or in the case of a point load, as the load point. The SDOF-system is designed in such way that the displacement u_{SDOF} reflects the system point displacement u_s that is

$$u_s = u_{SDOF} \tag{5.1}$$

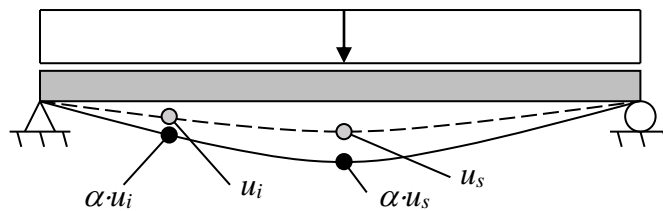


Figure 5.3 For a beam with linear elastic behaviour it is possible to describe the displacement along the beam by using a system point. If the system point is increased with the factor α , all the points will increase with the same magnitude, modified from (Johansson and Laine, 2012).

The transformation of the beam into a equivalent SDOF system is illustrated in Figure 5.4. The system point is given a mass m , the internal force $R(u)$ and the external force $F(t)$.

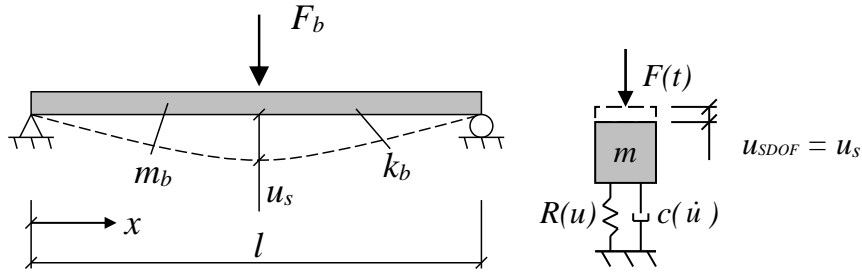


Figure 5.4 Transformation of the beam into an equivalent SDOF system, modified from (Johansson and Laine, 2012).

Transformation factors κ are used in order to convert actual structural elements, in this case a beam and a drop-weight, to an equivalent SDOF systems. The factors are used to keep the kinetic energy from the mass m and the work done by the forces F and R on the SDOF system at the same level as the energy and work performed on the beam. The real beam parameters of mass, stiffness and external load are multiplied with dimensionless transformation factors κ . By using transformation factors, the mass, stiffness and external load for the SDOF-system can be expressed as

$$m = \kappa_m m_b \quad (5.2)$$

$$k = \kappa_k k_b \quad (5.3)$$

$$F = \kappa_F F_b \quad (5.4)$$

where m_b , k_b and F_b corresponds to the actual beam properties and loading conditions. By using these three conditions and Equation (4.24) the expression for the discrete system is

$$\kappa_m m_b \ddot{u} + \kappa_k k_b u = \kappa_F F_b \quad (5.5)$$

which, for an arbitrary system, can be defined as

$$\kappa_m m_b \ddot{u} + \kappa_k R_b = \kappa_F F_b \quad (5.6)$$

where R_b describes the response of the beam subjected to static loading. Equation (5.5) can also be rewritten as

$$\frac{\kappa_m}{\kappa_F} m_b \ddot{u} + \frac{\kappa_k}{\kappa_F} k_b u = F_b \quad (5.7)$$

In accordance to Biggs (1964) the factor κ_k must always be equal the factor κ_F , that is

$$\kappa_k = \kappa_F \quad (5.8)$$

It is now possible to rewrite Equation (5.7) as

$$\kappa_{mF} m_b \ddot{u} + k_b u = F_b \quad (5.9)$$

where

$$\kappa_{mF} = \frac{\kappa_m}{\kappa_F} \quad (5.10)$$

This means that, in order to transform the beam into a SDOF system, it is only the mass of the beam m_b that need to be multiplied with the factor κ_{mF} .

The transformation factors depends on the support conditions, loading conditions and also the deformed shape of the beam, i.e elastic or plastic strain range. In this project the only factors introduced and treated is the ones for simply supported beams subjected to three-point loading. The transformation factors used within this project is presented in Table 5.1. A deviation of the factors is presented in Johansson and Laine (2012) and factors for different BC and strange ranges is presented in Biggs (1964).

Table 5.1 Transformation factors for simply supported beams subjected to three-point-loading (Biggs, 1964). Note that $\kappa_k = \kappa_F$.

Strain Range	Load factor, κ_F	Mass factor, κ_m	Load-mass factor, κ_{mF}
Elastic	1.00	0.49	0.49
Plastic	1.00	0.33	0.33

5.4 Transforming the Drop-weight to SDOF

The transformation of the drop-weight into an equivalent SDOF system is performed in a similar manner as the transformation of the beam, by using transformation factors. The transformation of the drop-weight is described in Lovén and Svavarsdóttir (2016) and this section is written based on that knowledge.

The main assumption for the converting of the drop-weight is that it only get an axial deformation at the impact. This means that the it can be represented as a bar and the transformation factors is determined from this assumption. The transformation of the drop-weight, represented as a bar, into an equivalent SDOF system can be seen in Figure 5.5. The system point u_s for the bar is chosen as the point where the largest deformation occurs and this is at the surface where the impact occurs, i.e at the base of the drop-weight.

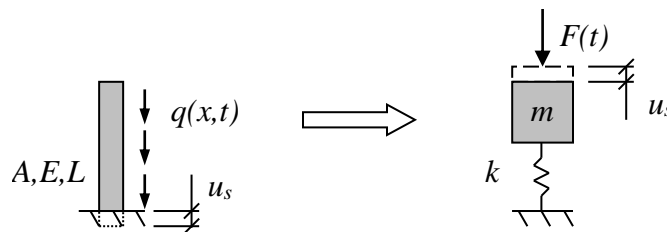


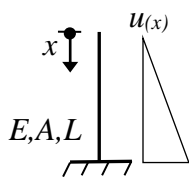
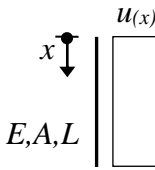
Figure 5.5 Transformation of the drop-weight, represented as a bar, into an equivalent SDOF system, inspired by (Lovén and Svavarsdóttir, 2016).

The transformation factors for the bar depends on if the bar or the surface for impact is seen as a rigid body. For an impact against a very rigid, i.e very stiff, body the base of the falling bar is considered as fixed. The assumption that the bar behaves as a rigid body gives another setup of transformation factors, which can be seen in Table 5.2. As in many other cases, the system with a falling drop-weight in this

project is somewhere in between a very stiff bar and a very stiff surface. Since the drop-weight is in solid steel with a much higher axial stiffness than the bending stiffness of the beam, the assumption used here is that this system behaves as a rigid bar and the transformation factors are chosen thereafter. Table 5.2 shows the two extreme cases and from this the transformation factors for the rigid bar is chosen as

$$\kappa_m = \kappa_k = \kappa_F = 1.00 \tag{5.11}$$

Table 5.2 Transformation factors for the drop-weight considered as a bar (Lovén and Svavarsdóttir, 2016).

Type of impact	κ_m	κ_F	κ_k	κ_{mF}
Rigid surface: 	0.333	0.50	0.50	0.67
Rigid bar: 	1.00	1.00	1.00	1.00

5.5 2DOF Systems

5.5.1 General Description

To describe the behavior of a collision between two bodies, in this case a drop-weight and a RC beam, in a simplified way it is convenient to use a 2DOF-system. The 2DOF-model consists of two SDOF-systems that is linked in order to describe the total response during the impact. The system used is illustrated in Figure 5.6.

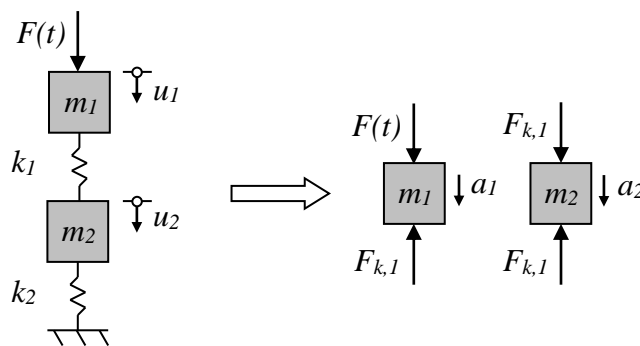


Figure 5.6 Illustration of the 2DOF-system used in order to describe the collision between two bodies. The drop-weight is represented by m_1 and the RC beam by m_2 .

By using Newton's Second Law the force equilibrium of the two free bodies, m_1 and m_2 , yields:

$$F_1(t) - F_{k,1} = m_1\ddot{u}_1 \quad (5.12)$$

$$F_2(t) - F_{k,2} = m_2\ddot{u}_2 \quad (5.13)$$

This can, by using constitutive relations be expressed as:

$$m_1\ddot{u}_1 + k_1(u_1 - u_2) = F_1(t) \quad (5.14)$$

$$m_2\ddot{u}_2 - k_1u_1 + (k_1 + k_2)u_2 = F_2(t) \quad (5.15)$$

where k_i corresponds to the spring stiffness, \ddot{u}_i to acceleration and u_i to displacement for the two bodies, respectively. The previous two equations can then be expressed in a matrix format as

$$\begin{bmatrix} m_1 & 0 \\ 0 & m_2 \end{bmatrix} \begin{bmatrix} \ddot{u}_1 \\ \ddot{u}_2 \end{bmatrix} + \begin{bmatrix} k_1 & -k_1 \\ -k_1 & k_1 + k_2 \end{bmatrix} \begin{bmatrix} u_1 \\ u_2 \end{bmatrix} = \begin{bmatrix} F_1(t) \\ F_2(t) \end{bmatrix} \quad (5.16)$$

By introducing the transformation factors the expression is

$$\begin{bmatrix} \kappa_{m,1}m_1 & 0 \\ 0 & \kappa_{m,2}m_2 \end{bmatrix} \begin{bmatrix} \ddot{u}_1 \\ \ddot{u}_2 \end{bmatrix} + \begin{bmatrix} \kappa_{F,1}k_1 & -\kappa_{F,1}k_1 \\ -\kappa_{F,1}k_1 & \kappa_{F,1}k_1 + \kappa_{F,2}k_2 \end{bmatrix} \begin{bmatrix} u_1 \\ u_2 \end{bmatrix} = \begin{bmatrix} \kappa_{F,1}F_1(t) \\ \kappa_{F,2}F_2(t) \end{bmatrix} \quad (5.17)$$

and by using the following relations:

$$\alpha_m = \frac{\kappa_{m,1}}{\kappa_{m,2}} \quad (5.18)$$

$$\alpha_F = \frac{\kappa_{F,1}}{\kappa_{F,2}} \quad (5.19)$$

$$\kappa_{mF,2} = \frac{\kappa_{m,2}}{\kappa_{F,2}} \quad (5.20)$$

it can be expressed as

$$\kappa_{mF,2} \begin{bmatrix} \alpha_m m_1 & 0 \\ 0 & m_2 \end{bmatrix} \begin{bmatrix} \ddot{u}_1 \\ \ddot{u}_2 \end{bmatrix} + \begin{bmatrix} \alpha_F k_1 & -\alpha_F k_1 \\ -\alpha_F k_1 & \alpha_F k_1 + k_2 \end{bmatrix} \begin{bmatrix} u_1 \\ u_2 \end{bmatrix} = \begin{bmatrix} \alpha_F F_1(t) \\ F_2(t) \end{bmatrix} \quad (5.21)$$

which can be presented as

$$\mathbf{M}\ddot{\mathbf{u}} + \mathbf{K}\mathbf{u} = \mathbf{F}(t) \quad (5.22)$$

Note that the viscous damping c introduced in Section 4.5 is neglected in the expression for the equation of motion in this case, this is further discussed in Section 5.2. The solution of Equation (5.21) can be found both analytically and numerically. Due to the complexity of such system it is preferable, though, to use a numerically solution method, by example the central difference method used in this project and described in Section 5.6. This is especially true for a nonlinear case when k varies with u .

5.5.2 2DOF for a Drop-weight and RC Beam System

To describe the impact collision between the drop-weight and the RC beam the transformation factors introduced in Section 5.3 and 5.4 are applied to Equations (5.18), (5.19) and (5.20). No external forces $F_i(t)$ is considered to act on the two bodies. The dynamic impact load is instead given as a prescribed initial velocity of body 1, the drop-weight, from which a movement of body 1 u_1 is determined. The fact that the load transformation factor $\kappa_F = 1.00$ for both bodies, see Tables 5.1 and 5.2, gives that $\alpha_F = 1.00$. This means that Equation (5.21) now, for the specific case, becomes

$$\kappa_{mF,2} \begin{bmatrix} \alpha_m m_1 & 0 \\ 0 & m_2 \end{bmatrix} \begin{bmatrix} \ddot{u}_1 \\ \ddot{u}_2 \end{bmatrix} + \begin{bmatrix} k_1 & -k_1 \\ -k_1 & k_1 + k_2 \end{bmatrix} \begin{bmatrix} u_1 \\ u_2 \end{bmatrix} = \begin{bmatrix} 0 \\ 0 \end{bmatrix} \quad (5.23)$$

if the response is assumed to be elastic, and

$$\kappa_{mF,2} \begin{bmatrix} \alpha_m m_1 & 0 \\ 0 & m_2 \end{bmatrix} \begin{bmatrix} \ddot{u}_1 \\ \ddot{u}_2 \end{bmatrix} + \begin{bmatrix} R_1 & -R_1 \\ -R_1 & R_1 + R_2 \end{bmatrix} \begin{bmatrix} u_1 \\ u_2 \end{bmatrix} = \begin{bmatrix} 0 \\ 0 \end{bmatrix} \quad (5.24)$$

if the response is elastoplastic, with the relation between R and u described in Equation (2.3). However, there is a need of modifying these equations for the 2DOF-system in this case. If the collision is elastic, there will be a time when the drop-weight is moving away from the beam. The spring between the masses, denoted $R_1(u_1)$ in Figure 5.6, is in this case in tension. But in reality, there is nothing that connects the two bodies which means that the stiffness when the drop-weight is moving away from the beam must be equal to zero. To be able to capture this behaviour the Equation (2.3) is extended to

$$R_i = \begin{cases} k_i \cdot u & \text{if } u \leq u_{el,1} \\ R_{m,i} & \text{if } u > u_{el,1} \\ 0 & \text{if } u \leq 0 \end{cases} \quad (5.25)$$

The maximum internal resistances for the drop-weight and the beam is derived in different ways. For the beam, it can be determined from the maximum moment at the ultimate limit state for a point load at the midspan, that is

$$R_{m,2} = \frac{4M_u}{L} \quad (5.26)$$

The beam is also subjected to a static load, its own self-weight g_{beam} , which gives a lower resistance than stated in Equation (5.26). This is illustrated in Figure 5.7 and the internal resistance for the beam now becomes

$$R_{m,2,mod} = R_{m,2} - R_{stat} = \frac{4M_u}{L} - \frac{g_{beam}L}{2} \quad (5.27)$$

The stiffness parameter of the beam, k_2 in Figure 5.7, is calculated as

$$k_2 = \frac{48E_{cm}I_{II}}{L^3} \quad (5.28)$$

where I_{II} is the moment of inertia in state II.

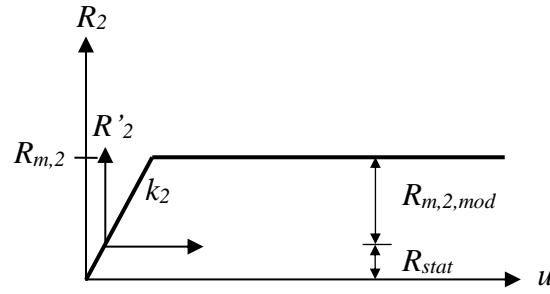


Figure 5.7 Illustration of the internal resistance of the beam when the static load, as the self-weight of the beam, is taken into account. Modified from (Lozano and Makdesi, 2017).

The internal resistance of the drop-weight $R_{m,1}$ is instead determined from the strength of the material f and the impact area A_{imp} as

$$R_{m,1} = f \cdot A_{imp} \quad (5.29)$$

where the value of f depends on not only the strength of the drop-weight but also on the local behaviour of the concrete where the impact occurs. This means that the two extremes for f is the compressive strength of concrete f_{cm} and yielding of the reinforcement steel f_{ym} . This gives that the condition for $R_{m,1}$ is

$$f_{cm} A_{imp} \leq R_{m,1} \leq f_{ym} A_{imp} \quad (5.30)$$

According to a study made by Lovén and Svavarsdóttir (2016) a reasonable value of the internal resistance of the drop-weight is $R_{m,1} = 50$ kN. This value was generated by comparing different values in the 2DOF-model with the results from the FEA.

The stiffness of the drop-weight k_1 can be determined according to

$$k_1 = \frac{E_{sm} A}{L} \quad (5.31)$$

where A and L is the area and length of the body, respectively.

5.6 Central Difference Method

The central difference method (CDM) is an explicit method used to solve the equation of motion (Carlsson and Kristensson, 2012). As described in Section 5.2 the viscous constant c is neglected and the solution method is derived with the same assumption. In Carlsson and Kristensson (2012) the CDM derivation is performed with c included, but here it is excluded.

The central difference scheme used in the method can be seen in Figure 5.8. The velocity at the observed time i is expressed as

$$\dot{\mathbf{u}}_i = \frac{\mathbf{u}_{i+1} - \mathbf{u}_{i-1}}{2\Delta t} \quad (5.32)$$

which can be used to get the acceleration as

$$\ddot{\mathbf{u}}_i = \frac{\frac{\mathbf{u}_{i+1} - \mathbf{u}_i}{\Delta t} - \frac{\mathbf{u}_i - \mathbf{u}_{i-1}}{\Delta t}}{\Delta t} = \frac{\mathbf{u}_{i+1} - 2\mathbf{u}_i + \mathbf{u}_{i-1}}{(\Delta t)^2} \quad (5.33)$$

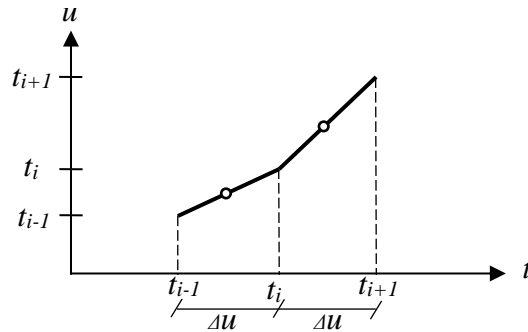


Figure 5.8 The central difference scheme used in the CDM, modified from (Carlsson and Kristensson, 2012).

Implementing Equations (5.32) and (5.33) in the equation of motion, Equation (5.22), gives

$$\mathbf{M} \frac{\mathbf{u}_{i+1} - 2\mathbf{u}_i + \mathbf{u}_{i-1}}{(\Delta t)^2} + \mathbf{K}\mathbf{u}_i = \mathbf{F}_i(t) \quad (5.34)$$

where \mathbf{u}_i and \mathbf{u}_{i-1} are the known factor that are used to solve \mathbf{u}_{i+1} . This expression can be solved by introducing the initial conditions:

$$\mathbf{u}(0) = \mathbf{u}_0 \quad (5.35)$$

$$\ddot{\mathbf{u}}(0) = \ddot{\mathbf{u}}_0 \quad (5.36)$$

$$\ddot{\mathbf{F}}(0) = \ddot{\mathbf{F}}_0 \quad (5.37)$$

for an initial value of $i = 0$. For a lumped mass-spring system the matrix \mathbf{M} is diagonal which means that the solution, for solving \mathbf{u}_{i+1} , can be expressed as

$$\mathbf{u}_{i+1} = (\Delta t)^2 \mathbf{M}^{-1} \left(\mathbf{F}_i(t) - \left(\mathbf{K} - \frac{2}{(\Delta t)^2} \mathbf{M} \right) \mathbf{u}_i - \frac{1}{(\Delta t)^2} \mathbf{M} \mathbf{u}_{i-1} \right) \quad (5.38)$$

which means that the solution is found by using information from previous time steps, i and $i - 1$, and is therefore an explicit solution method. To get \mathbf{u}_{i-1} in the first time step, where $i = 0$, a specific starting step \mathbf{u}_{-1} expressed as

$$\mathbf{u}_{-1} = \mathbf{u}_0 - \Delta t \dot{\mathbf{u}}_0 + \frac{\Delta t^2}{t} \ddot{\mathbf{u}}_0 \quad (5.39)$$

There is a risk that the solution gained with the CDM is unstable if the time step is not chosen short enough. Instability means that the errors in the initial conditions continues to grow for each iteration.

In Lozano and Makdesi (2017) the critical time step Δt_{crit} for which the actual time step Δt need to be less than is

$$\Delta t_{crit} = \frac{2}{\omega_{max}} = \frac{T_n}{\pi} \quad (5.40)$$

where ω_{max} is the highest eigenfrequency determined from $\det(\mathbf{K}-\omega^2\mathbf{M}) = 0$. In Lozano and Makdesi (2017) it is further described that selecting a time step smaller than Δt_{crit} gives a stable algorithm but when a higher accuracy is wanted the time step should be even smaller than the critical value. A suggested time step is one percent of the load duration t_l , that is

$$\Delta t \leq \begin{cases} \Delta t_{crit} \\ t_l \\ 100 \end{cases} \quad (5.41)$$

6 Experimental Procedure

6.1 General Description

A total of 18 beams were casted and tested under different load conditions. The casting was made in two batches and the beams were named after in which batch they were casted. The beams from batch 1 were named 1-9 while the beams from batch 2 were named from 10-18. The beams was then divided into different test series, where each serie was subjected to a certain load condition and test procedure. The name of the series and the associated loading conditions are summarized in Table 6.1. The specimens of Series-1 to Series-4 were initially tested dynamically by releasing a drop-weight of different weight at two different heights. For Series-1, Series-2 and Series-3 the impact was repeated and the number of drops is presented in Table 6.1. Afterwards, the residual capacity was determined by a static four-point loading test. Three beams from each batch were only tested statically by means of four-point bending test and these are henceforth referred to as the undamaged beams. A number of 30 concrete cubes were casted to determine the material properties according to standards and recommendations. The strength of the steel reinforcement was determined from seven test specimens.

Both the dynamic and static tests of the beams were painted white with a black pattern on one side, in order to increase the contrast. During the testing this side was exposed to a camera that was positioned in front of the beam. The cameras frame-rate was 5 000 fps during the impact loading tests whilst it was decreased to 0.33 fps during the static tests. The recorded images was later processed in the DIC software GOM Correlate 2017.

Table 6.1 Classification of beams and testing conditions.

Beam	Test series	Batch	Drop-weight [kg]	Height [m]	Nr. of drops
1-3	Series-2	1	10	5	2
4-6	Series-1	1	10	2.5	4
7-9	Undamaged	1	Only static loading		
10-12	Series-4	2	20	5	1
13-15	Series-3	2	20	2.5	2
16-18	Undamaged	2	Only static loading		

6.2 Manufacturing of Concrete Beams

6.2.1 Introduction

This section covers the methodology used when manufacturing the test specimens as well as describing the different tests made on the fresh concrete. All of the work were carried out at the laboratory of structural Engineering at Chalmers University of Technology with supervision by Research Engineer Sebastian Almfeldt and Senior Lecturer Joosef Leppänen.

6.2.2 Geometry of the Specimens

The geometry of the casted beams can be seen in Figure 6.1. The total length of the beam was 1 180 mm with a cross-section of dimensions 100 x 100 mm. Four reinforcement bars were symmetrically placed in each corner. The aim was to keep the distance from the center of the reinforcement bars to the concrete surface at 20 mm. The location of the reinforcement bars after concrete hardening is discussed further in Section 8.2.4.

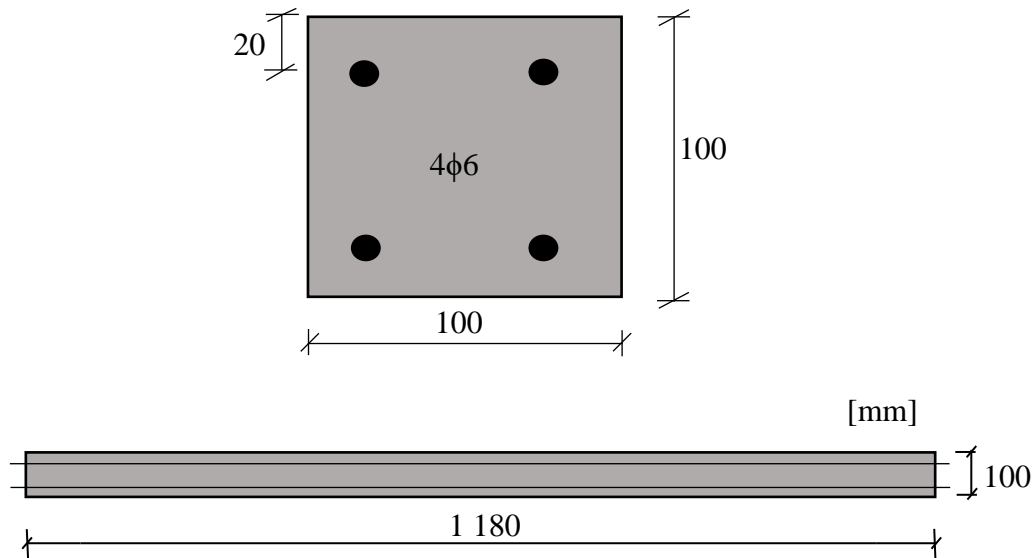


Figure 6.1 Geometry of the concrete beams.

6.2.3 Manufacturing of Moulds

The same beam moulds that were used by Lozano and Makdesi (2017), Ekström (2017) as well as Lovén and Svavarsdóttir (2016) were also used in this project. The moulds were cleaned from old dirt and greased with a non-reactive release material to make sure that the concrete would come off the mould smoothly after hardening.

Pre-drilled holes at the end of the moulds, from previous years, were used to put the reinforcement bars in place, with a distance of 20 mm from the bottom of the mould to the centre of the bottom reinforcement. The reinforcement should have a diameter of 6 mm but it was observed that this was not always the case. The bar cross-section was not entirely circular and the diameter varied between 5 - 6 mm, which is a big difference in percentage. Observations made by Lozano and Makdesi (2017) that the reinforcement are bent downwards due to its own weight and due to the impact of the concrete when the moulds are filled, were taken into account. A small plastic cube with a height of 19 mm were placed under the bottom reinforcement, in the middle of the mould, and the bottom reinforcement were hung up approximately at 1/3 of the beam's length from each side, as shown in Figure 6.2. After the reinforcement were hung up, the plastic cube were removed. This should result in a distance of approximately 22 mm from the bottom to the centre of the reinforcement, while the goal is 20 mm. The reason for this choice was that it was deemed probable that the bars would still deform a few millimeters since the steel wire was not completely straight and also due to the weight of the concrete when casting. Regardless of whether

the bars deformed or not, it was assumed that they would be on approximately the same height in all specimens, which is an improvement from the experiments in 2017 when a large dispersion was observed. From Figure 6.2 it can also be observed how the transverse hangers for the steel wire is placed on nails. This is done to prevent them from getting stuck in the concrete when casting.



Figure 6.2 Picture showing how the bottom reinforcement were hung up.

The moulds for the different test to determine material properties was also cleaned and greased. Two different moulds were used for the test cubes, one with smooth edges and one with a notch on one side. This is further explained in Section 8.2.2.

6.2.4 Casting

The concrete mixture were developed by Ingemar Löfgren at Thomas Concrete Group. The strength of the concrete was aiming at C28/35 and a water-cement ratio of 0.60. The mixture is presented in Table 6.2. The air content of the concrete was assumed to be 1.5 % and the target slump height was 200 (± 20) mm. The actual air content and slump height of the concrete mixed in this project is presented in Section 6.2.5. In total, 18 RC-beams, 24 cubes for compressive and tensile splitting strength tests and 6 cubes for wedge splitting tests (WST), which is used to determine the fracture energy G_F , were casted. The concrete was mixed in two batches and therefore half of the beams and cubes corresponds to each batch, see Table 6.3.

Table 6.2 Concrete mix per batch. The amount of concrete for each batch was 175 litres.

Name	Supplier	Moisture [%]	Weight [kg]
Sand 0/8 Sköllunga	Ucklums grus	5.29	165.8
Stone 5/8 Vikan	Skanska	0.67	16.9
Stone 8/16 Vikan	Skanska	2.10	143.4
Glenium 51/18	BASF	-	0.98 (batch 1), 0.90 (batch 2)
Byggcement CEM II	Cementa	-	57.8
Water	-	-	23.8

Table 6.3 Distribution of specimens for the two batches.

Batch	Beam nr	Compressive test, f_c	Tensile splitting test, f_{ct}	WST, G_F
1	1-9	6	6	3
2	10-18	6	6	3

In order to get better results from the testing it had been preferable to mix the concrete in one batch only but in this case the size of the mixer was limiting. The mixture used in this project was a normal concrete mixture, i.e different from 2017 when self-compacting concrete (SCC) was used (Lozano and Makdesi, 2017). SCC, in contrast to normal concrete, has a higher viscosity and flows into the formwork to enclose the reinforcement, without any need of vibration. Two types of vibration was used in this project, one for each batch. For batch 1, a vibrator rod was used and for batch 2, a vibra-table was used, see Figure 6.3. The reason for changing vibrating method was that the vibrator rod stopped working after the casting of the first batch. Afterwards, it was concluded that the use of the vibra-table gave a better finish of the surface, see Figure 6.4 for the difference.



(a) Vibrating rod (Batch 1).

(b) Vibra-table (Batch 2).

Figure 6.3 Vibrating methods used.



(a) Batch 1

(b) Batch 2

Figure 6.4 Difference in finish of the two batches.

6.2.5 Tests Made on Fresh Concrete

In previous master thesis's of this research project there was no testing of the fresh concrete (Lovén and Svavarsdóttir, 2016), (Lozano and Makdesi, 2017). From the experiments made by Lozano and Makdesi (2017) there is some results that indicates a difference in the concrete behaviour between the two batches that was casted. Therefore, it was suggested that two tests of the fresh concrete should be made, a slump-test and an air content test. These tests were performed according to the standards CEN (2009b) and CEN (2009c). A third standard was used, CEN (2009a), and it describes how a representative sample is taken from the concrete batch. In this section the results from the testing is presented and the two standards for testing is briefly described. The slump test is used as a method to determine the consistence of the concrete. The apparatus needed for the test is a mould with a base diameter of $200 (\pm 2)$ mm, top diameter of $100 (\pm 2)$ mm and a height of $300 (\pm 2)$ mm. A compacting rod is also needed for the compacting of the concrete. The mould is placed on a horizontal surface and then filled with concrete in three layers, each approximately one-third of the height of the mould. Each layer is compacted with 25 strokes from the compacting rod. Once the mould is filled with concrete it is gently lifted upwards, with no lateral or torsional motion being imparted to the concrete. Immediately after removing the mould the slump height h is measured as the distance between the top part of the mould and the highest point of the slumped test specimen, presented in Figure 6.5. The entire operation, from the start of the filling until measuring the slump, should not take more than 150 seconds. The slump height is rounded to the nearest 10 mm. The arrangement used for the slump test can be seen in Figure 6.6.

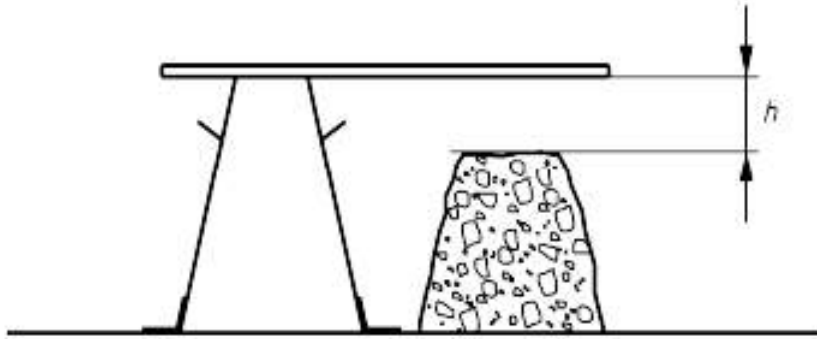


Figure 6.5 Slump measurement according to CEN (2009b).



Figure 6.6 Arrangement for slump test.

The slump height h for the two batches can be seen in Table 6.4. Both batches were inside the aim given in the concrete recipe, which was $200 (\pm 20)$ mm. The first batch had a slightly higher viscosity and this is believed to be due to the use of more superplasticiser. The slump tests were performed until the concrete had the desired viscosity, leading to that 2 slump tests were performed on each batch. Since the slump height for the first batch was high, the amount added in the second batch was smaller and that also gave a lower slump height.

The air content was determined with the pressure gauge method and this method employs the principle of Boyle-Mariotte's law. The approach is that a concrete sample is placed in a sealed container, with an unknown volume of air in the concrete. Then a known volume of air at a known pressure is merged into the concrete container. From the resulting pressure it is then possible to determine the air content of the concrete. The air content from the two batches is presented in Table 6.4. The gauge pressure meter used to determine the air content can be seen in Figure 6.7.



Figure 6.7 Gauge pressure meter used for determining of air content.

Table 6.4 Air content and slump height of the two batches.

Batch	Air content, [%]	Slump height, h [mm]
1	2.5	220
2	2.0	180

6.3 Experimental Setup for Dynamic Testing

The dynamic testing took place 26 days after casting of the concrete beams. The beams were placed on a testing rig with two supports that was bolted in the concrete slab. By this arrangement the supports themselves did not move which made it easier to replace the beam after each impact. The beam was simply supported and only prevented from displacing in the downward direction and the distance between the supports was 1.0 m. The arrangement is shown schematically in Figure 6.8. Figure 6.9 shows how it was arranged in the lab.

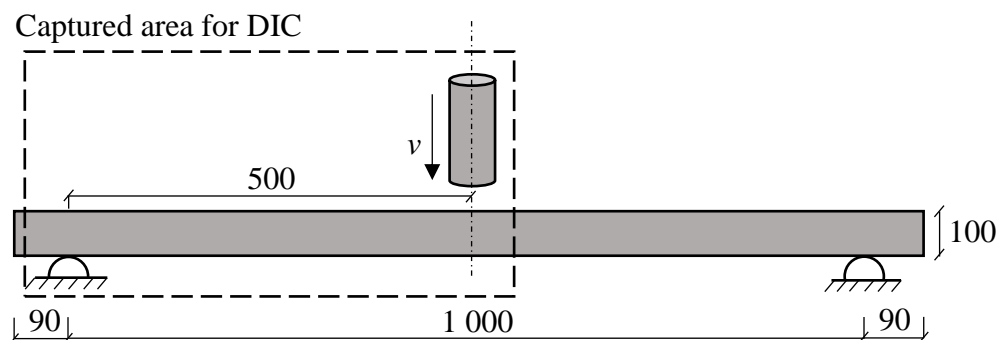


Figure 6.8 Conditions and BC during dynamic testing. All dimensions are in mm.



(a) Placing of the beam. On top of the beam is the two drop-weights.

(b) Photo showing the guiding tube.

Figure 6.9 Setup for dynamic testing. Note the black and white pattern painted on the drop-weights and the beam.

The drop-weight was hoisted in a vertical guiding tube to the desired height and then released to hit the beam in the center point, both in the length and width direction. For the beams with repeated impacts the beam was repositioned at the supports after each impact. The drop-weight was a cylindrical steel rod with a rounded tip. The dimensions of the drop-weight can be seen in Figure 6.10.

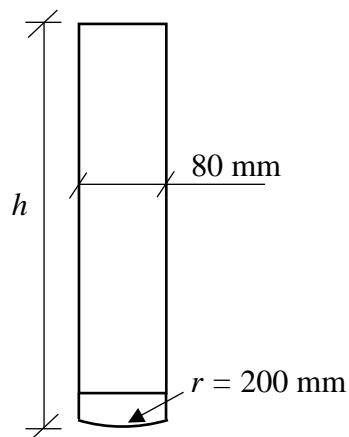


Figure 6.10 Dimensions of the drop-weight with different h depending if it's 10 or 20 kg.

The beams, as well as the drop-weights, were painted white with a black pattern prior the testing. This increased contrast gave the opportunity to better capture the beam response during the impact with a high-speed camera. The specifications of the camera and the conditions for the camera setup is listed below:

- Highspeed camera Photron SA4.
- Distance from front of beam to camera body: 2 225 mm.
- Tamron Zoom lens 28-75. Zoom adjusted at 75.
- Solution 1024 x 512 pixels.
- Spatial scale calibrated with 60 mm gauge block -> 60 mm = 98.1 pixel -> 1 pixel = 0.61162 mm.
- Frame rate 5 000 fps.
- Manual triggering with center trigger which captures 1 s before and 1 s after impact.
- Approximately 100 ms (500 frames) was later saved for each test.

The image sequence from the high speed camera was later processed in GOM Correlate 2017.

6.4 Experimental Setup for Static Testing

6.4.1 Introduction

The static testing took place during day 27 - 29 after casting and was performed in order to determine the capacity of the undamaged beams as well as the residual capacity of the beams subjected to impact loading. The original intention of the static testing was to perform a three point bending test in the same manner as was done in the experiments made by Lozano and Makdesi (2017). Due to the severe damage in the midpoint of some beams, though, it was decided to do a four-point bending test instead to avoid the risk of local crushing of concrete at the point load.

The beam was simply supported on two roller supports. Two point loads was applied 0.35 m from the supports and the loading was deformation-controlled. The point loads was applied with rollers that was attached to the same plate which in turn was jointed at the midpoint, where the force was applied using a uniaxial compression/tension hydraulic jack. Hence, the point loads were of equal magnitude. The conditions for the four-point bending test can be seen in Figure 6.11 and the test setup as well as the DIC equipment used can be seen in Figure 6.12. The DIC equipment captured the behaviour of the beam and the frames were afterwards processed in GOM Correlate 2017. The equipment was different from that used in the dynamic testing and consisted in this case of two cameras which captures a 3D-view. The system used was Aramis 3D 12M, distributed by GOM. The dimension of lenses was 24 mm and the measured volume was approximately 1 350 x 1 000 mm. However, the 3D-view was never used during the processing of the test results.

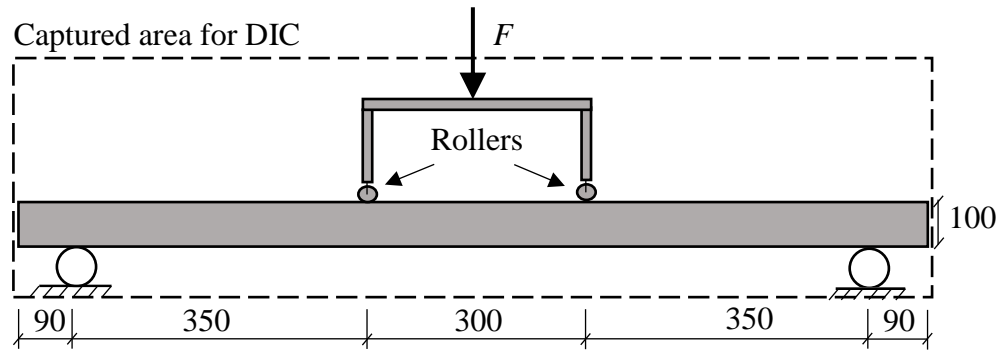


Figure 6.11 Conditions for four-point static testing. All dimensions are in mm.



(a) Setup.

(b) DIC equipment.

Figure 6.12 Lab conditions for four-point static testing.

6.4.2 Static Testing of Damaged Beams

The damaged beams were placed in the four-point bending rig and subjected to the deformation-controlled load until failure occurred. The loading rate was 2 mm/min.

6.4.3 Static Testing of Undamaged Beams

The undamaged beams were subjected to a number of unloadings and reloadings. The reason was to investigate the change of beam stiffness during the loading. The loading was deformation-controlled

and the loading rate for both loading and unloading was 2 mm/min until a deformation of 40 mm was reached, thereafter it was increased to 10 mm/min until failure. The displacements at unloading was 10, 20 and 40 mm. The beam was at these points unloaded with 4 mm and thereafter it was reloaded again until the next unloading occurred. The loading history is shown schematically in Figure 6.13.

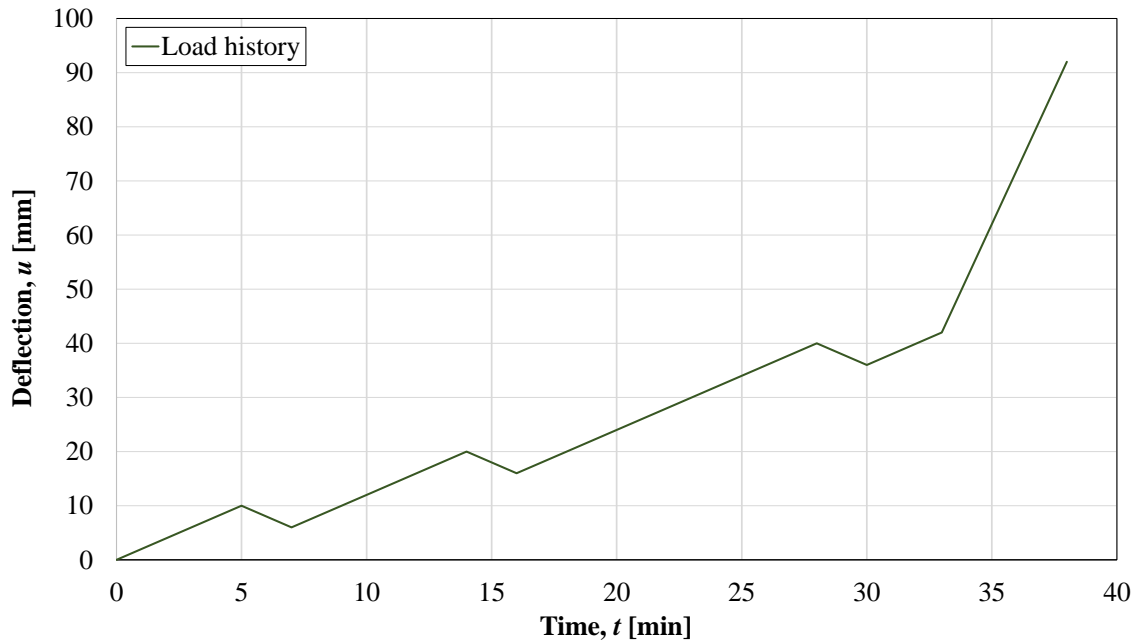


Figure 6.13 Loading history for static testing of the undamaged beams.

7 Predictions

7.1 Introduction

This chapter presents a description on how the calculations were performed when predicting the response of the beam, both under static and impact loading. The boundary- and loading conditions is described in Chapter 6 and the geometry of the beam cross-section can be seen in Figure 7.1.

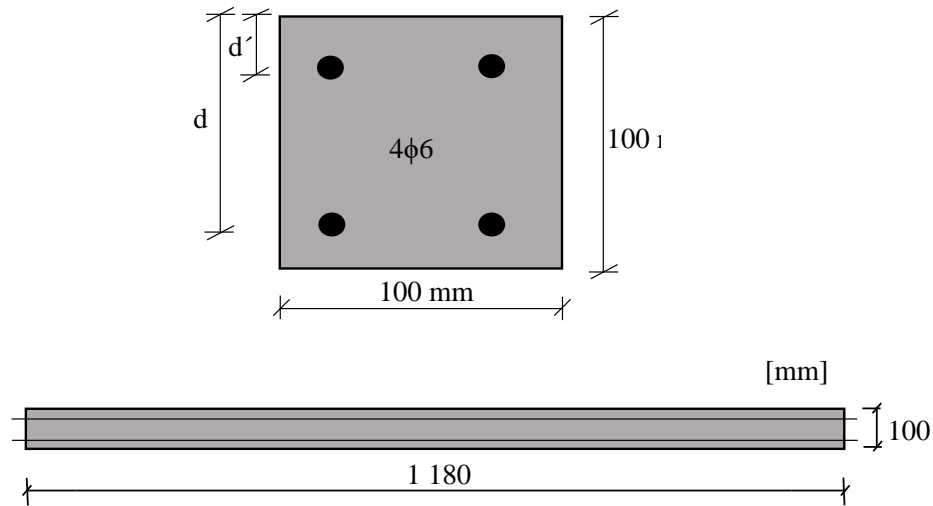


Figure 7.1 Geometry of the concrete beams.

The real material properties of the steel and concrete as well as the measured position of the reinforcement was used in the calculations to increase the correlation between the predicted values and the values obtained in the experiments. These material properties is presented in Section 8.2, where it can be seen that the tensile strength of the concrete is unusually high. Consequently, the tensile strength used from this point was calculated according to the equations presented in Section 2.3.2.3, which are based on the compressive strength that has more reasonable values from the testing. The load capacity in the ultimate limit state is calculated as well as the load at yielding and cracking. Furthermore, the load-deflection curve under static loading is also determined. All calculations regarding load capacity and load-deflection curve can be found in Appendix K. The plastic rotation is also calculated according to the different methods described in Section 3.4. The calculations was made with the software Mathcad Prime 4.0 and is also presented in Appendix K. The load capacities is evaluated using two different steel stresses while the proof stress is used when determining the plastic rotation capacity.

The response of the beam during the different impacts was predicted with a simplified 2DOF according to the theory described in Chapter 5. The software MATLAB R2017b was used to make the script, which was based on the script made by Lozano and Makdesi (2017). The MATLAB script can be found in Appendix L.

The results from these theoretical predictions are then compared to the results from the experiments and the FE model in subsequent chapters.

7.2 Load Capacity

7.2.1 Ultimate Limit State

The procedure when determining the load capacity is based on recommendations given in (Engström, 2013). It is assumed that the ultimate concrete strain, $\epsilon_{cu} = 3.5 \text{ ‰}$, is reached and that the reinforcement is yielding. It is also assumed that the stress distribution in the compressive zone follows the parabolic relation described in Section 2.3.2 and that the strain distribution is linear, presented in Figure 7.2.

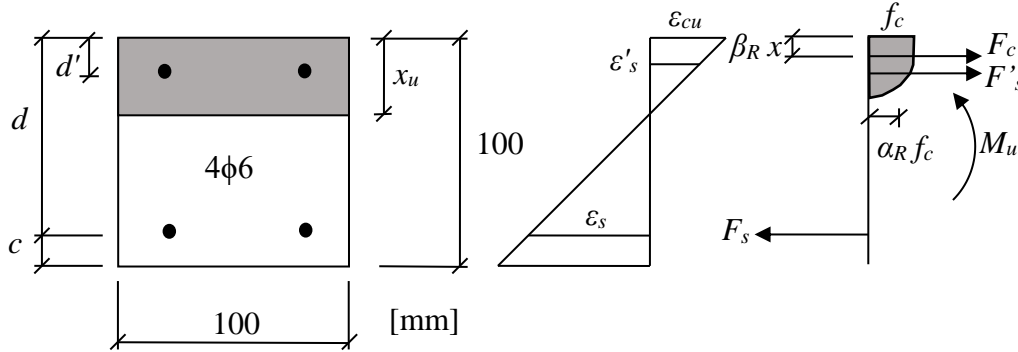


Figure 7.2 Cross-section of the beam.

By assuming that the neutral axis is located below the top reinforcement and neglecting the influence of reinforcement under compression, the equilibrium conditions can be expressed as

$$\alpha_R f_c b \cdot x_u = f_y A_s \quad (7.1)$$

$$M_u = \alpha_R f_c b \cdot x_u (d - \beta_R x_u) \quad (7.2)$$

where the value of x_u from Equation (7.1) can be inserted in Equation (7.2) to obtain the moment capacity of the beam. The values of the stress block factors α_R and β_R is obtained from Table B5.3 in Engström (2013) and has the values

$$\alpha_R = 0.81 \quad (7.3)$$

$$\beta_R = 0.42 \quad (7.4)$$

The assumption that the steel is yielding has to be checked with the following equation

$$\epsilon_s = \frac{d - x_u}{x_u} \epsilon_{cu} > \epsilon_{sy} = \frac{f_y}{E_s} \quad (7.5)$$

It was found that the height of the compressive zone was less than d' , which means that the top reinforcement was subjected to low tensile stress. This means that the top reinforcement should be added to Equations (7.1) and (7.2) and be subjected to a low tensile stress between zero and f_y . This was also

observed by Lozano and Makdesi (2017) where the top reinforcement proved to add an additional 4.6 % to the capacity. Since the conditions in this thesis is very similar to the ones used in Lozano and Makdesi (2017), this addition to the capacity will be made to count for the top reinforcement.

Two different values of the reinforcements yield stress was used to create a lower and an upper value of the predicted capacity. Both the proof stress $f_{0.2}$ and the ultimate stress f_u , see Section 8.2.3, was therefore set as the yield stress in the calculations. Table 7.1 shows a summary of the calculated ultimate moments as well as the ultimate load which can be applied when considering 4-point loading. The relation between the moment and the load can be expressed by the following equation but it should be noted that this expression gives the value of one point load only.

$$F_u = \frac{M_u}{0.35L} \quad (7.6)$$

Table 7.1 Maximum moment and force in the ultimate limit state for different yield stresses.

f_{yd} [MPa]	Layers of reinforcement	M_u [kNm]	F_u [kN]
513	Top and bottom	2.2	12.7
	Bottom only	2.1	12.1
623	Top and bottom	2.7	15.2
	Bottom only	2.6	14.6

7.2.2 Cracking and Yielding

The moment acting on the section when cracking occurs can be calculated based on the moment of inertia and the flexural tensile strength of the concrete as

$$M_{cr} = \frac{f_{ct,fl} I_I}{h/2} \quad (7.7)$$

The moment acting on the section when yielding occurs is calculated in a similar manner to the ultimate moment and is also described in (Engström, 2013). The strain in the steel ϵ_{sy} is known but not the strain in the concrete, which is less than ϵ_{cu} in this case. An initial concrete strain ϵ_{cc} is assumed and based on that, the height of the compressive zone can be calculated with the following equation, not including effects of top reinforcement.

$$x_y = \frac{\epsilon_{cc}}{\epsilon_{cc} - \epsilon_{sy}} d \quad (7.8)$$

The assumed strain is also used to determine the stress block factors, which in this case will have to be interpolated between two values in Table B5.3 in Engström (2013). When the stress block factors and the height of the compressive zone is determined there should be equilibrium in the section, which is checked by the following equation:

$$\alpha_R f_c b \cdot x_y - f_y A_s \approx 0 \quad (7.9)$$

$$M_y = \alpha_R f_c b \cdot x_y (d - \beta_R x_y) \quad (7.10)$$

This is an iterative process which becomes a bit time consuming to perform since both the height of the compressive zone and the stress block factors depends on the initial guess of the concrete strain. The height of the compressive zone is located approximately at the same level as the top reinforcement which means that it can be neglected in this case. Table 7.2 shows a summary of the moment and force of the different cases.

Table 7.2 *Moment and external force at the onset of cracking and yielding.*

f_{yd} [MPa]	State	M_{cr} or M_y [kNm]	F_{cr} or F_y [kN]
513	Onset of cracking	0.7	4.2
	Onset of yielding	2.0	11.7
623	Onset of cracking	0.7	4.2
	Onset of yielding	2.4	13.9

7.2.3 Theoretical Load-deflection Curve

The different stiffness's should be calculated in order to create a load-deflection curve for the beam. The stiffness in state I and the stiffness between cracking and ultimate state is needed to create a tri-linear response while the stiffness in state II is of interest when creating a bi-linear response. First of all the moment of inertias needs to be calculated as

$$I_I = \frac{b \cdot h^3}{12} + (\alpha_s - 1) A_s \left(d - \left(\frac{h}{2} \right) \right)^2 + (\alpha_s - 1) A'_s \left(\left(\frac{h}{2} \right) - d' \right)^2 \quad (7.11)$$

$$I_{II} = \frac{b \cdot x_{II}^3}{3} + (\alpha_s - 1) A'_s (x_{II} - d')^2 + \alpha_s A_s (d - x_{II})^2 \quad (7.12)$$

where

$$\alpha_s = \frac{E_{sm}}{E_{cm}} \quad (7.13)$$

and the position of the neutral axis calculated from an area balance. The stiffness in state I and II can be calculated from elementary cases as

$$k = \frac{48 E_{cm} I}{a \cdot L^2 \left(3 - \frac{4a^2}{L^2} \right)} \quad (7.14)$$

where $a = 0.35$ m is the distance to the point load from the support. It should be noted that this expression only is valid when two point loads are applied at the same distance from each support and when the beam has constant modulus of elasticity and moment of inertia. When this stiffness is known it is possible to determine the deflection at cracking and at ultimate load. The stiffness between cracking and ultimate state can now be determined as the difference in load divided by the difference in deflection between

cracking and ultimate state. Figure 7.3 shows the load-deflection relation for both a tri-linear and a bi-linear response. The beam is assumed to behave plastically after the ultimate load is reached. In this case the top reinforcement is also taken into account. The state II stiffness k_{II} was calculated to 2.46 kN/mm.

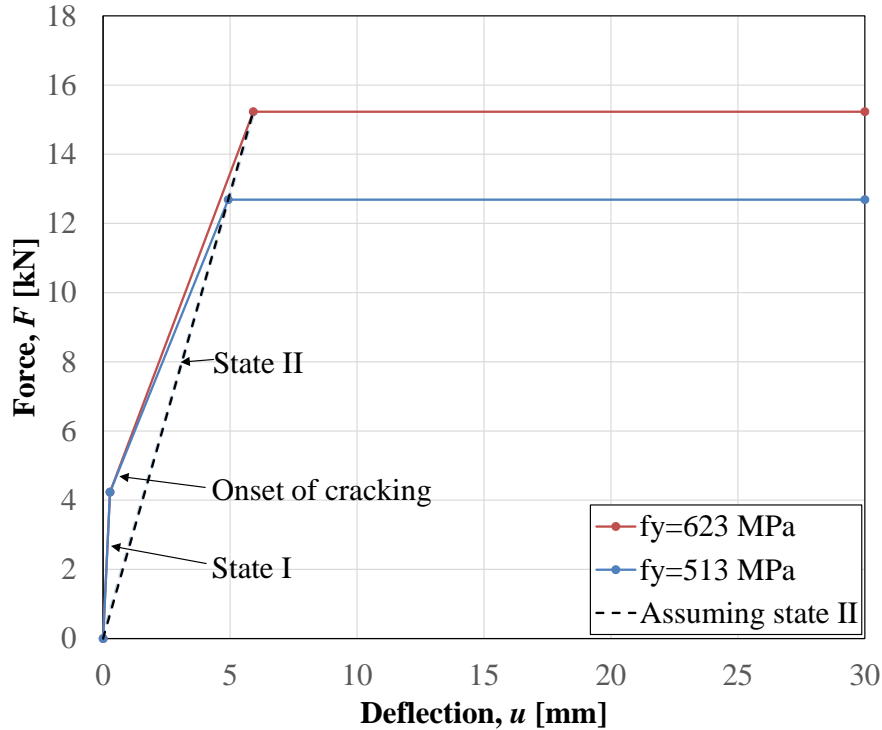


Figure 7.3 Theoretical load-deflection curve for different values of yield stress when the top layer of reinforcement is taken into account.

7.3 Rotational Capacity

7.3.1 Introduction

Most of the methods described in Chapter 3 are based on cross-sections with top reinforcement subjected to compressive stress and bottom reinforcement subjected to tensile stress. Therefore, the top reinforcement is neglected in the calculations made on rotational capacity. One of the most common input parameter for the different methods are the distance from the point of maximum moment to the zero moment region l_0 which in this case is the same as the distance between the supports and a point load, namely 0.35 m. Another common input parameter is the distance from the top edge to the bottom reinforcement d which is taken as the measured value 77 mm.

7.3.2 Eurocode 2

The position of the neutral axis in the ultimate limit state is $x_u = 9.7$ mm. The ratio between the neutral axis and the distance d can be calculated as

$$\frac{x_u}{d} = 0.126 \quad (7.15)$$

when using the provided graph the rotational capacity can be determined as $\theta_{ref.EC} = 0.031$ mrad. This is however only valid for beams with a slenderness $\lambda = 3$. The slenderness of the actual beam can be calculated as

$$\lambda = \frac{l_0}{d} = 4.53 \quad (7.16)$$

which gives the correction factor

$$\kappa_\lambda = \sqrt{\frac{\lambda}{3}} = 1.23 \quad (7.17)$$

The corrected plastic rotation capacity can then be determined as

$$\theta_{tot.EC} = \kappa_\lambda \theta_{ref.EC} = 38 \text{ mrad} \quad (7.18)$$

which needs to be divided by 2 since the angle referred to in EC2 is twice as large as the angle measured from the test results. The final plastic rotation capacity according to EC2 is therefore

$$\theta_{pl.EC} = \frac{\theta_{tot.EC}}{2} = 19 \text{ mrad} \quad (7.19)$$

7.3.3 Betonghandboken (ABC-Method)

The three factors A , B and C needs to be determined to be able to calculate the plastic rotation capacity. Equation (3.20) is used to calculate A since measured values from the laboratory is used. The mechanical ratio of the compression reinforcement ω'_s is set to zero since the compression reinforcement is subjected to tensile forces as well as the fact that no stirrups were used. The mechanical ratio of the shear reinforcement ω_v is also set to zero since there is no shear reinforcement present. The mechanical ratio of the tension reinforcement is calculated as

$$\omega_s = \frac{A_s f_y}{b \cdot d f_c} = 0.102 \quad (7.20)$$

and the factor A can therefore be determined as

$$A = 1 - 5\omega_s = 0.49 \quad (7.21)$$

The factor B was set to 1.0 meaning that it is steel with high ductility. The steel classifications in Table 3.2 is outdated but it was assumed that steel type C corresponds to the old steel class Ks 60.

Since the plastic hinge is formed in the span the factor C is calculated with Equation (3.27) as

$$C = 7 \left(\frac{l_0}{d} \right) = 31.7 \quad (7.22)$$

When all factors are obtained the plastic rotation capacity is calculated as

$$\theta_{pl.95.ABC} = A \cdot B \cdot C \cdot 10^{-3} = 16 \text{ mrad} \quad (7.23)$$

It should be noted that the plastic rotation capacity obtained here corresponds to the value when 95 % of the moment capacity is reached on the descending branch, as described in 3.

7.3.4 Tamminens D-factor

The factor k is set to 0.3 due to that the concrete approximately corresponding to class K30, which corresponds to C25/30 in the new standards. The factor D can be calculated as

$$D = \frac{k}{d} = 3.9 \quad (7.24)$$

which gives a rotation capacity

$$\theta_{pl.95.Tamminen} = A \cdot B \cdot C \cdot D \cdot 10^{-3} = 60 \text{ mrad} \quad (7.25)$$

7.3.5 Bk25

Bk25 consists of two different methods, one where the plastic hinge is formed in the field and one where the plastic hinge is formed over a support. It was assumed that the plastic hinge is formed in the field, since this seems most reasonable. The plastic hinge length is calculated as

$$l_{pl} = 0.5d + 0.15L = 0.19 \text{ m} \quad (7.26)$$

The dominant failure mode needs to be specified by calculating ω_s and ω_{crit} as

$$\omega_s = \frac{A_s f_y}{b \cdot d f_c} = 0.102 \quad (7.27)$$

$$\omega_{crit} = \frac{0.8\epsilon_{cu}}{\epsilon_{cu} + \epsilon_{su}} = 0.026 \quad (7.28)$$

Since ω_s is larger than ω_{crit} , the dominant failure mode is crushing of concrete. The plastic rotation capacity can now be calculated as

$$\theta_{pl.Bk25.f} = \frac{0.4\epsilon_{cu}}{\omega_s} \left(1 + 0.3 \frac{L}{d} \right) = 67 \text{ mrad} \quad (7.29)$$

It should be noted that this capacity is significantly larger than the values obtained from Eurocode and Betonghandboken. This may be due to that Bk25 is based on a concrete beam which is subjected to a uniformly distributed load. However, four point loading is somewhere between three point loading and uniformly distributed load and the result is therefore interesting to compare with the actual values obtained in the experiments.

7.3.6 Methods based on Equivalent Plastic Hinge Length

Equation (3.50) is used to calculate the rotation capacities for the methods which is based on equivalent plastic hinge length. Therefore, the first step is to calculate the plastic curvature. The curvature at failure φ_u can be calculated as

$$\varphi_u = \frac{\varepsilon_{s,1}}{d - x_u} = 0.36 \text{ 1/m} \quad (7.30)$$

where $\varepsilon_{s,1}$ is the steel strain at failure when $\varepsilon_{cu} = 3.5 \text{ ‰}$ and $f_{ym} = 513 \text{ MPa}$. The curvature at yielding can be calculated as

$$\varphi_y = \frac{\varepsilon_{sy}}{d - x_y} = 0.046 \text{ 1/m} \quad (7.31)$$

The plastic curvature can then be determined as

$$\varphi_{pl} = \varphi_u - \varphi_y = 0.314 \text{ 1/m} \quad (7.32)$$

The equivalent plastic hinge length l_{pl} is then determined in each method and the plastic rotation capacity can be calculated with Equation (3.50). A summary of the results can be seen in Table 7.3.

Table 7.3 Summary of plastic rotation capacities based on equivalent plastic hinge length.

Method	l_{pl} [mm]	θ_{pl} [mrad]
Baker and Amarkone	66	21
ACI-ASCE Committee 428, lower	36	11
ACI-ASCE Committee 428, upper	88	28
Paulay and Priestley	96	30
Panagiotakos and Fardis, cyclic	42	13
Panagiotakos and Fardis, monotonic	63	20

7.4 Predictions with 2DOF

7.4.1 Overview

As mentioned the 2DOF script in this project was based on the script made by Lozano and Makdesi (2017), with some adjustment to describe the different loading conditions and the beam stiffness obtained in this project. In the following description of the 2DOF model setup the subscripts 1 and 2 refers to the drop-weight and the beam, respectively. The script can be seen in Appendix L.

The model uses a bi-linear elasto-plastic relationship, described in Section 2.2.4, for the response of both the drop-weight and the beam. The internal resistance of the beam was calculated with both the average yield stress, $f_y = 513 \text{ MPa}$, and a theoretical upper value assuming that the onset of yielding was equal to the ultimate steel stress, i.e $f_y = f_u = 623 \text{ MPa}$. The load capacities presented later in this section is for three-point loading, and is hence not to be mixed up with the load capacities presented in Section 7.2, which is the capacities for four-point loading.

The impact load is introduced as a weight and velocity of body 1. The velocity depends on the drop height as

$$v_0 = \sqrt{2g \cdot h} \quad (7.33)$$

which for the heights of 2.5 m and 5.0 m gives $v_0 = 7.0$ m/s and $v_0 = 9.9$ m/s respectively.

7.4.2 Internal Resistance

The internal resistance for the drop-weight was chosen as

$$R_{m,1} = 50 \text{ kN} \quad (7.34)$$

according to the study made by Lovén and Svavarsdóttir (2016), see Section 5.5.2. This value yields an impact that is close to plastic impact for the load cases studied here.

The maximum internal resistance of the beam is determined by equations (5.26) and (5.27). The calculation of the load capacity $R_{m,2}$ is presented in Appendix K and the modified internal resistance $R_{m,2,mod}$, where the self-weight is taken into account, is calculated in the script, Appendix L. The internal resistances used in the script is presented Table 7.4.

7.4.3 Stiffness

The stiffness of body 1 was determined according to

$$k_1 = \frac{E_{sm} A_1}{L_1} \quad (7.35)$$

where A_1 and L_1 is the area and length of the drop-weight cylinder. The stiffness k_1 is different for the two drop-weights due to the difference in length.

The beam stiffness was determined according to

$$k_2 = \frac{48E_{cm} I_{II}}{L_2^3} \quad (7.36)$$

where I_{II} is the moment of inertia in state II, calculated according to Equation (7.12) and presented in Appendix K. Note that Equation (7.36) is the stiffness for three-point loading and should not be mixed with Equation (7.14), which is the stiffness for four-point loading. The calculated stiffness's is presented in Table 7.4.

7.4.4 Transformation Factors

The response of the drop-weight is considered as plastic and the transformation factors for a stiff bar is used, see Section 5.4. The factors are presented in Table 7.4.

The combined transformation factor for the beam, $\kappa_{mF,1}$, should be defined somewhere between the elastic and plastic values presented in Table 5.1. This is since the elasto-plastic material response is used for the calculations of stiffness and internal resistance of the beam. However, the transformation factors for the beam within this project is chosen considering a fully plastic response which is in line with the factors used by Lozano and Makdesi (2017). The transformation factors are presented in Table 7.4.

Table 7.4 Summary of values used in 2DOF model.

Body	f_{yd} [MPa]	$R_{m,i}$ [kN]	$R_{m,i,mod}$ [kN]	k_i [MN/m]	$\kappa_{mF,i}$ [-]
Drop-weight 10 kg, 1	-	50.0	-	3 900	1.000
Drop-weight 20 kg, 1	-	50.0	-	2 000	1.000
Beam, 2	513	8.5	8.4	1.8	0.333
	623	10.2	10.1	1.8	0.333

7.4.5 Results from 2DOF Predictions

7.4.5.1 Deflections

Due to the difficulties with determining the yield stress the predictions was done with both the predicted yield stress f_y and the ultimate stress f_u of the steel. Predictions were performed for all four different loading conditions and this, together with the different choices of steel strength gave a total of 8 predictions. A summary of the results from the 2DOF predictions of the first impact is shown in Table 7.5. Graphs showing the response can be seen in Figure 7.4. The maximum deflection u_{max} is defined as

$$u_{max} = u_{el} + u_{pl} \quad (7.37)$$

Table 7.5 Summary of the results from 2DOF after first impact.

Drop height, h [m]	Weight, m [kg]	Impact vel, v [m/s]	Resistance, $R_{m,2,mod}$ [kN]	Elastic def, u_{el} [mm]	Max def, u_{max} [mm]	Plastic def, u_{pl} [mm]
2.5	10	7.0	8.4	4.3	18.4	14.1
2.5	10	7.0	10.1	5.1	16.1	11.0
5.0	10	9.9	8.4	4.3	34.6	30.3
5.0	10	9.9	10.1	5.1	29.5	24.4
2.5	20	7.0	8.4	4.3	43.9	39.7
2.5	20	7.0	10.1	5.1	37.3	32.2
5.0	20	9.9	8.4	4.3	85.4	81.1
5.0	20	9.9	10.1	5.1	71.8	66.7

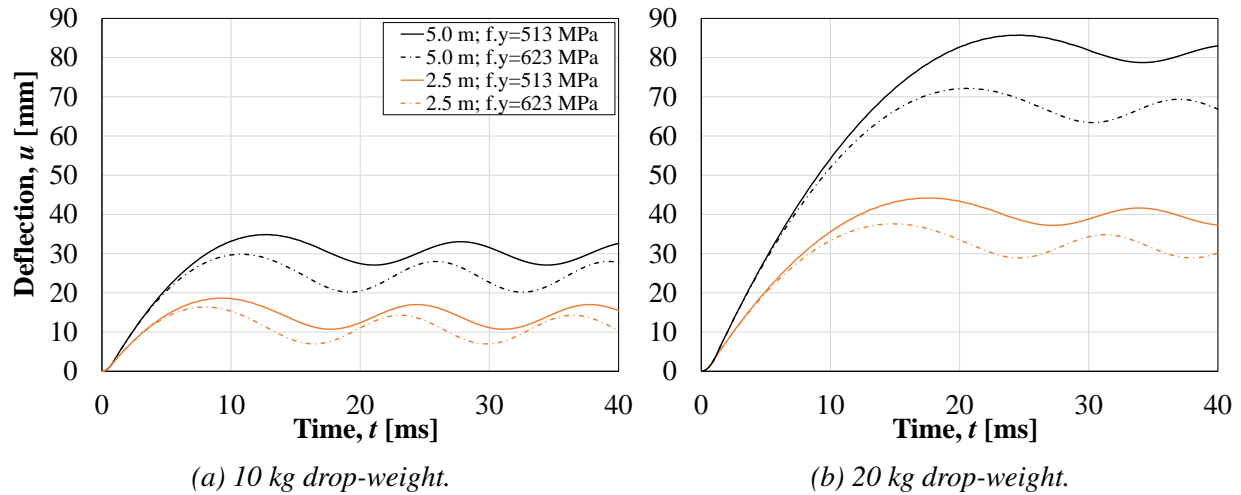


Figure 7.4 2DOF response of the beam midpoint during different impact conditions.

The total plastic deformation during the repeated impact was predicted by assuming that the plastic deformation would be the same for every impact. The total plastic deformation is presented in Table 7.6. The most critical load case from the predictions is thus when the beam is hit one time with 20 kg from 5 metres.

Table 7.6 Summary of the results from 2DOF after several impacts.

Drop height, h [m]	Weight, m [kg]	Resistance, $R_{m,2,mod}$ [kN]	Plastic def, u_{pl} [mm]	No. of impacts, n	Total def, $u_{pl,tot}$ [mm]
2.5	10	8.4	14.1	4	56.4
2.5	10	10.1	11.0	4	44.0
5.0	10	8.4	30.3	2	60.6
5.0	10	10.1	24.4	2	48.8
2.5	20	8.4	39.7	2	79.4
2.5	20	10.1	32.2	2	64.4
5.0	20	8.4	81.1	1	81.1
5.0	20	10.1	66.7	1	66.7

7.4.5.2 Impulse

Another parameter of interest is the impulses. These were also studied using the 2DOF model. The main part of interest was the relation between the impulses, for later comparison with the experimental results. During these predictions the resistance $R_{m,1}$ was, to ensure a perfectly elastic impact, changed to 10 000 kN. With R_m , u_{el} and u_{pl} from the 2DOF script the internal work W_i was calculated according to Equation (4.17). From this the characteristic impulse I_k was calculated using Equation (4.12). The results from the predicted impulses is presented in Table 7.7.

Table 7.7 Summary of the results from 2DOF predictions of characteristic impulse.

Drop height, h [m]	Weight, m [kg]	Impulse I_k [Ns]	Relation, $I_{k,2.5}/I_{k,5.0}$ [-]
2.5	10	63.1	-
5.0	10	89.1	0.71
2.5	20	89.1	-
5.0	20	126.1	0.71

8 Experimental Results

8.1 Introduction

The results from the experiments is presented within this chapter, together with some comments about deviations in the results.

Firstly, the results from the material testing is treated. Parameters such as modulus of elasticity, compressive strength and tensile strength is presented. The focus is to present the average values, but results from all specimens is presented in appendices.

Secondly, the results gathered from the high-speed camera footages recorded during the impact load tests is presented. The results of interest, among others, is the deflection over time, deformed shape of the beam over time, impact forces and the strain fields.

Lastly, the information gathered during the static testing is presented. Load-deflection graphs is presented as well as the values of maximum force, stiffness during cyclic loading, internal work and rotation capacities.

8.2 Material Properties

8.2.1 Introduction

The average values of the material properties that was obtained during the experiments are presented within this section. The individual value of each specimen, as well as a description of the test procedure and photos of the test apparatus used, is presented in Appendix A for concrete tests and Appendix B for steel tests.

8.2.2 Concrete Properties

As described in Section 6.2.4 a total of 30 cubes were casted to measure the properties of the concrete. The concrete was evaluated by measuring the density, compressive strength, tensile strength and fracture energy and were performed at two different occasions, namely 26 and 28 days after casting. The compressive strength and tensile strength was determined according to the standards (CEN, 2009e) and (CEN, 2009f), respectively. The density was determined according to CEN (2009g). To be able to predict the fracture energy of the concrete a WST was performed according to the recommendations given in (Löfgren *et al.*, 2004). A summary of the material parameters gathered during the material testing is presented in Table 8.1. It should be noted that the tensile strength seems unrealistic high and should be used with care; the reason for this is unknown. A calculated value of the tensile strength was therefore used in the calculations instead, this is further treated in Section 7.1.

Table 8.1 Summary of mean values of the material parameters of the concrete.

	Density ρ [kg/m ³]	Compressive strength f_{cm} [MPa]	Tensile strength f_{ctm} [MPa]	Fracture energy G_F [Nm/m ²]
Batch 1	2364	35.6	4.66	138
Batch 2	2404	38.1	4.77	136
Average	2384	36.8	4.72	137.1

8.2.3 Steel Properties.

A summary of the results from the testing of the reinforcement steel can be seen in Table 8.2.

Table 8.2 Mean values of steel properties.

Proof stress $f_{0.2}$ [MPa]	Ultimate stress f_u [MPa]	Young's Modulus E_s [GPa]	Ultimate strain ϵ_{su} [%]
513	623	196	10.6

8.2.4 Location of Reinforcement

As described in Section 6.2.3 the reinforcement bars in the bottom layer were hung up with steel wires to improve the position of the tensile reinforcement compared to previous years. After the testing was done the beams were sawn in pieces and the position of the bars was measured. The dynamic loaded beams were sawn in two places, approximately one third of the beams length from the support, since they were too damaged to measure in the middle of the beam. The beams that were only subjected to static loading were sawn in one place, approximately in the middle of the beam, since they were not as severely damaged as the other beams. There were no clear difference between the dynamic loaded beams and the ones subjected to only static load which means that the bars can be assumed to be straight along the length of the beam. The distance from the bottom of the beam to the center of the reinforcement varied between 22.0 mm and 23.5 mm with a mean value of 22.8 mm which gives a distance d of 77.2 mm. This means that the bars were placed a few millimeters too high. However, this is still an improvement compared to the work done by Lozano and Makdesi (2017) since the variation of the distance is much lower. An improvement for further work could be to decrease the height of the plastic piece that were placed below the bars to 16.5 mm instead of the 19.0 mm bar that were used in this project.

The position of the top reinforcement were also measured and a greater dispersion of the results could be seen there, between 20.0 mm to 28.0 mm. The position of this reinforcement will not influence the results as much as the bottom reinforcement but a recommendation for further work could be to be more careful when putting the bars in place and correct their position by visually determining if the bar looks straight. Another recommendation that applies for both the top and bottom reinforcement is to be careful when casting since it is easy to accidentally move the bars during the process.

8.3 Dynamic Testing

8.3.1 Introduction

The experiments started with the dynamic testing and this section treats the results gathered from the high-speed camera footage of the impact event, that was later processed in the DIC software GOM Correlate 2017. The results presented covers the deflections over time at beam midpoint, deflected beam response over the whole beam length and the strain fields. The section is divided in one part that only treats the response during the first impact and one part that treats the repeated impacts. Beams in Series-4 was only subjected to one impact and is therefore only treated in the first part. Photos of the beams after the dynamic testing can be seen in Appendix C.

8.3.2 Methodology

As mentioned in Section 6.3 the impact was recorded with a high speed camera and the frames were afterwards processed in the DIC software GOM Correlate 2017. In the software the user, among other settings, specify the facet size and point distance of the mesh pattern, named surface component in the software, generated to display the strain fields of the test specimens. An analysis of different combinations of facet sizes and point distances were made and is presented in Appendix D. It was found out that it was appropriate to use a surface component with a facet size of 15 pixels and a point distance of 5 pixels and a high accuracy computation, which is a choice specified by the user.

From the surface component it was then possible to show the major strain fields and these were chosen to be displayed against the reference stage. The strain field images presented in this section shows the strains during the propagation of cracks in the first 2 ms, the strains at maximum deflection and also the remaining strains, after the impact event has occurred.

By constructing a facet point component it was possible to follow a specific point during the impact. The deflections presented were measured at the centermost point of the beam, both in length and height direction. For some beams, though, large local damages occurred at beam midpoint which made it impossible to follow the midpoint of the beam during the image sequence. For these beams, a point outside of the locally damaged part was used instead to measure the response, which influences the results. Even though the result is a bit less accurate it was deemed to be ok. There were more than one way to measure the deflections and this is discussed in Appendix F.

The velocity and acceleration of the drop-weight were analysed by choosing several facet point components, from where the average behaviour was calculated. The physical quantities of interest were the impact force, impulse load and the velocity at impact.

A single section was also constructed along the longitudinal axis of the beam, at the geometrical center, from which it was possible to determine the deformed shape for different times.

8.3.3 Midpoint Deflection over Time during First Impact

8.3.3.1 Introduction

As mentioned, some of the beams was subjected to more than one impact. But since the beams in Series-4 was subjected to one impact only and the fact that the 2DOF script is designed to predict the response during the first impact, this section presents the response during the first impact only. The impact velocities are presented and taken as the average velocity during 3 ms before impact.

8.3.3.2 Series-1

The deflection-time relation from the tests of Series-1 are summarized in Table 8.3. The response during the first 40 ms after impact can be seen in Figure 8.1, where the deflection is taken as the difference between a point in the centre of the beam and a point at the left support.

Table 8.3 Summary of the results from the impact load testing of Series-1 ($h = 2.5$ m, $m = 10$ kg).

Beam	v_0 [m/s]	u_{max} [mm]	u_{pl} [mm]
4	7.0	12.1	5.9
5	7.0	11.4	5.1
6	7.0	11.8	5.1
Average	7.0	11.7	5.4

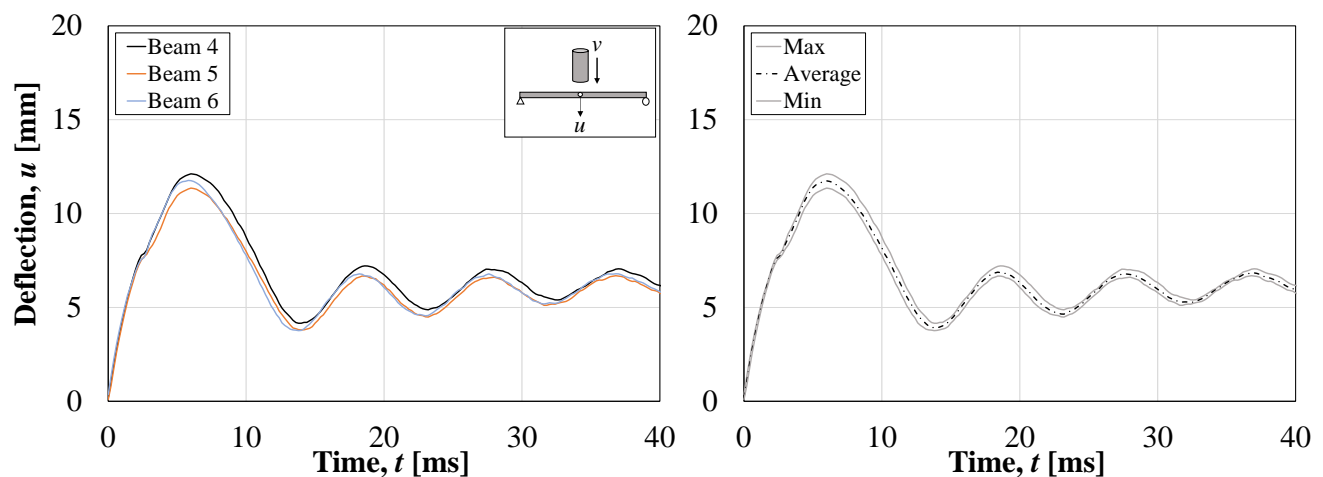


Figure 8.1 Deflection of midpoint over time for Series-1 ($h = 2.5$ m, $m = 10$ kg). The right hand figure shows the average response and the outer envelopes marks the maximum and minimum recorded deflections for the tested beams.

The impact velocity corresponds well with the theoretical value, presented in Table 7.5 which indicates that the drop-weight consequently was hoisted to the desired height. Possible effects that also affect the impact velocity are air resistance and friction resistance between the drop-weight and the steel rods used for the guiding tube. The influence of these effects were negligible during the testing. The three tested beams shows a very similar response and the conclusion is that the average response can be used for later comparisons with the predicted response.

8.3.3.3 Series-2

The results from the tests of Series-2 are summarized in Table 8.4. The response during the first 40 ms after impact can be seen in Figure 8.2.

Table 8.4 Summary of the results from the impact load testing of Series-2 ($h = 5.0$ m, $m = 10$ kg).

Beam	v_0 [m/s]	u_{max} [mm]	u_{pl} [mm]
1	9.9	22.1	14.6
2	9.9	21.4	13.8
3	9.9	22.4	14.3
Average	9.9	22.0	14.2

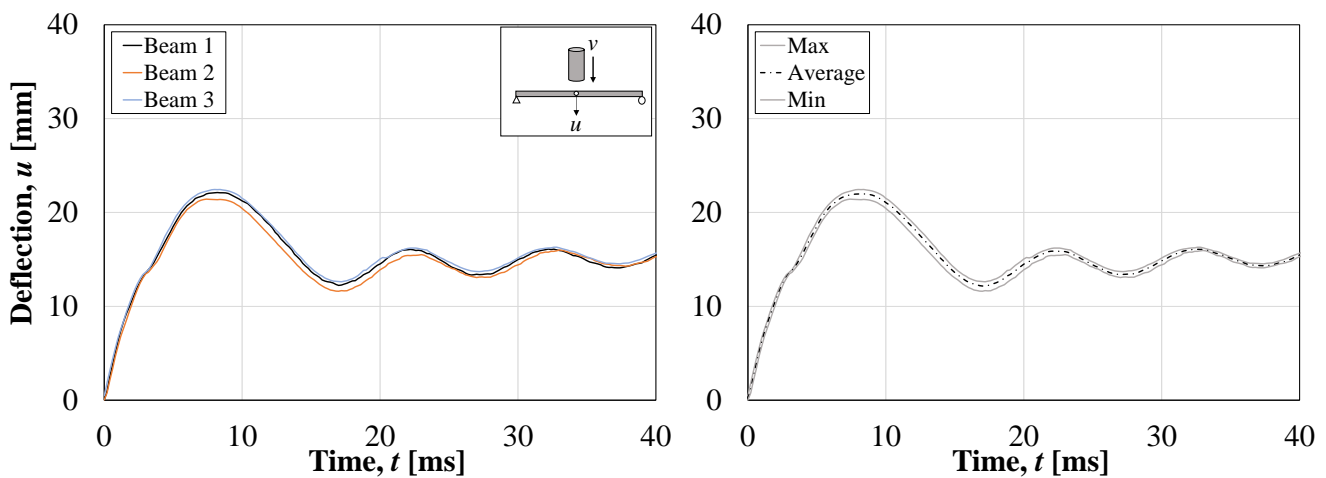


Figure 8.2 Deflection of midpoint over time for Series-2 ($h = 5.0$ m, $m = 10$ kg). The right hand figure shows the average response and the outer envelopes marks the maximum and minimum recorded deflections for the tested beams.

The impact velocity corresponds well with the theoretical value. The three tested beams shows a similar response and the average value is considered as the characteristic response for the beams in the series.

8.3.3.4 Series-3

The results from the tests of Series-3 are summarized in Table 8.5. The response during the first 40 ms after impact can be seen in Figure 8.3.

Table 8.5 Summary of the results from the impact load testing of Series-3 ($h = 2.5$ m, $m = 20$ kg).

Beam	v_0 [m/s]	u_{max} [mm]	u_{pl} [mm]
13	7.0	27.5	20.1
14	7.0	27.3	20.3
15	7.0	29.0	21.8
Average	7.0	27.9	20.7

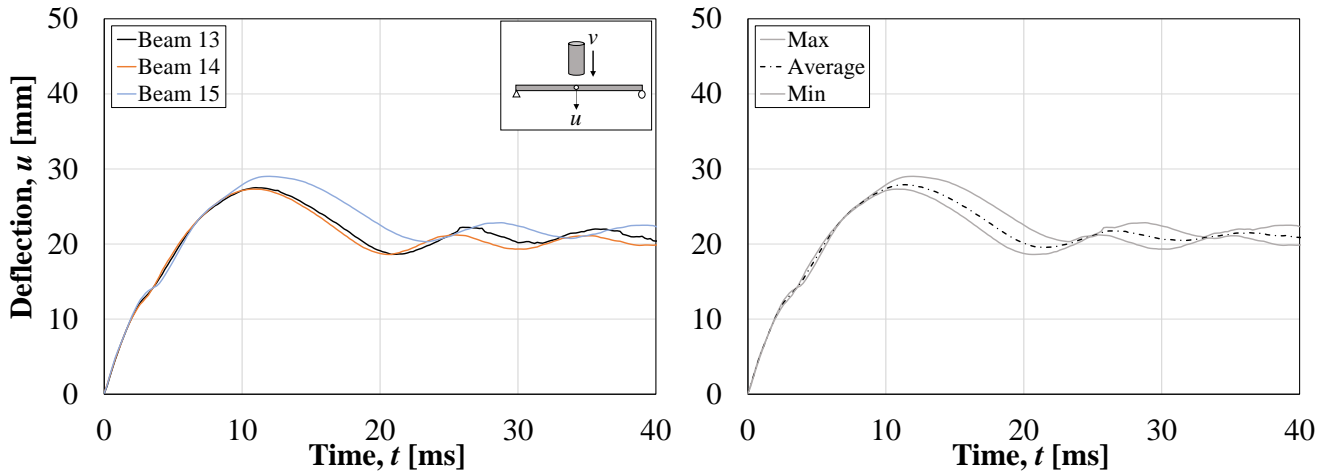


Figure 8.3 Deflection of midpoint over time for Series-3 ($h = 2.5$ m, $m = 20$ kg). The right hand figure shows the average response and the outer envelopes marks the maximum and minimum recorded deflections for the tested beams.

The drop-weight in this series was hoisted to the same height as Series-1. Since the mass does not influence the impact velocity it should be the same as in Series-1, which is also the case.

Beam 15 shows slightly higher values for both u_{max} and u_{pl} which indicates that this beam had decreased stiffness. However, the difference is less than 10 % from the two others beams tested and the average value for all beams is used as the characteristic response in the further studies.

8.3.3.5 Series-4

The results from the tests of Series-4 are summarized in Table 8.6. The response during the first 40 ms after impact can be seen in Figure 8.4.

Table 8.6 Summary of the results from the impact load testing of Series-4 ($h = 5.0$ m, $m = 20$ kg).

Beam	v_0 [m/s]	u_{max} [mm]	u_{pl} [mm]
10	9.8	59.8	46.1
11	9.9	54.8	41.9
12	9.9	57.7	45.8
Average	9.9	57.4	44.6

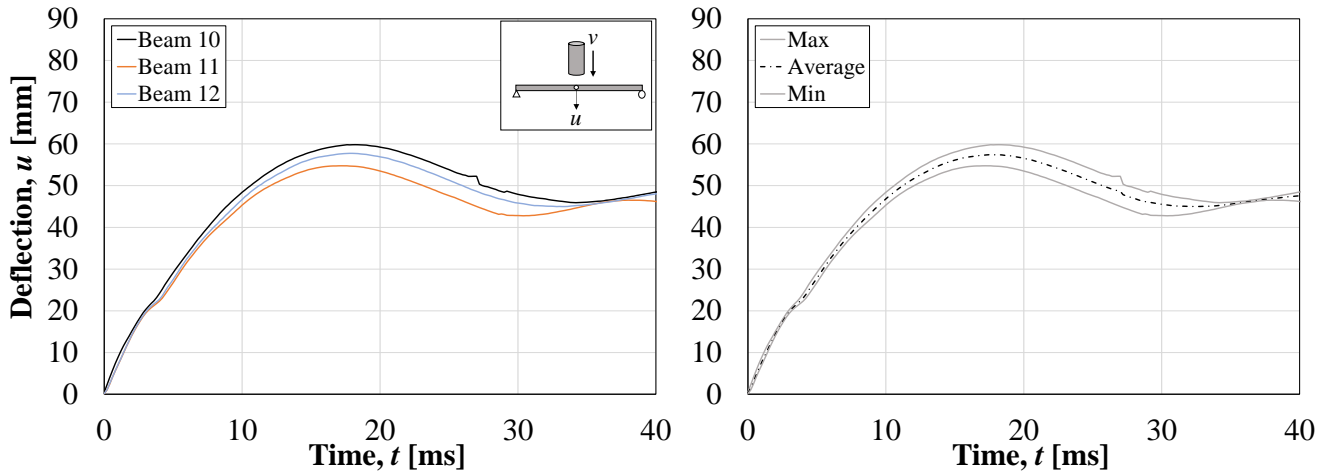


Figure 8.4 Deflection of midpoint over time for Series-4 ($h = 5.0$ m, $m = 20$ kg). The right hand figure shows the average response and the outer envelopes marks the maximum and minimum recorded deflections for the tested beams.

The impact velocity of Beam 10 has an impact velocity that is somewhat low. This is most likely due to human error during the experiments, where the drop-weight was not hoisted into the desired height. However, beam 10 has the largest value of u_{max} which indicates that the lower impact velocity has a minor effect.

The average curve in Figure 8.4 is considered as the characteristic response of the series.

8.3.3.6 Comparison of Deflection over Time

The average curve for deflection over time for all the tested series can be seen in Figure 8.5. The beams in Series-2 and Series-3 shows a similar behaviour during the first 5 ms and afterward Series-3 continues to reach a higher maximum deflection a few ms later.

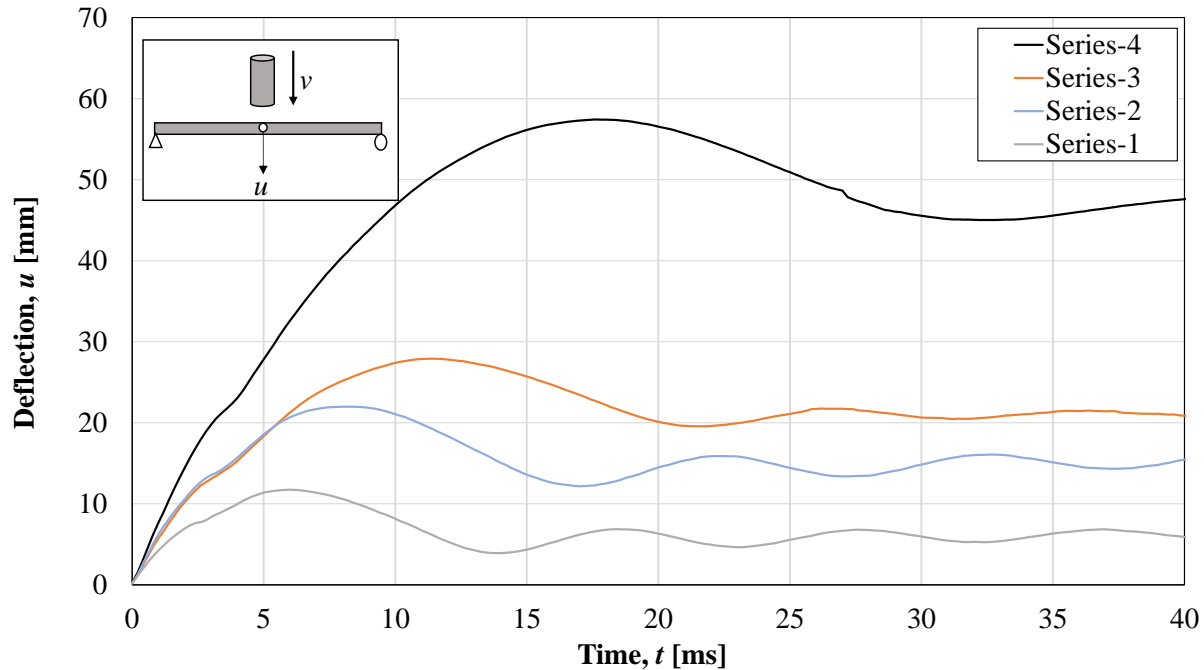


Figure 8.5 Average midpoint deflection for all series in the impact load testing.

8.3.4 Midpoint Deflection over Time during Repeated Impacts

8.3.4.1 Introduction

The results from the repeated impacts is presented within this section. The beams in Series-4 was, as mentioned, only subjected to one impact and is therefore not treated. The results presented within this section are further discussed and compared with the predicted response in Chapter 10.

8.3.4.2 Series-1

The response of the beams in Series-1, after four drops, is summarized in Table 8.7 and 8.8. Note that Table 8.7 presents the additional deflections after each impact, i.e the initial deflection at each impact is taken as zero, whilst Table 8.8 presents the total values. The deflection over time is, together with the average response, presented in Figure 8.6-8.8. Figure 8.9 shows the average response during all four drops. In Figure 8.7 there is an irregular response of Beam 5 during approximately 20 - 25 ms. The reason for this is that dust from the impact zone prevents the camera to capture the selected facet points. However, the dust disappears after a few ms and the curve is once again consistent.

Table 8.7 Summary of the additional deflections for beams in Series-1 ($h = 2.5$ m, $m = 10$ kg). All values are in mm.

Beam	Drop 1		Drop 2		Drop 3		Drop 4	
	u_{max}	u_{pl}	Δu_{max}	Δu_{pl}	Δu_{max}	Δu_{pl}	Δu_{max}	Δu_{pl}
4	12.1	5.9	13.2	6.1	15.7	6.6	30.3	20.4
5	11.4	5.1	12.9	6.1	14.4	7.5	16.7	3.6
6	11.8	5.1	12.0	5.0	14.1	5.9	15.6	3.4
Average	11.7	5.4	12.7	5.7	14.7	6.7	20.9	9.1

Table 8.8 Summary of the total deflections for beams in Series-1 ($h = 2.5$ m, $m = 10$ kg). All values are in mm.

Beam	Drop 1		Drop 2		Drop 3		Drop 4	
	u_{max}	u_{pl}	u_{max}	u_{pl}	u_{max}	u_{pl}	u_{max}	u_{pl}
4	12.1	5.9	19.1	12.0	27.7	18.6	48.9	39.0
5	11.4	5.1	18.0	11.2	25.6	18.7	35.4	22.3
6	11.8	5.1	17.1	10.1	24.2	16.0	31.6	19.4
Average	11.7	5.4	18.1	11.1	25.8	17.8	38.6	26.9

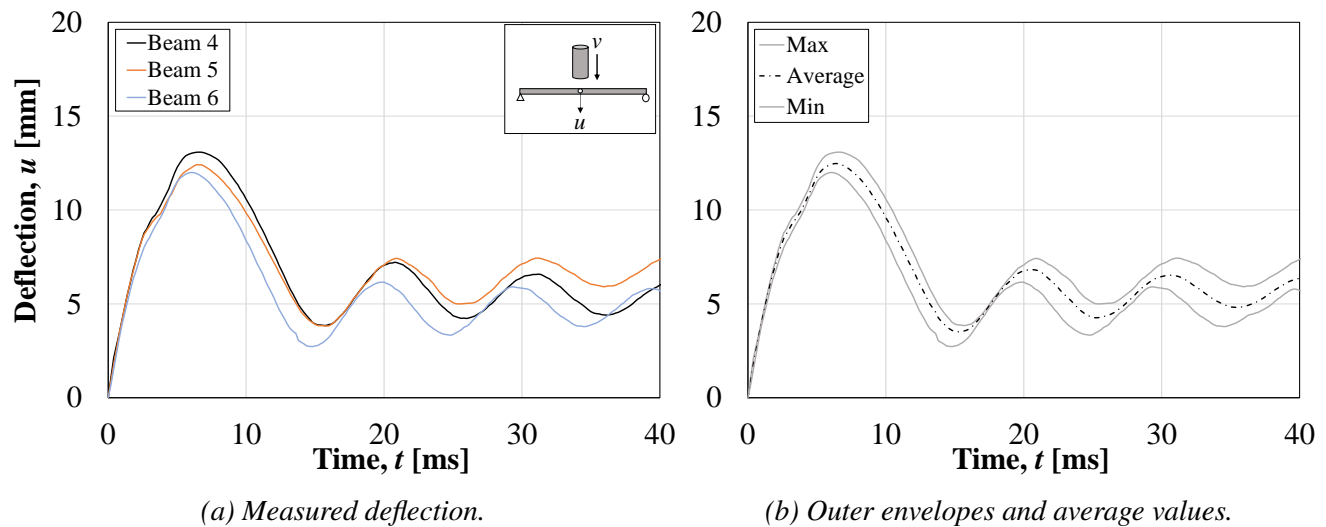
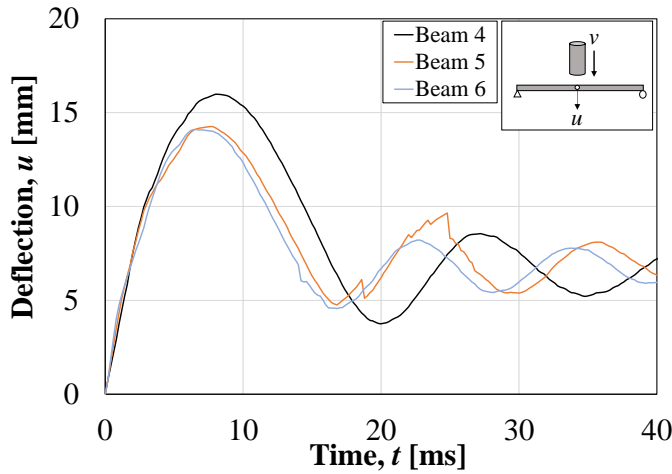
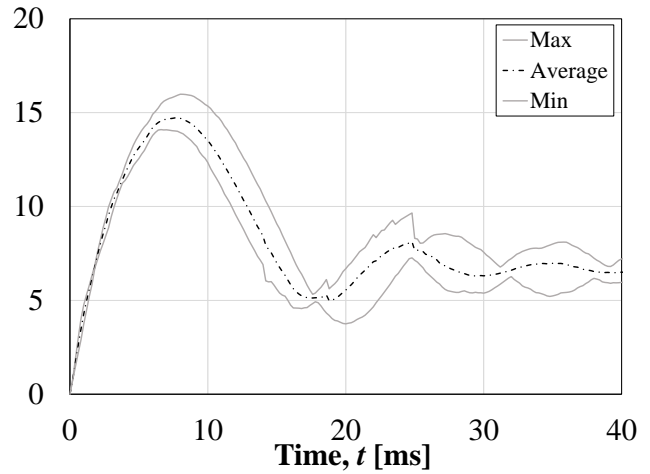


Figure 8.6 Deflection over time for the second drop.

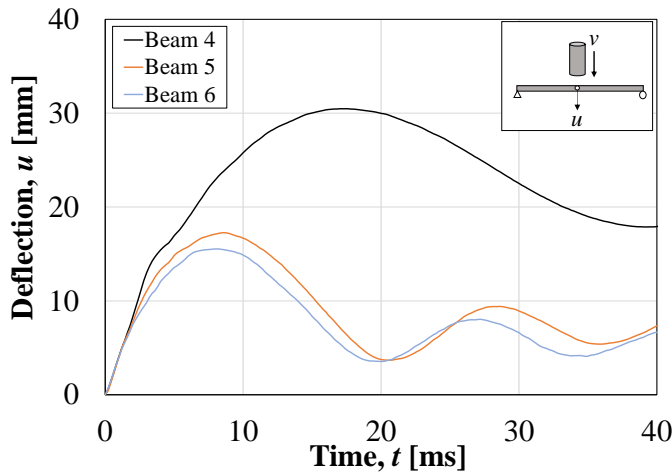


(a) Measured deflection.

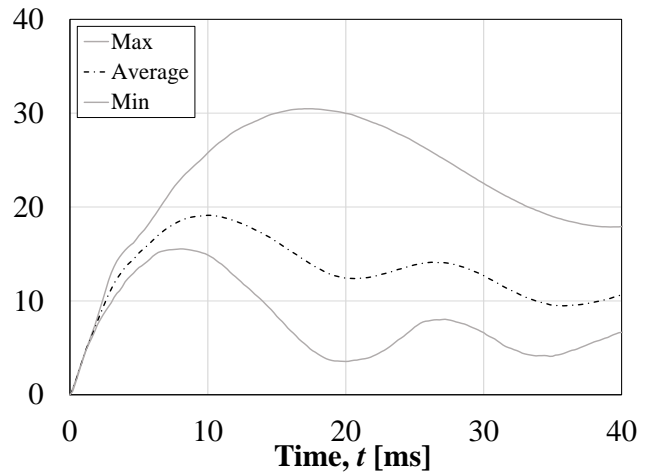


(b) Outer envelopes and average values.

Figure 8.7 Deflection over time for the third drop.



(a) Measured deflection.



(b) Outer envelopes and average values.

Figure 8.8 Deflection over time for the fourth drop.

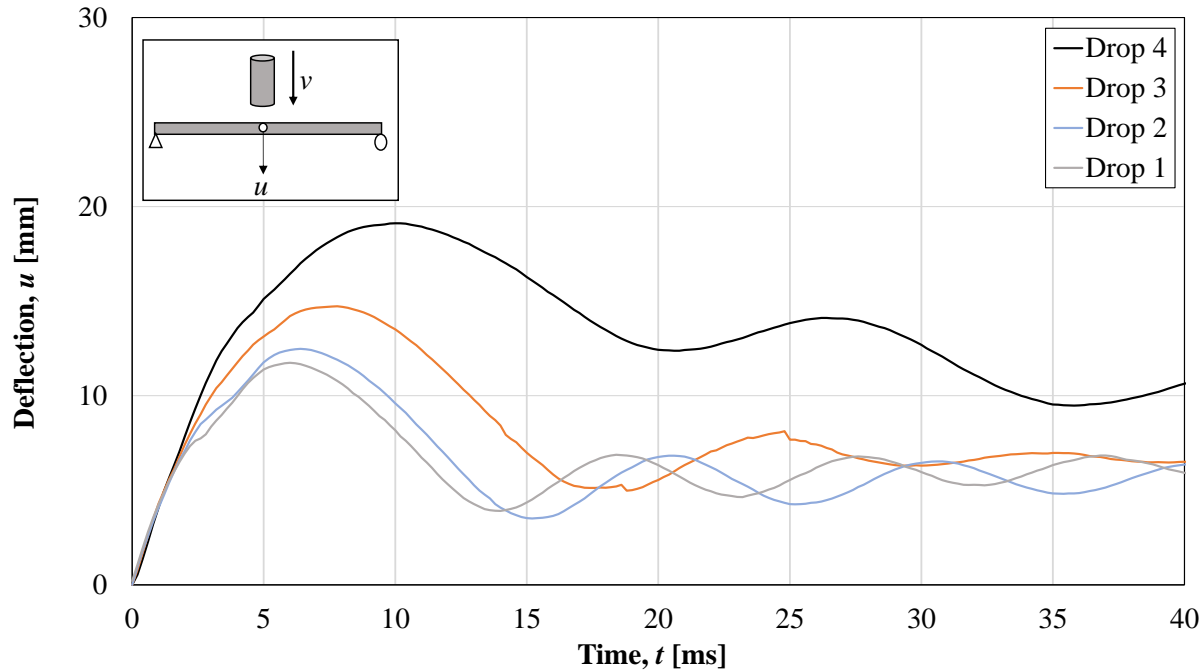


Figure 8.9 Average midpoint deflection for the repeated impacts.

It is clear that there is a small deviation between the response of Beam 4 and the two other beams. It can be seen already after the second and the third drop but a major deviation occurs at the fourth impact. This is due to severe local damage at the mid part of Beam 4. Figure 8.9 shows that the stiffness decreases after each impact; i.e the deflection obtained increases at each impact.

8.3.4.3 Series-2

The response of the beams in Series-2 are summarized in Table 8.9. The response during the second impact is presented in Figure 8.10. Figure 8.11 shows the average response of the series during the two impacts.

Table 8.9 Summary of the deflections for beams in Series-2 ($h = 5.0$ m, $m = 10$ kg). All values are in mm.

Beam	Drop 1		Drop 2			
	u_{max}	u_{pl}	Δu_{max}	u_{max}	Δu_{pl}	u_{pl}
1	22.1	14.6	23.4	38.0	16.4	31.0
2	21.4	13.8	26.5	40.3	14.3	28.1
3	22.4	14.3	26.2	40.5	16.9	31.2
Average	22.0	14.2	25.4	39.6	15.9	30.1

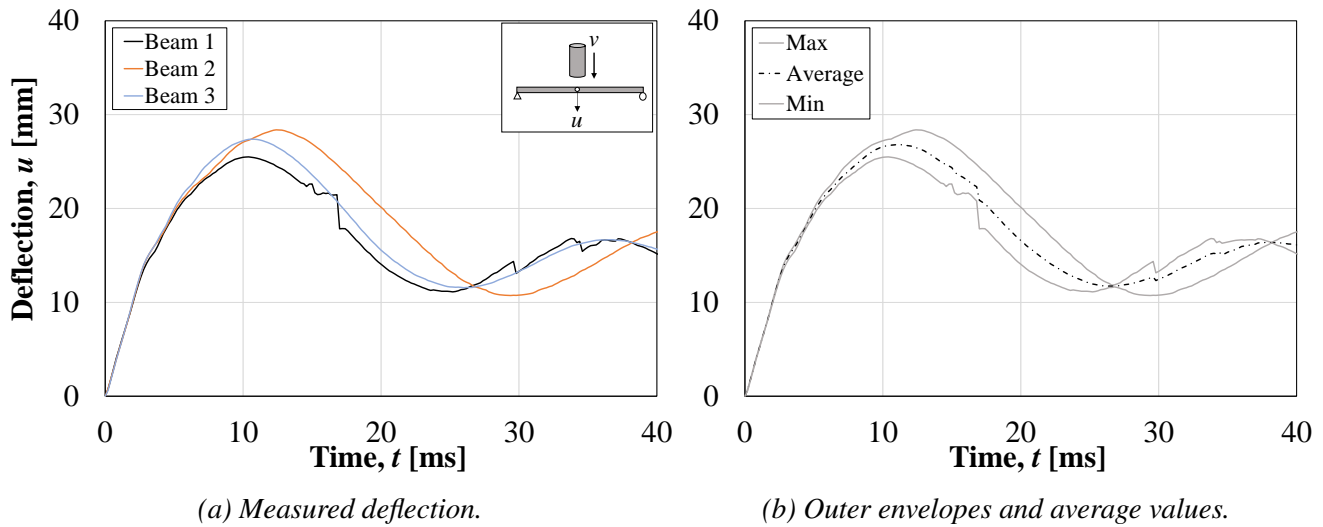


Figure 8.10 Deflection over time for the second drop.

The response during the second impact is similar for all beams. Beam 2 has a slightly lower plastic deformation u_{pl} and it can also be seen that the response of this beam is shifted a bit in time. However, when looking at the outer envelopes, it can be stated that the average curve represents the behaviour very well. From Figure 8.11 it is clear that the stiffness decreases after the first impact has occurred.

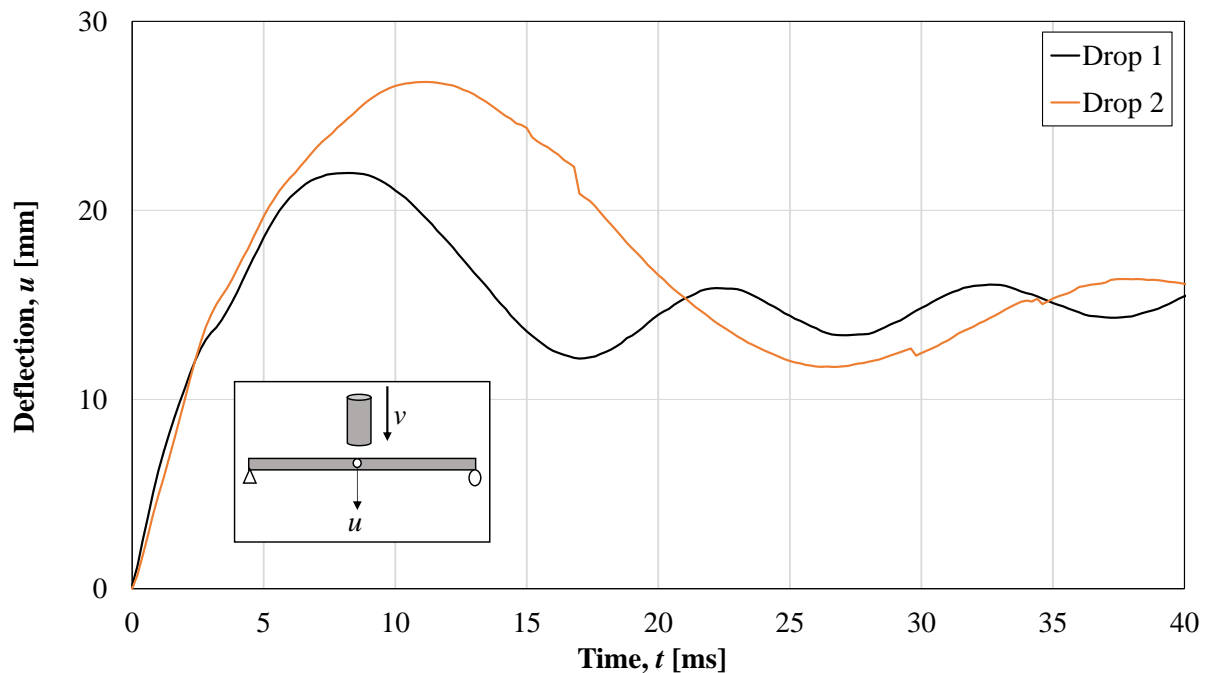


Figure 8.11 Average midpoint deflection for the repeated impacts.

8.3.4.4 Series-3

The response of the beams in Series-3 is summarized in Table 8.10. The response during the second impact is presented in Figure 8.12. Figure 8.13 shows the average response of the series during the two impacts.

Table 8.10 Summary of the deflections for beams in Series-3 ($h = 2.5$ m, $m = 20$ kg). All values are in mm.

Beam	Drop 1		Drop 2			
	u_{max}	u_{pl}	Δu_{max}	u_{max}	Δu_{pl}	u_{pl}
13	27.5	20.1	33.9	54.0	20.8	40.9
14	27.3	20.3	31.8	54.4	24.1	44.4
15	29.0	21.8	30.7	61.2	27.4	49.2
Average	27.9	20.7	32.1	56.5	24.1	44.8

The beams shows a similar response and the conclusion is that the average curve represents the behaviour very well. Figure 8.13 shows how the stiffness has decreased after the first impact.

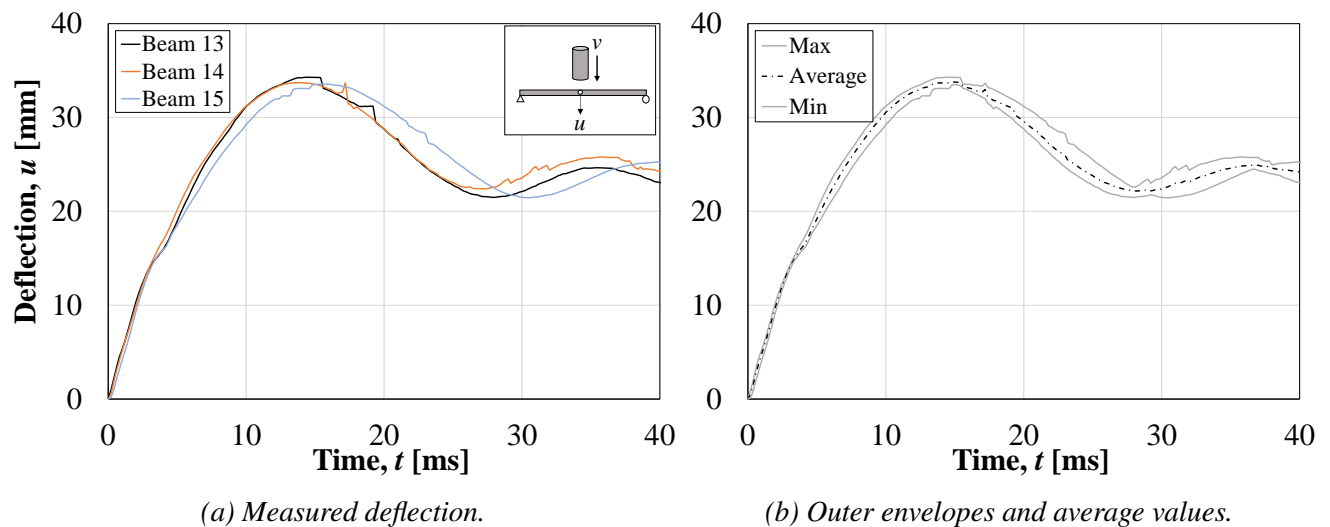


Figure 8.12 Deflection over time for the second drop.

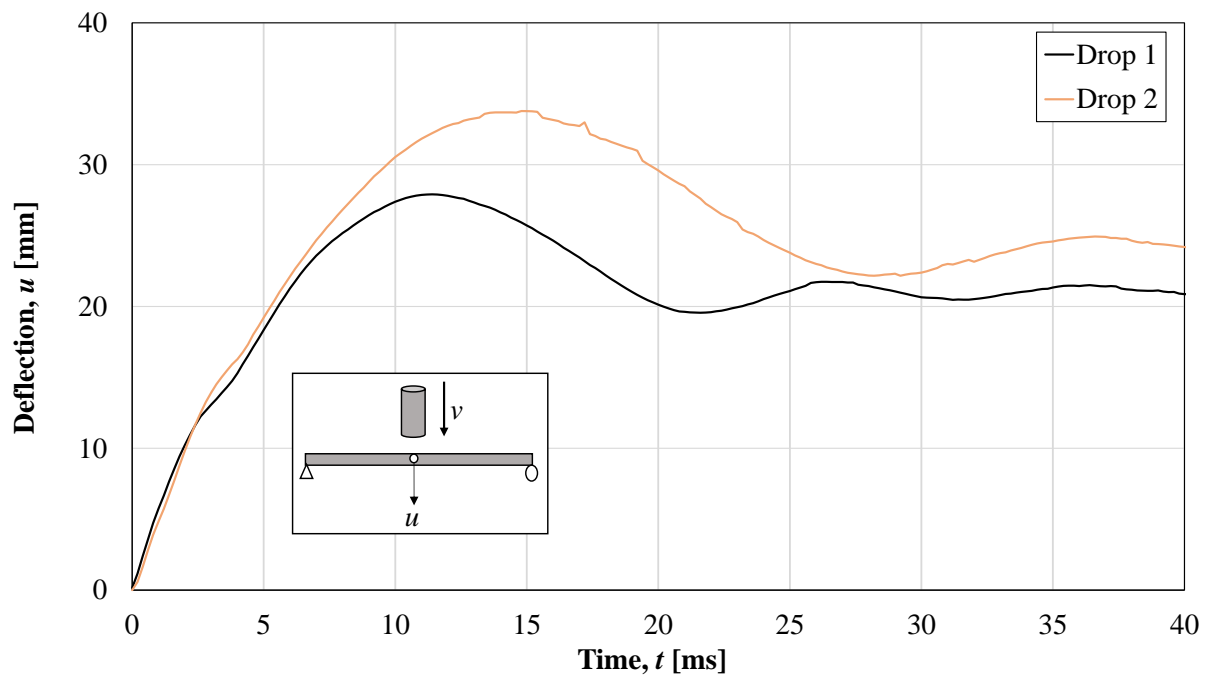


Figure 8.13 Average midpoint deflection for the repeated impacts.

8.3.5 Strain Fields from DIC during First Impact

The crack pattern can be evaluated by looking at the strain fields. In GOM Correlate the major strains of a surface component can be selected and this renders the coloured images presented further in this section. The limits of the colorscale can be specified by the user. As mentioned, the intention in this project was to detect the cracks. At a strain of 2 % it was possible to visually see a crack in the photos, and therefore this was determined as the upper limit. The lower limit was set to 1.2 % so that most of the noise was damped out.

The beam response during the first two ms in Series-1 can be seen in Table 8.11. The beams shows a similar strain field where flexural cracks forms at the bottom edge at midspan, directly below the impact region. For Beam 5 and Beam 6 one major crack occurs whilst two cracks forms for Beam 4. Beam 4 was also the beam within the series that had the most damages after all four impacts, see Section 8.3.4.2. At 0.4 ms bending cracks in the upper region of all beams can be observed. These cracks closes and can no longer be detected after 1.0 ms, this behaviour is further discussed in Section 8.3.7. Minor shear cracks can be detected at maximum deflection.

Table 8.11 Strain fields of beams in Series-1 ($h = 2.5$ m, $m = 10$ kg) during the first two ms, at maximum deflection and at the end of the test.

[ms]	Beam 4	Beam 5	Beam 6
0.2			
0.4			
0.6			
1.0			
2.0			
	 $t = 6.0, u_{max} = 12.1$	 $t = 6.0, u_{max} = 11.4$	 $t = 5.8, u_{max} = 11.8$
	 $u_{pl} = 5.9$	 $u_{pl} = 5.1$	 $u_{pl} = 5.1$
%	 1.2 1.3 1.4 1.5 1.6 1.7 1.8 1.9 2.0		

The response of the beams in Series-2 can be seen in Table 8.12. Unlike Series-1, shear cracking occurs at the impact region, as well as a flexural crack. The overall crack pattern is similar but the response of Beam 2 has some deviations compared to the other two beams, both concerning the crack pattern and the deflections. Unfortunately, spalling occurred in some parts of the beams and this can be seen as the white areas in the strain field images. .

Table 8.12 Strain fields of beams in Series-2 ($h = 5.0$ m, $m = 10$ kg) during the first two ms, at maximum deflection and at the end of the test.

[ms]	Beam 1	Beam 2	Beam 3
0.2			
0.4			
0.6			
1.0			
2.0			
	 $t = 8.2, u_{max} = 22.1$	 $t = 7.4, u_{max} = 21.4$	 $t = 8.4, u_{max} = 22.4$
	 $u_{pl} = 14.6$	 $u_{pl} = 13.8$	 $u_{pl} = 14.3$
%			

The response during the first two ms of the beams in Series-3 can be seen in Table 8.13. The three beams shows different behavior compared to each other. In Beam 13 and Beam 14 one distinct flexural crack is formed below the impact area, whereas Beam 15 has pronounced shear cracks. After 0.6 ms a shear crack appears in Beam 13 as well but not in other beams. The impact region of Beam 15 is more damaged than for the two other beams and the plastic deformation was also larger for this beam. At the last image, after the impact event, of Beam 13 and Beam 15 there is an area with high strains. This is an error that occurred in GOM Correlate and does not reflect the real behaviour.

Table 8.13 Strain fields of beams in Series-3 ($h = 2.5$ m, $m = 20$ kg) during the first two ms, at maximum deflection and at the end of the test.

[ms]	Beam 13	Beam 14	Beam 15
0.2			
0.4			
0.6			
1.0			
2.0			
	 $t = 11.0, u_{max} = 27.5$	 $t = 10.8, u_{max} = 27.3$	 $t = 12.0, u_{max} = 29.0$
	 $u_{pl} = 20.1$	 $u_{pl} = 20.3$	 $u_{pl} = 21.8$
%			

The response during the first two ms of the beams in Series-4 can be seen in Table 8.14. Overall, the beams show a similar crack pattern where major flexural cracks, together with shear cracks, occur at the impact region. Several cracks appear at the upper part of the beam during the first ms and after 2.0 ms they are no longer visible. Beam 10 has a flatter shear crack propagating to the left of the impact region. This beam has also the largest plastic deformation. The blank areas at the upper part of the beam indicate the local spalling of concrete in the impact region. Unfortunately, an image after the impact event was not made in this series.

Table 8.14 Strain fields of beams in Series-4 ($h = 5.0$ m, $m = 20$ kg) during the first two ms, at maximum deflection and at the end of the test.

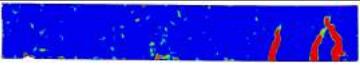
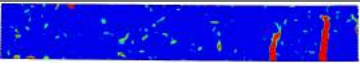
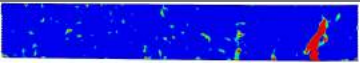
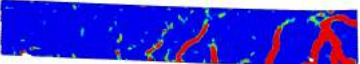
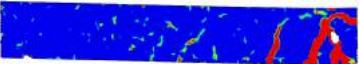
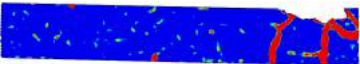
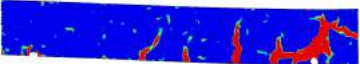
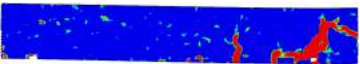
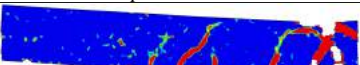
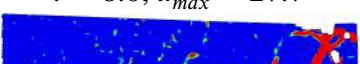
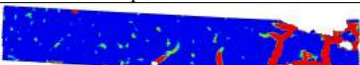
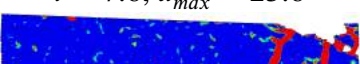
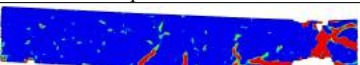
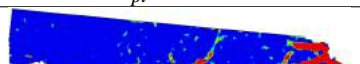
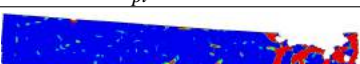
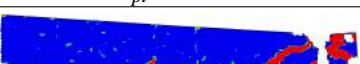
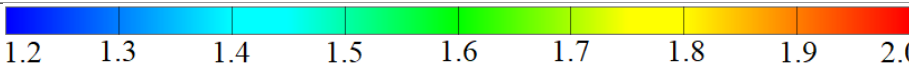
[ms]	Beam 10	Beam 11	Beam 12
0.2			
0.4			
0.6			
1.0			
2.0			
	 $t = 18.2, u_{max} = 59.8$ $u_{pl} = 46.1$	 $t = 17.2, u_{max} = 54.8$ $u_{pl} = 41.9$	 $t = 18.0, u_{max} = 57.7$ $u_{pl} = 45.8$
%			

8.3.6 Strain Fields from DIC during Repeated Impacts

This section presents the strain fields from the repeated impacts for each beam. The maximum deflection and which time it occurred at is presented together with the gathered plastic deflection after each drop. It should be noted that the residual strain field from the last drop is missing in each case, this is since the camera stops taking photos before the beam stops moving. The residual strain field for the rest of the drops can be found by taking the first image before the drop-weight hits the beam in the subsequent drop. However, the plastic deformation from the last drop can be found by measuring the deformation before the static test begins, as described in Appendix F.

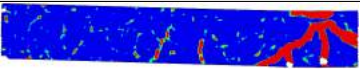
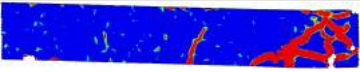
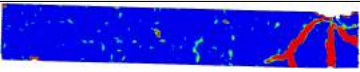
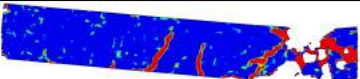
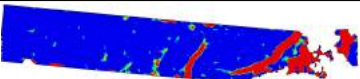
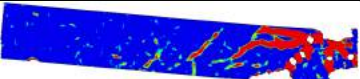
Strain fields of Series-1 is presented in Table 8.15 where it can be clearly seen that parts of the compressive zone were crushed after each drop, which is illustrated by white areas in the top of the beam. The white areas in the bottom of the beam represents parts in the tensile zone that have loosened from the beam during the impact. It can also be seen that new cracks open during the drops and that it gets harder to find any similarities between the three beams as the number of drops increase.

Table 8.15 Strain fields at maximum deflection and after impact for beams in Series-1.

Drop	Beam 4	Beam 5	Beam 6
1	 $u_{pl} = 5.9$	 $u_{pl} = 5.1$	 $u_{pl} = 5.1$
2	 $t = 6.6, u_{max} = 19.1$  $u_{pl} = 12.0$	 $t = 6.4, u_{max} = 18.0$  $u_{pl} = 11.2$	 $t = 6.0, u_{max} = 17.1$  $u_{pl} = 10.1$
3	 $t = 8.0, u_{max} = 27.7$  $u_{pl} = 18.6$	 $t = 7.6, u_{max} = 25.6$  $u_{pl} = 18.7$	 $t = 6.4, u_{max} = 24.2$  $u_{pl} = 16.0$
4	 $t = 17.4, u_{max} = 49.0$ $u_{pl} = 39.0$	 $t = 8.6, u_{max} = 35.4$ $u_{pl} = 22.3$	 $t = 8.0, u_{max} = 31.6$ $u_{pl} = 19.4$
%			

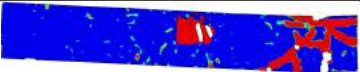
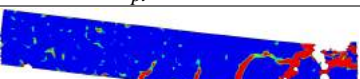
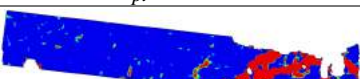
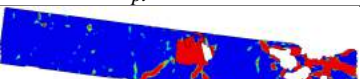
Strain fields of Series-2 are presented in Table 8.16 where it can be seen that the compressive zone gets crushed during the second impact and that parts of the tensile zone have loosened from the beam here as well. The beams behave in a pretty similar way.

Table 8.16 Strain fields at maximum deflection and after impact for beams in Series-2.

Drop	Beam 1	Beam 2	Beam 3
1	 $u_{pl} = 14.6$	 $u_{pl} = 13.8$	 $u_{pl} = 14.3$
2	 $t = 10.4, u_{max} = 38.0$ $u_{pl} = 31.0$	 $t = 12.4, u_{max} = 40.3$ $u_{pl} = 28.1$	 $t = 10.6, u_{max} = 40.5$ $u_{pl} = 31.2$
%			

Strain fields of Series-3 are presented in Table 8.17 where it can be seen that the compressive zone gets crushed and that parts of the tensile zone have fallen off. All of the beams have severe damage in the compressive zone and a lot of damages in the tensile zone. There is however a large variation between the beams.

Table 8.17 Strain fields at maximum deflection and after impact for beams in Series-3.

Drop	Beam 13	Beam 14	Beam 15
1	 $u_{pl} = 20.1$	 $u_{pl} = 20.3$	 $u_{pl} = 21.8$
2	 $t = 14.4, u_{max} = 54.0$ $u_{pl} = 40.9$	 $t = 14.2, u_{max} = 52.1$ $u_{pl} = 44.4$	 $t = 12.0, u_{max} = 52.5$ $u_{pl} = 49.2$
%			

8.3.7 Deformed Shape

The deformed shape over time for the first impact are shown for Beam 4 (from Series-1) and Beam 12 (from Series-4). These beams were considered to well represent the overall behaviour of the two series, based on the deflection-time relation response during the first impact. The reason for choosing beams from Series-1 and Series-4 was to compare the behaviour between the extremes of the impact conditions. The information was collected by constructing a single section line in GOM Correlate that selects all facet points along a line from one side to the other of the beam. Figure 8.14 and 8.15 shows the deformed shape of Beam 4 and Beam 12, respectively, during the first 2.0 ms. It is clear that only a small part of the beam deforms during the first measurements. The rest of the beam serves at this stage as a restraint for the inner, deflected, part of the beam. Consequently, the beam initially behaves as a double-fixed beam with a short span and this gives tension in the upper part of the beam, resulting in cracks in the

transition between the active and the inactive portion of the beam. It is a clear difference of the response between the two studied beams. Beam 12 shows a larger local displacement at the impacted part. This is due to the shear cracks that are initiated in this beam. The deformed shape of this beam is also more triangular than for Beam 4.

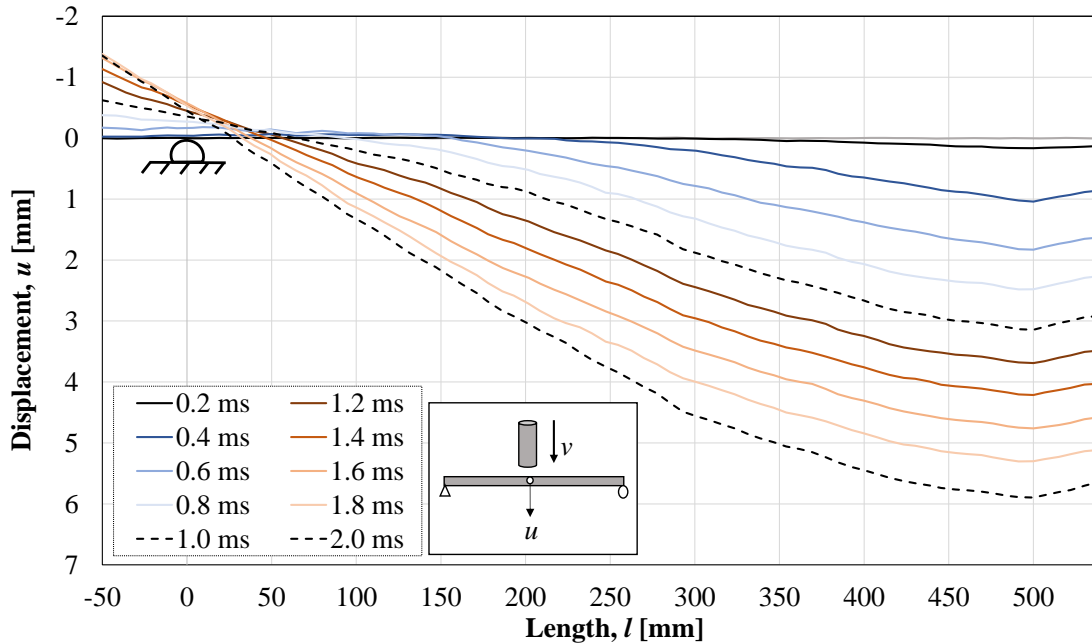


Figure 8.14 Deformed shape of Beam 4 at different times after impact.

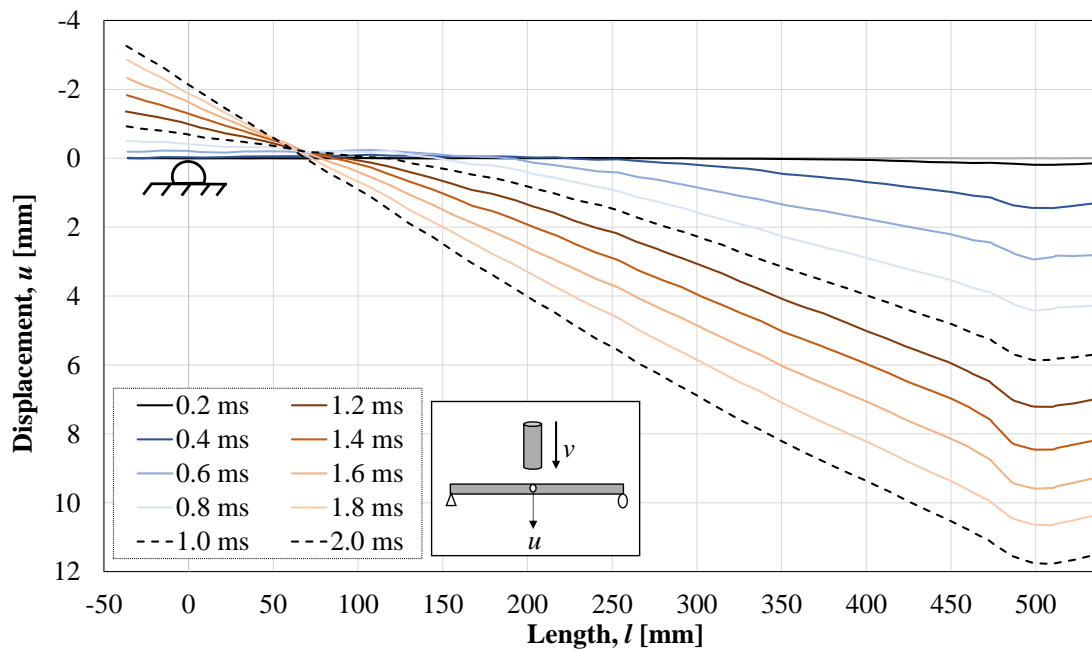


Figure 8.15 Deformed shape of Beam 12 at different times after impact.

The relative deformed shape at different times is illustrated in Figure 8.16 and 8.17. The values of the deflections in these figures were normalized to the maximum deflection at all studied stages.

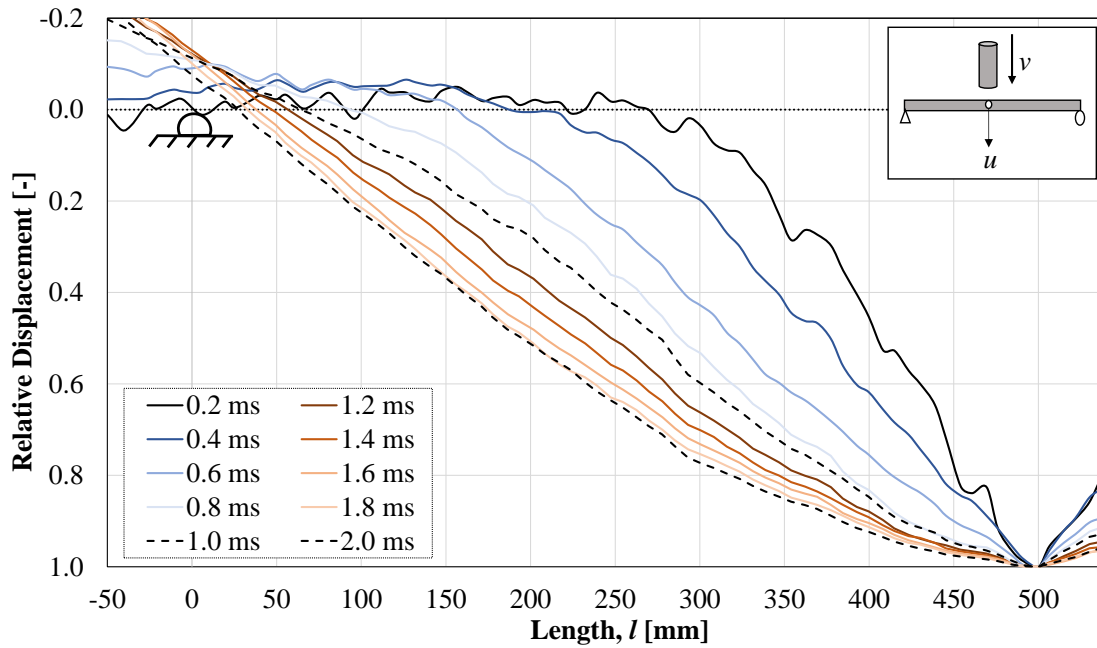


Figure 8.16 Relative deformed shape of Beam 4 at different times after impact.

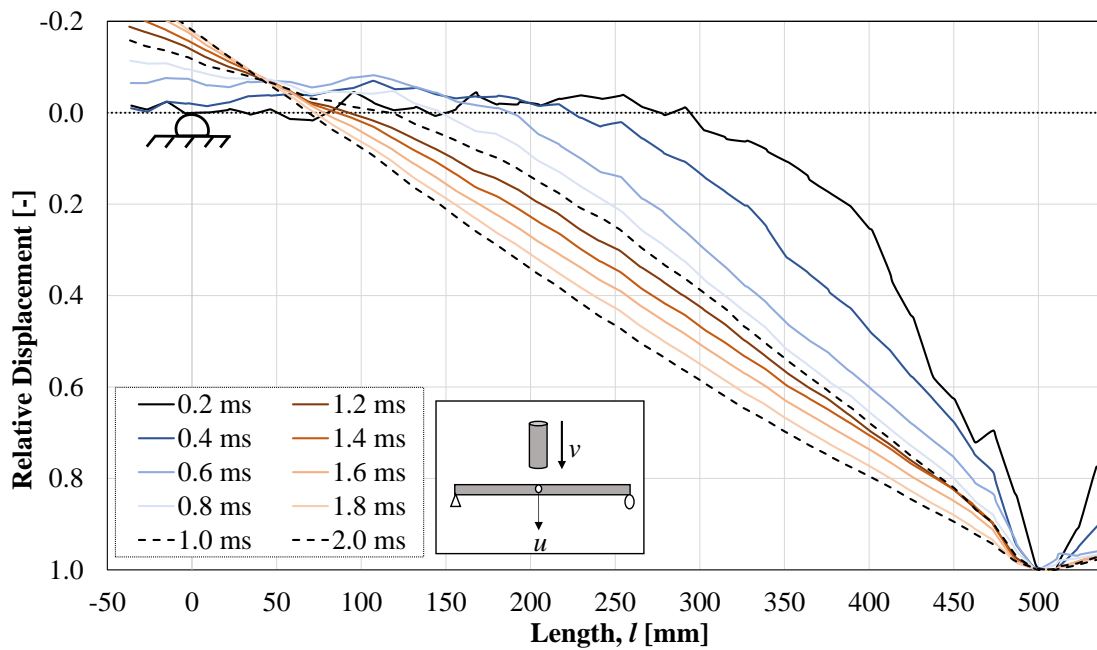


Figure 8.17 Relative deformed shape of Beam 12 at different times after impact.

8.3.8 Velocities of Initial Deflection

It is also of interest to examine the velocity at which the deflections propagates during the first ms. The velocities was gathered by looking at how the active portion of the beam increased for each time step of 0.2 ms. The velocity was calculated as

$$v = \frac{x(t_2) - x(t_1)}{t_2 - t_1} \quad (8.1)$$

where x is the transition point between the active and inactive portion of the beam, see Figure 8.18. A study of the shear velocities was made on Beam 4 and Beam 12 and the results from the study of shear velocities is presented in Table 8.18. It was not possible to include the velocity between 0 - 0.2 ms. This due to the fact that the impact does not occur exactly at the time when the high-speed camera takes a photo. In other words, the time step between the first and second photo is not with certainty 0.2 ms.

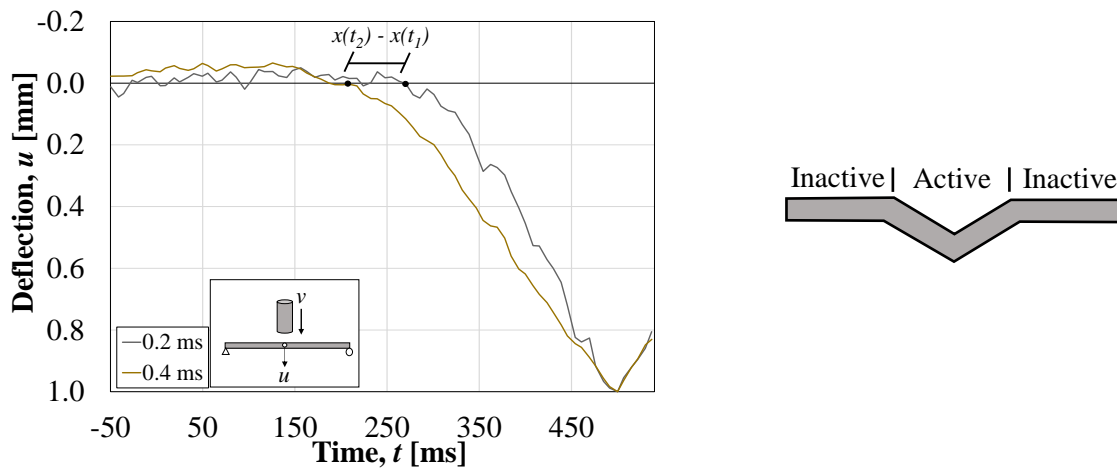


Figure 8.18 Transition point between active and inactive part.

Table 8.18 Shear velocities of Beam 4 and Beam 12. All values are in m/s.

Beam	0.4 ms	0.6 ms	0.8 ms	1.0 ms	1.2 ms	1.4 ms	1.6 ms
4	837	425	262	229	46	75	30
12	795	366	237	132	125	49	60

It is clear that the velocity decreases for each time step of 0.2 ms. After a few time steps the velocity decreases significantly and then stabilizes. In this study the time at which this decrease occurs was determined as the time it takes for the active portion to span the entire beam spa. In Beam 4 this was after approximately 1.0 ms and in Beam 12 it was after 1.2 ms. The Beams shows a similar response.

In Yi *et al.* (2016) the shear wave propagation is studied and a suggestion to calculate the time t_0 needed for the active beam portion to span the entire beam is given as

$$t_0 = \frac{L_0}{2v_s} \quad (8.2)$$

where L_0 is the span of the beam and v_s is the velocity at which the stress wave is transferred within the

concrete. The velocity v_s corresponds to the shear velocity and can be calculated as

$$v_s = \sqrt{\frac{G}{\rho}} \quad (8.3)$$

where G is the shear modulus, calculated as

$$G = \frac{E}{2(1 + \nu)} \quad (8.4)$$

and ρ is the density of concrete. The parameters needed to calculate t_0 within this project is presented in Table 8.19.

Table 8.19 Parameters for calculating t_0 .

ρ [kg/m ³]	G [GPa]	L_0 [m]
2384	19.5	1.0

From Equations (8.2) and (8.3) the theoretical value of the time t_0 was 0.2 ms and thus 5 - 6 times smaller than the measured time which was approximated as 1.0 - 1.2 ms.

8.3.9 Impact Force and Impulse Load

8.3.9.1 Introduction

The force acting on the beam during the impact and the impulse load is presented within this section. In GOM Correlate the acceleration is calculated as the second derivative of the displacement. The noise that occurs in the displacements therefore gives even worse noise in the acceleration. In an attempt to get rid of this noise a number of points were constructed at the drop-weight, from where the acceleration was established. This was done for every beam during the first impact and the force F presented for every beam within this section is the average value of several such points. The peak value of the impact force occurs after 3 ms in the following graphs within this section.

The impulse load is also estimated within this section and a further description of how the impulse was calculated can be found in Appendix H.

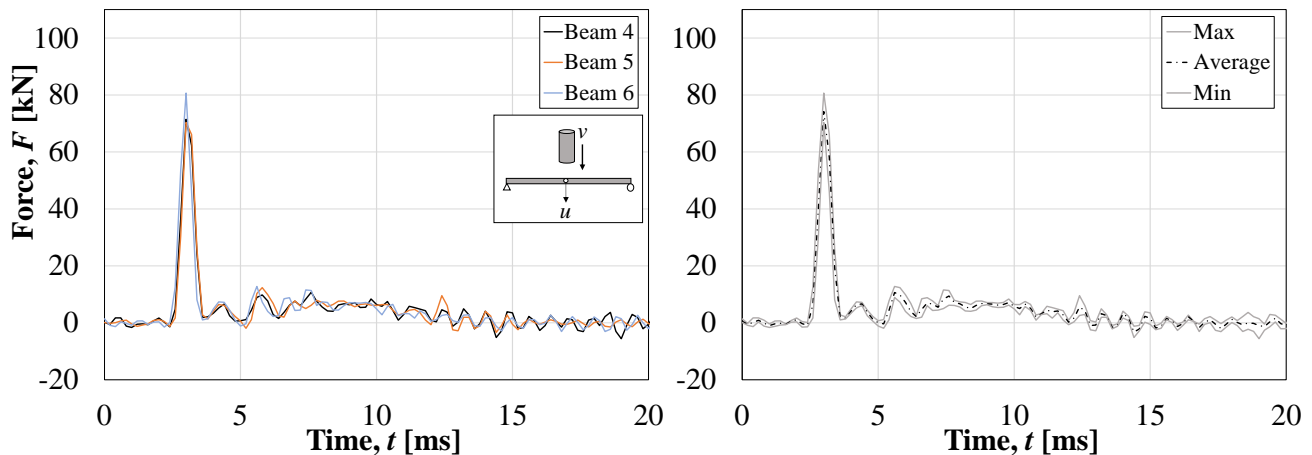
8.3.9.2 Series-1

The peak value of the force F_{imp} acting on the beam during the impact and the impulse I is presented in Table 8.20. The force - time relationship for the drop-weight acting on the beam during the impact is presented in Figure 8.19. The total impulse I_{tot} is defined as

$$I_{tot} = I_{ini} + I_{post} \quad (8.5)$$

Table 8.20 Peak value of the impact force F_{imp} and the impulse I for Series-1.

Beam	F_{imp} [kN]	I_{ini} [Ns]	I_{post} [Ns]	I_{tot} [Ns]	I_{ini}/I_{tot} [%]
4	71.5	39.5	47.6	87.1	45.4
5	70.3	39.0	49.5	88.5	44.1
6	80.7	40.3	48.3	88.6	45.5
Average	74.2	39.6	48.5	88.0	45.0



(a) Measured force.

(b) Outer envelopes and average values.

Figure 8.19 Force over time for Series-1.

From the results in Table 8.20 it seems that F_{imp} is more than 10 % higher than the for the two other beams but the fact that the time step between two values is 0.2 ms has a marked influence in this case. Figure 8.20 shows the trend line of second order polynomial for the three beams from where it is clear that the peak value of beam 6 occurs at the top of the trend line. The peak value of Beam 4 and Beam 5 occurs on the other hand somewhere between two measurements and therefore a lower value is obtained. However, it seems that the peak value is higher for Beam 6 but not as much as indicated in Table 8.20. The impulse values are similar for the beams and this indicates that the method used to evaluate the impulses is reasonable.

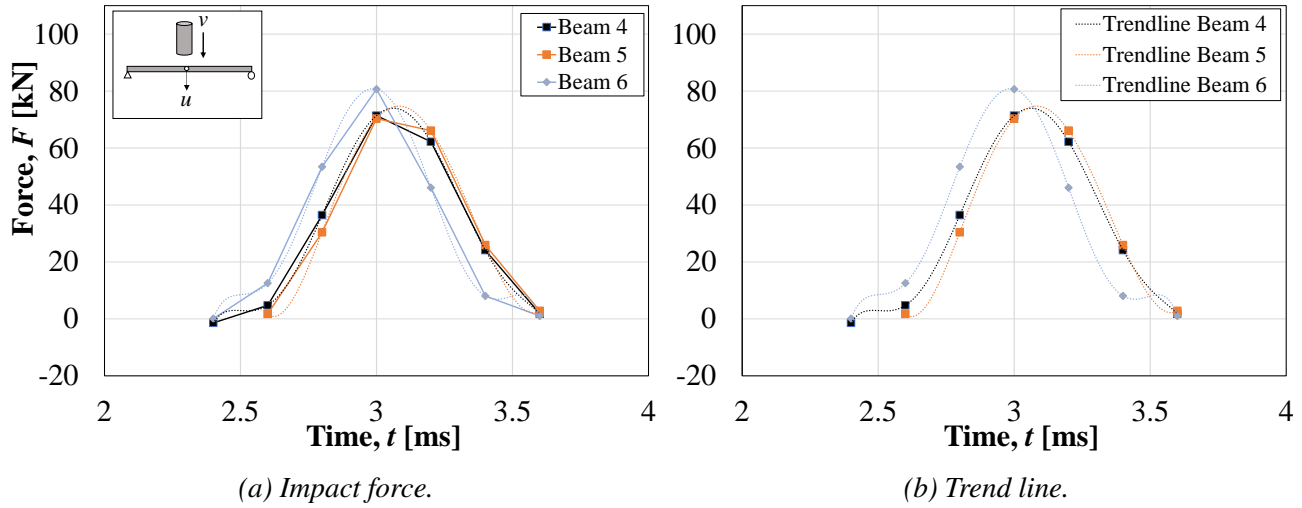


Figure 8.20 Graphs showing the trend line for Series-1.

8.3.9.3 Series-2

The peak value of the force F_{imp} acting on the beam during the impact and the impulse can be seen in Table 8.21. The force - time relationship for the drop-weight acting on the beam during the impact can be seen in Figure 8.21.

Table 8.21 Peak value of the impact force F_{imp} and the impulse I for Series-2.

Beam	F_{imp} [kN]	I_{ini} [Ns]	I_{post} [Ns]	I_{tot} [Ns]	I_{ini}/I_{tot} [%]
1	97.1	53.0	68.4	121.4	43.6
2	99.7	52.6	69.3	121.9	43.2
3	101.4	53.0	67.5	120.5	44.0
Average	99.4	52.9	68.4	121.3	43.6

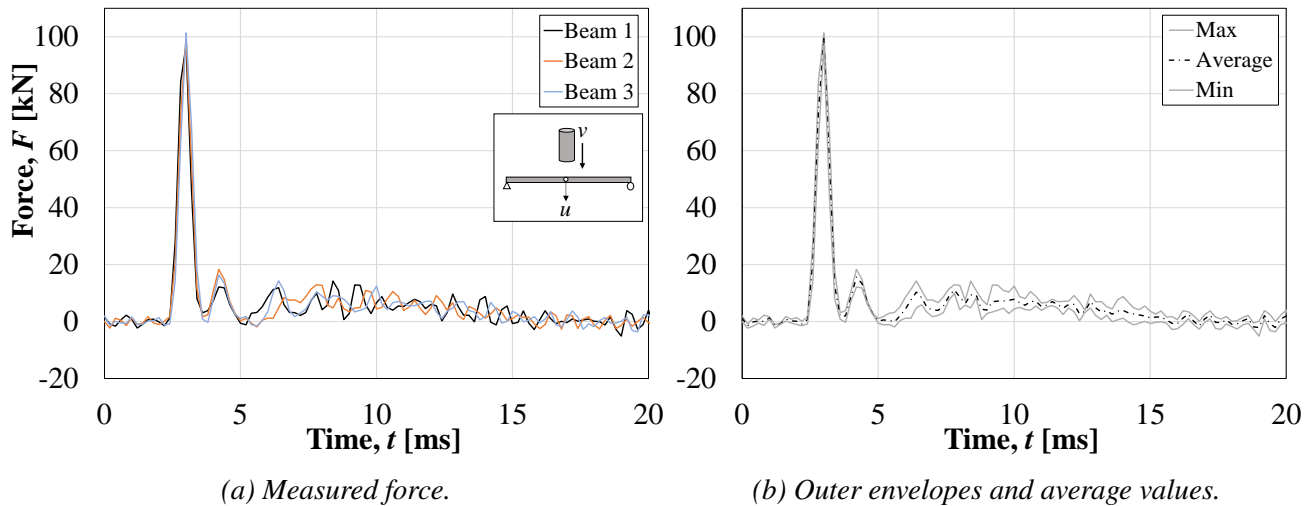


Figure 8.21 Force over time for Series-2.

8.3.9.4 Series-3

The peak value of the force F_{imp} acting on the beam during the impact and the impulse can be seen in Table 8.22. The force - time relationship for the drop-weight acting on the beam during the impact can be seen in Figure 8.22.

Table 8.22 Peak value of the impact force F_{imp} and the impulse I for Series-3.

Beam	F_{imp} [kN]	I_{ini} [Ns]	I_{post} [Ns]	I_{tot} [Ns]	I_{ini}/I_{tot} [%]
13	79.1	50.3	119.6	169.9	29.6
14	83.9	52.3	120.0	172.3	30.4
15	80.3	49.6	117.1	166.7	29.8
Average	81.1	50.7	118.9	169.6	29.9

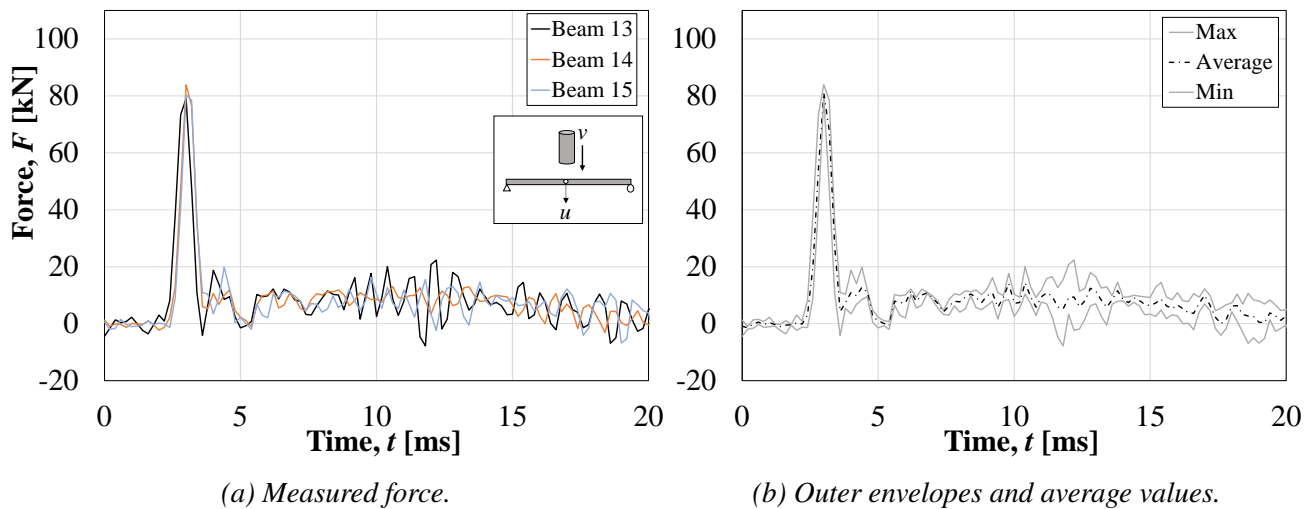


Figure 8.22 Force over time for Series-3.

8.3.9.5 Series-4

The peak value of the force F_{imp} acting on the beam during the impact and the impulse can be seen in Table 8.23. The force - time relationship for the drop-weight acting on the beam during the impact can be seen in Figure 8.23.

Table 8.23 Peak value of the impact force F_{imp} and the impulse I for Series-4.

Beam	F_{imp} [kN]	I_{ini} [Ns]	I_{post} [Ns]	I_{tot} [Ns]	I_{ini}/I_{tot} [%]
10	109.3	67.9	162.3	230.2	29.5
11	108.3	67.0	162.3	229.3	29.2
12	104.9	66.0	158.1	224.1	29.4
Average	81.1	67.0	160.9	227.9	29.4

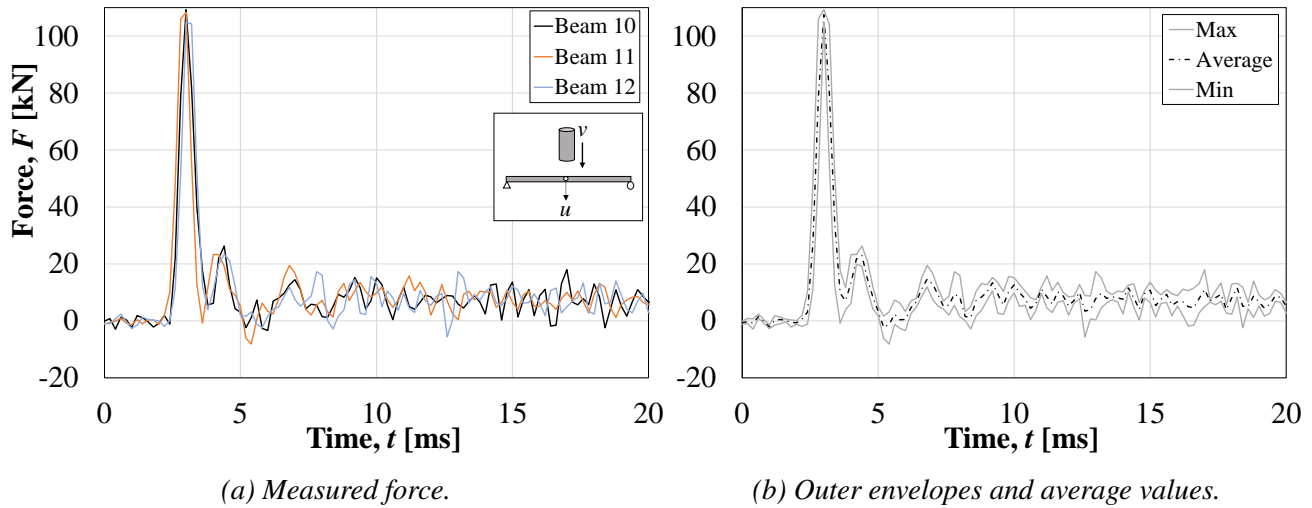


Figure 8.23 Force over time for Series-4.

8.3.9.6 Comparison of Impact Force

The average curve of the force-time relation for all four test series can be seen in Figure 8.24. As expected, the highest peak value of the impact force occurs in Series-4. The impact force of Series-2 is higher than Series-3. Although, by looking at Figure 8.5, the deflection of Series-2 is lower than Series-3, meaning that higher F_{imp} does not always mean higher deflections. It is instead the impulse I that can be related to the deflections.

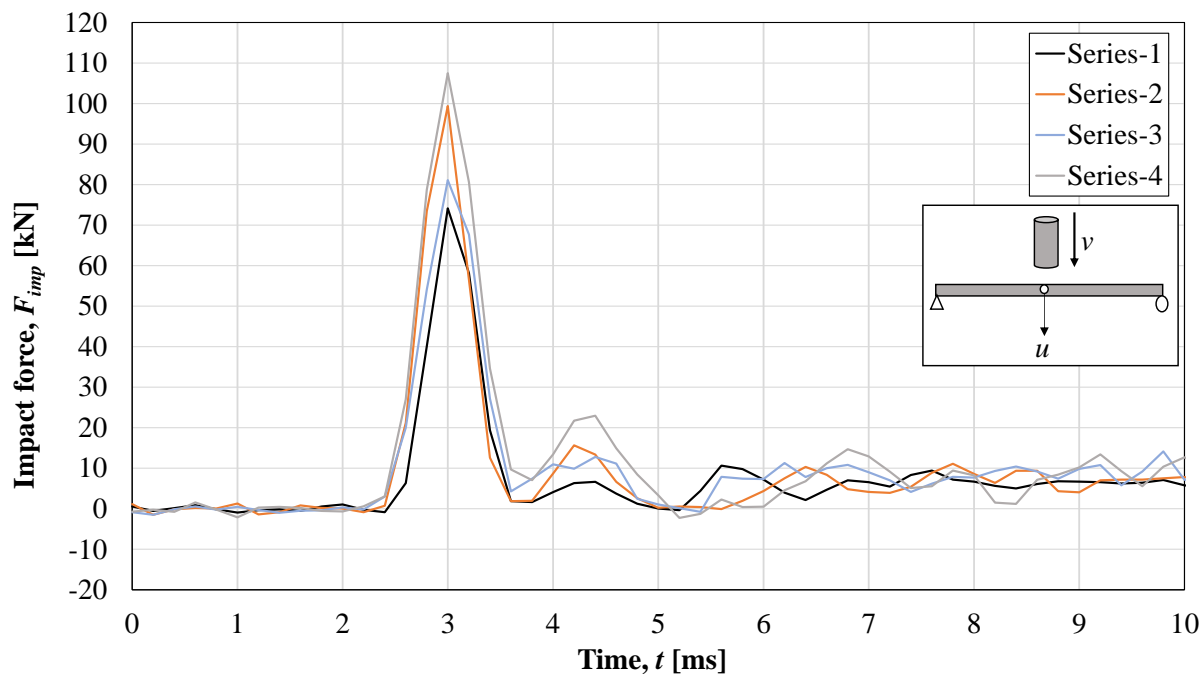


Figure 8.24 Average force over time for all tested series.

8.3.9.7 Comparison of Impulse Load

The average values of the impulse loads for the four series can be seen in Table 8.24. Series-1 and Series-2 has almost the same value of the relation I_{ini}/I_{tot} and the same pattern can be seen for Series-3 and Series-4. This shows that the relation seems to be dependent of the mass and not the drop-height. It was also found that the relation I_{post}/I_{tot} corresponds very well with the relation between the masses that is used for the total kinetic energy in a plastic collision in Equation (4.32), that is

$$E_{k,tot} = \frac{m_1}{m_1 + m_2} E_{k,0} \quad (8.6)$$

With $m_1 = 10$ or 20 kg and $m_2 = m_b \cdot \kappa_m = 8$ kg the relation is 55 % and 71 %, respectively.

Table 8.24 Average values of impulse load.

Name	I_{ini} [Ns]	I_{post} [Ns]	I_{tot} [Ns]	I_{ini}/I_{tot} [%]	I_{post}/I_{tot} [%]
Series-1	39.6	48.5	88.0	45.0	55.0
Series-2	52.9	68.4	121.3	43.6	56.4
Series-3	50.7	118.9	169.6	29.9	70.1
Series-4	67.0	160.9	227.9	29.4	70.6

8.4 Static Testing

8.4.1 Introduction

The purpose of statically loading the beams until failure was to evaluate the residual capacity after the dynamic loading, compared to the undamaged beams. This section presents the results from the static testing in means of load-deflection curves. These curves describes the behaviour of the beam very well and can also be used to calculate rotational capacity, internal work and other interesting parameters. The results presented here is compared to the predicted values in Chapter 10. As mentioned before, the load condition applied in the static tests was four-point bending. It should be noted that the deflection in the graphs are the mean value of the deflection at the two points where the load is applied, this is since the sensor measuring the deflection is placed in the center of the apparatus, see Appendix G. Appendix G also presents the plastic deflection of each beam after the dynamic loading, measured with the method presented there. Photos of the beams after the static test can be seen in Appendix E.

8.4.2 Undamaged Beams

The load-deflection relationship of the undamaged beams can be seen in Figure 8.25, where both beams from batch 1 and 2 are presented. Based on these values Figure 8.26 presents the maximum, minimum and average values of the beams. Based on these two graphs, some important key parameters are calculated and shown in Tables 8.25, 8.26 and 8.27.

First of all, some important notations have to be made from the data of Beam 7. Initially, the load-deflection relationship showed almost a horizontal part for the first 2 mm. This might be because some gravel where stuck between the apparatus and the beam, resulting in very low load during the crushing of this gravel, or that some other mistake was made during the test. Due to this fact, the first 2 mm of the data has been removed to make sure that the results are reasonable. As a result of this, it looks like the unloading process for Beam 7 happens earlier compared to the other beams even tough this is not the case.

Another disturbing fact that was observed when analysing the data from Beam 7 is that the reinforcement ruptured before the third unloading process. This is not a problem itself, since this also happened for Beam 9 as well. The difference in the response of Beam 7 is that a large part of the compression zone fell loose from the beam and got stuck between the two loading bars. This resulted in a new equilibrium where the top reinforcement started to act like tensile reinforcement and the loosened concrete part functioned as a balancing compressive zone. This provided a capacity of 10 kN up to a deflection of 70 mm, where the beam failed. Hence, This data is not representative for the behaviour of the beam and it was therefore decided to remove all the data once the bottom reinforcement ruptured.

All the beams show a very similar behaviour up to the second unloading, except for Beam 16 which shows a somewhat lower capacity. The reason for this is unknown and it can not be coupled to the batch number since Beam 17 and 18 are from the same batch and show a very capacity, even at high deflections. One possible explanation for this behaviour could be that the location of the reinforcement differed compared to the other beams, unfortunately Beam 16 was not one of the beams that were sawn in pieces and got the final reinforcement positions measured, see Section 8.2.4. After the second unloading process, the beams show a slight difference in behaviour. This depends on how the concrete crushing takes place. The part where a graph is vertical represents where the reinforcement is torn off. Beam 16, 17 and 18 show two separate vertical parts, this is due to that the two bars did not rupture at the same time. No clear difference can be seen between the batches and the combined envelope, which is presented in Figure 8.26, will therefore be used when comparing the data with the damaged beams, regardless of which batch it belongs to. It should be noted that the average value in Figure 8.26 is the average value of the six beams, not the average value between the maximum and minimum value.

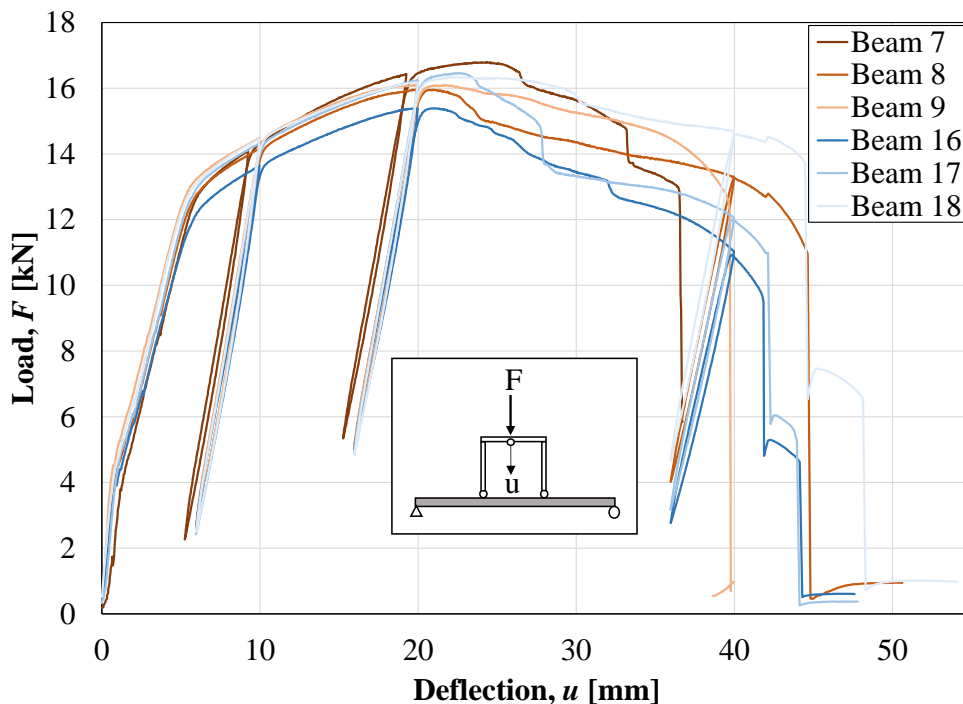


Figure 8.25 Load-deflection relationship for the undamaged beams. Beam 7, 8 and 9 is from batch 1 and beam 16, 17 and 18 is from batch 2.

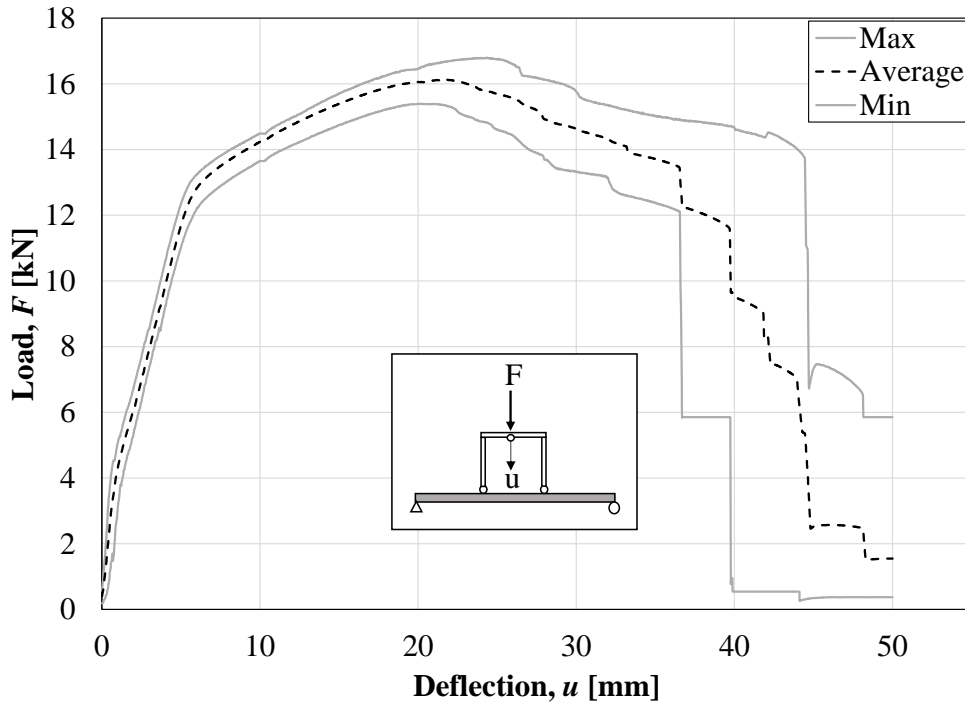


Figure 8.26 Outer envelopes and average values of the load-deflection relationship for the undamaged beams.

Table 8.25 shows the maximum load and deflection for all of the undamaged beams. It is also of interest to investigate how the stiffness of the beam changes at each unloading step. Hence, $k_{II,m}$ represents the stiffness in state II and k_i is the stiffness at unloading and reloading 1, 2 and 3. These four stiffnesses were calculated from the results by dividing the difference in force by the difference in deflection, resulting in the stiffness. The method is schematically shown in Appendix I, where Beam 17 serves as an example. When analysing the results it is a bit confusing that the measured state II stiffness $k_{II,m}$ is lower than the stiffness in the first unloading process. The expected behaviour was that the stiffness's should be approximately the same. One possible cause of this error could be the difficulty of locating exactly where the reinforcements starts to yield, which has been assumed graphically in this case. Another possible source of error is that the initial force is not exactly zero but 0.1-0.2 kN. This was done by purpose to make sure that the loading bars were in contact with the beam before the test began.

Table 8.26 shows a summary of the calculated plastic rotations at different load percents, according to the method described in Section 3.4.2. The capacities are quite similar around 100-95 % but starts to differ a lot at 90 %. This is because the type of failure has a significant impact on the result. When studying Figure 8.25 closer, it can be seen that Beam 17 has a significant loss of strength at $u \approx 28$ mm, which leads to very similar values of $\theta_{pl.90\%}$ and $\theta_{pl.85\%}$. Beam 8, on the other hand, has a small decrease in that part of the diagram, resulting in a large difference between $\theta_{pl.90\%}$ and $\theta_{pl.85\%}$.

Table 8.25 Values of maximum load and deflection together with different stiffness's.

Beam nr	u_{fail} [mm]	$F_{100\%}$ [kN]	$k_{II,m}$ [kN/mm]	k_1 [kN/mm]	k_2 [kN/mm]	k_3 [kN/mm]
7	36.7	16.8	2.15	2.89	2.70	-
8	44.6	16.0	2.25	2.79	2.61	2.34
9	39.7	16.1	2.32	2.90	2.66	-
16	41.8	15.4	1.99	2.68	2.53	2.19
17	42.1	16.5	2.23	2.89	2.75	2.31
18	44.5	16.3	2.23	2.93	2.76	2.52
Average	41.6	16.2	2.20	2.85	2.67	2.34

Table 8.26 Values of plastic rotation at different load levels.

Beam nr	$\theta_{pl.100\%}$ [mrad]	$\theta_{pl.95\%}$ [mrad]	$\theta_{pl.90\%}$ [mrad]	$\theta_{pl.85\%}$ [mrad]	$\theta_{pl.80\%}$ [mrad]
7	47	58	71	76	82
8	37	49	67	91	103
9	42.0	66	85	92	97
16	35	50	59	73	84
17	43	53	60	62	74
18	45	67	95	109	110
Average	42	57	73	84	92

Table 8.27 shows a summary of the internal work at different load levels, calculated according to Appendix J, where Beam 17 serves as an example again. The method to calculate the internal work is described in Section 4.4 as well. The values of the internal work at different load levels can be coupled to the plastic rotation at the same load level, since the calculation procedure is based on the same methodology. For example, Beam 8 and 16 has low values of $\theta_{pl.100\%}$, meaning that they also have low values of $W_{pl.100\%}$. The total internal work is very much dependent on when the beam reaches failure since it represents the total area under the load-deflection diagram. Beam 8 and 18 has the highest values of u_{fail} , leading also to the highest values of W_{tot} .

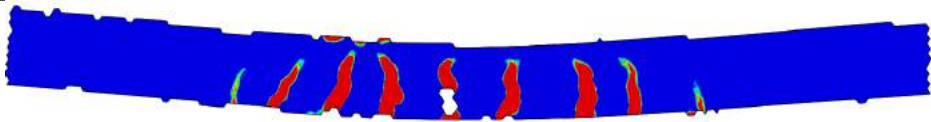
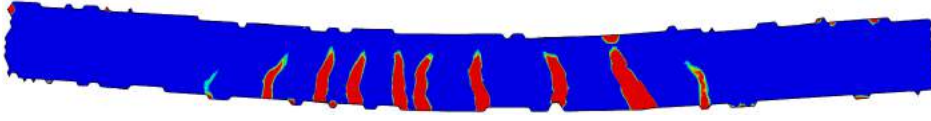
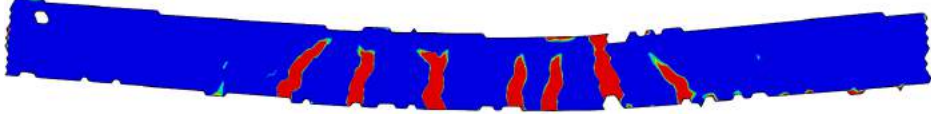
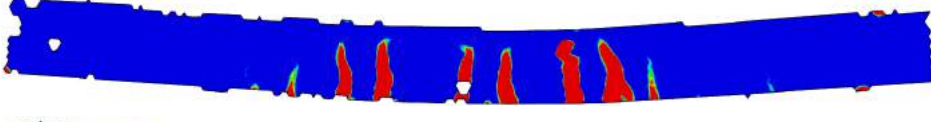
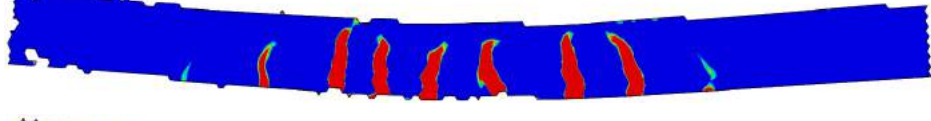
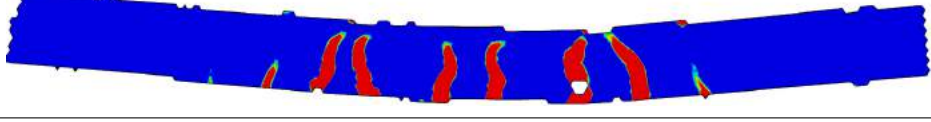
Table 8.27 Values of internal work at different load levels.

Beam nr	W_{tot} [Nm]	$W_{pl.100\%}$ [Nm]	$W_{pl.95\%}$ [Nm]	$W_{pl.90\%}$ [Nm]	$W_{pl.85\%}$ [Nm]	$W_{pl.80\%}$ [Nm]
7	516	263	322	394	419	445
8	613	196	260	353	470	529
9	565	230	359	458	494	515
16	552	179	260	304	369	415
17	584	238	288	328	335	394
18	677	245	372	517	587	594
Average	585	225	310	392	446	482

8.4.3 Strain Fields of Undamaged Beams

Table 8.28 shows the strain fields of the undamaged beams at 95 % of the maximum load, on the descending branch of the load-deflection diagram. At this point, all of the major cracks have appeared. The beams show a similar behaviour and bending cracks in the bottom of the beam are present in all cases. The limits of the colorscale are discussed in Section 8.3.5. The reason why the edges of the beams are not straight is because the DIC had problems finding a clear pattern along the edges. However, this does not affect the result.

Table 8.28 Strain field visualization for the undamaged beams at 95 % of the maximum load.

Deflection / Time	Strain fields of undamaged beams
Beam 7 $u_{95\%} = 28.3 \text{ mm}$ $F_{95\%} = 16.0 \text{ kN}$	
Beam 8 $u_{95\%} = 23.7 \text{ mm}$ $F_{95\%} = 15.2 \text{ kN}$	
Beam 9 $u_{95\%} = 29.4 \text{ mm}$ $F_{95\%} = 15.3 \text{ kN}$	
Beam 16 $u_{95\%} = 24.9 \text{ mm}$ $F_{95\%} = 14.6 \text{ kN}$	
Beam 17 $u_{95\%} = 25.4 \text{ mm}$ $F_{95\%} = 15.6 \text{ kN}$	
Beam 18 $u_{95\%} = 30.5 \text{ mm}$ $F_{95\%} = 15.5 \text{ kN}$	
Principal strain [%]	

8.4.4 Series-1

Beams 4, 5 and 6 were subjected to four drops from a weight of 10 kg from 2.5 m prior to its static loading to failure. The load-deflection curves from the tests can be seen in Figure 8.27. Some key parameters can be seen in Table 8.29 and the internal work can be seen in Table 8.30.

First of all, all the damaged beams are assumed to have already utilized their full capacity as soon as the load capacity reaches 5 kN on the descending branch of the load-deflection diagram. Looking back at Figure 8.25, it can be observed that 5 kN is the lowest load which a beam with only one reinforcement bar left can carry, which in this case is Beam 16. This decision was made to be able to compare the different dynamic test results with each other, since the beams which does not experience rupture of reinforcement carries a low amount of load up to very high deflections. This will be further discussed in Section 8.4.8.

Hence, k_{dam} is the stiffness of the damaged beam, which has been measured in the same way as $k_{I.I.m}$ for the undamaged beams according to Appendix I. One should note that the rotational capacities are not presented for the damaged beams. This is because the methodology described in Section 3.4.2 is not valid since the maximum load for the damaged beams in all the series is lower than $F_{80\%}$ for the undamaged beams. It is therefore of interest to compare the internal work of the damaged beams to the undamaged beams instead. It can be seen as a measurement on how much energy the damaged structure still can absorb before failure. The internal work for the damaged beams were calculated according to Appendix J as well and in this case $W_{100\%}$ corresponds to the internal work at $F_{100\%}$ for the damaged beam.

In Figure 8.27 it can be seen that Beam 4 never reaches a capacity of 5 kN and it is therefore assumed to have utilized its full capacity before the static testing began. No results from Beam 4 will therefore be presented. There is also a big difference between Beam 5 and 6, where Beam 6 shows a significantly larger amount of remaining internal work. Beam 6 experienced crushing of concrete while it is hard to see from the test results which failure mode Beam 5 had. The reason for the big difference observed for beam 4 to 6 is the number of drops and the uncertainties it causes. If there is local crushing of the concrete in the area where the drop-weight hits, the damage will increase rapidly during the next impact. The data presented from Series-1 should therefore be used with care and a larger amount of beams should be tested to see if the result follows any pattern.

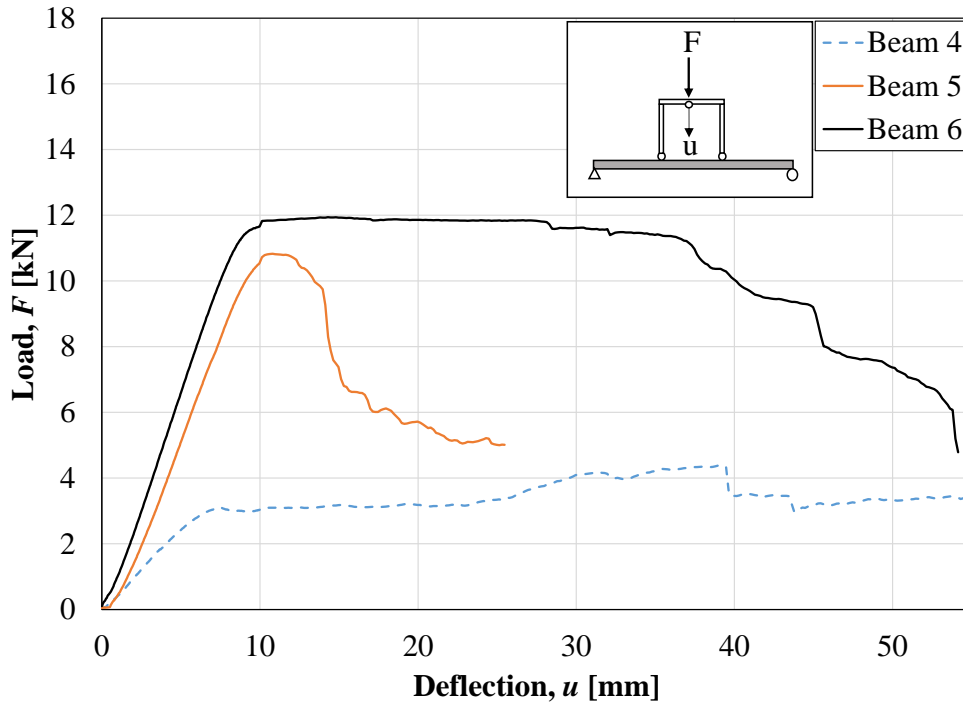


Figure 8.27 Load-deflection relationship for Series-1.

Table 8.29 Summary of key parameters for Series-1

Beam nr	$F_{100\%}$ [kN]	u_{fail} [mm]	k_{dam} [kN/mm]
4	-	-	-
5	10.8	25.5	1.04
6	11.9	54.1	1.31
Average	11.4	39.8	1.18

Table 8.30 Summary of internal work for Series-1.

Beam nr	W_{tot} [Nm]	$W_{pl.100\%}$ [Nm]	$W_{pl.95\%}$ [Nm]	$W_{pl.90\%}$ [Nm]	$W_{pl.85\%}$ [Nm]	$W_{pl.80\%}$ [Nm]
4	-	-	-	-	-	-
5	161	5	31	46	53	60
6	527	63	323	345	370	393
Average	344	34	177	196	212	227

When comparing the damaged beams to the envelope of the undamaged beams, see Figure 8.28, it can be seen that the initial deflection varies a lot and that any pattern between the beams is hard to see. This large variation might be, as mentioned before, because of the uncertainties that numerous drops brings. Beam 5 is failing at lower deflections than the average value of the undamaged beams, while Beam 6 shows a very satisfactory capacity and fails at very high deflections. The initial deflection was

measured in GOM Correlate 2017 right before the static testing began and the method used is described in Appendix F.

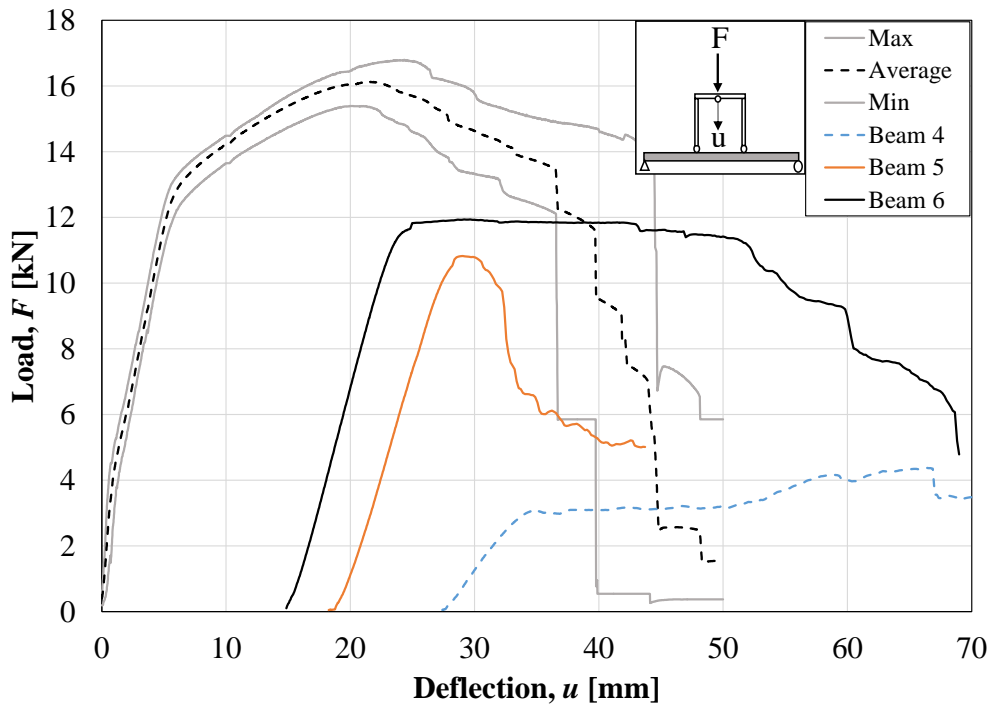


Figure 8.28 Load-deflection relationship for Series-1 together with envelope of undamaged beams.

The average data from the undamaged beams with the average data from Series-1 are presented in Table 8.31, where the proportion of the damaged beams compared to the undamaged beams are presented in percent, i.e the value from the damaged beams is divided by the value from the undamaged beams.

Table 8.31 Comparison of data from undamaged beams and Series-1, average values.

Beam type	F_{max} [kN]	W_{tot} [Nm]	$k_{II,m}$ (k_{dam}) [kN/mm]	k_3 (k_{dam}) [kN/mm]
Undamaged	16.2	585	2.20	2.34
Series-1	11.4	344	(1.18)	(1.18)
Proportion [%]	70	59	54	50

8.4.5 Series-2

Beams 1, 2 and 3 were subjected to two drops from a weight of 10 kg from 5 m. The load-deflection curve can be seen in Figure 8.29 and some key parameters can be seen in Table 8.32 and the internal work can be seen in Table 8.33.

It can be seen that Beam 2 does not reach the required capacity of 5 kN and is therefore not included in the comparison. Otherwise, Beam 1 and 3 shows similar behaviour. Beam 3 experienced rupture of reinforcement while Beam 1 reached failure due to crushing of concrete.

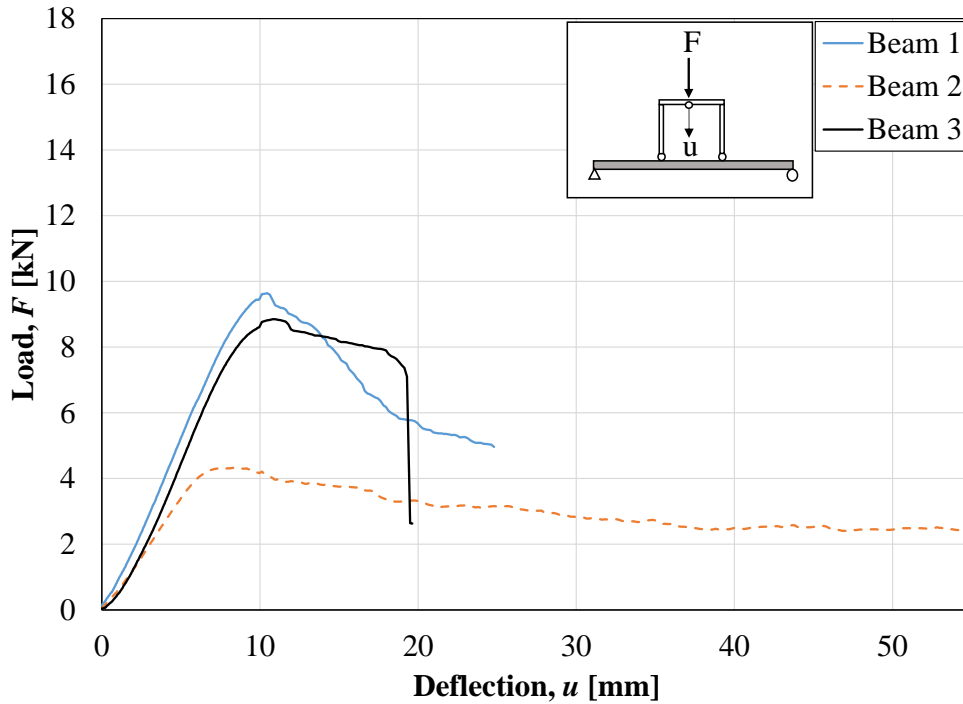


Figure 8.29 Load-deflection relationship for Series-2.

Table 8.32 Summary of key parameters for Series-2.

Beam nr	$F_{100\%}$ [kN]	u_{fail} [mm]	k_{dam} [kN/mm]
1	9.6	24.8	1.03
2	-	-	-
3	8.9	19.6	0.91
Average	9.3	22	0.97

Table 8.33 Summary of internal work for Series-2.

Beam nr	W_{tot} [Nm]	$W_{pl.100\%}$ [Nm]	$W_{pl.95\%}$ [Nm]	$W_{pl.90\%}$ [Nm]	$W_{pl.85\%}$ [Nm]	$W_{pl.80\%}$ [Nm]
1	153	12	23	42	54	65
2	-	-	-	-	-	-
3	122	10	32	70	86	93
Average	138	11	28	56	70	79

When combining the damaged beams to the envelope of the undamaged beams, see Figure 8.30, it can be seen that the initial deflection is similar between the beams and that beam 1 and 3 follows a similar pattern. They are however not carrying any significant amount of load and reaches failure at lower deflections than the average value of the undamaged beams.

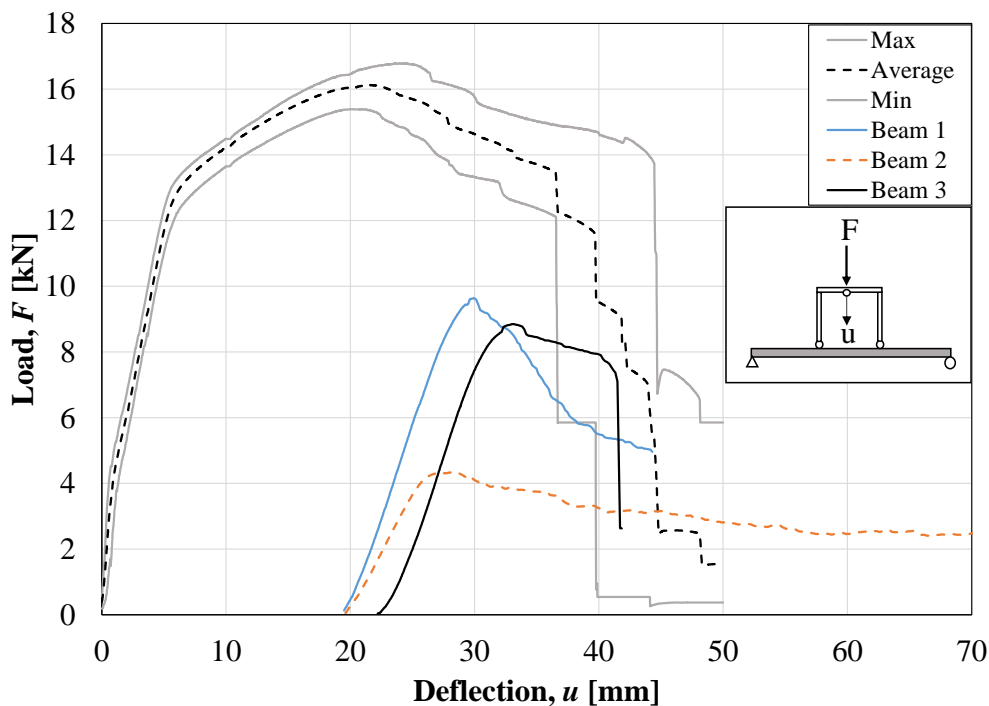


Figure 8.30 Load-deflection relationship for Series-2 together with envelope of undamaged beams.

The average data from the undamaged beams with the average data from Series-2 are presented in Table 8.34, where the proportion of the damaged beams compared to the undamaged beams are presented in percent, i.e the value from the damaged beams is divided by the value from the undamaged beams.

Table 8.34 Comparison of data from undamaged beams and Series-2, average values.

Beam type	F_{max} [kN]	W_{tot} [Nm]	$k_{II,m}$ (k_{dam}) [kn/mm]	k_3 (k_{dam}) [kn/mm]
Undamaged	16.2	585	2.20	2.34
Series-2	9.3	138	(0.97)	(0.97)
Proportion [%]	57	24	44	41

8.4.6 Series-3

Beams 13, 14 and 15 were subjected to two drops from a weight of 20 kg from 2.5 m. The load-deflection curve can be seen in Figure 8.31, some key parameters can be seen in Table 8.35 and the internal work can be seen in Table 8.36.

It can be observed that the beams show a similar behaviour up to their ultimate capacity. Beam 13 and 14 had rupture of reinforcement as failure mode while Beam 15 reached failure due to crushing of concrete. Beam 14 had a significant lower u_{fail} than the other beams and the reason for this is unknown. Due to the early rupture of Beam 14 it has significantly lower W_{tot} than the other beams. Beam 13 has very high $W_{pl.}$ at high percentages since the curve has a very long plateau where the ultimate capacity is utilized.

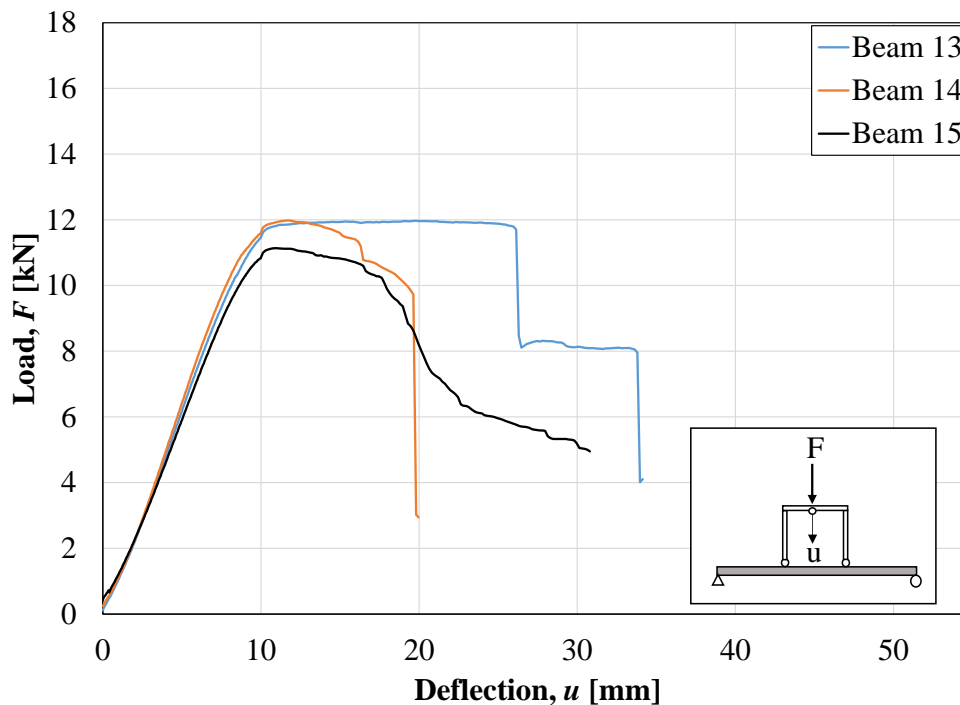


Figure 8.31 Load-deflection relationship for Series-3.

Table 8.35 Summary of key parameters for Series-3.

Beam nr	$F_{100\%}$ [kN]	u_{fail} [mm]	k_{dam} [kN/mm]
13	12.0	33.8	1.23
14	12.0	20.0	1.25
15	11.2	30.8	1.11
Average	11.7	28.2	1.20

Table 8.36 Summary of internal work for Series-3.

Beam nr	W_{tot} [Nm]	$W_{pl.100\%}$ [Nm]	$W_{pl.95\%}$ [Nm]	$W_{pl.90\%}$ [Nm]	$W_{pl.85\%}$ [Nm]	$W_{pl.80\%}$ [Nm]
13	317	121	200	205	211	216
14	173	26	79	89	119	133
15	229	9	74	93	108	118
Average	240	52	118	129	146	156

When comparing the damaged beams to the envelope of the undamaged beams, see figure 8.32, it can be seen that the initial deflection of the beams are very similar. All of the beams are failing at higher deflections compared to the average value of the undamaged beams.

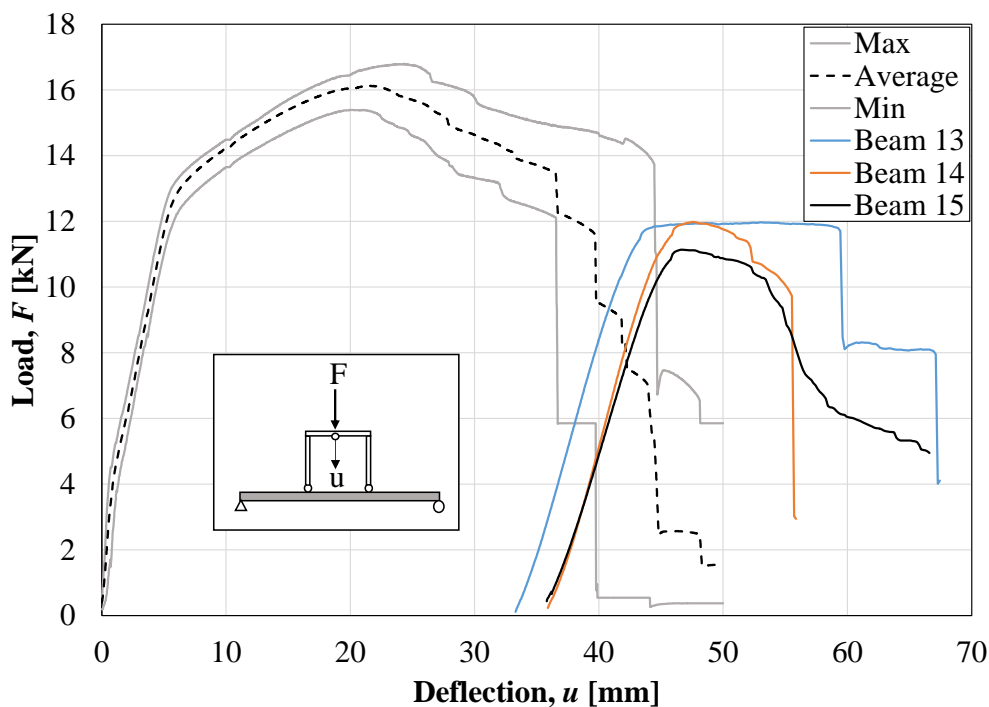


Figure 8.32 Load-deflection relationship for Series-3 together with envelope of undamaged beams.

The average data from the undamaged beams with the average data from Series-3 are presented in

Table 8.37, where the proportion of the damaged beams compared to the undamaged beams are presented in percent, i.e the value from the damaged beams is divided by the value from the undamaged beams.

Table 8.37 Comparison of data from undamaged beams and Series-3, average values.

Beam type	F_{max} [kN]	W_{tot} [Nm]	$k_{II,m}$ (k_{dam}) [kn/mm]	k_3 (k_{dam}) [kn/mm]
Undamaged	16.2	585	2.20	2.34
Series-3	11.7	240	(1.20)	(1.20)
Proportion [%]	72	41	55	51

8.4.7 Series-4

Beams 10, 11 and 12 were subjected to a single drop from a weight of 20 kg from 5 m. The load-deflection curve can be seen in Figure 8.33, some key parameters can be seen in Table 8.38 and the internal work can be seen in Table 8.39.

It can be observed that the beams have a very similar behaviour up to their ultimate capacity, from which Beam 11 differs from the other beams. Beam 10 and 12 has almost a horizontal plateau at the ultimate capacity while Beam 11 has steeper decrease in load capacity with increasing deflection. This is because Beam 11 failed due to crushing of concrete while Beam 10 and 12 failed due to rupture of reinforcement. It can be seen in Table 8.39 that the total internal work is slightly lower for Beam 11 but the internal work at different load levels is much lower, this is also due to the fact that the curve lack a clear load plateau.

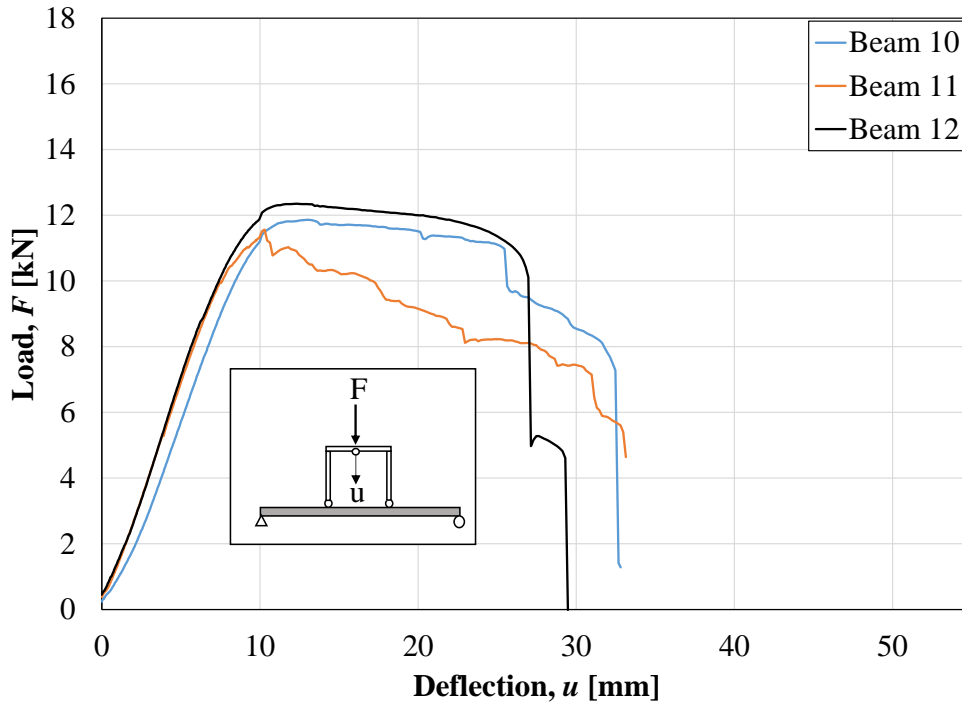


Figure 8.33 Load-deflection relationship for Series-4.

Table 8.38 Summary of key parameters for Series-4.

Beam nr	$F_{100\%}$ [kN]	u_{fail} [mm]	k_{dam} [kN/mm]
10	11.9	32.5	1.12
11	11.6	40.1	1.25
12	12.4	27.1	1.30
Average	12	33.2	1.22

Table 8.39 Summary of internal work for Series-4.

Beam nr	W_{tot} [Nm]	$W_{pl.100\%}$ [Nm]	$W_{pl.95\%}$ [Nm]	$W_{pl.90\%}$ [Nm]	$W_{pl.85\%}$ [Nm]	$W_{pl.80\%}$ [Nm]
10	299	28	147	181	189	207
11	270	13	33	54	100	121
12	282	36	167	205	221	228
Average	284	26	117	147	170	185

When comparing the beams from Series-4 with the envelope of the undamaged beams, see Figure 8.34, it can be seen that the initial deflection is similar for the beams, except for beam 11 which is somewhat lower. All of the beams reaches failure at higher deflections than the average value of the undamaged beams.

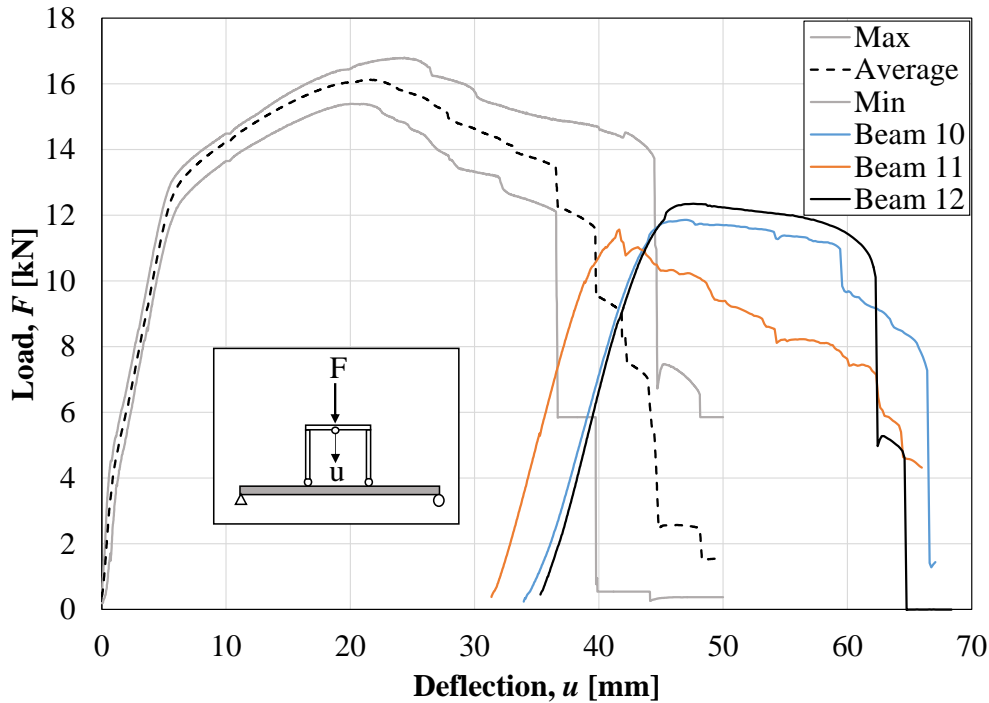


Figure 8.34 Load-deflection relationship for Series-4 together with envelope from undamaged beams.

The average data from the undamaged beams with the average data from Series-4 are presented in Table 8.40, where the proportion of the damaged beams compared to the undamaged beams are presented in percent, i.e the value from the damaged beams is divided by the value from the undamaged beams.

Table 8.40 Comparison of data from undamaged beams and Series-4, average values.

Beam type	F_{max} [kN]	W_{tot} [Nm]	$k_{II,m}$ (k_{dam}) [kn/mm]	k_3 (k_{dam}) [kn/mm]
Undamaged	16.2	585	2.20	2.34
Series-4	12.0	284	(1.22)	(1.22)
Proportion [%]	74	49	55	52

8.4.8 Comparison of Series-1-4

All of the beams from Series-1-4 is presented in Figure 8.35 where it can be seen that the beams show a similar behaviour up to their ultimate capacity. From that point they start to differ a lot. It can also be seen here that the beams with the highest and lowest residual capacity, Beam 6 and 4 respectively, were from Series-1. When looking at the average values for the series, which is presented in Table 8.41, it can be seen that Series-2 show the smallest residual capacity regarding ultimate load and deflection. Series-2 also has the lowest stiffness which indicates that it was severely damaged. Series-4 shows the highest ultimate load capacity as well as the largest ultimate deflection. Both of the beams that did not reach the required capacity of 5 kN were subjected to more than one impact. Based on that and the previous stated

information, a conclusion that numerous drops are undesirable can be made. Observations made during the tests were that the beams subjected to numerous drops were subjected to crushing of concrete in the compressive layer of the beam, which in turn leads to a lower capacity. In some cases, parts of the beam in the tensile zone loosened from the beam and fell to the floor during the last impact, something that affected the capacity as well. These problems is something that the current 2DOF for example does not take into account and the occurrence of it seems to be very random and based on our results, hard to predict.

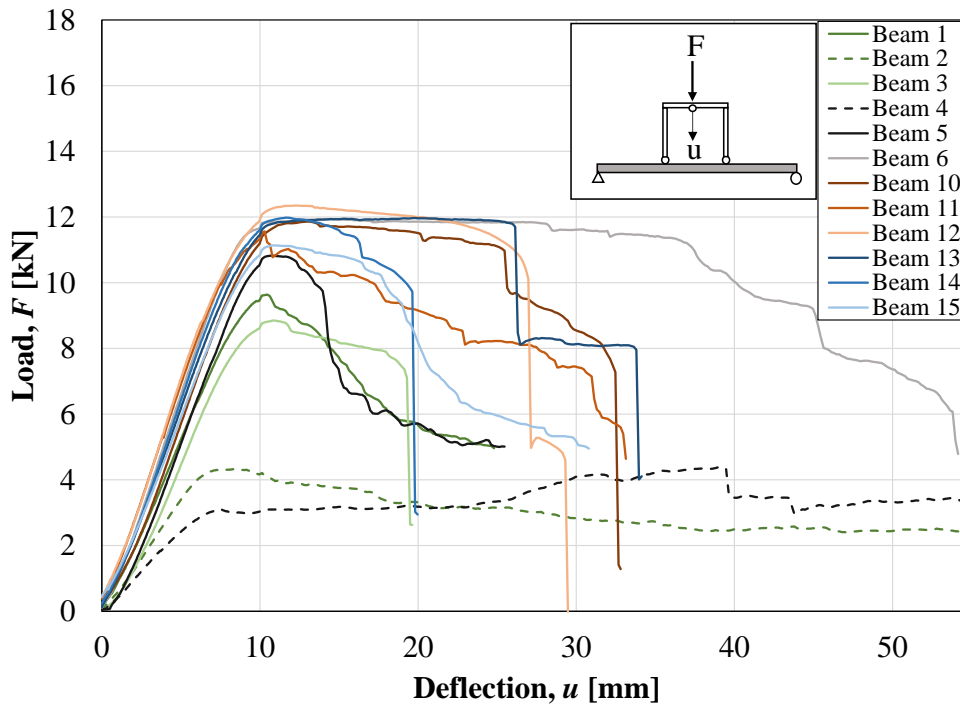


Figure 8.35 Load-deflection relationship for Series-1-4.

Table 8.41 Summary of key parameters for Series-1-4.

Series	$F_{100\%}$ [kN]	u_{fail} [mm]	k_{dam} [kN/mm]
Series-1	11.4	39.8	1.18
Series-2	9.3	22	0.97
Series-3	11.7	28.2	1.20
Series-4	12.0	33.2	1.22

In Figure 8.36 all the damaged beams are presented with its initial deflection, i.e the plastic deformation from the dynamic testing. The beams from Series-1 and Series-2, which are black and green, show a significantly lower initial deflection compared to Series-3 and Series-4, which are blue and orange. This can be coupled to the drop-weight since they were subjected to the same weight. The height of the drop does not seem to affect the results substantially and a conclusion that the weight of the drop-weight is the dominant factor can be made. It can also be seen that even though the beams from Series-3 and -4

had the largest plastic deformations from the dynamic testing, they also had larger residual load capacity compared to Series-1 and -2. The low residual capacity of Series-1 and -2 is the significant crushing of concrete that takes place where the drop-weight hits the beam.

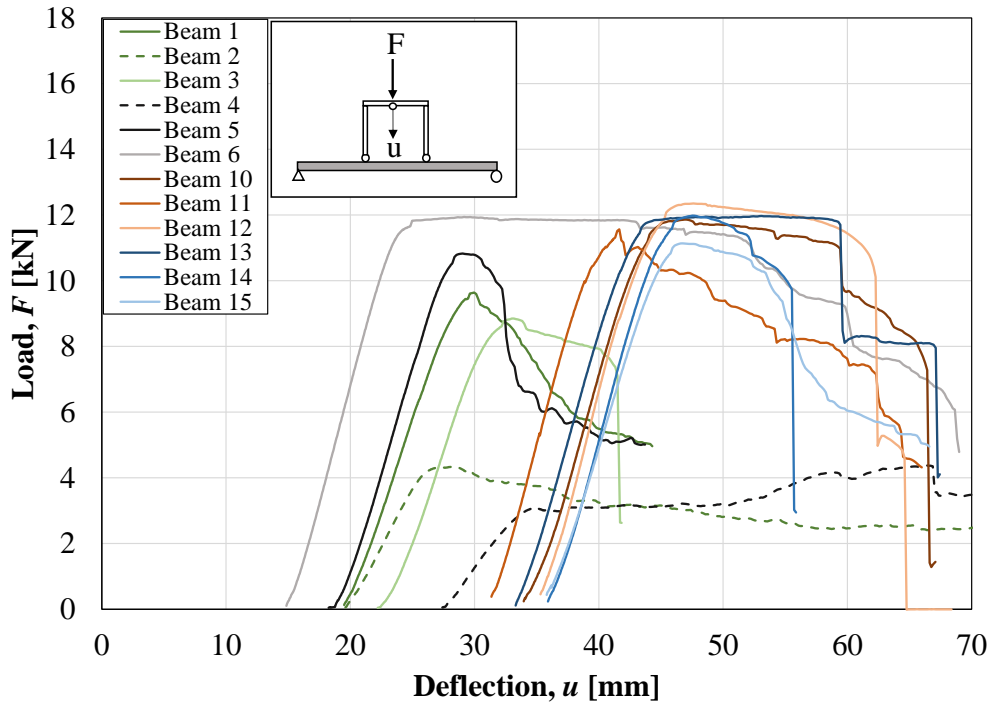


Figure 8.36 Load-deflection relationship for Series-1-4, including initial deflection.

When analysing the internal work performed by the damaged beams it is more difficult to draw any conclusions. The failure mode has a large influence on the internal work and the decision used here to assume that the capacity is utilized as soon as the beams reaches 5 kN on the descending branch, will also affect the result. If all of the data from the beams that experienced crushing of concrete would be used, they would end up with very large total internal work. What can be seen here is that Series-2 has the lowest values of internal work, both total and at different load levels. The results from Series-3 and Series-4 are similar and Series-1 shows the largest values. The uncertainties described before regarding the data from Series-1 should be kept in mind.

Table 8.42 Summary of internal work for Series-1-4.

Series	W_{tot} [Nm]	$W_{pl.100\%}$ [Nm]	$W_{pl.95\%}$ [Nm]	$W_{pl.90\%}$ [Nm]	$W_{pl.85\%}$ [Nm]	$W_{pl.80\%}$ [Nm]
Series-1	344	34	177	196	212	227
Series-2	138	11	28	56	70	79
Series-3	240	52	118	129	146	156
Series-4	284	26	117	147	170	185

Table 8.43 presents a summary the proportions of the damaged beams compared to the undamaged beams, presented in percent. The stiffness of the damaged beams corresponds to roughly half the stiffness's $k_{II,m}$ and k_3 , where Series-2 has some lower values. Series-3 and Series-4 show very similar values for all the parameters while Series-1 and Series-2 differ a lot.

Table 8.43 Comparison of data from undamaged beams and Series-1-4, average values.

Series	F_{max} [%]	W_{tot} [%]	$k_{II,m}$ (k_{dam}) [%]	k_3 (k_{dam}) [%]
Series-1	70	59	54	50
Series-2	57	24	44	41
Series-3	72	41	55	51
Series-4	74	49	55	52

9 Finite Element Modelling in LS-DYNA

9.1 LS-DYNA Theory

9.1.1 Introduction

The software LS-DYNA, developed by the Livermore Software Technology Corporation (LSTC), were also used to predict the results from the tests performed. The model used within this thesis was developed by Munther and Runebrant (2018) and more detailed information about the theory behind the program and the model can be found in that report or in the manuals provided by LSTC, namely (LSTC, 2014). It is hard to model numerous drops on the same beam and therefore only the first drop was modeled with the program. The keyword file (k-file) used can be seen in Appendix M.

9.1.2 Model and Elements

The beam, drop-weight and supports were modelled as solid parts and the supports were locked in both x- y- and z-direction. The drop-weight was located 1 mm above the beam and prescribed with an initial velocity, depending on which load case that was active. The beam is not tied to the supports, meaning that it could move after impact, resulting in a behaviour which is representative to the real conditions. The model can be see in Figure 9.1.

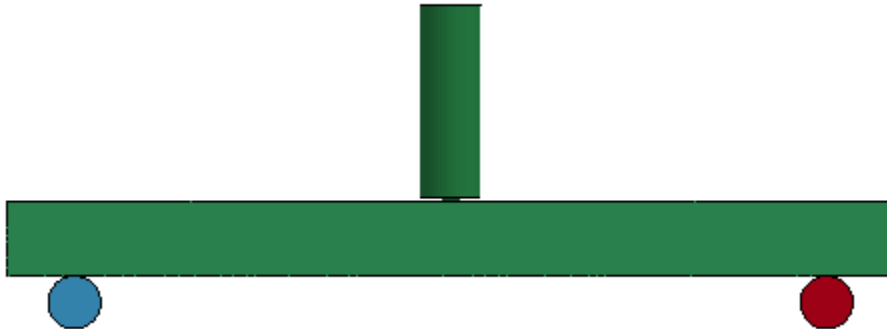


Figure 9.1 LS-DYNA model.

The beam were modelled using solid 4 node tetrahedron elements with one integration point since it was concluded by Lozano and Makdesi (2017) to correspond better to the experimental results, and the drop-weight and the supports are modelled with solid hexahedron elements with constant stress. The reinforcement was modelled as beam elements with one integration point, with bond slip included.

9.1.3 Material Model

9.1.3.1 Concrete

The material model used is called Concrete Damage Plastic Model 2, CDPM2, and was developed by Grassl, *et al.* (2013) as an extension to the first model, CDPM presented by (Grassl and Jirasek, 2006). This model is called 273-CONCRETE_DAMAGE_PLASTIC_MODEL.

The recommendations provided in Grassl (2016) was used when the material parameters were chosen and a summary of the chosen parameters can be seen in Table 9.1, the parameters now shown are set to the default values. This is one of the few changes that was made in the model provided by Munther and Runebrant (2018) since the intention in this project was to use the material properties evaluated from the tests.

The density, Young's modulus, tensile strength and compressive strength were obtained from the test results. Note, though, that the tensile strength was set to the value calculated from the compressive strength, as described in Section 7.1. The material was set to not be strain rate dependent and therefore the value of the hardening parameter was set to 0.01 in accordance with the recommendation of (Grassl, 2016). The eccentricity parameter was calculated as

$$ECC = \frac{1 + \varepsilon}{2 - \varepsilon} \quad (9.1)$$

where

$$\varepsilon = \frac{f_t(f_{bc}^2 - f_c^2)}{f_{bc}(f_c^2 - f_t^2)} \quad (9.2)$$

and

$$f_{bc} = 1.16f_c \quad (9.3)$$

The tensile threshold value is based on the materials fracture energy and tensile strength and in Grassl (2016) it is also recommended for tetrahedral meshes to reduce the value by a factor. The parameter can be calculated as

$$WF = 0.56 \frac{4.444G_F}{f_t} \quad (9.4)$$

since a bilinear damage formulation is used. EFC is a parameter which controls the compressive damage softening branch and has a default value of 0.0001. The model had problems converging when this value was used and these convergence problems occur due to local compressive failure at the point where the drop-weight hits the beam (Grassl, *et al.* 2018). If this problem occur Grassl, *et al.* (2018) gives recommendations of using a ten times larger value, namely 0.001, to make the model converge. This was also observed by Lozano and Makdesi (2017) during their work. This recommendation was applied in the model and no further convergence problems occurred.

Table 9.1 Summary of indata for material model CDPM2 which is material no.273 in LS-DYNA.

Name in LS-DYNA	Description	Value
RO	Density	2384 kg/m ³
E	Young's modulus	32.53 GPa
ECC	Eccentricity parameter	0.5173
FT	Tensile strength	2.821 MPa
FC	Compressive strength	36.83 MPa
HP	Hardening parameter	0.01
WF	Tensile threshold	0.122 mm
STRFLG	Strain rate flag	0
EFC	Softening branch parameter	0.001

9.1.3.2 Reinforcement

The reinforcement used in the model was the multilinear model described in (Munther and Runebrant, 2018). This choice was made to make the model as close to the reality as possible. The real properties of the steel was used.

9.1.3.3 Supports and Drop-weight

The supports and the drop-weight were modelled as linear elastic, which is suitable if the strains are expected to be small (LSTC, 2014). The density of the drop-weight was changed instead of the dimensions when the weight is increased from 10 to 20 kg. This choice was made since it is very time consuming to change the dimensions of the model compared to changing the density and it was concluded that the size of the drop-weight was not an important parameter.

9.1.4 Interaction between Reinforcement and Concrete

To be able to simulate the real behaviour of the beam better, a bond-slip relation between the concrete and reinforcement was included in the model. A simplified approach to model the bond-slip is presented in Munther and Runebrant (2018) and is described by defining the bond τ_b which is dependent on the slip s as

$$\tau_b(s) = \begin{cases} \tau_{max} \left(\frac{s}{s_1} \right)^{0.4} & \text{if } s < s_1 \\ \tau_{max} & \text{if } s \geq s_1 \end{cases} \quad (9.5)$$

where s_1 is the limit from where the bond is assumed to be constant. The value of s_1 can according to CEB-FIP (2012) be assumed as 1 mm and τ_{max} can be calculated as

$$\tau_{max} = 2.5 \sqrt{f_{cm}} \quad (9.6)$$

When the measured value of $f_{cm} = 36.8$ MPa was used, the maximum bond value was determined as $\tau_{max} = 15.2$ MPa.

9.2 LS-DYNA Predictions

9.2.1 Introduction

The results from LS-DYNA are presented within this section. Firstly, the deflection over time at midpoint is presented for all four loading conditions, namely 10 kg or 20 kg drop-weight from 2.5 m and 5.0 m. Secondly, the response of the whole beam was studied by looking at the deflection over length. Lastly, the crack pattern was studied by looking at the maximum principal strain over the first two ms and at the maximum deflection. These results will be compared to the experimental data in Chapter 10.

The intention when performing the analyses was to use the material data gathered during the experiments. But, for some unidentified reason, the analysis of the conditions with a 20 kg drop-weight was terminated after such a short while that the results was unusable. It was found that a solution was to use a lower mean tensile strength f_{ctm} than the measured value, which was 4.7 MPa. Instead a theoretical value, based on the compressive strength, was used. This gave $f_{ctm} = 2.8$ MPa. It was still possible to run the analysis with the 10 kg drop-weight and a comparison between the measured and theoretical values can be seen in Figure 9.2. It is clear that the change in tensile strength does not influence the maximum deflection substantially.

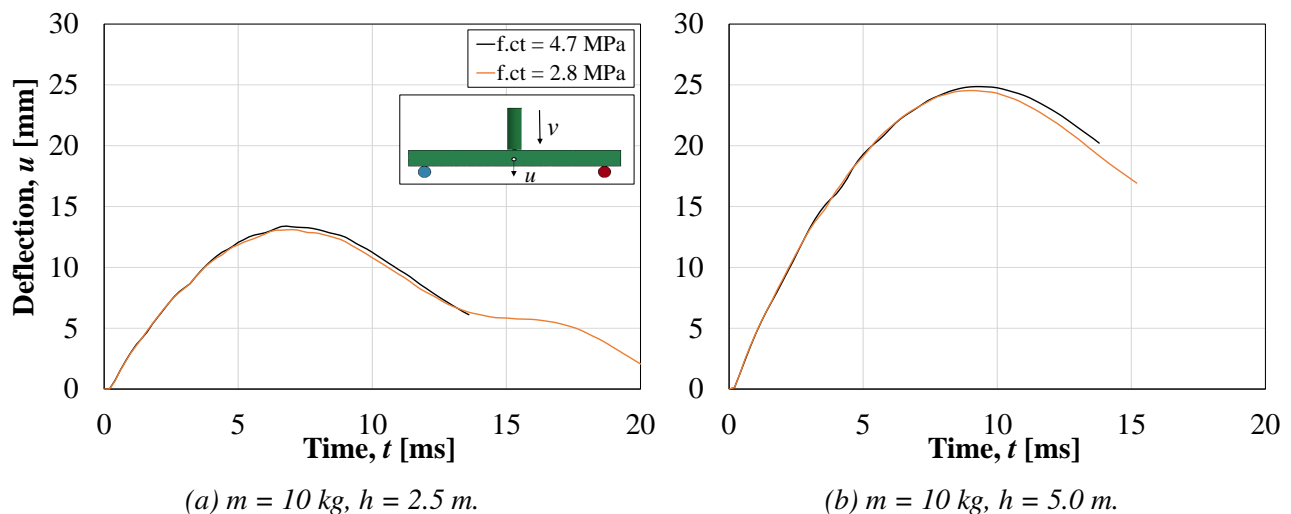


Figure 9.2 Graphs showing the difference in response if $f_{ctm} = 4.7$ MPa (measured value) or $f_{ctm} = 2.8$ (theoretical value) is used in the analysis.

9.2.2 Midpoint Deflection over Time

The predicted deflection-time relation for all four testing conditions can be seen in Figure 9.3. The deflection was extracted by choosing the center most point, both in length and height direction, and plotting the vertical deflection over time. The maximum deflections are summarized in Table 9.2.

Table 9.2 Maximum deflections from LS-DYNA predictions.

Conditions	Maximum deflection, u_{max} [mm]
m = 10 kg, h = 2.5 m	13.1
m = 10 kg, h = 5.0 m	24.5
m = 20 kg, h = 2.5 m	30.0
m = 20 kg, h = 5.0 m	56.9

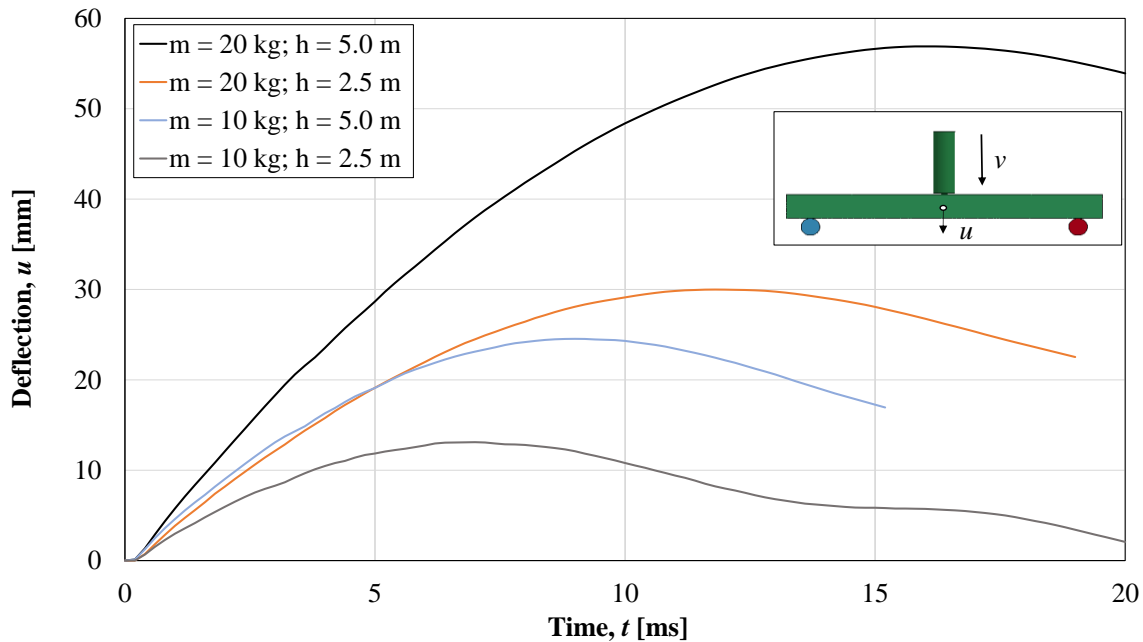


Figure 9.3 Average midpoint deflection for all series in the impact load testing.

9.2.3 Deflection-length Relationship

Another interesting result from the FE-modelling is the deflection over beam length. This was extracted by creating a longitudinal path in the model, from where the z-displacements for all nodes were plotted. This was done for Series-1 and Series-4 and the results can be seen in Figures 9.4 and 9.5.

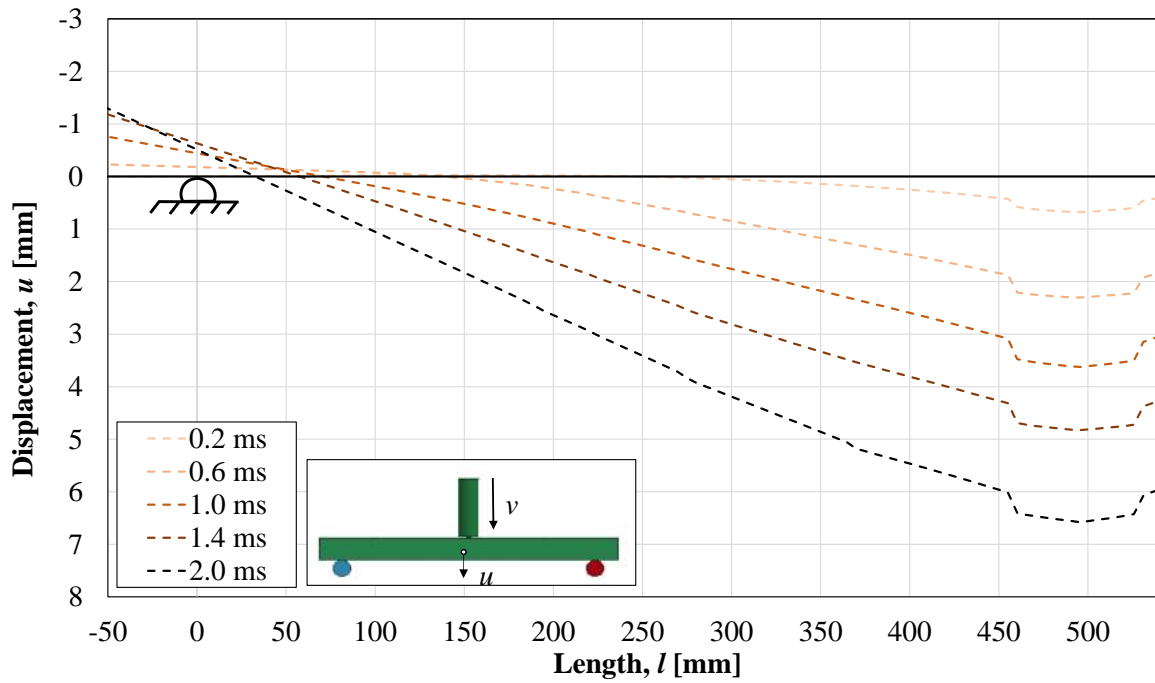


Figure 9.4 Predicted deflection-length relationship for Series-1.

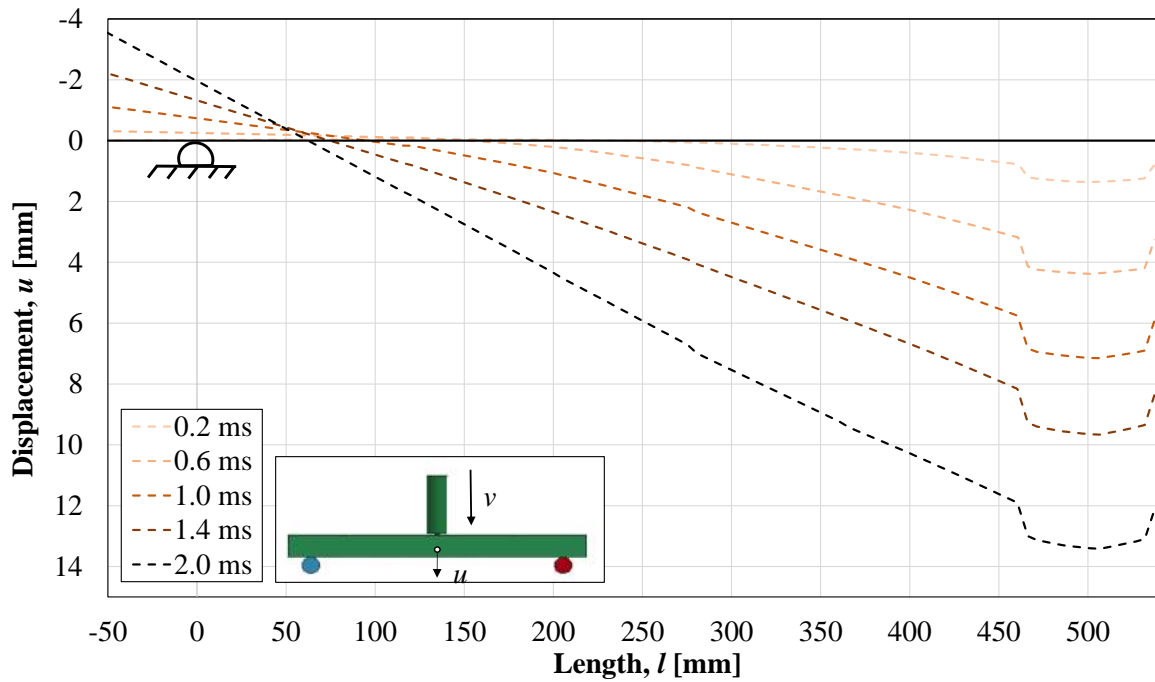


Figure 9.5 Predicted deflection-length relationship for Series-4.

The relative deformed shape at different times is illustrated in Figure 9.6 and 9.7. The values of the deflections in these figures were normalized to the maximum deflection at all studied stages. It can be seen that the beam shows a similar response in both cases.

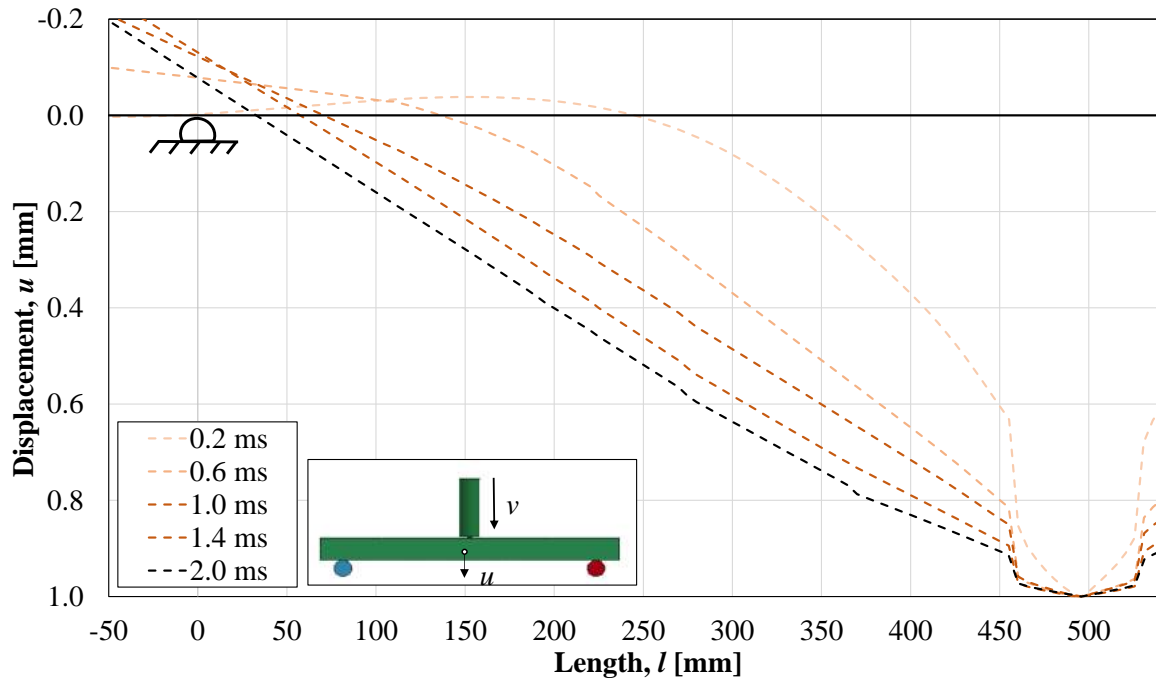


Figure 9.6 Predicted relative deformed shape for Series-1.

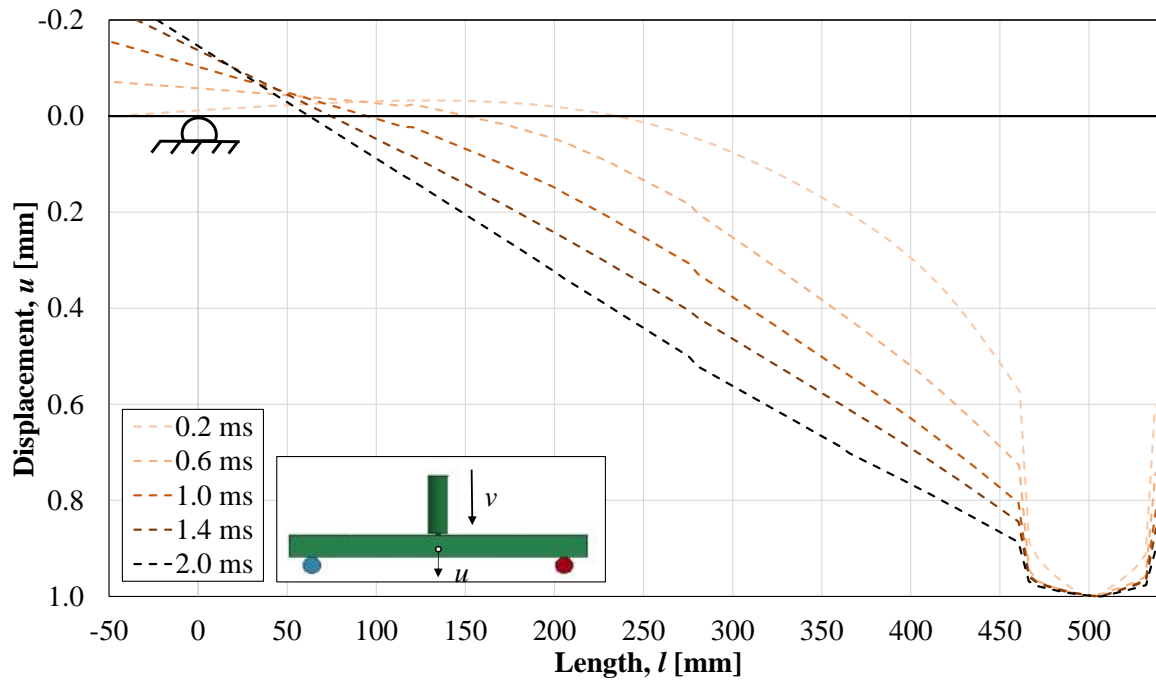


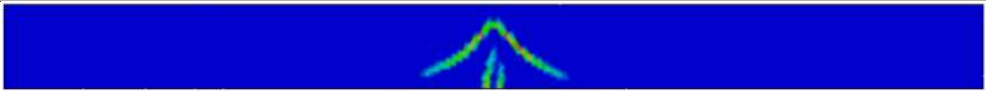
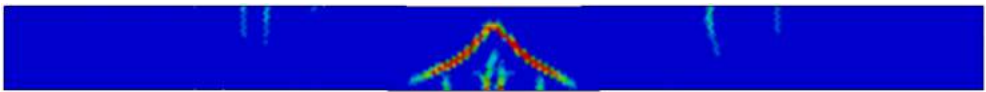
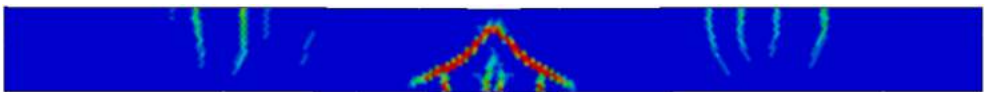
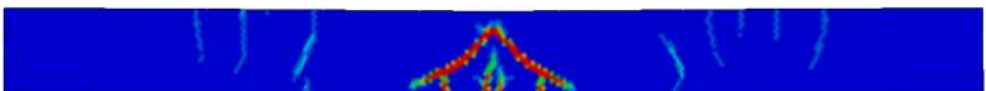
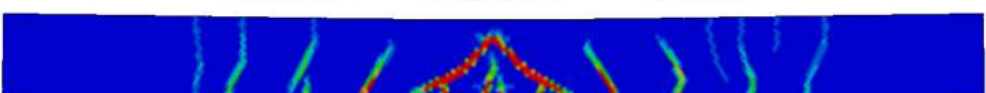
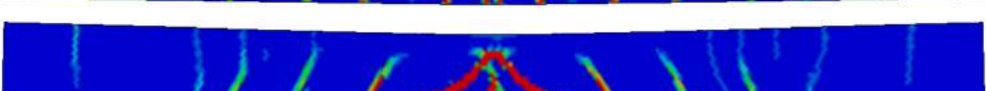
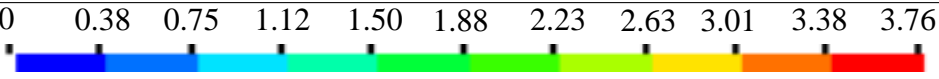
Figure 9.7 Predicted relative deformed shape for Series-4.

9.2.4 Strain Fields

Strain fields for the different load cases can be seen in Table 9.3-9.6. The strains and deflections are shown at the same time-steps as in Section 8.3.5 as well as the strains at maximum deflection. The limits of the colorscale for the principal strain was determined according to the cracking strain calculated as 3.76 % in Lozano and Makdesi (2017), which approximately corresponds to a fully opened crack. The strain concentrations that is visible in the graphs indicates that a crack is formed.

When subjected to a drop from 2.5 m from a 10 kg drop-weight it can be seen that no extensive damage takes place where the weight hits the beam. Both shear cracks and bending cracks are formed from the bottom of the beam as well as small bending cracks in the top of the beam during the impact. A maximum deflection of 13.1 mm is obtained after 7.0 ms.

Table 9.3 Strain field visualization from LS-DYNA for $m = 10$ kg, $h = 2.5$ m conditions.

Deflection / Time	$m = 10$ kg, $h = 2.5$ m
$t = 0.2$ ms $u = 0.7$ mm	
$t = 0.4$ ms $u = 1.5$ mm	
$t = 0.6$ ms $u = 2.3$ mm	
$t = 1.0$ ms $u = 3.6$ mm	
$t = 2.0$ ms $u = 6.5$ mm	
$t = 7.0$ ms $u = 13.1$ mm	
Principal strain [%]	 0 0.38 0.75 1.12 1.50 1.88 2.23 2.63 3.01 3.38 3.76

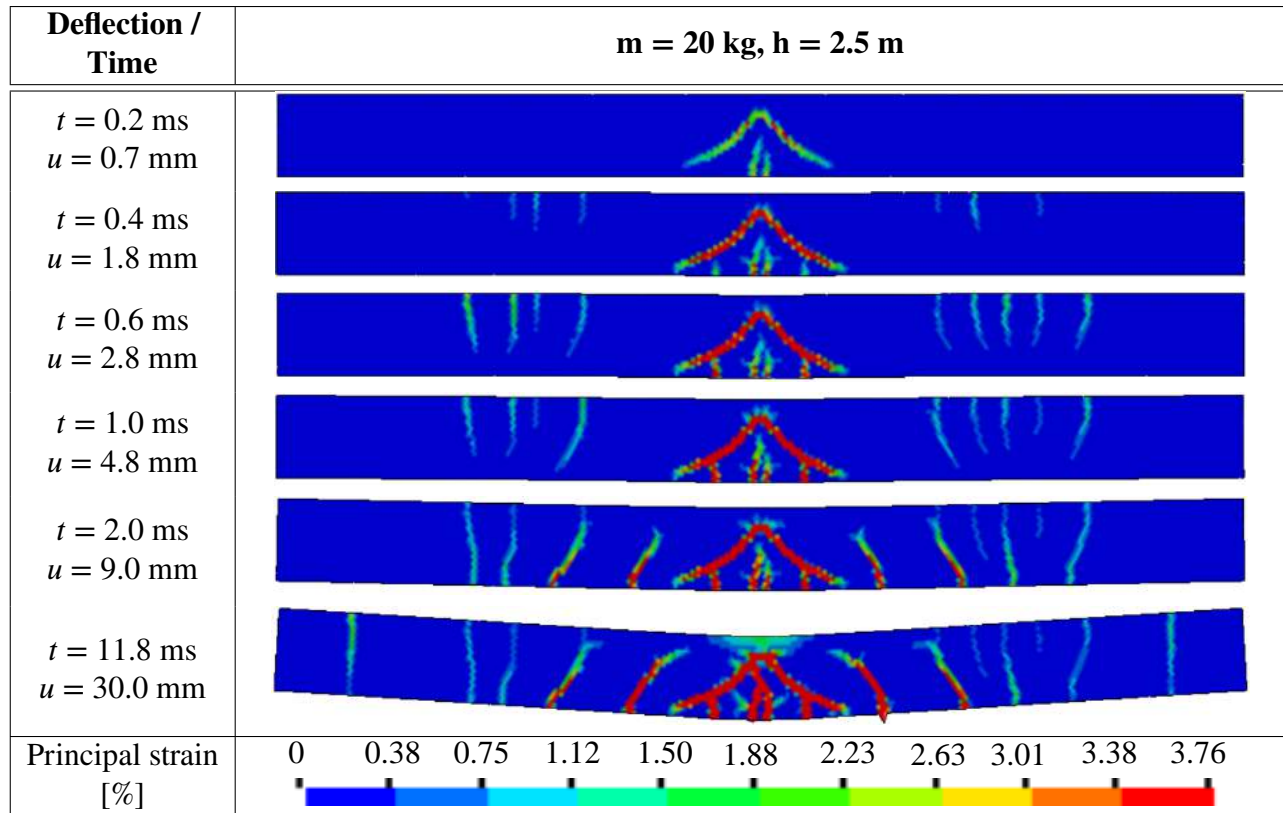
When the beam was subjected to a drop from 5 m from a 10 kg drop-weight it can be seen that the behaviour looks similar as the previous case (10 kg from 2.5 m), with the difference that the cracks is more distinct. Some local damage can also be observed where the drop-weight hits the beam, which means that crushing of concrete is to be expected. A maximum deflection of 24.5 mm is obtained after 9.0 ms, which is almost twice as large as in the first case but happens only 2.0 ms later. By looking at the deflection at different time-steps it can be seen that the displacement increases more rapidly in this case compared to the previous one.

Table 9.4 Strain field visualization from LS-DYNA for $m = 10$ kg, $h = 5.0$ m conditions.

Deflection / Time	$m = 10$ kg, $h = 5.0$ m
$t = 0.2$ ms $u = 1.3$ mm	
$t = 0.4$ ms $u = 2.5$ mm	
$t = 0.6$ ms $u = 3.6$ mm	
$t = 1.0$ ms $u = 5.6$ mm	
$t = 2.0$ ms $u = 9.9$ mm	
$t = 9.0$ ms $u = 24.5$ mm	
Principal strain [%]	0 0.38 0.75 1.12 1.50 1.88 2.23 2.63 3.01 3.38 3.76

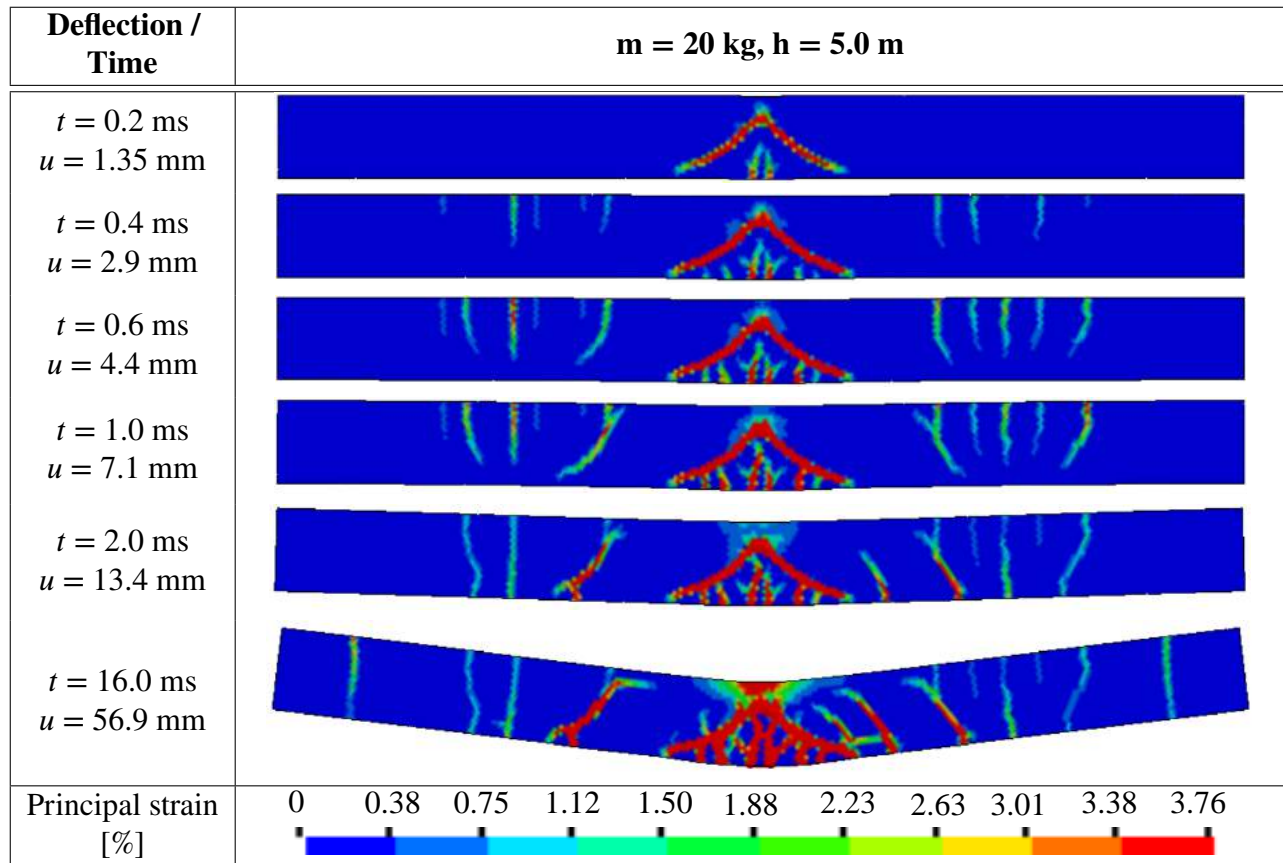
When the beam was subjected to a drop from 2.5 m from a 20 kg drop-weight the crack propagation looks a lot like the previous case (10 kg from 5 m), with the difference that the cracks propagate a bit slower in this case. This can of course be coupled to that the displacement increases more slowly compared to the previous case. The same amount of local damage as in the previous case in the top of the beam can be observed as well. A maximum deflection of 30.0 mm is obtained after 11.8 ms.

Table 9.5 Strain field visualization from LS-DYNA for $m = 20$ kg, $h = 2.5$ m conditions.



When the beam was subjected to a drop from 5 m from a 20 kg drop-weight the cracks are more concentrated to the centre of the beam and the magnitude of them increase. A large number of bending cracks and shear cracks are mixed in the bottom centre of the beam and the cracks propagate faster compared to the other cases as well as the deflection. A large local damage can be observed where the drop-weight hit the beam, which means that crushing of concrete is to be expected. A maximum deflection of 56.9 mm is obtained after 16 ms.

Table 9.6 Strain field visualization from LS-DYNA for $m = 20$ kg, $h = 5.0$ m conditions.



10 Comparison with Experiments

10.1 Introduction

In this section a verification of the predictions made with hand calculations, 2DOF and LS-DYNA are presented. Comments about the difference between the predictions and the results obtained during the experiments can be found within this section. See Chapter 8 for comments concerning deviations in the test results.

10.2 Verification of Load Capacity Predictions

10.2.1 General

Figure 10.1 presents the envelope of the load-deflection relationship for the undamaged beams, together with the predicted relationship obtained from hand calculations. The predicted ultimate load capacity is lower than the one obtained from the tests for both steel strengths, mentioned in Section 7.2. There is however a good correspondence in state I and II where the predicted values only overestimates the real behaviour a little. The reason for the underestimation of the ultimate load capacity is unknown. In the hand calculations both layers of reinforcement are considered which provides an extra 4.6 % to the load capacity, see Section 7.2,. The real position of the reinforcement as well as the real material properties, which is described in Section 8.2, are used in the hand calculations. However, the self-weight of the beam is not included in the calculations, since this effect is assumed to be small enough to be ignored. Both the predicted and the measured load capacities are presented in Table 10.2.

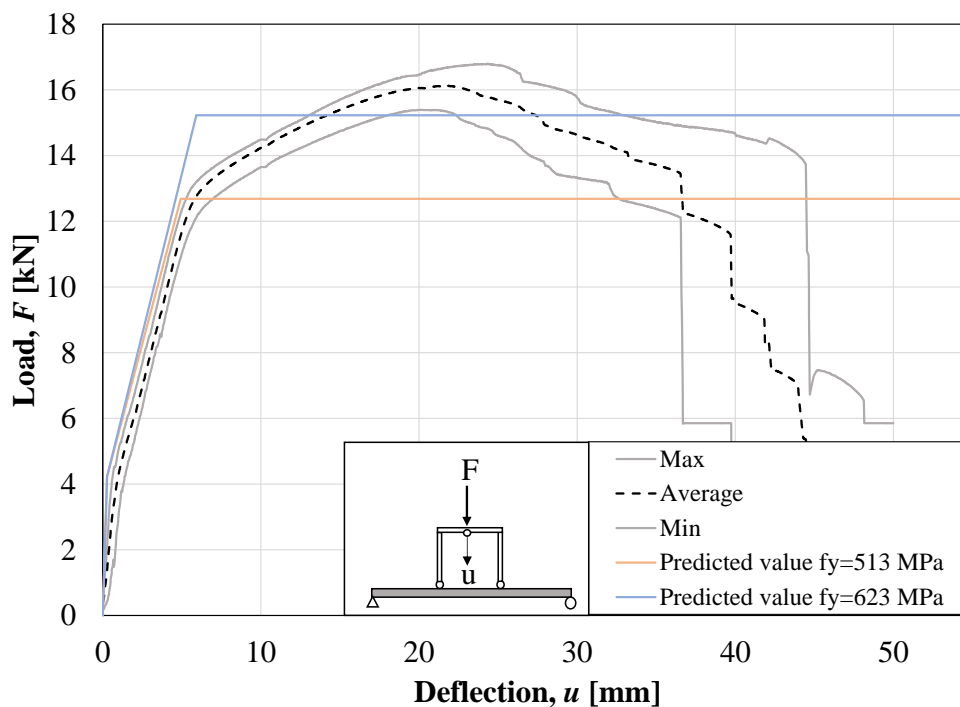


Figure 10.1 Predicted load-deflection relationship for two steel strengths together with envelope for the undamaged beams.

10.2.2 Verification using Internal Work

The internal work, calculated according to Appendix J, can be used to determine an equivalent load that the beams can carry, at different percentages of the ultimate load, and can be expressed as

$$F_{eq.\%} = \frac{W_{pl.\%}}{u_{pl.\%}} \quad (10.1)$$

It can be seen as a measurement on how much of the load the beams can carry after it has reached its ultimate value. In design, the curve is assumed to be horizontal at the ultimate value, see Figure 10.1 where the calculated equivalent load can be seen together with the predicted values and the average envelope from the tests. Table 10.1 shows a summary of the equivalent loads for all the undamaged beams and Table 10.2 shows a comparison with the predicted values and the value obtained from the tests. Figure 10.2 shows the predicted load-deflection relationship together with the mean value of the equivalent load-deflection relationship.

It can be seen that the average equivalent load F_{eq} is 15.0 - 15.5 kN. This is higher than the load capacity $F_u = 15.2$ kN obtained with high steel strength, down to 85 %. By looking at Table 10.2 it is safe to say that it could have been assumed that $u_{pl.85\%}$ can be utilized when designing the beams. It can also be seen that the values of $F_{eq.95\%}$ sometimes is higher than $F_{eq.100\%}$ which means that with regard to internal energy, the beams has a higher load capacity at 95% than at the ultimate load. Beam 16, which showed a lower capacity in general, also shows a lower capacity here.

Table 10.1 Summary of equivalent load $F_{eq.\%}$ based on internal work and plastic deflection.

Beam nr	$F_{eq.100\%}$ [kN]	$F_{eq.95\%}$ [kN]	$F_{eq.90\%}$ [kN]	$F_{eq.85\%}$ [kN]	$F_{eq.80\%}$ [kN]
7	16.0	15.9	15.8	15.8	15.6
8	15.2	15.3	15.1	14.8	14.7
9	15.6	15.6	15.5	15.3	15.2
16	14.6	14.8	14.7	14.5	14.2
17	15.7	15.7	15.6	15.5	15.2
18	15.7	15.8	15.6	15.4	15.4
Average	15.5	15.5	15.4	15.2	15.1

Table 10.2 Average equivalent loads together with predicted values and test results.

$F_{eq.100\%}$ [kN]	$F_{eq.95\%}$ [kN]	$F_{eq.90\%}$ [kN]	$F_{eq.85\%}$ [kN]	$F_{eq.80\%}$ [kN]	F_u fy = 513 MPa [kN]	F_u fy = 623 MPa [kN]	$F_{100\%}$ from test [kN]
15.5	15.5	15.4	15.2	15.1	12.7	15.2	16.2

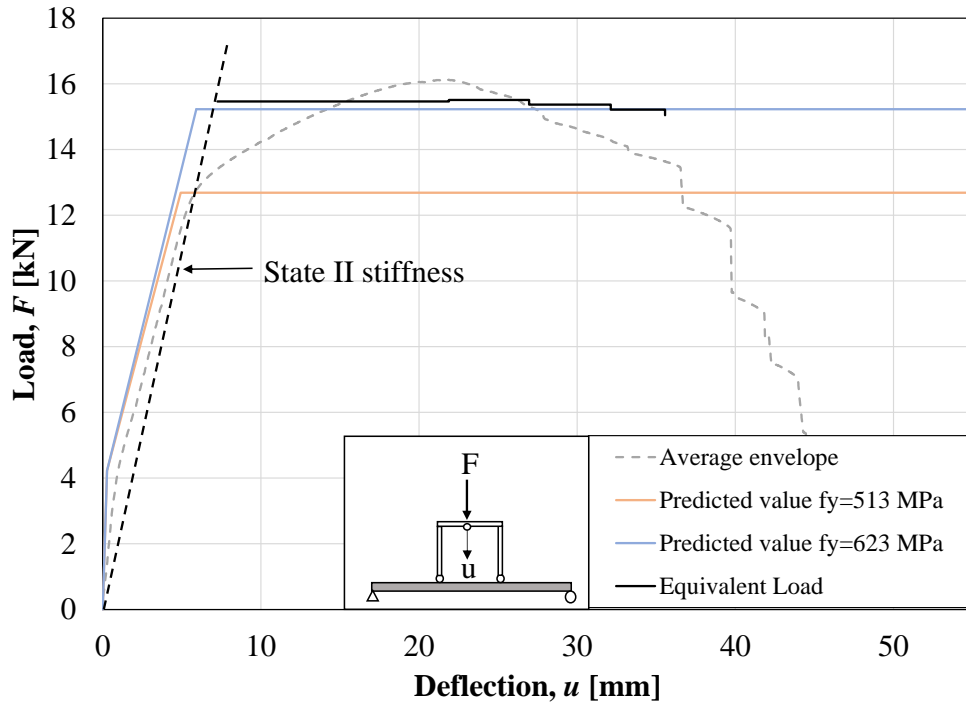


Figure 10.2 Equivalent load-deflection relationship together with predicted relationship and envelope.

10.3 Verification of Rotational Capacity Predictions

Figure 10.3 presents the calculated plastic rotation capacity for all the methods described in Section 3.4, together with the calculated values for the undamaged beams, for different percentages of the ultimate load. As mentioned in Section 3.4, the method from Betonghandboken (ABC-method) and Tamminen should correspond to $\theta_{pl,95\%}$ while the other methods should correspond to $\theta_{pl,100\%}$.

It can be seen that all of the methods except Bk25 and Tamminen underestimates the plastic rotation capacity significantly. The reason for this underestimation could be the loading condition which was four-point loading. In the experiments made by Lozano and Makdesi (2017), which used a similar beam with the only difference that three-point loading were used instead, the rotational capacity $\theta_{pl,100\%}$ were calculated to be 22 mrad. This would correspond much better to the calculated capacities from the rest of the methods. However, it is difficult to describe why the methods presented in Arbulu (2006) gives the results they do since the information provided there is sparse, but the fact that 22 mrad is closer to the values obtained indicates that these methods works well for three-point loaded structures.

The method provided by Bk25 generates a result between $\theta_{pl,90\%}$ and $\theta_{pl,95\%}$. The reason why this method provides a more reasonable result could be that it is developed to work on impulse loaded structures, which in this case is an air-blast, resulting in a uniformly distributed load. Four-point loading is somewhere between three-point loading and a uniformly distributed load. The method provided by Tamminen generates a result equivalent with $\theta_{pl,95\%}$. The difference between this method and Betonghandboken is that Tamminen takes the height of the member into account. If the size of the member is the factor that makes almost all of the methods underestimate the capacity remains untold and further investigations should be made, which is not in the scope of this report.

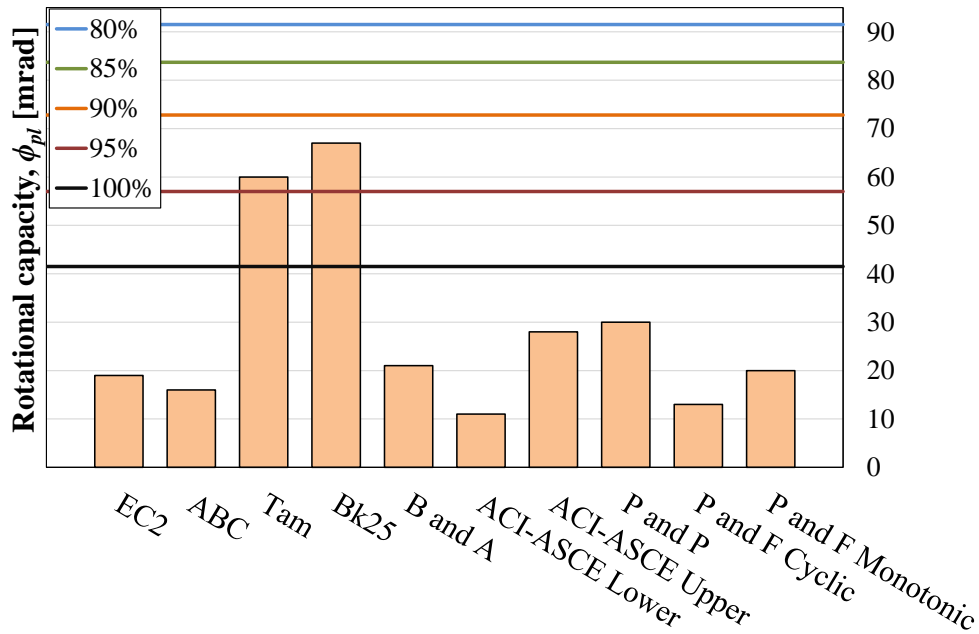


Figure 10.3 Predicted plastic rotation capacity together with the capacity obtained from test results.

10.4 Verification of Stiffness Predictions

Table 10.3 presents the average values of the stiffness's measured from the static testing of the undamaged beams, which are described in Section 8.4.2, together with the predicted state II stiffness k_{II} from Section 7.2.3. $k_{II,m}$ is the stiffness during the first loading, up to where the reinforcement starts to yield and k_i is the stiffness's during the different unloading processes. As mentioned in Section 8.4.2 it is strange that $k_{II,m}$ is lower than the stiffness k_i . If that possible error is neglected it can be seen that k_{II} corresponds to a value between k_2 and k_3 , meaning that the predicted stiffness is somewhat underestimating the real stiffness of the beam. A possible reason for this could be that the calculated E_c is not completely correct.

Table 10.3 Summary of the measured stiffness's from the undamaged beams together with the calculated stiffness in state II.

k_{II} [kN/mm]	$k_{II,m}$ [kN/mm]	k_1 [kN/mm]	k_2 [kN/mm]	k_3 [kN/mm]
2.46	2.20	2.85	2.67	2.34

10.5 Verification of 2DOF Predictions

10.5.1 Deflections

In Figure 10.4 and 10.5 the predicted deflection-time response, for the first drop, of the 2DOF model is compared with the beam response obtained in the experiments. It can be seen that the 2DOF model overestimates the deflection for all cases since the resisting force used in the 2DOF model is conservatively low.

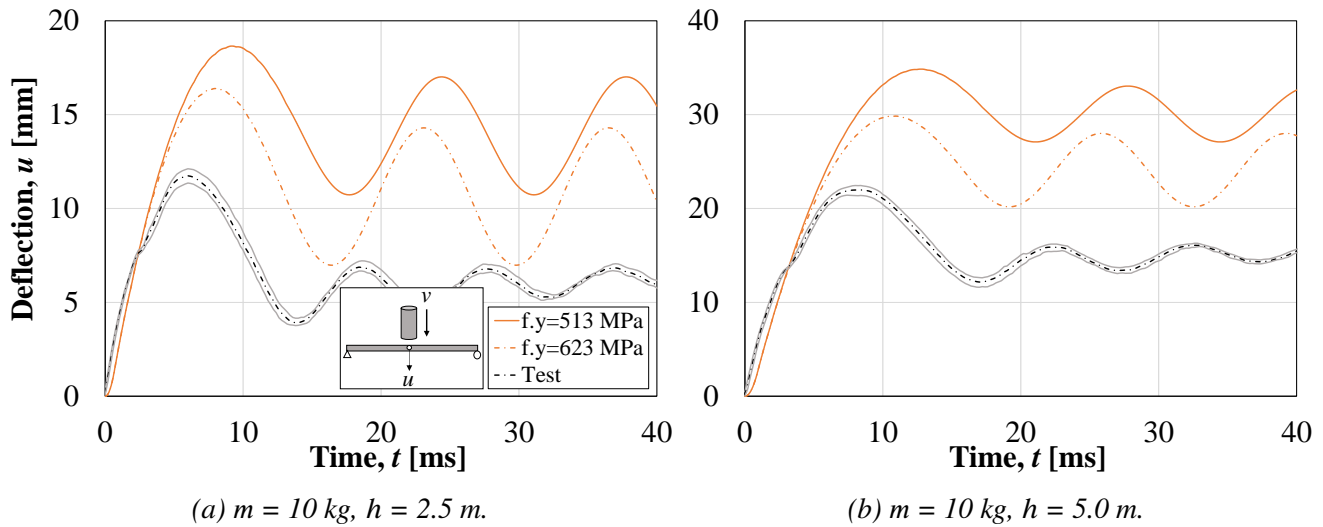


Figure 10.4 Comparison of midpoint deflection over time for 2DOF model and experimental results.

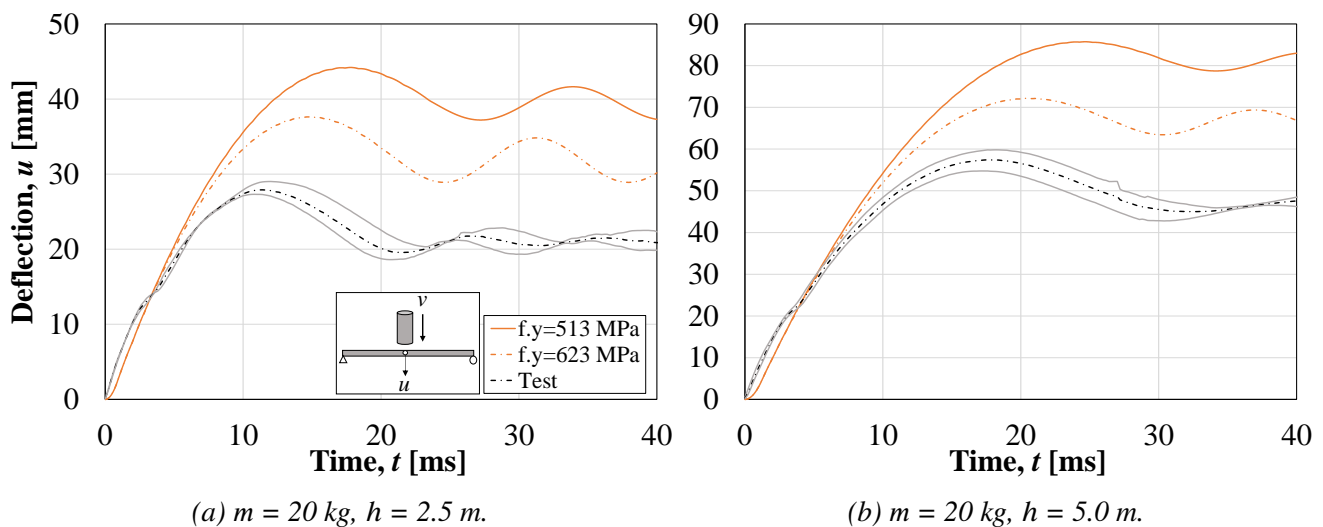


Figure 10.5 Comparison of midpoint deflection over time for 2DOF model and experimental results.

The predicted maximum and plastic deflections for the first drop are compared to the values obtained from the tests in Table 10.4 and Table 10.5. Further, in Table 10.6 the total plastic deflection after several drops is presented. It can be seen that the 2DOF model overestimates the plastic deflection a lot, both after the first drop and after all of the drops. One of the reasons behind this is that the underestimated load capacity in Section 10.2.1 results in an underestimation of the resistance as well, therefore a higher deflection is expected from the 2DOF model. Another reason is that the 2DOF model does not take the influence of high strain rate into account, which would increase the stiffness and strength of the concrete and reinforcement, this is discussed in Section 2.4. Hence, the influence of strain rate would therefore result in a smaller deflection in the 2DOF model.

It can be seen that the predictions are a bit more accurate regarding the total plastic deflection. The reason behind this is that the 2DOF model assumes that the beam have the same stiffness after each drop.

In reality, though, the beams experience a loss of stiffness when the compressive zone is damaged during impact. This means that after each drop, the stiffness of the beams gets closer to the value assumed in the 2DOF model.

Table 10.4 Comparison of plastic deflection after the first drop from 2DOF and experimental results.

Series	Steel strength f_y [MPa]	Plastic def (2DOF) $u_{2DOF.pl}$ [mm]	Measured plastic def u_{pl} [mm]	$u_{pl}/u_{2DOF.pl}$ %
1	513	14.1	5.4	38
	623	11.0		49
2	513	30.3	14.2	47
	623	24.4		58
3	513	39.7	20.7	52
	623	32.2		64
4	513	81.1	44.6	55
	623	66.7		67

Table 10.5 Comparison of maximum deflection after the first drop from 2DOF and experimental results.

Series	Steel strength f_y [MPa]	Max. def (2DOF) $u_{2DOF.max}$ [mm]	Measured max. def u_{max} [mm]	$u_{max}/u_{2DOF.max}$ %
1	513	18.4	11.7	64
	623	16.1		73
2	513	34.6	22.0	64
	623	29.5		75
3	513	43.9	27.9	64
	623	37.3		75
4	513	85.4	57.4	67
	623	71.8		80

Table 10.6 Comparison of total plastic deflection from 2DOF and experimental results.

Series	Steel strength f_y [MPa]	Total plastic def (2DOF) $u_{2DOF.pl}$ [mm]	Total measured def u_{pl} [mm]	$u_{pl}/u_{2DOF.pl}$ %
1	513	56.4	26.9	48
	623	44.0		61
2	513	60.6	30.1	50
	623	48.8		62
3	513	79.4	44.8	56
	623	64.4		70
4	513	81.1	44.6	55
	623	66.7		67

10.5.2 Impulse

The predicted impulses and the impulses from the experiments are compared in Table 10.7. It is the peak value of the impulse I_{ini} , see Appendix H, that is used for this comparison. It can be seen that the impulses is overestimated with the 2DOF model but the relation between the impulses are well in agreement. The relation is described by dividing the impulse from 2.5 m with the impulse from 5.0 m for the same drop-weight, namely Series-1 with Series-2 and Series-3 with Series-4.

Table 10.7 Comparison of predicted impulses and the experimental results.

Series,	Impulse 2DOF, I_k [Ns]	Impulse DIC, I_{ini} [Ns]	Relation 2DOF, $I_{k,2.5}/I_{k,5.0}$ [-]	Relation DIC, $I_{ini,2.5}/I_{ini,5.0}$ [-]
1	63.1	39.6	-	-
2	89.1	52.9	0.71	0.75
3	89.1	50.7	-	-
4	126.1	67.0	0.71	0.76

10.6 LS-DYNA

10.6.1 Midpoint Deflection over Time

The midpoint deflection over time for the different loading conditions are compared in Figure 10.6 and 10.7. Note the difference of axis values in the figures. The LS-DYNA models were interrupted at various times. At most, for Series-1, it worked during the first 20 ms. However, the model worked through the maximum value at each condition, and was hence deemed to be satisfactory. It appears that both the 2DOF and LS-DYNA model somewhat overestimates the maximum deflection of Series-1, Series-2 and Series-3. For Series-4, that is $m = 20$ kg and $h = 5.0$ m, the LS-DYNA predicts a behaviour close to the experimental results. Even though, it seems that the post peak behaviour differs where the LS-DYNA curve returns in a slightly steeper slope.

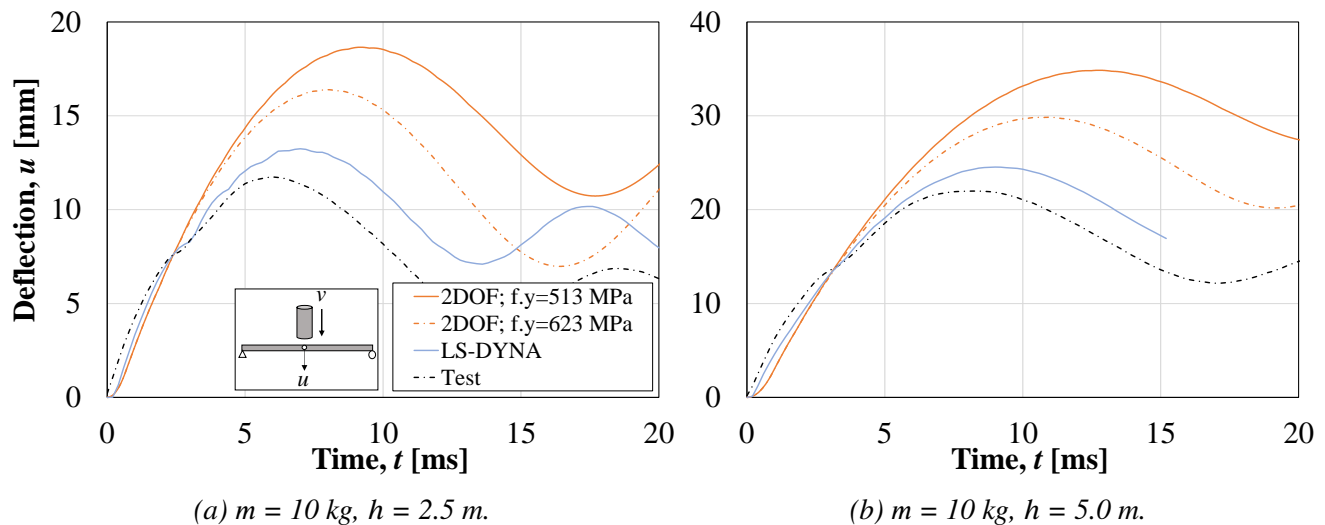


Figure 10.6 Comparison of midpoint deflection over time for 2DOF model, LS-DYNA and experimental results.

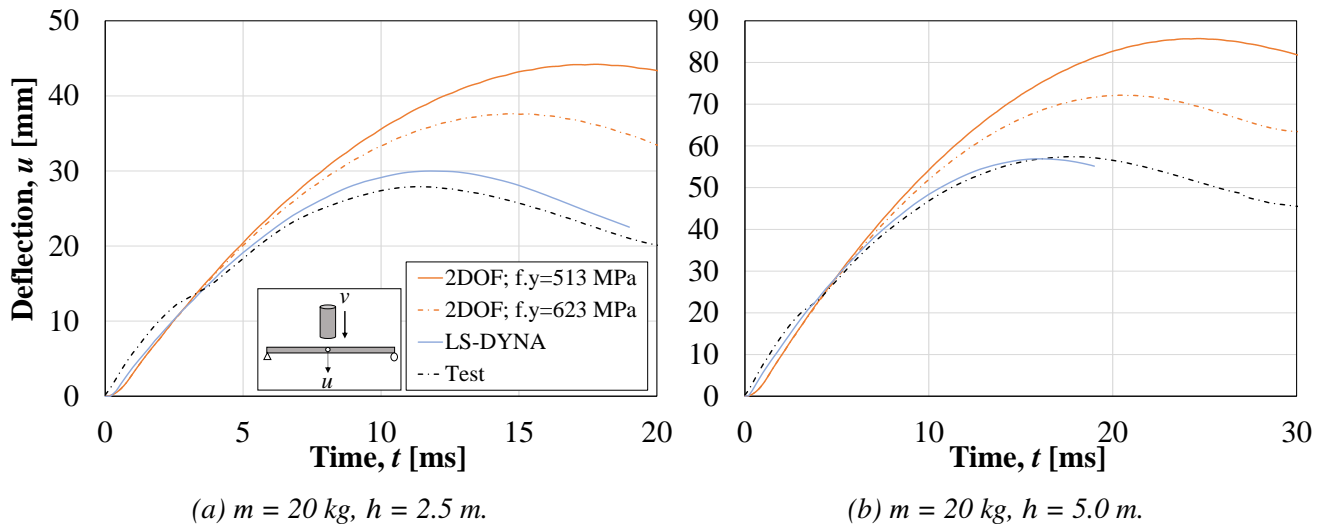


Figure 10.7 Comparison of midpoint deflection over time for 2DOF model, LS-DYNA and experimental results.

10.6.2 Deflection-length Relationship

A comparison of the beam response in LS-DYNA and from the experiments can be seen in Figure 10.8 and Figure 10.9, for Series-1 and Series-4 respectively. Beam 4 represents Series-1 and Beam 12 represents Series-4. The figures show the deflection over length at five time steps during the first 2 ms and the overall resemblance is accurate. Although, the modelled beam has a local deflection in the impact zone that does not occur in Beam 4 but can be detected to some extent in Beam 12. This local deflection is due to the shear cracks that appear, addressed further in Section 10.6.3. It is also worth mentioning the fact that the impact does not occur exactly at the time when the high-speed camera takes a photo. In other words, the time step between the first and second photo is not with certainty 0.2 ms with the consequence that the beam from the experiment shows a slower response.

The relative deformed shape, where the values of the deflections has been normalized to the maximum deflection at all studied stages, can be seen in Figure 10.10 and 10.11. The results show an overall good correspondence but the result is more accurately predicted in Series-4.

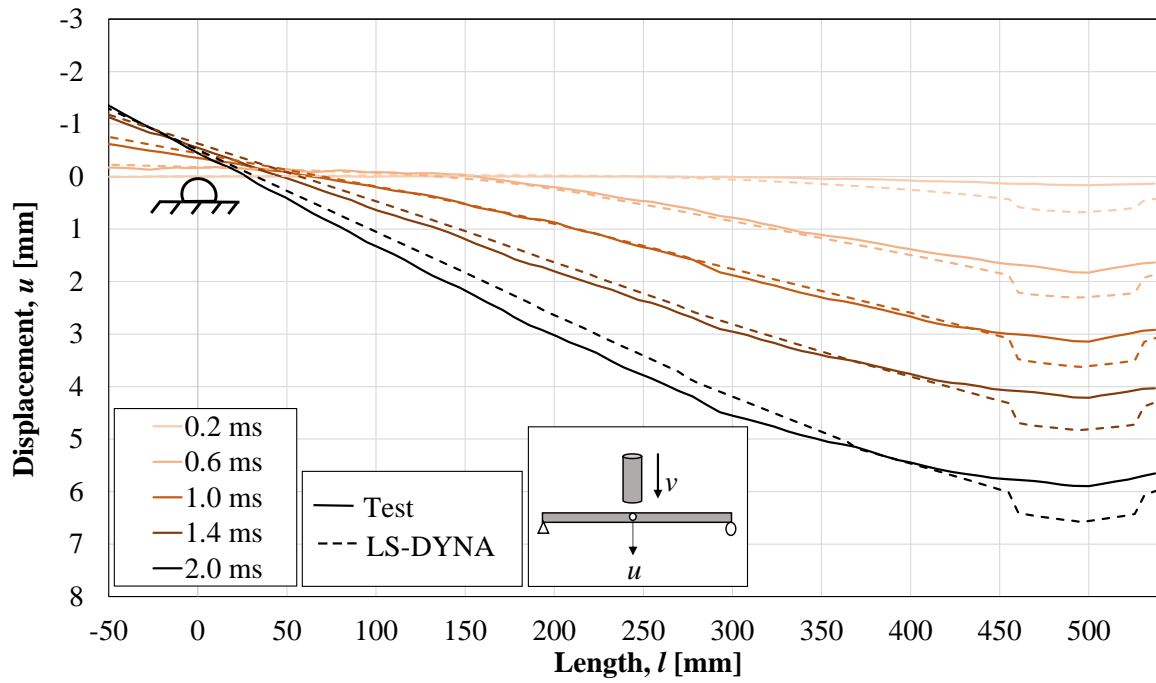


Figure 10.8 Comparison of deflection-length relationship for Series-1.

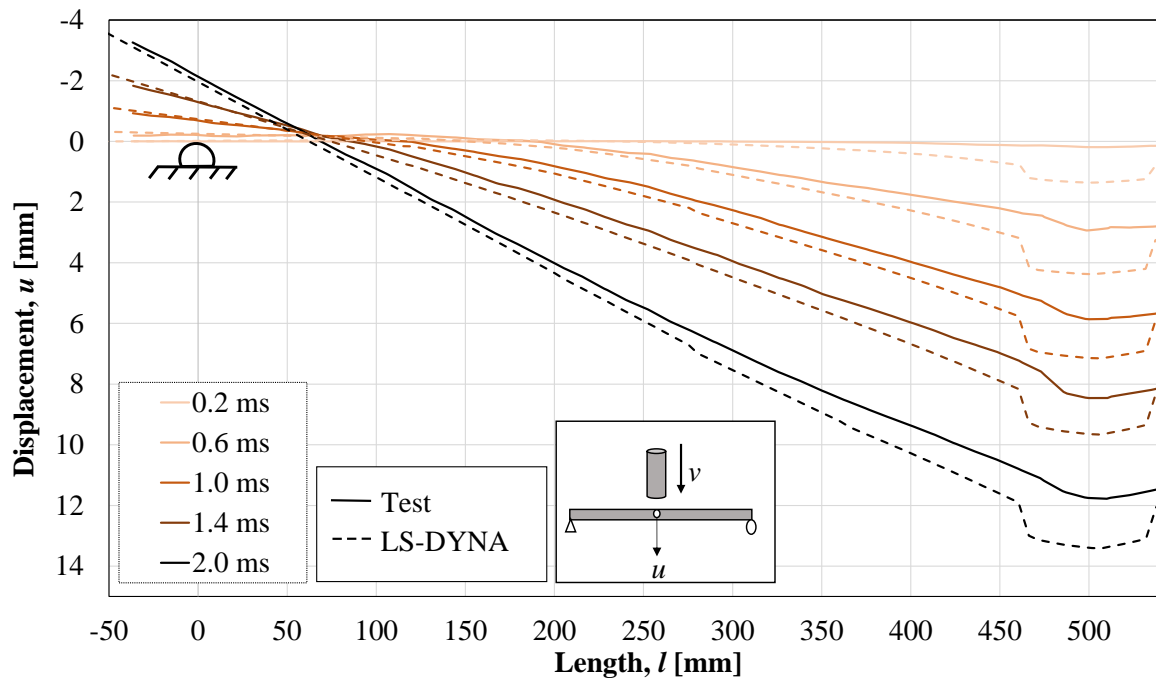


Figure 10.9 Comparison of deflection-length relationship for Series-4.

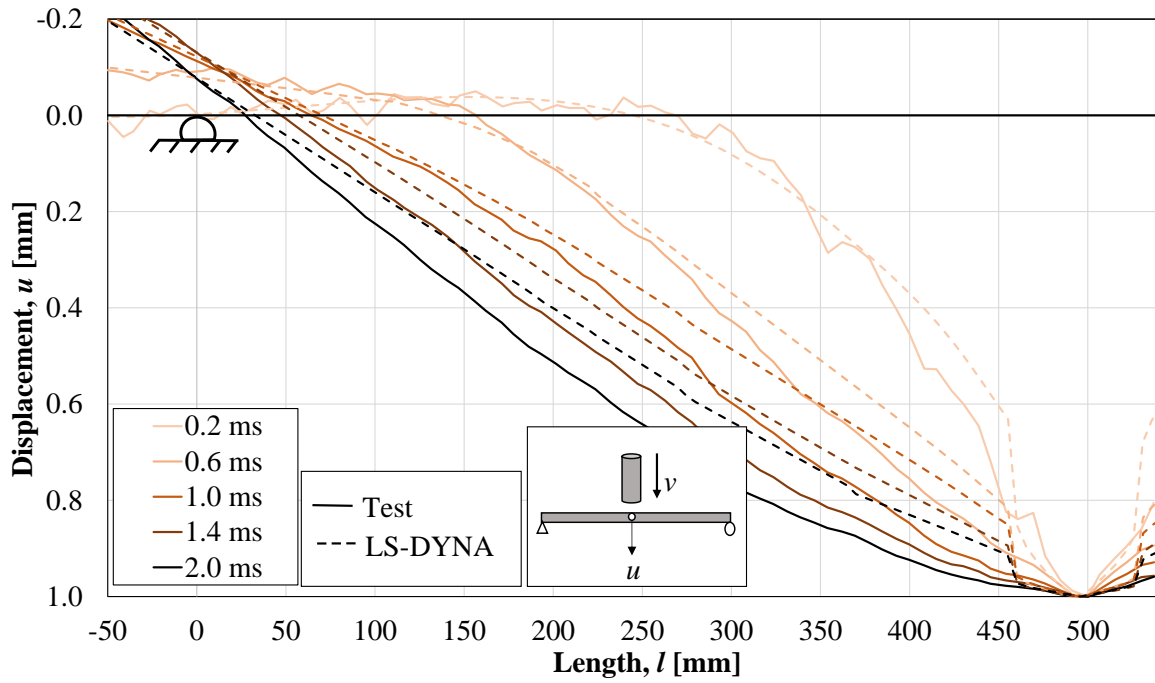


Figure 10.10 Comparison of relative deformed shape for Series-1.

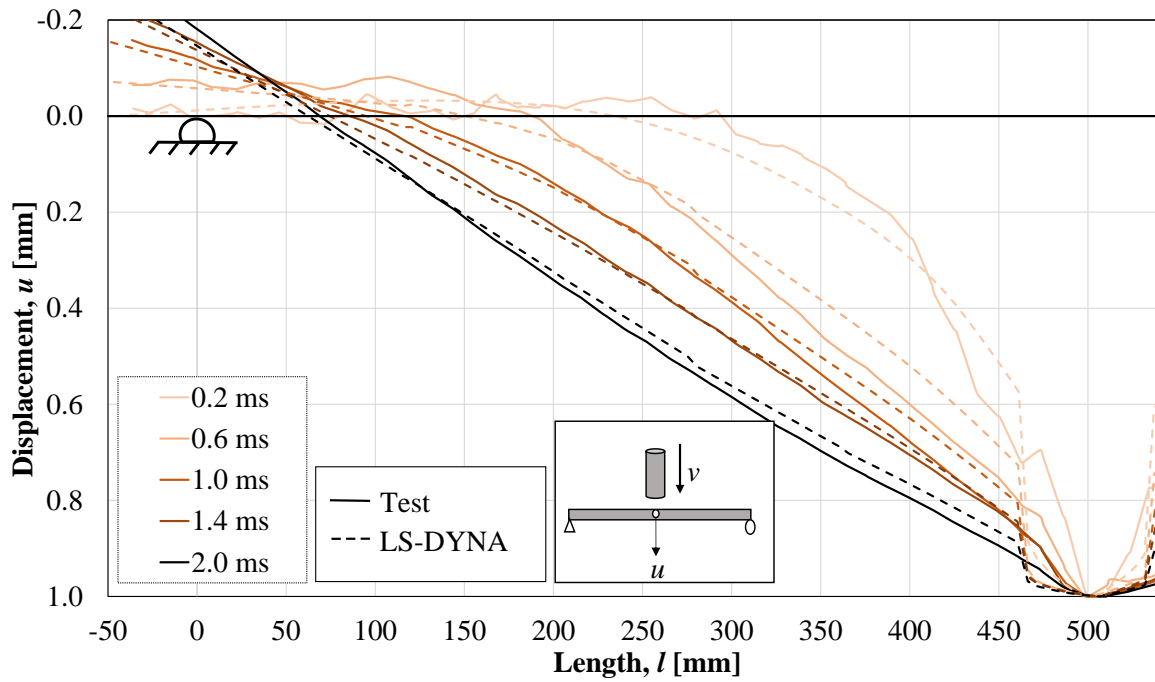


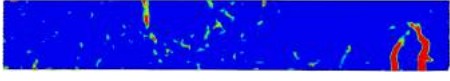
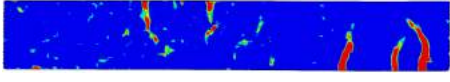
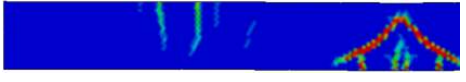
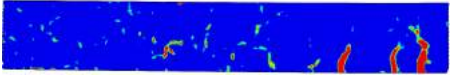
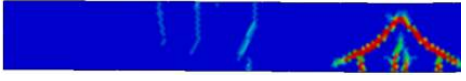
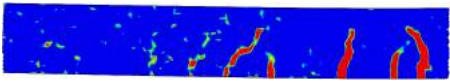
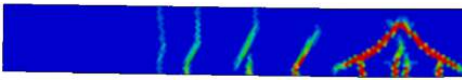
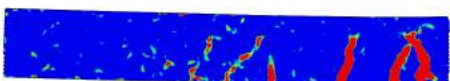
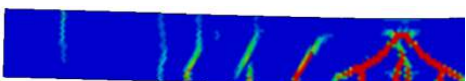
Figure 10.11 Comparison of relative deformed shape for Series-4.

10.6.3 Strain Fields

It is also of interest to study how well the propagation of cracks is predicted with LS-DYNA. Therefore, the strain fields of one beam from each batch is compared with the strain fields from the model, see Table 10.8 - 10.11. The beam to compare with was considered representative of the whole series. The strain fields are shown in a few steps between 0.2 ms - 2.0 ms and at maximum deflection.

In Series-1, see Table 10.8, LS-DYNA shows shear cracks at the impact region, which are not present in Beam 4. However, these shear cracks were present during the subsequent drops. The cracks in the upper region, though, corresponds very well and the cracks that propagates a certain distance from the midpoint at approximately 2.0 ms are also well predicted. The maximum deflection at the midpoint is higher in LS-DYNA and this is likely partly due to the shear cracks at the impact region.

Table 10.8 Comparison of strain fields from experiments and LS-DYNA of Series-1 ($m = 10$ kg, $h = 2.5$ m).

t [ms] u [mm]	Series-1, Beam 4	t [ms] u [mm]	LS-DYNA
$t = 0.2$ $u = 1.0$		$t = 0.2$ $u = 0.7$	
$t = 0.4$ $u = 1.9$		$t = 0.4$ $u = 1.5$	
$t = 0.6$ $u = 2.8$		$t = 0.6$ $u = 2.3$	
$t = 1.0$ $u = 4.3$		$t = 1.0$ $u = 3.6$	
$t = 2.0$ $u = 7.0$		$t = 2.0$ $u = 6.5$	
$t = 8.2$ $u = 12.1$		$t = 9.0$ $u = 13.1$	

The predictions of Series-2, see Table 10.9 corresponds better with the strain fields than for Series-1. In this case the shear cracks from LS-DYNA is also present in the test series, in this case Beam 1. By a closer look at the right hand upper crack it is visible that this crack propagates all the way through the beam. At first, it appears after 0.6 ms in the upper part. At 2.0 ms it has instead propagated through the beam and is instead visible as a bending crack at a certain distance from the midpoint. This is a behaviour that is captured from the predicted strain field as well. In the images from the maximum deflection, it is also possible to detect the local damages in the upper part of the impacted area.

Table 10.9 Comparison of strain fields from experiments and LS-DYNA of Series-2 ($m = 10\text{ kg}$, $h = 5.0\text{ m}$).

t [ms] u [mm]	Series-2, Beam 1	t [ms] u [mm]	LS-DYNA
$t = 0.2$ $u = 1.0$		$t = 0.2$ $u = 1.3$	
$t = 0.4$ $u = 2.5$		$t = 0.4$ $u = 2.5$	
$t = 0.6$ $u = 3.8$		$t = 0.6$ $u = 3.6$	
$t = 1.0$ $u = 6.3$		$t = 1.0$ $u = 5.6$	
$t = 2.0$ $u = 10.6$		$t = 2.0$ $u = 9.9$	
$t = 6.0$ $u = 22.1$		$t = 7.0$ $u = 24.5$	

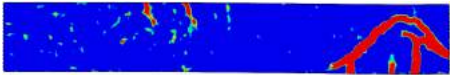
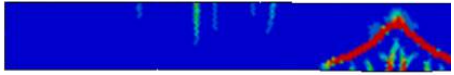
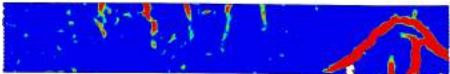
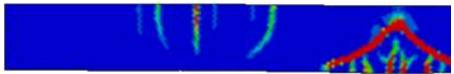
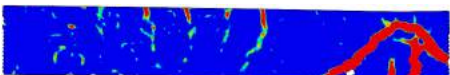
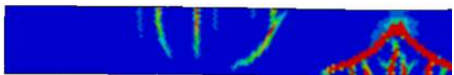
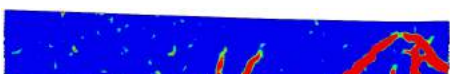
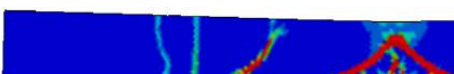
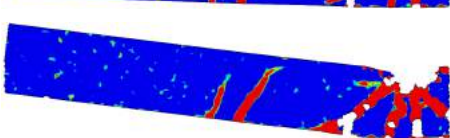
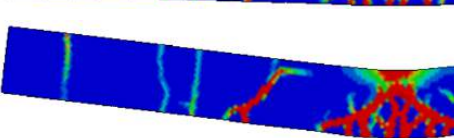
The predicted strain fields of Series-3, see Table 10.10, corresponds also relatively well with the real response, in this case Beam 15. The shear cracks are predicted as well as the bending cracks in the upper part. The local damage where the drop-weight hit the beam is also predicted in a correct way.

Table 10.10 Comparison of strain fields from experiments and LS-DYNA of Series-3 ($m = 20\text{ kg}$, $h = 2.5\text{ m}$).

t [ms] u [mm]	Series-3, Beam 15	t [ms] u [mm]	LS-DYNA
$t = 0.2$ $u = 1.2$		$t = 0.2$ $u = 0.7$	
$t = 0.4$ $u = 2.5$		$t = 0.4$ $u = 1.8$	
$t = 0.6$ $u = 3.7$		$t = 0.6$ $u = 2.9$	
$t = 1.0$ $u = 5.9$		$t = 1.0$ $u = 4.8$	
$t = 2.0$ $u = 10.4$		$t = 2.0$ $u = 9.0$	
$t = 12.0$ $u = 29.0$		$t = 11.8$ $u = 30.0$	

The comparison of strain fields of Series-4, represented by Beam 11, and LS-DYNA can be seen in Table 10.11. In the predicted strain field a total of three larger cracks occurs at the upper part, whilst a total of five smaller cracks occurs at Beam 11. However, the overall response is well predicted. The blank area in the mid part of Beam 11 means that spalling of concrete has occurred. This local damage is well predicted and shown as the strain concentration at the impact zone in LS-DYNA.

Table 10.11 Comparison of strain fields from experiments and LS-DYNA of Series-4 ($m = 20 \text{ kg}$, $h = 5.0 \text{ m}$).

t [ms] u [mm]	Series-4, Beam 11	t [ms] u [mm]	LS-DYNA
$t = 0.2$ $u = 2.3$		$t = 0.2$ $u = 1.4$	
$t = 0.4$ $u = 4.0$		$t = 0.4$ $u = 2.9$	
$t = 0.6$ $u = 5.7$		$t = 0.6$ $u = 4.4$	
$t = 1.0$ $u = 8.9$		$t = 1.0$ $u = 7.1$	
$t = 2.0$ $u = 15.1$		$t = 2.0$ $u = 13.4$	
$t = 18.2$ $u = 59.8$		$t = 16.0$ $u = 56.9$	

11 Discussion

This chapter consists of a discussion and general observations made during the thesis work. The experimental procedure will be treated as well as the interpretation of the results.

Regarding the material properties some differences were observed between the two batches and it would be preferred to mix all the concrete in one batch to make sure that the same properties are obtained. However, the differences were relatively small and are therefore deemed to be of small effect. An attempt to fix the problem observed by Lozano and Makdesi (2017) that the reinforcement was bent downwards during the casting was made, but not completely successful. The principle by using steel wires was correct but, as mentioned in Section 8.2.4, the reinforcement was placed too high.

The 2DOF model was used to predict the deflection-time relationship for the beams and it was discovered that the model overestimates the deflections for the first drop in all four test series. This was expected since the same result was obtained in previous thesis's within the same subject and the same way of thinking was applied in the 2DOF model used here. When predicting the response during repeated impacts it could be seen that Series-4 had the greatest total plastic deflection, followed by Series-3, -2 and -1 in that order. When analysing the experimental results, it can be seen that this is not the case and that the deflections are closer to the predicted value when repeated impacts are considered, compared to when only the first drop is considered. This means that the model overestimates the plastic deflection during the first impact but underestimates the additional plastic deflections during the repeated impacts. During the tests it was observed that extensive damage occurred at the impact area, i.e the compressive zone got crushed and the beam became less stiff. The model assumes the same stiffness and resistance after each drop and therefore the overestimated prediction gets closer to reality after each drop. However, this does not mean that the model is better to describe repeated impacts compared to single impacts since the reason the prediction gets better is not included at all in the model.

The reason why the 2DOF model overestimates the deflections during the first impact could be that the load capacity that were calculated by hand proved to be an underestimation, see Figure 10.1, leading to a less strong beam in the 2DOF model. Another reason for the overestimation could be that the 2DOF model does not include strain rate effects which would have lead to an increased predicted stiffness of the beam, resulting in lower deflections.

The extensive damage during repeated impacts caused problems with the DIC since the software is dependent on a clear pattern which it can relate to during the entire impact. The crushing of concrete in the top of the beam caused the software to lose the parts of the beam that were crushed and gravel that fell down in front of the beam made the postprocessing hard. In some cases, parts of the tensile zone loosened from the beam together with the painted pattern. During the next drop the software could not capture the newly emerged parts which had no pattern painted on them. If the tests were to be performed again it could be a good idea to protect the top of the beam with some kind of loading plate or protective rubber on the drop-weight to distribute the force better, resulting in less damages on the top of the beam.

The study of the acceleration of only one facet point in GOM Correlate proved to give unreasonable results with large deviations between them. Instead, the methodology was to average the acceleration of

a number of facet points, resulting in values that corresponded well between the impact sequences. The acceleration was used to calculate the impact force and the impulse. In the absence of predictions there is no comparison of the impact force. However, there is a good stability in the results. The time interval over which the impulse lasted was overestimated, resulting in higher values. However, the accuracy in the value of the impulse was evaluated by looking at the relation between the peak value and the total impulse in the 2DOF model and this showed a good resemblance.

When performing the static loading, the loading condition was changed to four-point loading due to the extensive damage in the impact zone. This was not ideal but a choice that had to be made to make sure that reasonable results were obtained. The severe damage the beams suffered also lead to that the rotational capacity could not be evaluated for the beams subjected to dynamic loading. These are two more reasons why the dynamic testing should be evaluated and modified so that the beam does not experience such severe damage during the testing.

It is interesting that the predicted load capacity proved to be an underestimation both when looking at the load-deflection relationship obtained from the static test and when looking at the internal work, though the method with the internal work was closer to the predicted value. It could be questioned why the internal work only was evaluated down to 80% on the descending branch of the load-displacement curve and the reason for this is that the failure mode has a large influence on the results obtained below that value. When the beam is subjected to rupture of reinforcement, the curve is completely vertical at that point which results in the same value for $W_{pl.80}$, $W_{pl.70}$ and so on. If crushing of concrete was the failure mode, the curve is sometimes almost vertical and sometimes almost horizontal which would result in a large dispersion between the results.

LS-DYNA proved to be a very powerful tool to predict the response, though it is very time consuming to use. It can however be tricky to make the model converge and during this thesis, problems running the model with a high tensile strength and the default value of the EFC-parameter occurred. A way to handle problems with the EFC-parameter could be found in literature, namely to increase it by a factor 10 to prevent crushing of concrete, but the problems regarding the tensile strength remained unsolved. One idea was that the high tensile strength lead to a lower value of WF which is a parameter controlling the softening branch of exponential tensile damage formulation, presented in Table 9.1. This seems odd since it was believed that a high tensile strength should lead to a higher WF. However, WF is mainly dependent on the fracture energy which should also be higher if the high tensile strength obtained from the tests was correct. It is therefore believed that the material model CDPM2 is designed to work for material parameters that has a reasonable proportion to each other. This further emphasizes the idea that the higher value of tensile strength obtained from the material tests was not correct.

12 Final Remarks

12.1 General Description

The aim of the thesis is to increase the understanding of the structural response of RC beams subjected to repeated impact loading and evaluate methods to predict this response. This was made by studying how impacts influences the capacity of simply supported reinforced concrete beams.

Firstly, to deepen the knowledge concerning structural dynamics and the response of impact loaded structures, a literature survey was done. Based on the information gathered in the literature survey a 2DOF model was developed. By hand calculations and the 2DOF model an experimental procedure that should provide interesting results was formed.

Secondly, the experiments were performed where the beams were subjected to four different combinations of impact loading. After the dynamic testing, the beams were tested statically until failure together with a number of undamaged beams to form a basis of comparison. Both the dynamic and static tests were captured with a high-speed camera and the images were afterwards processed using Digital Image Correlation (DIC). Parameters such as load capacity, deflection, rotation capacity, internal work, impulse and the strain fields were evaluated.

Lastly, the software LS-DYNA was used to perform dynamic finite element analyses (FEA). These results were compared with the results from the experiments and the 2DOF calculations. In the analysis 3D solid elements and the material model CDPM2 was used.

12.2 Conclusions

The main conclusion in this thesis was that the response during repeated impacts is hard to predict. This is mainly due to the extensive local damage that takes place where the drop-weight hits the beam and the large variation in the test results. Further, a large difference in response between dynamic and static loading was observed with regard to crack pattern. During static loading of undamaged beams, bending cracks could be observed in the bottom part of the beam. In the dynamic loaded beams both bending and shear cracks could be observed in the bottom part, as well as bending cracks in the top part of the beam during the first few ms.

The 2DOF model overestimates the deflections during the impacts but the accuracy is still good enough to recommend this tool for predicting the response, though there is room for improvements. For example, the 2DOF model does not account for the loss of stiffness when the concrete in the compression zone gets crushed.

Regarding plastic rotation capacity, it was concluded that Bk25 provides the best method to predict the plastic rotation capacity for four-point loaded RC beams. It was found that the loading conditions from which the different models are created for are not well stated and the suitability to use these methods on a four-point loaded structure can be questioned.

It can be concluded that DIC is a suitable tool for the study of the impact behaviour regarding strain fields, deflections and velocities. It might also be a suitable tool for the study of accelerations. It was

found that DIC has problems capturing the behaviour when the beam is damaged to such extent that the quality of the pattern is affected.

LS-DYNA proved to be a very powerful tool to predict the first impact, but a new way of thinking needs to be applied if repeated impacts are to be modelled. The FE model within this thesis shows a good correspondence regarding strain fields and deflections during the first impact.

12.3 Further Studies

The experiments performed in this thesis were designed in such a way that the beams were subjected to a certain number of drops, followed by static testing to see how much residual capacity that were left. It would be interesting to subject a larger number of beams to the same weight and drop height and test statically them after each drop. For example, 12 beams could be subjected to the same conditions, making it possible to test 3 beams statically after each drop and therefore be able to follow the behaviour after each impact in a more detailed way. A lot of factors could be changed during the experiments such as: New drop heights, weight of drop-weight, span length or dimensions of the beam, different types or amount of reinforcement and different location of the impact.

A problem that were observed during the experiments was the extent of the local damages where the drop-weight hit the beam. This is something that is not included in the 2DOF model and could be something to improve if repeated impacts are to be modelled in a more correct way. The effect of strain rate is also something that could be added to the 2DOF model to make it more close to the reality.

Another thing that could be made is to prevent the local damage in the top of the beam by placing some kind of protective layer on either the beam or the drop-weight. It could however cause some problems with how the impact is modelled.

Regarding the FE modelling in LS-DYNA it is clear that the possibility of modelling repeated impacts is something worth investigating. An idea could be to save the strain fields from the first drop and implement it as the initial strain field before the second drop. Another approach could be to identify elements which are deemed to have utilized their capacity during the first drop and remove them before the second drop is modelled. This is unfortunately something that did not fit in the scope of this thesis.

A certain variation was observed between the beams during the experiments when the information was processed through DIC. The reason behind this could be that the material properties varies within the beam and therefore it would be interesting to try to model this with LS-DYNA by randomizing the material data for the elements.

References

- ACI-ASCE-Committee-428 (1968). "Progress Report on Code Clauses for Limit Design". In: *ACI Journal* 65.
- Adhikary, S. D., B. Li, and K. Fujikake (2012). "Dynamic behavior of reinforced concrete beams under varying rates of concentrated loading". In: *International Journal of Impact Engineering* volume 47.
- Arbulu, A. G. B. (2006). *Plastic hinge length in high-rise concrete shear walls*. MSc Thesis.
- Baker, A. and A. Amarkone (1964). "Inelastic Hyperstatic Frames Analysis". In: *Proceedings of the International Symposium on the Flexural Mechanics of Reinforced Concrete, ASCE-ACI 50*.
- Biggs, J. (1964). *Introduction to Structural Dynamics*. McGraw-Hill.
- Boverket (2004). *Boverkets handbok om betongkonstruktioner, BBK 04*. Boverket.
- Carlsson, M. and R. Kristensson (2012). *Structural Response with regard to explosions - Mode superposition, damping and curtailment*. MSc Thesis.
- CEB-FIP (2012). *Model Code 2010*. Comité Euro-International du Béton.
- Cederwall, K., L. Elfgren, B. Engström, A. Hillerborg, Å. Holmberg, E. Hultin, I. Karlsson, S. Kinnunen, A. Losberg, M. Lorentsen, H. Nylander, T. Petersson, S. Sahlin, S. Svensson, B. Westerber, S. Öberg, and L. Östlund (1990). *Betonghandbok - Konstruktion*. Second. Stockholm: Cementa and AB Svensk byggtjänst.
- CEN (2004). *EN 1992-1-1 Eurocode 2: Design of concrete structures - Part 1-1: General rules and rules for buildings*. European Committee for Standardization.
- (2009a). *EN 12350-1: Testing fresh concrete - Part 1: Sampling*. European Committee for Standardization.
 - (2009b). *EN 12350-2: Testing fresh concrete - Part 2: Slump-test*. European Committee for Standardization.
 - (2009c). *EN 12350-7: Testing fresh concrete - Part 7: Air-content - Pressure methods*. European Committee for Standardization.
 - (2009d). *EN 12390-2: Testing hardened concrete - Part 2: Making and curing specimens for strength tests*. European Committee for Standardization.
 - (2009e). *EN 12390-3: Testing hardened concrete - Part 3: Compressive strength of test specimens*. European Committee for Standardization.
 - (2009f). *EN 12390-6: Testing hardened concrete - Part 6: Tensile splitting strength of test specimens*. European Committee for Standardization.
 - (2009g). *EN 12390-7: Testing hardened concrete - Part 7: Density of hardened concrete*. European Committee for Standardization.
- Cotsovos, D. and M. Pavlovic (2008). "Numerical investigation of concrete subjected to compressive impact loading. Part 1: A fundamental explanation for the apparent strength gain at high loading rates". In: *Computers and Structures* volume 86.

- Ekström, J. (2017). “Blast and Impact Loaded Concrete Structures”. PhD thesis. Chalmers University of Technology.
- Engström, B. (2011). *Bärande konstruktioner, Del 2, Chapter B7-B11*. Gothenburg: Chalmers University of Technology.
- (2013). *Bärande konstruktioner, Del 1, Chapter B1-B6*. Sixth. Gothenburg: Chalmers University of Technology.
 - (2015). *Design and Analysis of Continuous Beams and Columns*. Gothenburg: Chalmers University of Technology.
- Fortifikationsförvaltningen (1973). *Provisoriska anvisningar för dimensionering av armerade betongkonstruktioner som skydd mot verkan av konventionella vapen inom närmissområde*. Fortifikationsförvaltningen, Befästningsavdelningen.
- Fransson, H. (1997). *Rotation Capacity of Reinforced High Strength Concrete Beams*. Stockholm: Royal Institute of Technology.
- Grassl, P. (2016). *User manual for MAT_CDPM (MAT_273) in LS-DYNA*. URL: <http://petergrassl.com/Research/DamagePlasticity/CDPMLSDYNA/index.html> (visited on 04/26/2017).
- Grassl, P. and M. Jirasek (2006). “Damage-plastic model for concrete failure”. In: *International Journal of Solids and Structures* 43.
- Johansson, M. (2000). “Structural Behaviour in Concrete Frame Corners of Civil Defence Shelters”. PhD thesis. Chalmers University of Technology.
- Johansson, M. and L. Laine (2012). *Bebyggelsens motståndsförmåga mot extrem dynamisk belastning, Del 3 – Kapacitet hos byggnader*. Swedish Civil Contingencies Agency.
- Kheyroddin, A. and H. Naderpour (2007). *Plastic Hinge Rotation Capacity of Reinforced Concrete Beams*. International Journal of Civil Engineering.
- Latte, S. (1999). *Plastic Rotation Capacity of Reinforced Concrete Beams*. MSc Thesis.
- Löfgren, I., J. F. Olesen, and M. Flansbjer (2004). *Application of WST-method for fracture testing of fibre-reinforced concrete*. Chalmers University of Technology.
- Lovén, J. and E. S. Svavarsdóttir (2016). *Concrete Beams Subjected to Drop Weight impact*. MSc Thesis.
- Lozano, F. M. and J. A. Makdesi (2017). *Concrete Beams Subjected to Drop-Weight Impact and Static Load*. MSc Thesis.
- LSTC (2014). *LS-DYNA Keyword user’s manual - Volume I,II,II*. Livermore Software Technology Corporation.
- Munther, M. and J. Runebrant (2018). *Structural response of concrete beams subjected to drop weight impact*. MSc Thesis.
- Nyström, U. (2006). *Design with regard to explosions*. MSc Thesis.
- Panagiotakos, T. and M. Fardis (2001). “Deformations of Reinforced Concrete Members at Yielding and Ultimate”. In: *ACI Structural Journal* 98.

- Paulay, T. and M. Priestley (1992). "Seismic Design of Reinforced Concrete and Masonry Buildings". In: *John Wiley and Sons, New York*.
- Tamminen, S. (1993). *Rotationskapacitet för armerade betongbalkar i höghållfast betong*. MSc Thesis.
- Yi, W.-J., D.-B. Zhao, and S. K. Kunnath (2016). "Simplified Approach for Assessing Shear Resistance of Reinforced Concrete Beams under Impact Loads". In: *ACI Structural Journal* July-August 2016.

A Material Properties Testing of Concrete

A.1 Introduction

To determine the material properties of the beams, test cubes were casted at the same time, using concrete from the same batch. 12 cubes, with side of 150 mm and smooth edges, and three cubes with the same dimensions but with a notch in one side were casted from each batch, this gives a total of 30 test cubes. The smooth cubes were used to determine the compressive and tensile strength while the notched cubes were used to determine the fracture energy. To make sure that the concrete get the material properties expected, the cubes were casted and treated according to CEN (2009d). The standard give recommendations for every part of the process when casting and curing the specimens and only the most relevant parts will be treated here. The standard recommends different ways to compact the concrete and when using an internal vibrator it is stated that the dimensions of the vibrator should not exceed one quarter of the test specimen. Figure A.1 show the two different type of cubes as well as the vibrator that is well below the size limit.



Figure A.1 The two different test-cubes with the internal vibrator.

The procedure when greasing the inner surface, mentioned in Section 6.2.3, is also described in the standard. The specimens should be left in the mould for at least 16 hours, but not longer than 3 days, protected against dehydration at a temperature of 20 ± 5 °C. The specimens were left in the laboratory, where the temperature is around 20 °C, and covered by a plastic sheet to protect it from dehydration. After removal from the mould, the specimens should be cured in water at a temperature of 20 ± 2 °C. This was done after approximately 44 hours.

The first tests on the hardened concrete was made after 26 days, when the first dynamic tests were performed and the second tests were made after 28 days, when the first static tests were performed. The

cubes are named 1.1-1.15 and 2.1-2.15. The first number stands for which batch the cube corresponds to, namely 1 or 2, and the second number is the actual number of the cube. After 26 days, cube number 1-3 were tested for compressive strength and 4-6 were tested for tensile strength. After 28 days, cube number 7-9 and 10-12 were tested for compressive and tensile strength, respectively. Cube number 13-15 were tested for fracture energy after 28 days.

A.2 Density

The density of the concrete were determined according to CEN (2009g), which describes several different methods that can be used to determine the density. One of them consists of measuring the sides of the cube with a caliper. This should be done on 3 different places along each edge, preferably with a digital caliper, and then use the mean length of each side to determine the volume. The specimens were then weighted on a scale to be able to determine the density ρ based on the mass m and the volume V as

$$\rho = \frac{m}{V} \quad (\text{A.1})$$

A summary of the calculated densities are shown in Table A.1.

Table A.1 Calculated densities.

Batch 1						
Cube number	1.1	1.2	1.3	1.4	1.5	1.6
Density [kg/m ³]	2 377	2 363	2 354	2 353	2 381	2 375
Cube number	1.7	1.8	1.9	1.10	1.11	1.12
Density [kg/m ³]	2 364	2 372	2 354	2 360	2 362	2 353
Batch 2						
Cube number	2.1	2.2	2.3	2.4	2.5	2.6
Density [kg/m ³]	2 414	2 416	2 388	2 393	2 395	2 403
Cube number	2.7	2.8	2.9	2.10	2.11	2.12
Density [kg/m ³]	2 420	2 372	2 418	2 437	2 393	2404

Mean density batch 1 [kg/m ³]	2 364
Mean density batch 2 [kg/m ³]	2 404
Total mean density [kg/m ³]	2 384

It should be noted that the cubes were dried for 0.5-1 hour before weighted, and not oven dried. This might influence the mass a bit but it is considered negligible. Figure A.2 shows the digital caliper that were used when measuring the dimensions of each cube.



Figure A.2 Picture of the caliper used.

A.3 Compressive Strength

The compressive strength of the concrete was determined according to (CEN, 2009e). The test is pretty straightforward and the only parameter that needed to be defined in the apparatus was the loading rate, which was set to a constant value of 0.4 [MPa/s]. It was also necessary to check if the failure mode of each cube was similar to the ones presented in CEN (2009e). This can be seen in Figure A.3 which shows both the apparatus and an example of an allowed failure mode, which can be seen as small vertical cracks.



(a) Apparatus.

(b) Failure mode.

Figure A.3 Setup for compressive test.

The results from the compressive test is summarized in Table A.2. It should be noted that these values have been calculated from cube strength to cylinder strength with Equation (2.7)

Table A.2 Summary of cylinder compressive strengths.

Cube number	1.1	1.2	1.3	2.1	2.2	2.3
Strength (26d) [MPa]	36.6	36.3	35.8	37.7	38.2	36.9
Mean strength (26d) [MPa]	36.2			37.6		
Cube number	1.7	1.8	1.9	2.7	2.8	2.9
Strength (28d) [MPa]	34.3	34.3	36.2	39.7	37.7	38.2
Mean strength (28d) [MPa]	34.9			38.5		

Mean strength (26-28d) batch 1 [MPa]	35.6
Mean strength (26-28d) batch 2 [MPa]	38.1
Total Mean strength (26-28d) for batch 1 and 2 [MPa]	36.8

It can be observed that the compressive strength is lower after 28 days compared to 26 days for batch 1. This is not realistic and the results might be because of the low amount of cubes tested each day. It can also be seen that the compressive strength is overall greater for batch 2 than batch 1, this is reasonable since batch 2 also has a somewhat larger density which can be coupled to compressive strength.

A.4 Tensile Strength

The tensile strength was determined with a splitting test according to (CEN, 2009f). The loading rate was set to 0.05 [MPa/s] which is much lower than when testing the compressive strength. This is since the load required for splitting the specimen is much lower and therefore more sensitive to increased loads. The setup for the test can be seen in Figure A.4.



(a) Test setup.

(b) Failure mode.

Figure A.4 Setup for tensile test.

A summary of the results can be seen in Table A.3. It should be noted that the values given here are calculated from the test data, using Equation (2.12).

Table A.3 Summary of tensile strengths.

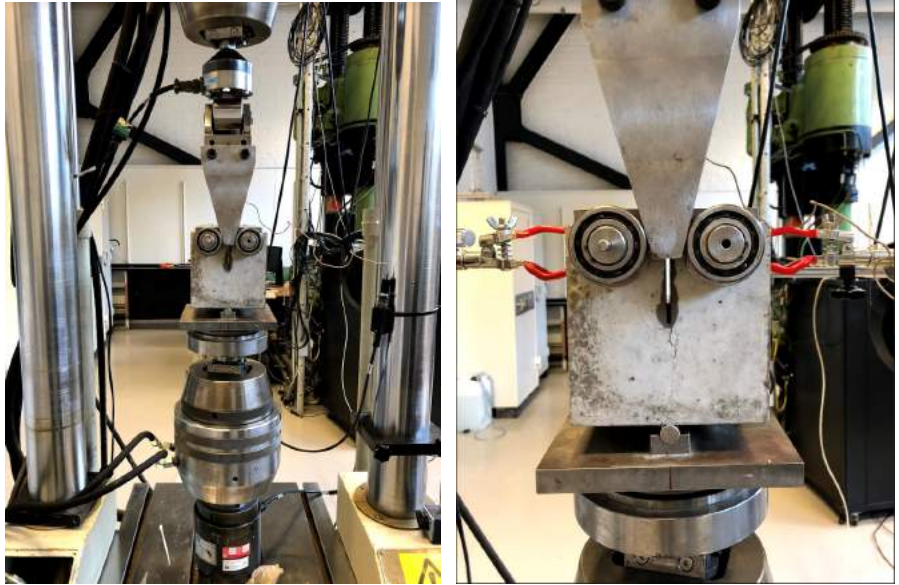
Cube number	1.4	1.5	1.6	2.4	2.5	2.6
Strength (26d) [MPa]	4.4	4.6	4.6	5.0	5.0	5.0
Mean strength (26d) [MPa]	4.5			5.0		
Cube number	1.10	1.11	1.12	2.10	2.11	2.12
Strength (28d) [MPa]	4.7	4.7	5.0	4.6	4.8	4.3
Mean strength (28d) [MPa]	4.8			4.6		

Mean strength (26-28d) batch 1 [MPa]	4.7
Mean strength (26-28d) batch 2 [MPa]	4.8
Total Mean strength (26-28d) for batch 1 and 2 [MPa]	4.7

It can be seen that the tensile strength is greater for batch 2 compared to batch 1 after 26 days, but lower after 28 days. This might be because of the low amount of cubes tested. The overall strength if you combine the results from 26 and 28 days is larger for batch 2, which corresponds well with the previous results for compressive strength in Section A.3.

A.5 Fracture Energy

To be able to predict the fracture energy G_F of the concrete a wedge splitting test (WST) was performed according to the recommendations given in (Löfgren *et al.*, 2004). The setup of the test can be seen in Figure A.5.



(a) Test setup.

(b) Zoomed in.

Figure A.5 Test setup for WST.

First of all, the area of the cross-section that will be fractured needs to be calculated. This is done by the measurements presented in Figure A.6.

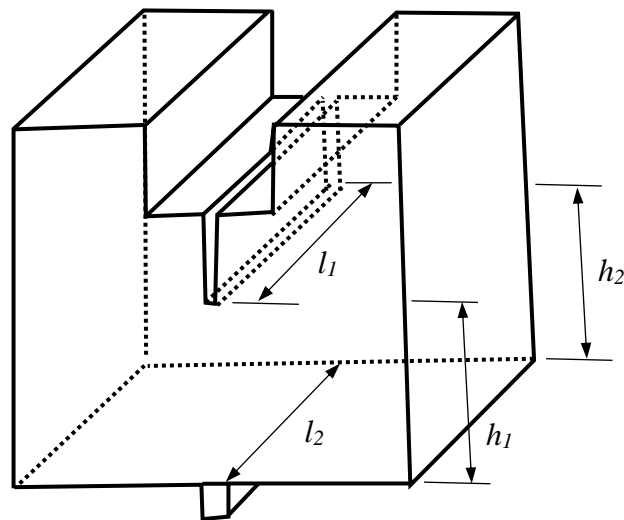


Figure A.6 Dimensions for WST.

The measured dimensions are presented in Table A.4.

Table A.4 Dimensions of cubes for WST.

Cube number	l_1 [mm]	l_2 [mm]	h_1 [mm]	h_2 [mm]	A [mm ²]
1.13	149.5	150.5	76.1	76.8	11473
1.14	149.5	149.6	75.5	75.4	11284
1.15	150.3	150.4	76.4	75.4	11405
2.13	150.2	150.4	75.1	75.0	11276
2.14	149.7	149.8	75.2	75.2	11262
2.15	150.4	150.3	75.3	75.3	11318

These measurements are, however, only theoretically valid. Figure A.7 shows the difference of failure mode for cube number 2.14 and 2.15 where it can be seen that the fractured area differs a lot. A more accurate way to determine the area would be to 3D-scan the fractured area. This is however not done here.

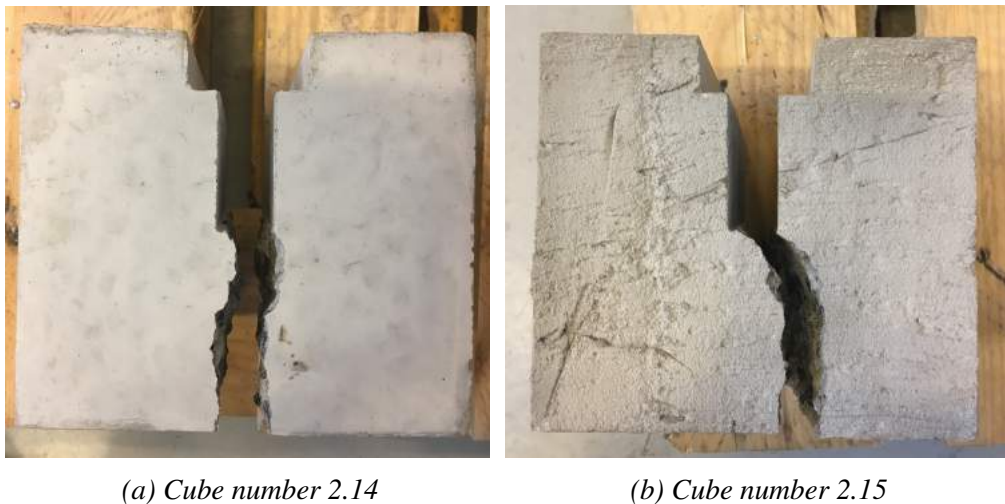


Figure A.7 Examples of different failure modes in WST.

The fracture energy is calculated as the area under the splitting load-CMOD (Crack mouth opening distance) diagram. Figure A.8 shows the diagram and Table A.5 shows a summary of the results.

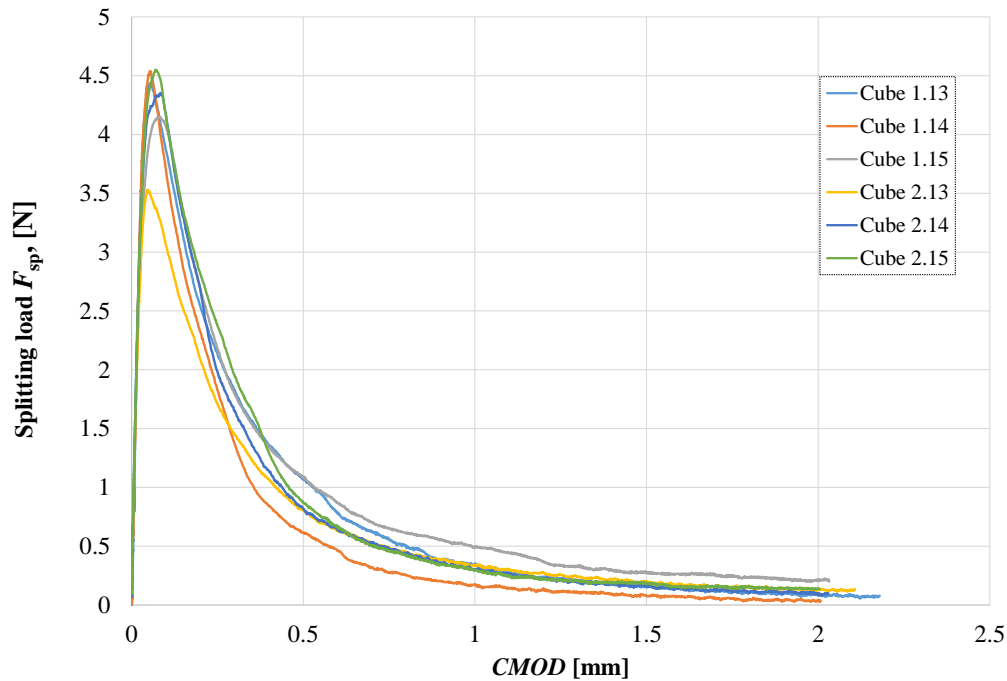


Figure A.8 Splitting load-CMOD diagram.

Table A.5 Summary of results from WST.

Cube number	Accumulated G_F [Nm/m^2]	Maximum Applied F_{sp} [N]	Maximum CMOD [mm]
1.13	143.6	4.4	2.2
1.14	111.2	4.5	2.0
1.15	160.0	4.2	2.1
2.13	124.8	3.5	2.1
2.14	137.7	4.4	2.0
2.15	145.6	4.6	2.0
Average G_F	137.1		
Average G_F Batch 1	138.3		
Average G_F Batch 2	136.0		

It can be seen that there is some dispersion in the results but the average fracture energy is almost the same for the two batches. The goal was to cancel the test as soon as $CMOD$ reached 2 mm since the capacity was deemed to be reached at that point. However, some of the tests continued after 2 mm but this contribution to the total fracture energy is almost negligible and therefore not corrected.

B Material Properties Testing of Steel

The tests of the steel properties were performed by Research Engineer Sebastian Almfeldt before the initiation of the thesis work. However, some information about the tests were given:

- Tested with an extensometer, 634.25F-24 SN:10504454C
- Speed was 0.5 mm/min up to 3 mm, followed by 4 mm/min until failure
- Extensometer was removed at 20 mm deformation (Except for the first sample where it was removed earlier)
- Length of the specimens were 305 mm

The properties of the steel were calculated with a provided template from Morgan Johansson and a summary of the steel properties can be seen in Table B.1 where a nominal diameter of 6 mm were used for the reinforcement.

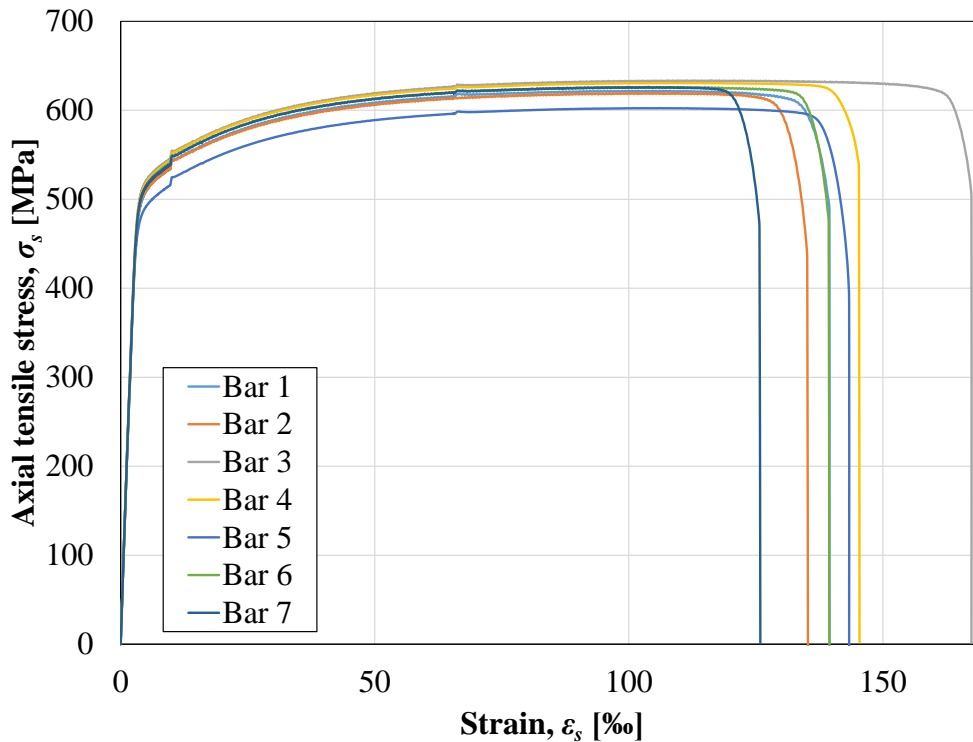


Figure B.1 Ultimate steel capacity.

Table B.1 Results of steel testing.

Bar sample	E_s [MPa]	ε_{su} [‰]	F_{max} [N]	f_u [MPa]	$f_{0.2}$ [MPa]
1	196	101	17.7	622	514
2	194	104	17.7	620	507
3	188	116	17.9	634	529
4	195	108	17.8	631	515
5	208	101	17.1	602	495
6	193	109	17.9	626	521
7	198	104	17.9	626	511
Average	196	106	17.7	623	513

C Damaged Beams After Testing

Figures C.1-C.8 show the damaged beams after they have been subjected to all of the drops in the dynamic testing.



Figure C.1 Beam 4-6 looking at the side of the beam.



Figure C.2 Beam 4-6 looking at the bottom of the beam.



Figure C.3 Beam 1-3 looking at the side of the beam.



Figure C.4 Beam 1-3 looking at the bottom of the beam.



Figure C.5 Beam 13-15 looking at the side of the beam.



Figure C.6 Beam 13-15 looking at the bottom of the beam.



Figure C.7 Beam 10-12 looking at the side of the beam.



Figure C.8 Beam 10-12 looking at the bottom of the beam.

D DIC Facet Analysis

After importing the frames to GOM Correlate 2017 the user has to specify the facet size and point distance to generate a mesh that is used for the DIC. For the facet size the length of a side is specified in pixels and the point distance is how many pixels there is between the midpoint of each facet, see Figure D.1. The mesh generated from two different facet and point distance combinations is presented in Figure D.2. It should be noted that only a triangular mesh structure is possible in GOM Correlate.

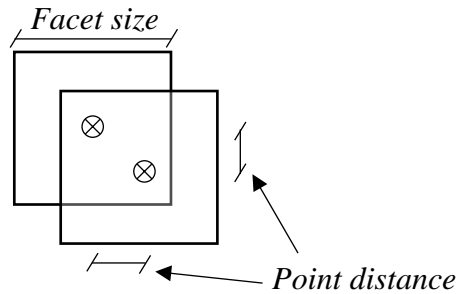
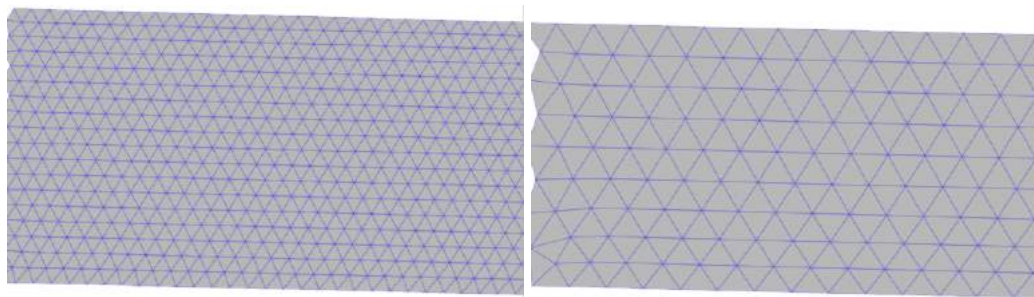


Figure D.1 Definition of facet size and point distance used to generate a mesh in GOM Correlate.



(a) Facet size = 15, point distance = 10. (b) Facet size = 25, point distance = 20.

Figure D.2 Mesh structure in DIC.

In order to find an appropriate combination of facet size and point distance to display the strain field a study was made on beam number 1, the first drop. The quantity for the comparison is the major strain and it is displayed against the reference stage (before impact). The upper limit for the strain was 5 % and the lower limit was 1 %. By using these limits the influence of the lower strain values were avoided out and minor cracks became more visible. The interpolation size was chosen to 1 and a high accuracy computation was used. The results from the analysis can be seen in Table D.1 and D.2. Based on this, it was determined that a facet size of 15 pixels and a point distance of 5 pixels was the most appropriate combination to visualize the cracks, without too much noise.

Table D.1 Strain field visualization with point a point distance of 5 pixels.

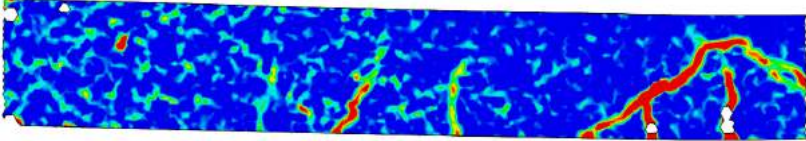
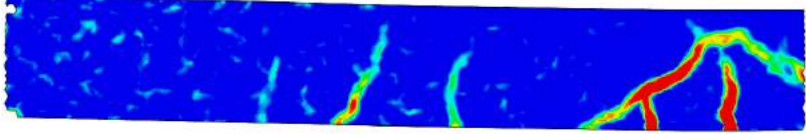
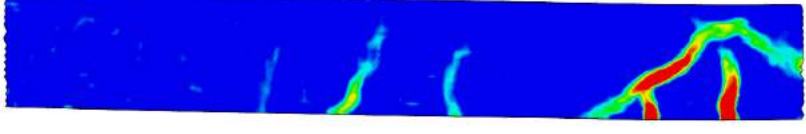
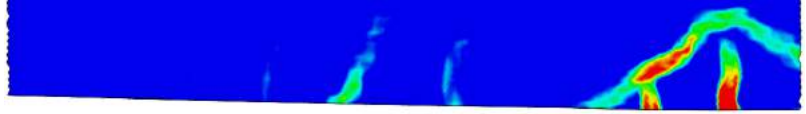
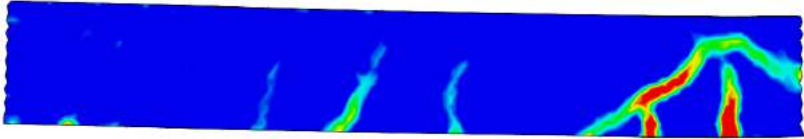
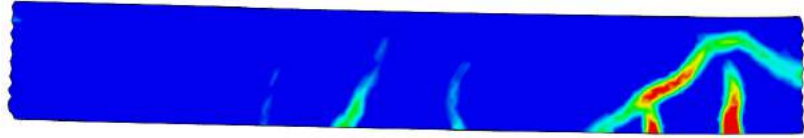
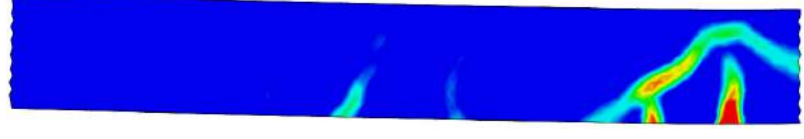
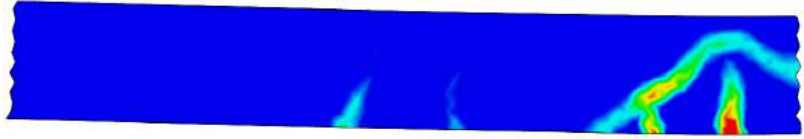
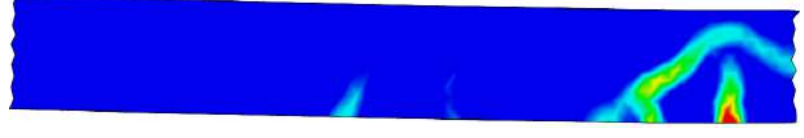
Facet size	Point distance = 5
10	
15	
20	
25	

Table D.2 Strain field visualization with point a point distance of 10-20 pixels.

Facet size	Point distance = 10
15	
20	
25	
Facet size	Point distance = 15
20	
25	
Facet size	Point distance = 20
25	

E Beams Subjected to Static Loading only

Figure E.1-E.4 show the undamaged beams after they have been subjected to static loading.



Figure E.1 Beam 7-9 looking at the side of the beam.

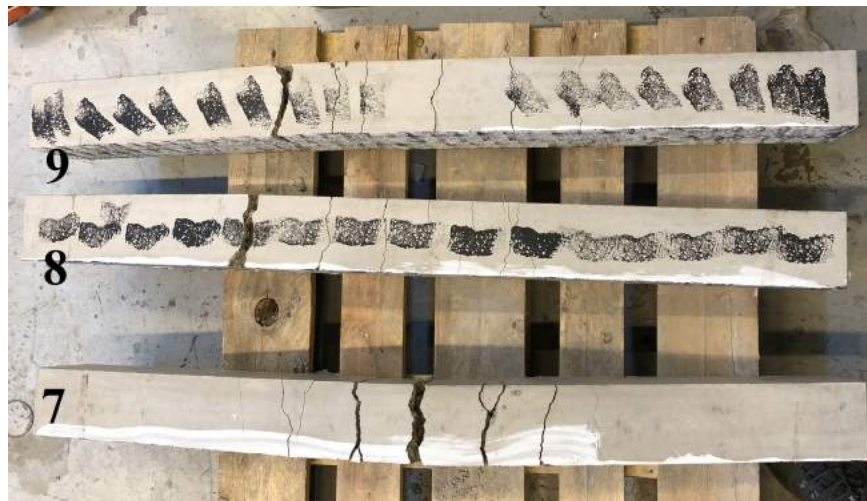


Figure E.2 Beam 7-9 looking at the side of the beam.



Figure E.3 *Beam 16-18 looking at the side of the beam.*



Figure E.4 *Beam 16-18 looking at the side of the beam.*

F Determination of Plastic Deformation at Midpoint

The plastic deformation after an impact was determined in GOM Correlate 2017. It existed two ways to determine the deformations, either by using the image sequence during the actual impact or by the sequence from the next impact.

F.1 Method 1 - Image Sequence from actual Impact

The deflections from the first image sequence was determined from the deflection-time curve. The fact that the beam has an upward movement after impact was taken into consideration by plotting the difference between a point at the support and the midpoint, see Figure F.1. Figure F.2 shows the deflection-time curve for beam 1. After a while there is no additional plastic deformation, but the beam still vibrates. The plastic deformation was determined as the average value of the last 5 ms.

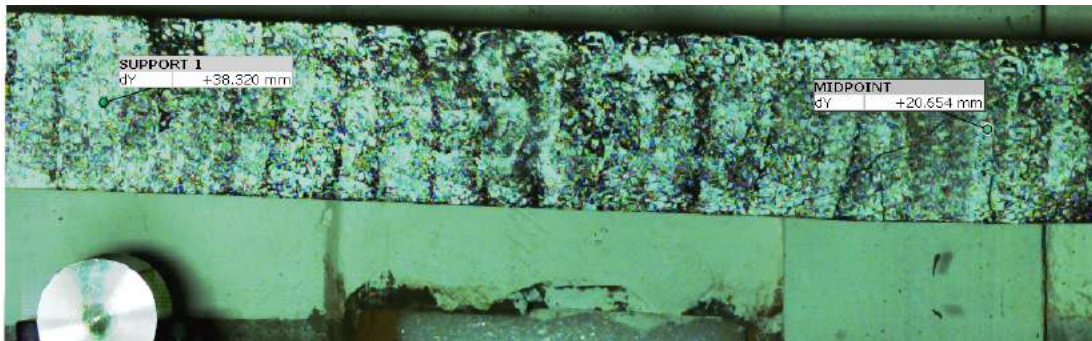


Figure F.1 Figure showing the beam moving in the upward direction. The midpoint deflection of the beam is measured as the difference between the midpoint and the support displacements.

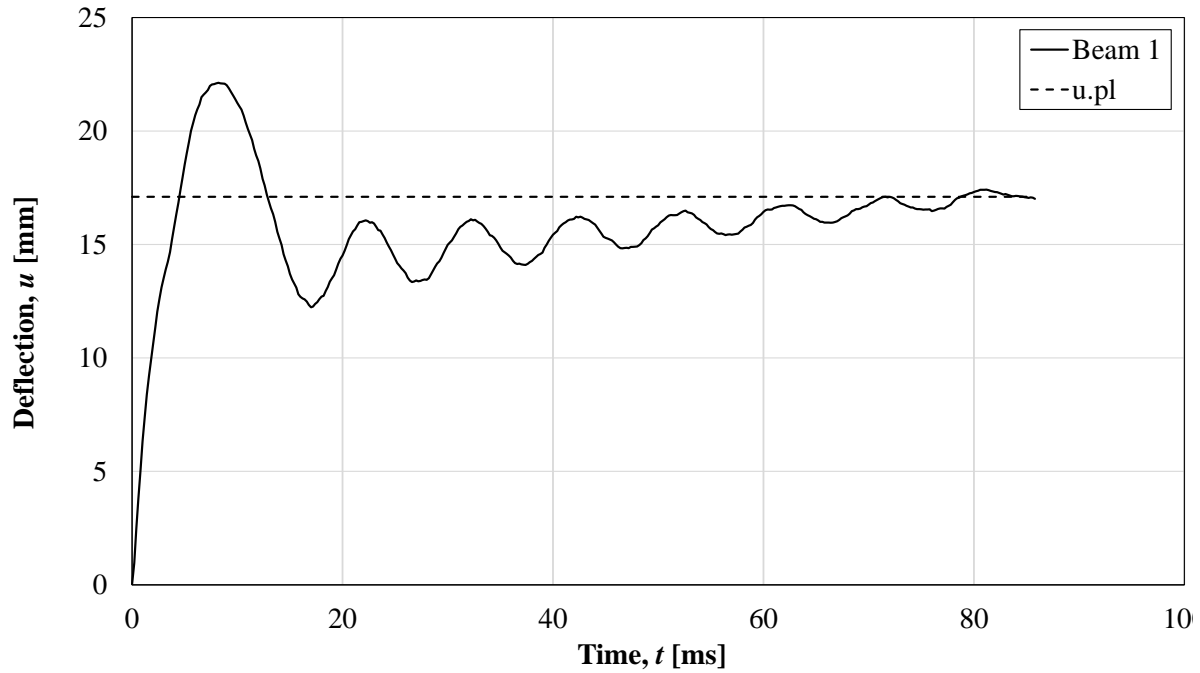


Figure F.2 Deflection-time for beam 1. The plastic deflection was determined as the average deflection of the last 5 ms.

F.2 Method 2 - From next Image Sequence

The first image (reference image) of the sequence taken at the first impact was used as the first image in the sequence taken at the second impact. The plastic deformation after the first impact was the difference in deflection of the midpoint of the reference image and the image before the second impact. Figure F.3 and F.4 show how the plastic deflection was determined.

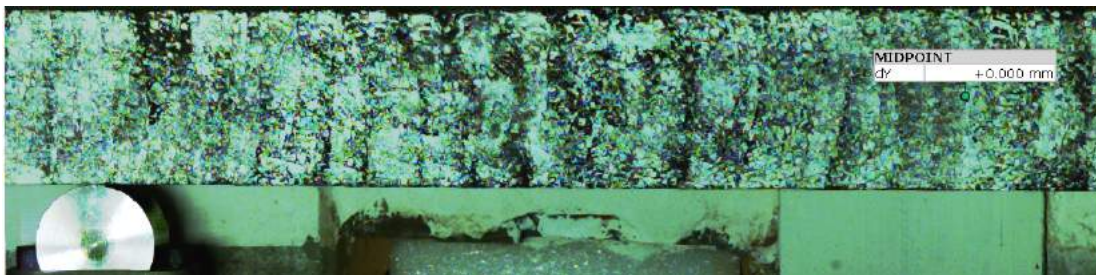


Figure F.3 First image (reference image) from the sequence taken at the first impact at beam 1.

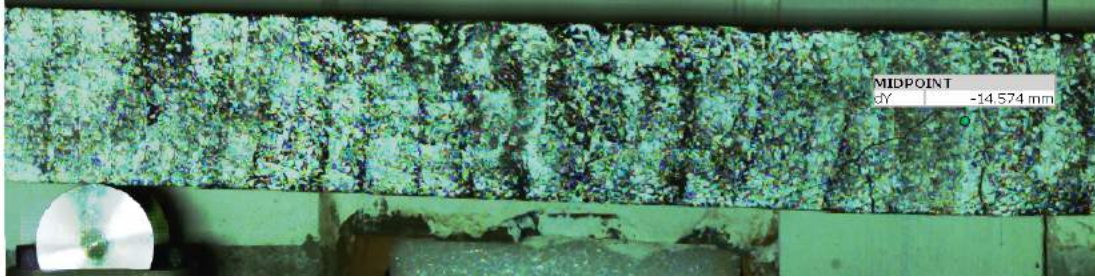


Figure F.4 First image from the sequence taken at the second impact at beam 1. Note that the second impact has not yet occurred.

Unfortunately, there was no beam image from the dynamic testing after the last impact. Instead, the plastic deformation in this case could be determined from the beam image for the static testing. How this was performed is schematically shown in Figure F.5. It should be noted that the deflection in this case was determined at the top of the beam and not in the middle. The reason for this was the local damage of the beam which made it difficult to locate the centre midpoint.

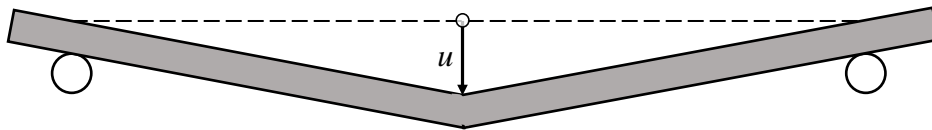


Figure F.5 How the plastic deformation after the last impact was determined.

F.3 Comparison of the Two Methods

The result from the two ways to determine the deformations is summarized in Table F.1. The comparison was carried out for the first drop of the 9 beams that were subjected to more than one drop. As can be seen the method by using the image sequence from first drop show higher deformations than the second method. A reason for the difference could be that the beam was rotating in the upward movement during the first sequence and therefore shows a different result. Since only half of the beam was captured during the dynamic response, this was impossible to investigate further and therefore the deformations was determined according to the second method.

Table F.1 Comparison of two methods used for determine the plastic deformations. All values is in mm.

Series	$u_{pl.1}$, method 1	$u_{pl.2}$, method 2	Difference	$u_{pl.1}/u_{pl.2}$ [%]
1	7.2	5.4	1.8	25
2	17.8	14.2	3.6	20
3	21.7	20.7	1.0	5

G Determination of Plastic Deformation in Static Tests

The plastic deformation at $0.35L$ from support was measured in GOM Correlate 2017. Firstly, a line was drawn at the top part of the beam, between the supports. Secondly, two vertical lines were drawn from the newly constructed line and the parts of the beam where the loads were applied. Lastly, the plastic deformation was calculated as the average between the two vertical lines, u_1 and u_2 . The method is also shown in Figure G.1. Table G.1 shows a summary of the plastic deformation of the beams after subjected to dynamic loading. These deformations are also referred to as the initial deflection when analysing the static tests in Section 8.4.

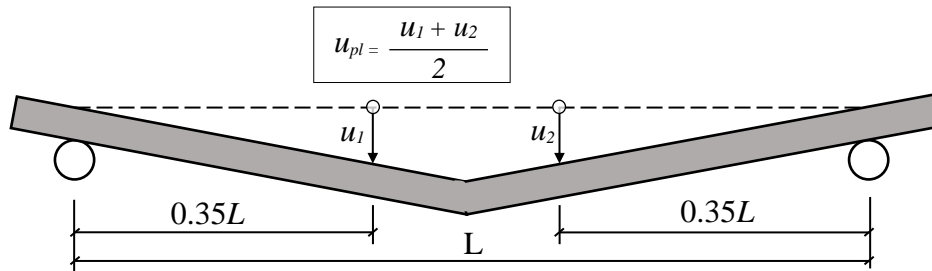


Figure G.1 How the plastic deformation at $0.35L$ was determined.

Table G.1 Plastic deformation of the beams in Series-1-4 after dynamic testing. Measured under the applied load. Values in mm.

Beam nr	1	2	3	4	5	6	10	11	12	13	14	15
u_{pl}	19.5	19.6	22.2	27.4	18.3	14.9	34.0	31.4	35.3	33.3	35.9	35.8

H Calculation of Impulse Load

The impulse was determined by calculating the area under the $F-t$ curve, constructed from the accelerations extracted in DIC. The total impulse I_{tot} was divided into two contributions, namely I_{ini} and I_{post} , where the first was the impulse during the first peak and the latter the impulse that occurred over a longer time. Figure H.1 schematically shows how the curve was estimated with a trend line. The trend line for I_{post} is a polynomial of degree two, which was integrated to get the area under the curve. The limit of the calculation was done from the moment the drop-weight hit the beam until I_{post} reached zero.

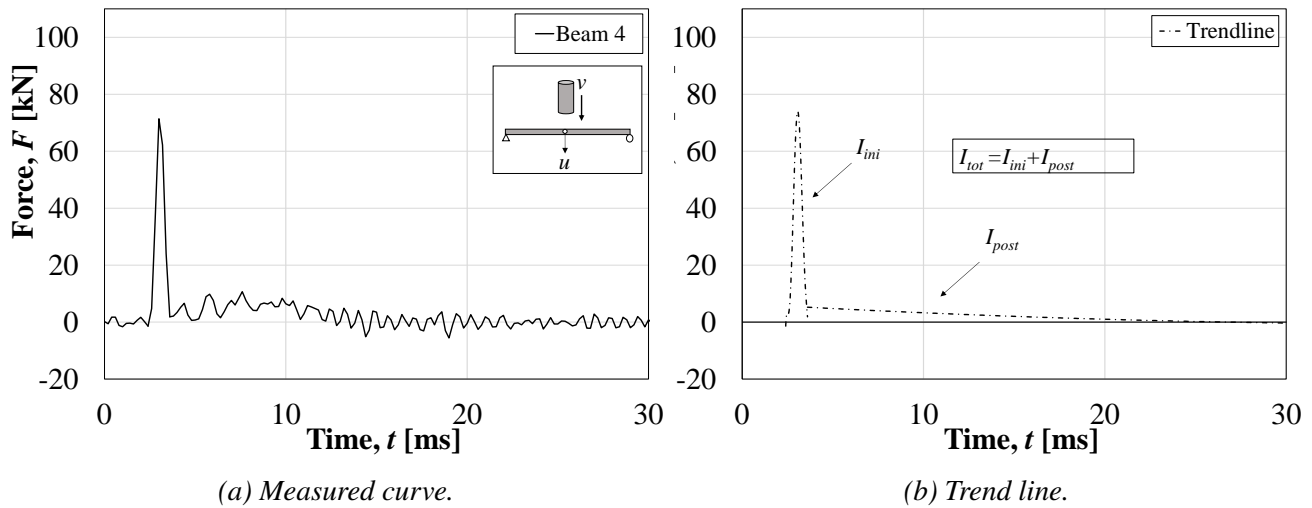


Figure H.1 Schematic showing of how the impulse load was determined.

I Calculation of Stiffness

It is important to reflect on how the stiffness's k_i is calculated since the curve has a parabolic shape with different shape, depending on if it is unloading or reloading, which can be seen in Figure I.1. The stiffness's presented here represents a mean value of the unloading and loading stiffness. A straight line has been assumed from the lowest values up to where the two lines cross each other, almost at the start of the unloading process and the stiffness k is calculated as

$$k = \frac{\Delta F}{\Delta u} \tag{I.1}$$

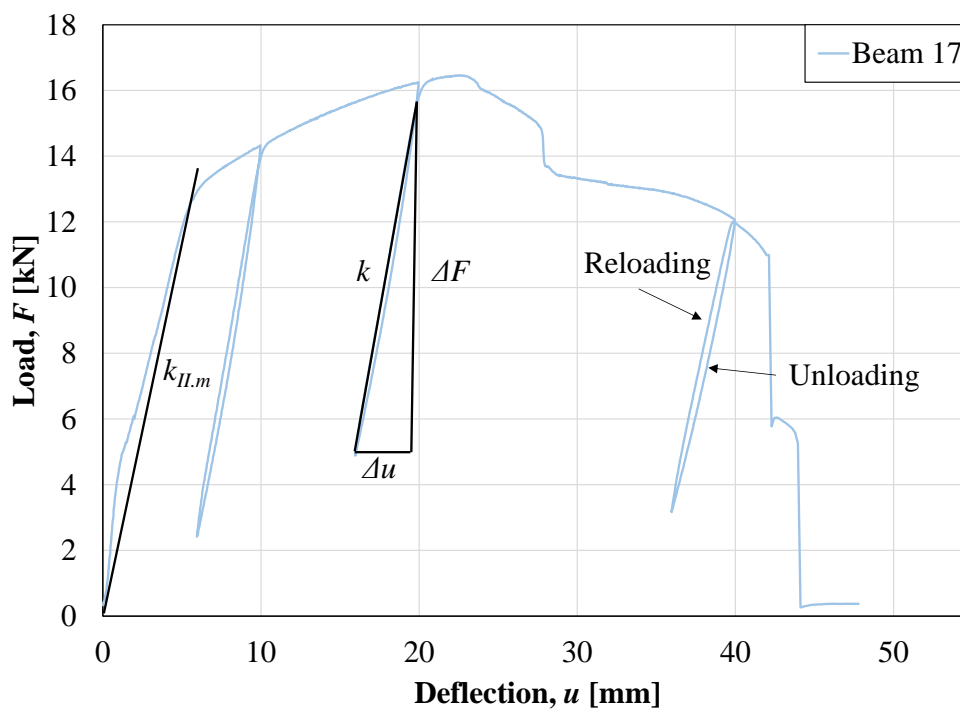


Figure I.1 Method for measuring the stiffness in different parts of the loading process.

J Calculation of Internal Work

The internal Work is calculated as the area under the load-deflection diagram, see Figure J.1. State II stiffness is assumed when calculating the plastic part of the internal work.

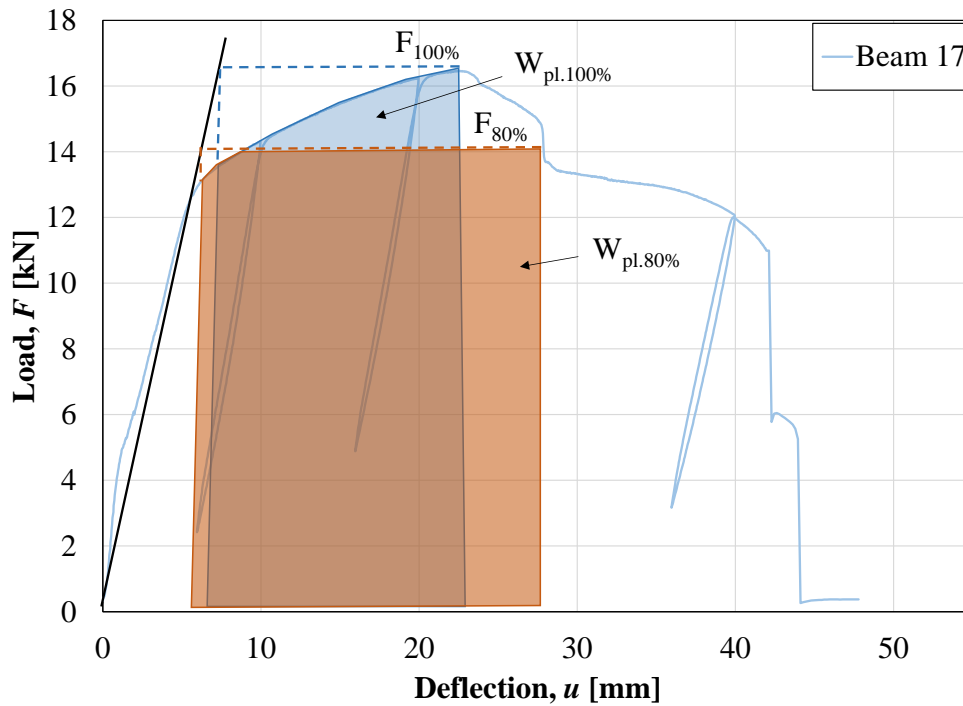


Figure J.1 Method for measuring the stiffness in different parts of the loading process.

K Mathcad Calculations

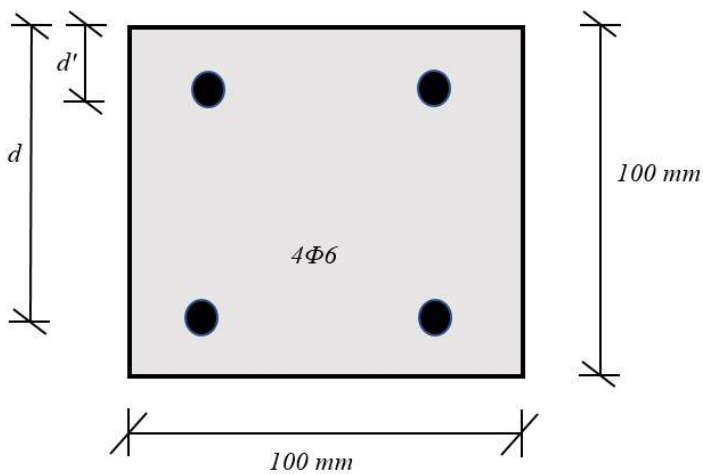
Load capacity of beam

$$\frac{M}{W} \leq \sigma_{\text{allow}}$$

Input data:

Geometry:

h	Beam height
b	Beam width
l	Effective span length
d	Bar diameter
A_s	Area of one bar
n_b	Number of bars in the bottom
n_t	Number of bars in the top



i	i	$\left(t - r \leq \right)$	>	Area of bottom reinforcement	
i	5	i	$\left(t - r \leq \right)$	>	Area of top reinforcement
			$\left(\right)$	Measured position of bars. From top edge to bottom reinforcement	
	5		$\left(\right)$	Measured position of bars. From top edge to top reinforcement.	

Material properties:

Concrete:

	$\left(\right)$	w	α	Mean compressive strength				
	6	$:=$	w	α	Characteristic compressive strength			
	970	$>$	w	α	Mean concrete tensile strength			
	$=7-6$	$=99$	$\left(\right)$	$=999$	Factor for flexural tensile strength			
F		$\left(r \right)$	>0	w	α	Flexural tensile strength		
n	$>>$	$=9$	6	970	$\left(o > r \right)$	p	α	Mean modulus of elasticity
	$9790t$							Ultimate concrete strain

Reinforcing steel:

	t	$=0$	w	α	Mean yield strength
	\rightarrow	0	w	α	Ultimate strength
n	\leq	p	α	Mean modulus of elasticity	
	$97-9$	$\left(\right)$	9790	Ultimate steel strain	
	n	$\left(\right)$	9790	Yield strain	

Design values

Partial factors are set to 1.0 which gives:

$\left(\right)$	0	$=7$	$=0$	w	α	Design compressive strength
------------------	-----	------	------	-----	----------	-----------------------------

$$\sigma = \sigma_y$$

Design yield stress

And so on...

Load capacity in Ultimate limit state considering only bottom reinforcement

$$\epsilon_s = \epsilon_{yk}$$

Stress block factors taken from Engström (2013). Table B5.3

$$\epsilon_s = \epsilon_{yk}$$

Assume yielding in the steel

$$x$$

$$x$$

Guessed position of neutral axis

$$\epsilon_s = \epsilon_{yk}$$

$$x$$

Calculated position of neutral axis. NOTE! Top reinforcement is in the tensile zone but is neglected anyway

$$x$$

$$x$$

$$M = \sigma_y A_s (d - \frac{x}{2})$$

Moment capacity

$$\epsilon_s = \epsilon_{yk}$$

Considering three point loading

$$M = \sigma_y A_s (d - \frac{x}{2})$$

Considering four point loading

$$M = \sigma_y A_s (d - \frac{x}{2})$$

Load capacity for two point loads acting 0.35m from each side

$$\kappa = \frac{1}{d^2}$$

Curvature at failure

Load capacity at yielding considering only bottom reinforcement

$\epsilon_{top} < \epsilon_{cr}$	Assume a concrete strain less than the ultimate strain
$\frac{4}{\epsilon_{top} > \epsilon_{cr}}$	Top reinforcement will be at neutral axis
$\epsilon_{top} > \epsilon_{cr} \Rightarrow \epsilon_{top} = \epsilon_{cr} \left(\frac{970}{970 - 4} \right)$	Interpolation from values in Table B5.3 in Engström (2013). 0.436 corresponds to 0.0006 and 0.546 to 0.0007
$\epsilon_{top} > \epsilon_{cr} \Rightarrow \epsilon_{top} = \epsilon_{cr} \left(\frac{970}{970 - 4} \right)$	Stress block factors taken from Engström (2013). Table B5.3. Also interpolated
$\epsilon_{top} > \epsilon_{cr} \Rightarrow \epsilon_{top} = \epsilon_{cr} \left(\frac{970}{970 - 4} \right)$	Should be around zero
$w_{top} = \epsilon_{top} \cdot \frac{6}{\epsilon_{top} > \epsilon_{cr}} \Rightarrow w_{top} = x$	Moment capacity
$O_{EM} = \frac{r}{v} \cdot w_{top} \Rightarrow O_{EM} = x$	Considering three point loading
$O_{EN} = \frac{w_{top}}{970t} \Rightarrow O_{EN} = x$	Considering four point loading
$O_{FIN} = O_{EN} \cdot \frac{970}{970 - 4} \Rightarrow O_{FIN} = x$	Load capacity for two point loads acting 0.35m from each side
$\frac{1}{6} \left(\frac{970}{970 - 4} \right)^6$	Curvature at yielding

Summary

$$w \quad \rightarrow \quad 0 = x$$

Moment at yielding

$$o \quad F_{IN} \quad \rightarrow \quad r = x$$

Total applied load at yielding

$$\quad \rightarrow \quad 97r =$$

Curvature at yielding

$$w \quad \rightarrow \quad 7 = 0 \quad x$$

Moment capacity

$$o \quad F_{IN} \quad \rightarrow \quad 7 = 0 \quad x$$

Load capacity

$$\quad \rightarrow \quad 97 =$$

Ultimate curvature

$$6 \quad \rightarrow \quad 97 =$$

Theoretical load-deflection relationship

State I

$$n = \frac{E_s}{E_c} \quad \text{Modular ratio}$$

Moment of inertia in state I

$$I_{sI} = \frac{b h^3}{12} + n A_s r^2 \quad \text{Moment of inertia in state I}$$

$$M_{cr} = \frac{F_s s_s}{970t} \quad \text{Cracking moment}$$

$$P_{cr} = \frac{M_{cr}}{970t} \quad \text{Considering four point loading. Total load per point when cracking occurs}$$

$$P_{cr} = \frac{M_{cr}}{970t} \quad \text{Load capacity for two point loads acting 0.35m from each side when cracking occurs}$$

State II

Start by considering moment of area around the neutral axis

$$I_{sII}$$

Assuming that top reinforcement is in the tensile zone

$$I_{sII} = \frac{b h^3}{12} + n A_s r^2 - n A_s r^2 \quad \text{Moment of inertia in state II}$$

$$I_{sII} = \frac{b h^3}{12} + n A_s r^2 - n A_s r^2 \quad \text{Moment of inertia in state II}$$

Stiffnesses

$$u_s = \frac{M}{I_{sI}} \quad \text{Stiffness in state I}$$

$$u_{sII} = \frac{M}{I_{sII}} \quad \text{Stiffness in state II}$$

Deformation considering only State II until ultimate load

$$O_{FEN} \Rightarrow \vec{x}$$

Peak load

$$O_{FEN} \Rightarrow \vec{u}_{ss}$$

Deflection at peak load

$$O_{FEN} \Rightarrow \vec{u}_{ss}$$

Vectors for plot

Deformation considering state I and state II

$$O_{FEN} \Rightarrow \vec{u}_s$$

Deformation at cracking

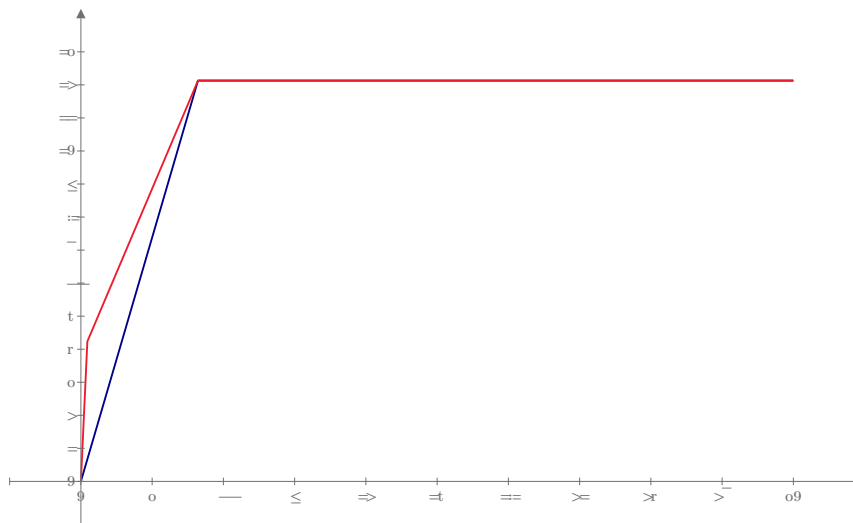
$$O_{FEN} \Rightarrow \vec{u}_{ss}$$

Stiffness between cracking and yielding

$$O_{FEN} \Rightarrow \vec{u}_{ss}$$

Vectors for plot

Load-deformation plot



$$\frac{O_{FEN} \Rightarrow \vec{x}}{O_{FEN} \Rightarrow \vec{u}_{ss}}$$

$$\frac{O_{FEN} \Rightarrow \vec{x}}{O_{FEN} \Rightarrow \vec{u}_{ss}}$$

Prediction of Plastic rotation capacity

Input data:

$v =$ Span length

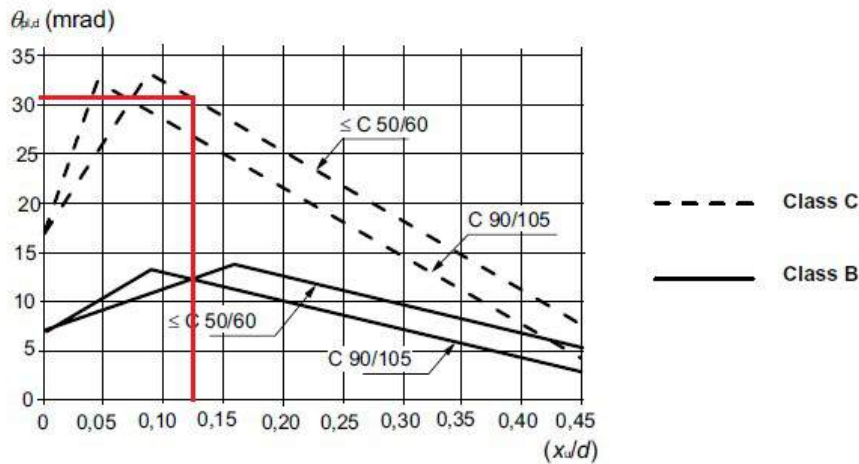
$l = 970t$ Distance to critical section from support

Eurocode 2

$\langle \bar{x} \rangle$

Position of neutral axis in ultimate state. Considering only bottom reinforcement

$\langle 97 \Rightarrow$



$\theta_{pl} = 970 =$

Plastic rotation for a beam with slenderness 3

$l = 9700$

Slenderness

$\sqrt{0.7} = 0.837$

Correction factor

$\theta_{pl} = 970 \cdot 0.837 =$

Corrected rotation capacity for real slenderness

$\theta_{pl} > 970 \cdot 0.837 =$

Consider that the angle referred in EC is twice the angle studied in this report

$$m_l = m_l \cdot I \cdot \frac{1}{7} =$$

Plastic deformation

Betonghandboken (ABC-Method)

$$5 \cdot 9$$

Mechanical ration of compression reinforcement. It is zero since it has been prven to be subjected to tensile forces

$$9$$

Mechanical ration of shear reinforcement. It is zero since there is no shear reinforcement present

$$i \quad (97 \cdot 9 >)$$

Mechanical ratio of tension reinforcement. The contribution of the top bars can be neglected since no stirrups were included

$$i = 4 \cdot 70 \quad 4 \cdot 0 \quad 56 \cdot t \quad (97 \leq$$

Factor A

$$97 \cdot t \quad i > 709 \quad y \cdot u ($$

$$k =$$

Factor B

$$i \cdot k \quad (97 \leq \quad 97 \leq = 7 \quad y \cdot u ($$

$$l \quad - \quad I \quad (\quad 0 = 7 \quad > =$$

Factor C

$$m_{OEkl} \quad i \cdot k \cdot l \quad = 9^{60} \quad (97 =$$

Plastic rotation

$$m_{OEkl} \quad m_{OEkl} \quad I \quad (\quad t \cdot r \Rightarrow$$

Plastic deformation

Bk25

$$97 \quad 4 \cdot 97 \cdot t \quad v \quad (97 = \leq$$

Plastic hinge is formed in the field
Plastic hinge length

$$F \quad \frac{97 =}{4} \quad (97 > =$$

Checking failure mode

$$(97 \cdot 9 >$$

$$m_{LOF} \quad \frac{97}{4} \quad = 4 \cdot 97 \cdot v \quad (97 =$$

ws > wcrit

$$R_{LO} \quad R_{LOF} \quad I \setminus > 0 \bar{t} \text{---}$$

Methods based on equivalent hinge length

Tamminens D-Factor

970 Factor depending on concrete class
 $m \setminus 0 \bar{t} = t$ Factor D

R_{OK} $i \ k \ l \ m \Rightarrow 9^{60} \setminus 970 \text{---}$ Plastic rotation

R_{OK} R_{OK} $I \setminus > \bar{t} = 0 \leq$ Plastic deformation

Baker and Amarkone

$K \ 97 \leq$ Cold worked steel
 $L =$ No axial load. P=0

$M \ 97 \leq 6$ $6 = 0 \bar{t} = w \alpha$ $\setminus 97 t$
 $\triangleq w \alpha$

$R_i \ K \ L \ M \ I \ r$ $\setminus t \bar{t} =$ Equivalent plastic hinge length

$R_i \ R_i \ \setminus 970 >$ Plastic rotation

ACI-ASCE Committee 428

$\varepsilon \ 979r \ 6$ $\setminus = \bar{t} \leq$ Strain ratio
 6

$\varepsilon \ w \ 6 \ w$ $\setminus =$ Moment ratio
 $w \ 6 \ w$

$I \setminus 970 t$ Not the value suggested in their method. But to calculate it according to their method, a uniformly distributed load is needed. Therefore, the value used in this report is used

R_{LSF} $\varepsilon \ 4 \ 970 \ I \ \varepsilon \ \varepsilon \ \setminus \ 0 \bar{t} \leq$ Lower value of l_p

$$E l s F \quad \varepsilon > 4 \rho \frac{M}{E l} \quad \left(\frac{M}{E l} \leq \frac{f_y}{E} \right) \quad \text{Upper value of } l_p$$

$$E l s F \quad E l s F \quad \left(\rho \leq \frac{f_y}{E} \right) \quad \text{Plastic rotation}$$

$$E l s F \quad E l s F \quad \left(\rho > \frac{f_y}{E} \right) \quad \text{Plastic rotation}$$

Paulay and Priestley

$$\left(\frac{M}{E l} \leq \frac{f_y}{E} \right) \quad \left(\frac{M}{E l} > \frac{f_y}{E} \right)$$

$$E l s F \quad \rho \leq \frac{f_y}{E} \quad \left(\frac{M}{E l} \leq \frac{f_y}{E} \right) \quad \text{Equivalent plastic hinge length}$$

$$E l s F \quad E l s F \quad \left(\rho > \frac{f_y}{E} \right) \quad \text{Plastic rotation}$$

Panagiotakos and Fardis

$$E l s F \quad \rho \leq \frac{f_y}{E} \quad \left(\frac{M}{E l} > \frac{f_y}{E} \right) \quad \text{Equivalent plastic hinge length. No slipping of reinforcement possible. One length for cyclic and one for monotonic loading}$$

$$E l s F \quad E l s F \quad \left(\frac{M}{E l} \leq \frac{f_y}{E} \right) \quad \text{Plastic rotation at cyclic loading}$$

$$E l s F \quad E l s F \quad \left(\frac{M}{E l} > \frac{f_y}{E} \right) \quad \text{Plastic rotation at monotonic loading}$$

Summary of rotational capacities in radians

$\theta_{rl} \leq$	Eurocode
$\theta_{OEkl} =$	Betonghandboken
$\theta_{LOF} =$	Bk25
$\theta_{OE} =$	Tamminens D-factor
$\theta_i \geq$	Baker and Amarkone
$\theta_{lsF} =$	ACI-ASCE Committee 428 lower value
$\theta_{lsF} \geq$	ACI-ASCE Committee 428 upper value
$\theta_{\alpha} =$	Paulay and Priestley
$\theta_{oF} =$	Panagiotakos and Fardis cyclic loading
$\theta_{oF} >$	Panagiotakos and Fardis monotonic loading

L MATLAB Script for 2DOF Model

```
%%%%%%%%%%%%%%%%%%%%%%%%%%%%%%%%%%%%%%%%%%%%%%%%%%%%%%%%%%%%%%%%%%%%%%%%%
%%%%%%%%%%%%%%%%%%%%%%%%%%%%%%%%%%%%%%%%%%%%%%%%%%%%%%%%%%%%%%%%%%%%%%%%%
%%%%%%%%%%%%%%%%%%%%%%%%%%%%%%%%%%%%%%%%%%%%%%%%%%%%%%%%%%%%%%%%%%%%%%%%%
Simplified 2DOF System
%%%%%%%%%%%%%%%%%%%%%%%%%%%%%%%%%%%%%%%%%%%%%%%%%%%%%%%%%%%%%%%%%%%%%%%%%
%%%%%%%%%%%%%%%%%%%%%%%%%%%%%%%%%%%%%%%%%%%%%%%%%%%%%%%%%%%%%%%%%%%%%%%%%
Jack Jönsson
Anton Stenseke
%%%%%%%%%%%%%%%%%%%%%%%%%%%%%%%%%%%%%%%%%%%%%%%%%%%%%%%%%%%%%%%%%%%%%%%%%
Modified from the version made by
Fabio Lozano Mendoza and Josef Makdesi Aphram
%%%%%%%%%%%%%%%%%%%%%%%%%%%%%%%%%%%%%%%%%%%%%%%%%%%%%%%%%%%%%%%%%%%%%%%%%
Chalmers University of Technology
%%%%%%%%%%%%%%%%%%%%%%%%%%%%%%%%%%%%%%%%%%%%%%%%%%%%%%%%%%%%%%%%%%%%%%%%%
15 - May - 2018
%%%%%%%%%%%%%%%%%%%%%%%%%%%%%%%%%%%%%%%%%%%%%%%%%%%%%%%%%%%%%%%%%%%%%%%%%
clear all
close all
clc

conditions=1;          % Indata for different impact conditions.
                      % 1 - 2.5 m, 10 kg
                      % 2 - 5.0 m, 10 kg
                      % 3 - 2.5 m, 20 kg
                      % 4 - 5.0 m, 20 kg

resistance=1;         % Indata for resistance
                      % 1 - resistance if yielding is at fy
                      % 2 - resistance if yielding is at fu

%%%%%%%%%%%%%%%%%%%%%%%%%%%%%%%%%%%%%%%%%%%%%%%%%%%%%%%%%%%%%%%%%%%%%%%%%

if conditions==1
    m_1 = 10;          % [kg] mass of the drop-weight
    L_d = 0.250;       % [m] Length Drop-weight
    height = 2.5;      % [m] Drop height
elseif conditions==2
    m_1 = 10;          % [kg] mass of the drop-weight
    L_d = 0.250;       % [m] Length Drop-weight
    height = 5.0;      % [m] Drop height
elseif conditions==3
```

```

    m_1 = 20;           %[kg] mass of the drop-weight
    L_d = 0.500;       %[m] Length Drop-weight
    height = 2.5;      % [m] Drop height
elseif conditions==4
    m_1 = 20;           %[kg] mass of the drop-weight
    L_d = 0.500;       %[m] Length Drop-weight
    height = 5.0;      % [m] Drop height
end

if resistance==1
    R_u=8.491e3;        % Resistance with fy
elseif resistance==2
    R_u=10.189e3;      % Resistance with fu
end

```

MATERIAL PROPERTIES

```

% Concrete
r_c = 2384;           % [kg/m^3] Mass density
E_c = 32.53e9;        % [Pa] Modulus of elasticity

% Steel
r_s = 7800;           % [kg/m^3] Mass density
E_s = 196e9;          % [Pa] Modulus of elasticity

```

GEOMETRY

```

A_1 = 5027e-6;        % [m^2] Area dropweight
A_2 = 0.1*0.1;        % [m^2] Area beam

L_b = 1;               % [m] Length Beam
L_d = L_d;             % [m] Length Drop-weight

```

TRANSFORMATION FACTORS

```

% Transformation factors for the beam

k_b_m_el = 0.486;     % Elastic mass transformation factor
k_b_m_pl = 0.333;     % Plastic mass transformation factor

k_b_F_el = 1;         % Elastic load transformation factor
k_b_F_pl = 1;         % Plastic load transformation factor

k_b_K_el = 1;         % Elastic stiffness transformation factor
k_b_K_pl = 1;         % Plastic stiffness transformation factor

% Transformation factors for the drop-weight

```

```

k_d_m = 1;           % Plastic mass transformation factor
k_d_F = 1;           % Plastic load transformation factor
k_d_K = 1;           % Plastic stiffness transformation factor

```

MASS PROPERTIES

```

m_1 = m_1;           % [kg] mass of the drop-weight
m_2 = r_c*A_2*L_b;   % [kg] mass of the beam

```

```
% Mass matrix
```

```
M = [m_1*k_d_m 0; 0 m_2*k_b_m_pl];
```

STIFFNESS PROPERTIES

```

I_b_ii = 1.121e-6;   % [m^4] Second moment of inertia of the beam
                    % corresponding to the stiffness in state II.
                    % Calculated beforehand for adjusted position of
                    % reinforcement bars

```

```

K_el_1 = A_1*E_s/L_d; % [N/m] Elastic stiffness of the drop-weight
K_el_2 = 48*E_c*I_b_ii/L_b^3; % [N/m] Elastic stiffness of the beam

```

```
% Initial stiffness matrix
```

```

K_el = [K_el_1 -K_el_1;
        -K_el_1 K_el_1+K_el_2];

```

MATERIAL RESPONSE

```
% Drop-weight
```

```

R_1 = 50000;         % [N] Plastic resistance
u_el_1 = R_1/K_el_1; % [m] Limit of elastic deformation
u_rd_1 = 50000;     % [m] Limit of plastic deformation

```

```
% Beam
```

```

R_2_sw = r_c*9.81*A_2*L_b/2; % [N] Reduction of plastic resistance
% due to self-weight

```

```
R_2 = R_u - R_2_sw; % [N] Plastic resistance.
```

```

u_el_2 = R_2/K_el_2; % [m] Limit of elastic deformation
u_rd_2 = 50;        % [m] Limit of plastic deformation

```

DETERMINATION OF EIGENFREQUENCIES

```
[L,X] = eig(K_el, M);      % "L" is a matrix containing the eigenvectors
                          % "X" is a matrix containing the eigenvalues
```

```
% Maximum eigenfrequency
```

```
w_max = sqrt(max(max(X)));
```

CRITICAL TIME STEP

```
h_crit = 2/w_max;         % [s] Maximum admissible value
```

```
h = 0.1e-4;               % [s] Chosen time step
```

```
t_end = 40e-3;           % [s] End of sequence
```

```
t = linspace(0,t_end,t_end/h); % Time vector
```

```
if h >= h_crit
```

```
    disp('ERROR, chosen time step too large')
```

```
end
```

INITIAL CONDITIONS

```
% Empty matrices
```

```
dofs = 2;                 % Number of degree of freedom
```

```
u = zeros(dofs, length(t)); % Empty matrix storing displacement vectors
```

```
v = zeros(dofs, length(t)-1); % Velocity vectors
```

```
a = zeros(dofs, length(t)-1); % Acceleration vectors
```

```
% Assigning initial values
```

```
u(:,1) = [0;0];          % Initial Displacement
```

```
height = height;         % [m] Drop height
```

```
%v_d = 8.86;             % [m/s] Initial velocity of drop-weight
```

```
% [measured value]
```

```
v_d = sqrt(2*9.81*height); % [m/s] Initial velocity of drop-weight
```

```
% % [theoretical value]
```

```
v(:,1) = [v_d; 0];      % Velocities at time t = 0
```

```
a_0 = inv(M)*(-K_el*u(:,1)); % Initial acceleration vector
```

```
a(:,1) = a_0;           % Initial acceleration as calculated before
```

```
u_b0 = u(:,1)-h*v(:,1)+h^2/2*a(:,1); % Displacement at time step n-1
```

```

% Initial plastic deformation

u_pl_1 = 0;          % Plastic deformation of rod
u_pl_2_pos = 0;     % Plastic deformation of beam in compression
u_pl_2_neg = 0;     % Plastic deformation of beam in tension

CENTRAL DIFFERENTIAL METHOD
for i =2:length(t)

    du = u(1,i-1)-u(2,i-1);    % [m] Relative displacement bewteen beam
                                %      and drop-weight

    u2 = u(2,i-1);            % [m] Downwards beam displacement

    % Determining resistance and stiffness of ficticious spring between
    % drop-weight and beam

    % If du = 0, set stiffness equal to elastic stiffness
    if du == 0;
        K_1 = K_el_1;
    % If spring is in tension, set stiffness to 0
    elseif du < u_pl_1;
        K_1 = 0;
    % If spring is in elastic range
    elseif du > u_pl_1 && du <= u_pl_1+u_el_1;
        R = K_el_1*(du-u_pl_1);
        K_1 = R/du;
    % If spring is in plastic range
    elseif du > u_pl_1+u_el_1
        K_1 = R_1/du;
        u_pl_1 = du-u_el_1;
    end

    % Determining resistance and stiffness of beam spring

    % If u2 = 0, set stiffness equal to elastic stiffness
    if u2 == 0;
        K_2 = K_el_2;
    % If spring is in elastic tension/compression
    elseif u2 > u_pl_2_pos - u_el_2 && u2 <= u_pl_2_pos + u_el_2
        R = K_el_2*(u2-u_pl_2_pos);
        K_2 = R/u2;
    % If spring is in plastic compression
    elseif u2 > u_pl_2_pos + u_el_2;

```

```

        K_2 = R_2/u2;
        u_pl_2_pos = u2-u_el_2;
% If spring is in plastic tension
elseif u2 <= u_pl_2_pos - u_el_2
        K_2 = -R_2/u2;
        u_pl_2_neg = abs(u2+u_el_2-u_pl_2_pos);
        u_pl_2_pos = u_pl_2_pos - u_pl_2_neg;
end

% Storing values of resistance for all time steps
Res(1,i-1) = K_1*du;
Res(2,i-1) = K_2*u2;

% Computing stiffness matrix
K = [(K_1) -(K_1); -(K_1) (K_1)+(K_2)];

% Calculation of displacement, velocity and acceleration
if i==2
    u(:,i) = inv(M/h^2)*(-(K-2*M/h^2)*u(:,i-1)-(M/h^2)*u_b0);
else
    u(:,i) = inv(M/h^2)*(-(K-2*M/h^2)*u(:,i-1)-(M/h^2)*u(:,i-2));
    v(:,i-1) = (u(:,i)-u(:,i-2))/(2*h);
    a(:,i-1) = (u(:,i)-2*u(:,i-1)+u(:,i-2))/h^2;
end
end

```

end

CALCULATION OF ENERGY

% External Work of Beam

```

DeltaWe(1) = 0;
We(1) = 0;
for i = 2:(length(t)-1)
    DeltaWe(i) = 0.5*(Res(1,i-1)+Res(1,i))*(u(2,i)-u(2,i-1));
    We(i) = We(i-1)+DeltaWe(i);
end

```

% Internal Work of Beam

```

DeltaWi(1) = 0;
Wi(1) = 0;
for i = 2:(length(t)-1)
    DeltaWi(i) = 0.5*(Res(2,i-1)+Res(2,i))*(u(2,i)-u(2,i-1));
end

```

```

    Wi(i) = Wi(i-1)+DeltaWi(i);
end

% Kinetic Energy
Wk(1)=0;
for i = 2:(length(t)-1)
    Wk(i) = m_2*k_b_m_pl*0.5*v(2,i-1)^2;
end

% Total Energy
Wt(1)=0;
for i = 2:(length(t)-1)
    Wt(i) = Wi(i)+Wk(i);
end

```

CREATING PLOTS

```
% Displacement vs Time plots
```

```

figure(1)
plot(t*1000,u(1,:)*1000,'LineWidth',3);
set(gca,'fontsize',16)
title('Displacement of mass 1', 'FontSize', 30)
xlabel('Time [ms]'); ylabel('Displacement [mm]');

```

```

figure(2)
plot(t*1000,u(2,:)*1000,'LineWidth',3);
set(gca,'fontsize',16)
title('Displacement of mass 2', 'FontSize', 30)
xlabel('Time [ms]'); ylabel('Displacement [mm]');

```

```
% Resistance vs Displacement
```

```

figure(3)
plot(u(2,1:length(u)-1)*1000,Res(2,+)/1000,'LineWidth',3);
set(gca,'fontsize',16)
title('Internal Resistance vs Displacement - Body 2', 'FontSize', 30)
xlabel('Displacement [mm]'); ylabel('Resistance [kN]');

```

```

%figure(4)
plot(u(1,1:1500)*1000-u(2,1:1500)*1000,Res(1,1:1500)/1000,'LineWidth',3);
set(gca,'fontsize',16)
title('Internal Resistance vs Displacement - Body 1', 'FontSize', 30)
xlabel('Displacement [mm]'); ylabel('Resistance [kN]');

```

```
%
```

```

%Resistance vs Time

figure(5)
plot(t(1:length(t)-1)*1000,Res(2,:)/1000,'LineWidth',3);
set(gca,'fontsize',16)
title('Internal Resistance vs Time - Body 2', 'FontSize', 30)
xlabel('Time [ms]'); ylabel('Resistance [kN]');
%
figure(6)
plot(t(1:1500)*1000,Res(1,1:1500)/1000,'LineWidth',3);
set(gca,'fontsize',16)
title('Internal Resistance vs Time - Body 1', 'FontSize', 30)
xlabel('Time [ms]'); ylabel('Resistance [kN]');

% Velocity vs Time

figure(7)
plot(t(1:(length(t)-1))*1000,v(1,:),'LineWidth',3);
set(gca,'fontsize',16)
title('Velocity of Body 1', 'FontSize', 30)
xlabel('Time [ms]'); ylabel('Velocity [m/s]');

figure(8)
plot(t(1:(length(t)-1))*1000,v(2,:),'LineWidth',3);
set(gca,'fontsize',16)
title('Velocity of Body 2', 'FontSize', 30)
xlabel('Time [ms]'); ylabel('Velocity [m/s]');

% Work vs Time

%figure(9)
plot(t(1:(length(t)-1))*1000,We(:),'LineWidth',3);
hold on
plot(t(1:(length(t)-1))*1000,Wi(:),'LineWidth',3);
hold on
plot(t(1:(length(t)-1))*1000,Wk(:),'LineWidth',3);
hold on
plot(t(1:(length(t)-1))*1000,Wt(:),'LineWidth',3);
set(gca,'fontsize',16)
title('External Work of Body 2', 'FontSize', 30)
xlabel('Time [ms]'); ylabel('Velocity [m/s]');

```

```
height;
v_init = v(1,2);
maxdisp = max(max(u(2,:)));
u_pl = maxdisp - u_el_2;

% To get the displacements and time in [mm] and [ms]
t=t*1000;
u=u*1000;
R_2
[height v_init maxdisp u_pl]
```


M LS-DYNA Input File

```

$# LS-DYNA Keyword file created by LS-PrePost(R) V4.5.4 - 07Nov2017
$# Created on Apr-21-2018 (09:37:17)
*KEYWORD
*TITLE
$#                               title
LS-DYNA keyword deck by LS-PrePost
*CONTROL_TERMINATION
$# endtim  endcyc  dtmin  endeng  endmas  nosol
      20.0    0   0.0   0.0  1.000000E8    0
*DATABASE_ELOUT
$#  dt  binary  lcur  iopt  option1  option2  option3  option4
      0.1    3    0    1      0      0      0      0
*DATABASE_GLSTAT
$#  dt  binary  lcur  iopt
      0.1    3    0    1
*DATABASE_MATSUM
$#  dt  binary  lcur  iopt
      0.1    3    0    1
*DATABASE_NCFORC
$#  dt  binary  lcur  iopt
      0.5    3    0    1
*DATABASE_NODFOR
$#  dt  binary  lcur  iopt
      0.5    3    0    1
*DATABASE_NODOUT
$#  dt  binary  lcur  iopt  option1  option2
      0.5    3    0    1    0.0      0
*DATABASE_RCFORC
$#  dt  binary  lcur  iopt
      0.1    0    0    1
*DATABASE_BINARY_D3PLOT
$#  dt  lcdt  beam  npltc  psetid
      0.2    0    0    0    0
$# iopt
      0
*DATABASE_EXTENT_BINARY
$#  neigh  neips  maxint  strflg  sigflg  epsflg  rltflg  engflg
      5     0     0     1     1     1     1     1

```

```

$# cmpflg ieverp beamip dcomp shge stssz n3thdt ialemat
      0      0      1      1      1      1      2      1

$# nintsld pkp_sen  sclp  hydro  msscl  therm  intout  nodout
      0      0      1.0      0      0      0

$#  dtdt  resplt  neipb  quadr  cubic
      0      0      0      0      0

*BOUNDARY_SPC_SET_ID
$#  id                      heading
      1BC left vertical
$#  nsid  cid  dofz  dofz  dofz  dofrx  dofry  dofrz
      1    0    0    0    1    0    0    0

*SET_NODE_LIST_TITLE
BC Left vertical
$#  sid  da1  da2  da3  da4  solver
      1  0.0  0.0  0.0  0.0MECH

$#  nid1  nid2  nid3  nid4  nid5  nid6  nid7  nid8
      10299 10300 10342 10343 11178 11179 11180 11181
      11182 11183 11184 11185 11186 11187 11188 11189
      11190 11191 11192 11193 11194 11195 11196 11197
      11198 11199 11200 11201 11202 11203 11204 11205
      11206 11207 11208 11209 11210 11211 11212 11213
      11214 11215 11216 11217      0      0      0      0

*BOUNDARY_SPC_SET_ID
$#  id                      heading
      2BC left horizontal
$#  nsid  cid  dofz  dofz  dofz  dofrx  dofry  dofrz
      2    0    1    1    0    0    0    0

*SET_NODE_LIST_TITLE
BC Left horizontal
$#  sid  da1  da2  da3  da4  solver
      2  0.0  0.0  0.0  0.0MECH

$#  nid1  nid2  nid3  nid4  nid5  nid6  nid7  nid8
      10288 10331 10958 10959 10960 10961 10962 10963
      10964 10965 10966 10967 10968 10969 10970 10971
      10972 10973 10974 10975 10976 10977      0      0

*BOUNDARY_SPC_SET_ID
$#  id                      heading
      3BC right vertical
$#  nsid  cid  dofz  dofz  dofz  dofrx  dofry  dofrz
      3    0    0    0    1    0    0    0

*SET_NODE_LIST_TITLE
BC Right vertical
$#  sid  da1  da2  da3  da4  solver
      3  0.0  0.0  0.0  0.0MECH

$#  nid1  nid2  nid3  nid4  nid5  nid6  nid7  nid8
      15381 15382 15424 15425 15886 15887 15888 15889
      15890 15891 15892 15893 15894 15895 15896 15897

```

```

15898 15899 15900 15901 15902 15903 15904 15905
15906 15907 15908 15909 15910 15911 15912 15913
15914 15915 15916 15917 15918 15919 15920 15921
15922 15923 15924 15925      0      0      0      0
*BOUNDARY_SPC_SET_ID
$# id heading
   4BC right horizontal
$# nsid  cid  dofz  dofz  dofz  dofz  dofz  dofz
   4      0      1      1      0      0      0      0
*SET_NODE_LIST_TITLE
BC Right horizontal
$#  sid  da1  da2  da3  da4  solver
   4    0.0  0.0  0.0  0.0  0.0MECH
$#  nid1  nid2  nid3  nid4  nid5  nid6  nid7  nid8
   15392 15435 16106 16107 16108 16109 16110 16111
   16112 16113 16114 16115 16116 16117 16118 16119
   16120 16121 16122 16123 16124 16125      0      0
*CONTACT_AUTOMATIC_SURFACE_TO_SURFACE_ID
$#  cid title
   1Contact-Weight-beam
$#  ssid  msid  sstyp  mstyp  sboxid  mboxid  spr  mpr
   3      8      3      3      0      0      0      0
$#  fs  fd  dc  vc  vdc  penchk  bt  dt
   0.0  0.0  0.0  0.0  0.0      0  0.01.00000E20
$#  sfs  sfm  sst  mst  sfst  sfmt  fsf  vsf
   1.0  1.0  0.0  0.0  1.0  1.0  1.0  1.0
*CONTACT_AUTOMATIC_SURFACE_TO_SURFACE_ID
$#  cid title
   2Contact-left support-beam
$#  ssid  msid  sstyp  mstyp  sboxid  mboxid  spr  mpr
   1      8      3      3      0      0      0      0
$#  fs  fd  dc  vc  vdc  penchk  bt  dt
   0.0  0.0  0.0  0.0  0.0      0  0.01.00000E20
$#  sfs  sfm  sst  mst  sfst  sfmt  fsf  vsf
   1.0  1.0  0.0  0.0  1.0  1.0  1.0  1.0
*CONTACT_AUTOMATIC_SURFACE_TO_SURFACE_ID
$#  cid title
   3Contact-right support-beam
$#  ssid  msid  sstyp  mstyp  sboxid  mboxid  spr  mpr
   2      8      3      3      0      0      0      0
$#  fs  fd  dc  vc  vdc  penchk  bt  dt
   0.0  0.0  0.0  0.0  0.0      0  0.01.00000E20
$#  sfs  sfm  sst  mst  sfst  sfmt  fsf  vsf
   1.0  1.0  0.0  0.0  1.0  1.0  1.0  1.0
*PART
$# title
Left support
$#  pid  secid  mid  eosid  hgid  grav  adpopt  tmid

```

```

      1      2      1      0      0      0      0      0
*SECTION_SOLID_TITLE
Support
$# secid  elform  aet
      2      1      0
*MAT_ELASTIC_TITLE
Weight and supports
$# mid      ro      e      pr      da      db not used
      1 0.007711 196000.0 0.3 0.0 0.0 0
*PART
$#                                     title
Right support
$# pid  secid  mid  eosid  hgid  grav  adpopt  tmid
      2      2      1      0      0      0      0      0
*PART
$#                                     title
Weight
$# pid  secid  mid  eosid  hgid  grav  adpopt  tmid
      3      3      1      0      0      0      0      0
*SECTION_SOLID_TITLE
Weight
$# secid  elform  aet
      3      1      0
*PART
$#                                     title
Reinforcement, top-front
$# pid  secid  mid  eosid  hgid  grav  adpopt  tmid
      4      1      5      0      0      0      0      0
*SECTION_BEAM_TITLE
Reinforcement
$# secid  elform  shrf  qr/irid  cst  scoor  nsm
      1      1      1.0      1      1      0.0      0.0
$# ts1  ts2  tt1  tt2  nsloc  ntloc
      6.0  6.0  0.0  0.0  0.0  0.0
*MAT_PIECEWISE_LINEAR_PLASTICITY_TITLE
Multi-linear reinforcement
$# mid      ro      e      pr      sigy  etan      fail  tdel
      5 0.0078 196000.0 0.3 0.0 0.0 1.00000E21 0.0
$# c      p      lcss  lcsr  vp
      0.0  0.0      0      0      0.0
$# eps1  eps2      eps3  eps4  eps5  eps6  eps7  eps8
      0.0  0.0016 0.0036 0.0128 0.0272 0.048 0.075 0.11
$# es1  es2      es3  es4  es5  es6  es7  es8
      420.0  500.0  520.0  560.0  590.0  610.0  620.0  623.0
*PART
$#                                     title
Reinforcement, top-back
$# pid  secid  mid  eosid  hgid  grav  adpopt  tmid

```

```

5 1 5 0 0 0 0 0
*PART
$# title
Reinforcement, bottom-front
$# pid secid mid eosid hgid grav adpopt tmid
6 1 5 0 0 0 0 0
*PART
$# title
Reinforcement, bottom-back
$# pid secid mid eosid hgid grav adpopt tmid
7 1 5 0 0 0 0 0
*PART
$# title
Beam
$# pid secid mid eosid hgid grav adpopt tmid
8 4 3 0 0 0 0 0
*SECTION_SOLID_TITLE
Concrete
$# secid elform aet
4 10 0
*MAT_CONCRETE_DAMAGE_PLASTIC_MODEL_TITLE
Beam Concrete-CDPM2
$# mid ro e pr ecc qh0 ft fc
3 0.0023841 32530.0 0.2 0.517283 0.3 2.8 36.83
$# hp ah bh ch dh as df fc0
0.01 0.08 0.003 2.01.00000E-6 15.0 0.85 0.0
$# type bs wf wf1 ft1 strflg failflg efc
1.0 1.0 0.122 0.0 0.0 0.0 0.0 0.001
*MAT_PLASTIC_KINEMATIC_TITLE
Reinforcement
$# mid ro e pr sigy etan beta
2 0.00785 200000.0 0.3 609.8 584.0 0.0
$# src srp fs vp
0.0 0.0 0.0 0.0
*MAT_ELASTIC_TITLE
Beam elastic concrete
$# mid ro e pr da db not used
4 0.0024 3470.0 0.2 0.0 0.0 0
*INITIAL_VELOCITY_GENERATION
$#nsid/pid styp omega vx vy vz ivatn icid
3 2 0.0 0.0 0.0 -7.0 0 0
$# xc yc zc nx ny nz phase irigid
0.0 0.0 0.0 0.0 0.0 0.0 0 0
*DEFINE_FUNCTION
$# fid heading
1Bond-slip between reinforcement and concrete
$# function
float force(float slip,float leng)

```

```

{
float force,pi,d,area,shear,pf,s1,s2,s3,tmax,tf;
pi = 3.1415926;
d = 6;
s1 = 1.0;
tmax = 15.172;
area = pi*d*leng;
if(slip < s1) {
shear = tmax*(slip/s1)**0.4;
} else{
shear = tmax;
}

force = shear*area;
return force;
}
*CONSTRAINED_BEAM_IN_SOLID_ID
$# coupid title
1reinforcementtop-front
$# slave master sstyp mstyp ncoup cdir
4 8 1 1 0 0 0 1
$# start end axfor
0.0 0.0 0 -1
*CONSTRAINED_BEAM_IN_SOLID_ID
$# coupid title
2reinforcementtop-back
$# slave master sstyp mstyp ncoup cdir
5 8 1 1 0 0 0 1
$# start end axfor
0.0 0.0 0 -1
*CONSTRAINED_BEAM_IN_SOLID_ID
$# coupid title
3reinforcementbottom-front
$# slave master sstyp mstyp ncoup cdir
6 8 1 1 0 0 0 1
$# start end axfor
0.0 0.0 0 -1
*CONSTRAINED_BEAM_IN_SOLID_ID
$# coupid title
4reinforcementbottom-back
$# slave master sstyp mstyp ncoup cdir
7 8 1 1 0 0 0 1
$# start end axfor
0.0 0.0 0 -1
*ELEMENT_SOLID
$# eid pid n1 n2 n3 n4 n5 n6 n7 n8
13000 1 10595 10643 13938 12838 10596 10596 12378 12378
13001 1 12838 13938 13939 12839 12378 12378 12379 12379

```

```

13002  1 12839 13939 13940 12840 12379 12379 12380 12380
.      .      .      .      .      .      .      .      .      .
.      .      .      .      .      .      .      .      .      .
.      .      .      .      .      .      .      .      .      .
931148  8 134688 141565 61788 141564 141564 141564 141564 141564
931149  8 82805 156946 128551 82812 82812 82812 82812 82812
931150  8 134688 107363 61394 61788 61788 61788 61788 61788
*ELEMENT_BEAM
$#  eid  pid    n1    n2    n3  rt1  rr1  rt2  rr2  local
34237  4 34330 34331 34332  0  0  0  0  2
34238  4 34331 34333 34334  0  0  0  0  2
34239  4 34333 34335 34336  0  0  0  0  2
.      .      .      .      .      .      .      .      .      .
.      .      .      .      .      .      .      .      .      .
.      .      .      .      .      .      .      .      .      .
35178  7 36214 36216 36217  0  0  0  0  2
35179  7 36216 36218 36219  0  0  0  0  2
35180  7 36218 36220 36221  0  0  0  0  2
*NODE
$#  nid      x      y      z      tc  rc
  1      0.0    -590.0    -35.0    0  0
  2     100.0    -500.0      0.0    0  0
  3      0.0    -500.0  1.672415e-015    0  0
.      .      .      .      .      .      .
.      .      .      .      .      .      .
.      .      .      .      .      .      .
196209  71.48462  -417.763    63.55512    0  0
196210  73.74369  -177.108    35.98502    0  0
196211  73.39993  -135.9213   35.75033    0  0
*END

```